

NEW DEVELOPMENTS in BIOLOGY, BIOMEDICAL & CHEMICAL ENGINEERING and MATERIALS SCIENCE

**Proceedings of the International Conference on Biology and Biomedical
Engineering (BBE 2015)**

**Proceedings of the International Conference on Chemical Engineering
and Materials Science (CEMS 2015)**

**Vienna, Austria
March 15-17, 2015**

NEW DEVELOPMENTS in BIOLOGY, BIOMEDICAL & CHEMICAL ENGINEERING and MATERIALS SCIENCE

Proceedings of the International Conference on Biology and Biomedical Engineering (BBE 2015)

Proceedings of the International Conference on Chemical Engineering and Materials Science (CEMS 2015)

**Vienna, Austria
March 15-17, 2015**

Copyright © 2015, by the editors

All the copyright of the present book belongs to the editors. All rights reserved. No part of this publication may be reproduced, stored in a retrieval system, or transmitted in any form or by any means, electronic, mechanical, photocopying, recording, or otherwise, without the prior written permission of the editors.

All papers of the present volume were peer reviewed by no less than two independent reviewers. Acceptance was granted when both reviewers' recommendations were positive.

Series: Recent Advances in Biology and Biomedicine Series | 8

ISSN: 1790-5125

ISBN: 978-1-61804-284-2

NEW DEVELOPMENTS in BIOLOGY, BIOMEDICAL & CHEMICAL ENGINEERING and MATERIALS SCIENCE

**Proceedings of the International Conference on Biology and Biomedical
Engineering (BBE 2015)**

**Proceedings of the International Conference on Chemical Engineering
and Materials Science (CEMS 2015)**

**Vienna, Austria
March 15-17, 2015**

Organizing Committee

Editors:

Professor Manijeh Razeghi, Center for Quantum Devices
Professor Valeri Mladenov, Technical University of Sofia, Bulgaria
Professor Photios A. Anninos, Democritus University of Thrace

Program Committee:

Prof. Peter Dieter, Faculty of Medicine 'Carl Gustav Carus', Dresden, Germany
Prof. Andrei Korobeinikov, Centre de Recerca Matematica, Barcelona, Spain
Prof. Wolfgang Wenzel, Institute for Nanotechnology, Germany
Prof. Seiji Shibasaki, Hyogo University of Health Sciences, Japan
Prof. Gary A. Lorigan, Miami University, USA
Prof. Ziad Fajloun, Universite Libanaise, Lebanon
Prof. Nikolai N. Modyanov, University of Toledo, USA
Prof. Dhavendra Kumar, University of South Wales, UK
Prof. Geoffrey Arden, European Vision Institute, UK
Prof. Photios Anninos, Democritus University of Thrace, Alexandroupolis, Greece
Prof. Charles A. Long, Prof. Emeritus, University of Wisconsin, Stevens Point, Wisconsin, USA.
Prof. Tuan Pham, James Cook University, Townsville, Australia
Prof. W. Lakin, University of Vermont, USA
Prof. Lucio Tommaso De Paolis, University of Salento, Italy
Prof. Jean-Michel Jault, Institut de Biologie Structurale, France
Prof. Hassane Oudadesse, University of Rennes 1, France
Prof. Anita H. Corbett, Emory University School of Medicine, Atlanta, GA, USA
Prof. Toshiharu Horie, Teikyo Heisei University, Japan
Prof. Vadim V. Sumbayev, University of Kent, UK
Prof. Andre Surguchov, University of Kansas Medical Center, Kansas City, USA
Prof. Rona R. Ramsay, University of St Andrews, North Haugh, St Andrews, UK
Prof. Daniel Martins-de-Souza, University of Cambridge, UK
Prof. Roberta Chiaraluce, Sapienza Universita di Roma, Roma, Italy
Prof. George Perry, The University of Texas at San Antonio, USA
Prof. Gertz I. Likhtenshtein, Ben-Gurion University of the Negev, Israel
Prof. Vivo Turk, Jozef Stefan Institute, Slovenia
Prof. Makoto Komiyama, University of Tsukuba, Japan
Prof. Shunsuke Meshitsuka, Tottori University, Japan
Prof. Jean-Michel Jault, Institut de Biologie Structurale, Jean-Pierre Ebel, France
Prof. Ziad Fajloun, Ecole Doctorale des Sciences et Technologie, Universite Libanaise Tripoli, Libya

Prof. Gang-Yu Liu, University of California, Davis Campus, CA, USA
Prof. Zhibing Zhang, University of Birmingham, Birmingham, UK
Prof. Jean-Francois Gohy, Université catholique de Louvain, Belgium
Prof. Waler Caseri, ETH, Zurich, Switzerland
Prof. Jacques Desbrieres, Universite De Pau Et Des Pays De L'Adour, France
Prof. Adrian Schumpe, Technical University of Braunschweig, Germany
Prof. Chris Bowen, University of Bath, Bath, UK
Prof. Jerzy Baldyga, Technical Univeristy Warszawska, Poland
Prof. Alirio Rodrigues, University of Porto, Portugal
Prof. Mostafa Barigou, University of Birmingham, Birmingham, UK
Prof. Jaime Wisniak, Ben-Gurion University of the Negev, Beer-Sheva, Israel
Prof. Sohail Murad, University of Illinois at Chicago, USA
Prof. Konstantinos E. Kakosimos, Texas A&M University at Qatar, Doha, Qatar
Prof. Raghunath V. Chaudhari, University of Kansas, USA

Prof. Xijun Hu, The Hong Kong University of Science and Technology, Kowloon, Hong Kong
 Prof. Deepak Kunzru, Indian Institute of Technology, Kanpur, India
 Prof. Amit Bandyopadhyay, AAAS Fellow , ASM International Fellow , AIMBE Fellow and ACerS Fellow, Washington State University, Pullman, State of Washington, USA
 Prof. Yong Ding, Georgia Institute of Technology, Atlanta, GA, USA
 Prof. Yulin Deng, Georgia Institute of Technology, Atlanta, GA, USA
 Prof. Paul H. Holloway, Distinguished Prof., University of Florida, Gainesville FL, USA
 Prof. Saad Khan, North Carolina State University, Raleigh, North Carolina, USA
 Prof. Manijeh Razeghi, Northwestern University, Evanston, IL, USA
 Prof. Igor Sevostianov, New Mexico State University, Las Cruces, New Mexico, USA
 Prof. Mohindar S. Seehra, West Virginia University, Morgantown, West Virginia, USA
 Prof. Tao Liu, Florida State University, Tallahassee, Florida, USA
 Prof. Daniel Guay, Institut National de la Recherche Scientifique (INRS), Universite du Quebec, Quebec, Canada
 Prof. Tian Tang, University of Alberta, Edmonton, Alberta, Canada
 Prof. Roland Frankenberger, University of Marburg, Marburg, Germany
 Prof. Mohamedally Kurmoo, Universite de Strasbourg, Strasbourg, France
 Prof. C. C. Sorrell, University of New South Wales, Sydney, NSW, Australia
 Prof. Concepcion Lopez, Universitat de Barcelona, Barcelona, Spain
 Prof. Alan Dalton, University of Surrey, Guildford, Surrey, UK
 Prof. Kourosh Kalantar-Zadeh, RMIT University, Melbourne, Australia
 Prof. Constantinos Tsitsilianis, University of Patras, Patras, Greece
 Prof. Tetsu Yonezawa, Hokkaido University, Kita Ward, Sapporo, Hokkaido Prefecture, Japan
 Prof. Daolun Chen, Ryerson University, Toronto, Ontario, Canada
 Prof. Mohamed M. Chehimi, Universite Paris Diderot, Paris, France
 Prof. Vincenzo Fiorentini, Universita degli studi di Cagliari, Cagliari, Italy
 Prof. Tamas Ungar, Eotvos Lorand University (ELTE), Budapest, Hungary
 Prof. Anthony W. Coleman, Universite Claude Bernard Lyon 1, Lyon, France
 Prof. Albert Chin, IEEE Fellow, OSA Fellow, National Chiao Tung University, Hsinchu, Taiwan
 Prof. Artur Cavaco-Paulo, Universidade do Minho, Braga, Portugal
 Prof. Yoshihiro Tomita, Kobe University, Kobe, Japan
 Prof. Jian Wang, Los Alamos National Laboratory, Los Alamos, NM, USA
 Prof. Byung K. Kim, Pusan National University, Busan, South Korea
 Prof. John T. Sheridan, University College Dublin, Belfield, Dublin, Ireland
 Prof. Chi-Wai Chow, National Chiao Tung University, Hsinchu, Taiwan
 Prof. Christian M. Julien, Universite Paris-6, Paris, France
 Prof. Chun-Hway Hsueh, National Taiwan University, Taipei, Taiwan
 Prof. Hyung-Ho Park, Yonsei University, Seodaemun-gu, Seoul, Korea
 Prof. Victor M. Castano, Universidad Nacional Autonoma de Mexico, Mexico City, Mexico
 Prof. Peter Chang, University of Saskatchewan, Saskatoon, Saskatchewan, Canada
 Prof. Dean-Mo Liu, National Chiao Tung University, HsinChu, Taiwan
 Prof. Rui Vilar, Instituto Superior Tecnico, Lisboa, Portugal
 Prof. Hugh J. Byrne, Dublin Institute of Technology, Dublin, Ireland
 Prof. Won-Chun Oh, Hanseo University, Seosan-si, Chungcheongnam-do, South Korea
 Prof. Yuanhua Lin, Tsinghua University, Haidian, Beijing, China
 Prof. S.C. Tjong, City University of Hong Kong, Sham Shui Po District, New Kowloon, Hong Kong
 Prof. Huan-Tsung Chang, National Taiwan University, Taipei City, Taiwan
 Prof. Yoshitake Masuda, National Institute of Advanced Industrial Science and Technology (AIST), Tokyo, Japan
 Prof. Jing Zhang, Donghua University, Shanghai, China
 Prof. Veronica Cortes de Zea Bermudez, Universidade de Tras-os-Montes e Alto Douro, Vila Real, Portugal
 Prof. Jun Zhang, Inner Mongolia University, Hohhot, Inner Mongolia, China
 Prof. Israel Felner, Hebrew University of Jerusalem, Jerusalem, Israel
 Prof. Sukhvinder Badwal, CSIRO Energy Technology, Australia

Prof. Te-Hua Fang, National Kaohsiung University of Applied Sciences (KUAS), Kaohsiung, Taiwan
Prof. Belkheir Hammouti, Mohammed Premier University, Oujda, Morocco
Prof. Mohd Sapuan Salit, Universiti Putra Malaysia, Selangor, Malaysia
Prof. Kwansoo Chung, Seoul National University, Seoul, South Korea
Prof. Zhongfang Chen, University of Puerto Rico, San Juan, Puerto Rico
Prof. Soon-Ku Hong, Chungnam National University, Daejeon, South Korea
Prof. Hannes Jonsson, University of Iceland, Reykjavik, Iceland
Prof. Byron Gates, Simon Fraser University, 8888 University Drive, Burnaby, B.C., Canada
Prof. Culea Eugen, Technical University of Cluj-Napoca, Cluj-Napoca, Romania
Prof. Vesselin Dimitrov, University of Chemical Technology and Metallurgy, Sofia, Bulgaria
Prof. Shadpour Mallakpour, Isfahan University of Technology, Isfahan, Iran
Dr. Stergios Pispas, National Hellenic Research Foundation (NHRF), Athens, Greece
Dr. Anna Lukowiak, Polish Academy of Science, Wroclaw, Poland
Dr. Dimitris Tsiourvas, NCSR "Demokritos", IAMPPNM, Dept. of Physical Chemistry, 15310 Aghia Paraskevi, Attiki, Greece.

Additional Reviewers

Jose Flores	The University of South Dakota, SD, USA
Abelha Antonio	Universidade do Minho, Portugal
Lesley Farmer	California State University Long Beach, CA, USA
Takuya Yamano	Kanagawa University, Japan
Miguel Carriegos	Universidad de Leon, Spain
Francesco Zirilli	Sapienza Universita di Roma, Italy
George Barreto	Pontificia Universidad Javeriana, Colombia
Eleazar Jimenez Serrano	Kyushu University, Japan
Tetsuya Yoshida	Hokkaido University, Japan
Philippe Dondon	Institut polytechnique de Bordeaux, France
Genqi Xu	Tianjin University, China
M. Javed Khan	Tuskegee University, AL, USA
Xiang Bai	Huazhong University of Science and Technology, China
Dmitrijs Serdjuks	Riga Technical University, Latvia
Hessam Ghasemnejad	Kingston University London, UK
José Carlos Metrôlho	Instituto Politecnico de Castelo Branco, Portugal
João Bastos	Instituto Superior de Engenharia do Porto, Portugal
Tetsuya Shimamura	Saitama University, Japan
Imre Rudas	Obuda University, Budapest, Hungary
Konstantin Volkov	Kingston University London, UK
Frederic Kuznik	National Institute of Applied Sciences, Lyon, France
James Vance	The University of Virginia's College at Wise, VA, USA
Angel F. Tenorio	Universidad Pablo de Olavide, Spain
Sorinel Oprisan	College of Charleston, CA, USA
Santoso Wibowo	CQ University, Australia
Jon Burley	Michigan State University, MI, USA
Kazuhiko Natori	Toho University, Japan
Shinji Osada	Gifu University School of Medicine, Japan
Francesco Rotondo	Polytechnic of Bari University, Italy
Deolinda Rasteiro	Coimbra Institute of Engineering, Portugal
Alejandro Fuentes-Penna	Universidad Autónoma del Estado de Hidalgo, Mexico
Moran Wang	Tsinghua University, China
Bazil Taha Ahmed	Universidad Autonoma de Madrid, Spain
Andrey Dmitriev	Russian Academy of Sciences, Russia
Masaji Tanaka	Okayama University of Science, Japan
Matthias Buyle	Artesis Hogeschool Antwerpen, Belgium
Kei Eguchi	Fukuoka Institute of Technology, Japan
Zhong-Jie Han	Tianjin University, China
Valeri Mladenov	Technical University of Sofia, Bulgaria
Ole Christian Boe	Norwegian Military Academy, Norway
Yamagishi Hiromitsu	Ehime University, Japan
Stavros Ponis	National Technical University of Athens, Greece
Minhui Yan	Shanghai Maritime University, China

Table of Contents

Drill-Ability Studies of Laser Drilled Micro Holes on CFRP Composites	11
<i>Anarghya A., Yatheesha R. B., Gurumurthy B. M., Nitish Rao, Ranjith B. S.</i>	
3D Biopolymer Scaffolds for Stem-Cell Culture in Biomedical Engineering	18
<i>Q. T. Nguyen, E. Al Tawil, A. Monnier, B. Deschrevel</i>	
An Intelligent Diagnostic System for Lung Cancer based on Principle Component Analysis - Wavelet Support Vector Machines Classifiers	23
<i>Derya Avci</i>	
Cytoplasmic Motion Visualization and Analysis of C. elegans Embryo	27
<i>C. Atupelage, K. Kyoda, S. Onami, H. Nagahashi</i>	
Development of a Portable System for Vibration Stimulation to Improvement of Walking Stability	33
<i>Park Min-Hwa, Kim Dong-Wook</i>	
An Automatic Diagnosis System for Hepatitis Diseases based on Extreme Learning Machine	38
<i>Derya Avci</i>	
Agent based Amino Acid Elongation Model: Influence of Ribosome Abundance on Polysome Formation	42
<i>Anton Semenchenko, Allbens Atman</i>	
Biological Impact of Certain Substituted Monoazo Thiazole-thiophene and Their Seleno Like Moieties: Part I	53
<i>Mohamed E. Khalifa , Adil A Gobouri</i>	
Grayscale and Binary Image Enhancement of Hand Vein Images to Aid Peripheral Intravenous Access	60
<i>Marlina Yakno, Junita Mohamad-Saleh, Bakhtiar Affendi Rosdi</i>	
Photocatalytic Oxidation and Morphology Control of TiO₂ Film	68
<i>Jinshu Wang, Bingxin Zhao, Hongyi Li</i>	
Nanomaterials Synthesis in Combustion	74
<i>Z. A. Mansurov</i>	
Rapid Screening 73 Antibiotic Drugs in Animal Feeds using Ultra-Performance Liquid Chromatography Coupled to FT-Orbitrap High Resolution Mass Spectrometry	83
<i>Yu-an Sun, Qiuxia Zhang, Wei Ke, Zhenxing Li, Ke Wang, Guoqing Wang</i>	

Scaling-Up Liquid-Liquid Extraction Experiments with Deep Eutectic Solvents	91
<i>Emad Ali, Sarwono Mulyono, Mohamed Hadj-Kali</i>	
Chemical Composition and Antibacterial Activity of Ceratonia Siliqua L. Growing in Boumerdes (Algeria)	96
<i>N. Meziou-Chebouti, A. Merabet, N. Behidj, M. Kirouani, S. Aliouat</i>	
A Novel Automatic Thresholding Method based on Shape of Histogram for Microscopic Blood Cell Images	100
<i>Engin Avci, Turker Tuncer, Resul Coteli, Esin Dogantekin</i>	
The Mechanism of PMF Nanoparticles in Invading A549 cells, A New Selective Drug Delivery for Cancer Therapy	104
<i>Gehan A-R. Ahmed, Faten A. Khorshid, Alaa Khedr, Salem M. El-Hamidy, Numan A. Salah</i>	
Planckian Distributions in Molecular Machines, Living Cells, and Brains: The Wave-Particle Duality in Biomedical Sciences	115
<i>Sungchul Ji</i>	
Authors Index	138

Drill-Ability Studies of Laser Drilled Micro Holes on CFRP Composites

Anarghya A, Yatheesha R.B., Gurumurthy B.M., Nitish Rao, Ranjith B.S.

Abstract— This paper begins with the introduction on composite materials and their production techniques. It further describes, the experimentation concerned with fiber reinforced polymer (FRP) composites where high strength reinforcing fibers are combined with polymer (plastic) matrix for achieving suitably high strength. The machinability of the CFRP is of the major concern with surface finishing of the order of micro-scale. The analysis of FRP laminates is based on the micro drilled holes by laser drill and the result so obtained is analyzed through scanning electron microscope (SEM). The consideration of the heat accumulated zones as a result of laser drilling is analyzed. The suitable parameters for obtaining a good surface finish with the least amount of heat accumulated zone by laser drilling on the Carbon Reinforced Plastics concludes the paper.

Keywords— CFRP; Composite Material; Laser Drilling; SEM; Reinforcement.

I. INTRODUCTION

A composite material is made by combining two or more materials, often ones that have very different properties. Unique properties of the resulting material can be obtained upon combination. As the materials do not blend into each other due to their different properties, they can be easily differentiated in the composite. The individual components remain distinct even though the structure is complete. The new material i.e. the composite obtained after the combination of

the individual materials will be preferable, as a result of the following reasons: -

Strength, lightness, inexpensive, as compared to the traditional method. Composites are made up of individual materials referred to as constituent materials. There are two main categories of constituent materials: matrix and reinforcement. One portion of each type is required. By maintaining the relative positions, the matrix material surrounds and supports the reinforcement materials. The matrix properties are enhanced by the reinforcements which imparts their special mechanical and physical properties. A synergism produces material properties unavailable from the individual constituent materials, while the wide variety of matrix and strengthening materials allows the designer of the product or structure to choose an optimum combination. The matrix material can be introduced to the reinforcement before or after the reinforcement material is placed into the mould cavity or onto the mould surface. [1]. The matrix material experiences a melding event, after which the part shape is essentially set. Depending upon the nature of the matrix material, this melding event can occur in various ways such as chemical polymerization or solidification from the melted state.

This work was supported by Professor S.S. Sharma, Mechanical Engineering Department, Manipal Institute of Technology, and the Mechanical Laboratory of Manipal Institute of Technology, Manipal for the providing with all the useful resources for the successful fulfilment of the experimentation.

Anarghya A completed his B.E. in Mechatronics Engineering from Manipal Institute of Technology, Manipal (phone: +919483961410; email: anarghya.murthy@yahoo.com)

Yatheesha R.B. is an assistant professor, Department of Mechanical Engineering, Don Bosco Institute of Technology, Bangalore (email: rambheerb@gmail.com)

Gurumurthy B.M. is an assistant Professor, Department of Mechanical Engineering, Manipal Institute of Technology, Manipal, India (email: gurumurthy.bm@manipal.edu)

Nitish Rao is a student of Automotive Technology, Technical University Eindhoven, The Netherlands (phone: +31618269086 email: nitish.rao16@gmail.com)

Ranjith B.S. completed his B.E. in Mechanical Engineering from Manipal Institute of Technology, Manipal (phone: +919743371872; email: ranjithbssg@yahoo.com)

II. METHODS TO PRODUCE COMPOSITE MATERIALS

Composite materials can be produced by a range of process. These processes vary from manual lay-up of reinforcement and hand application of resin to fully automated continuous processes. The most common techniques are:

- Hand or spray lamination
- Compression molding
- Resin injection
- Pultrusion
- Vacuum infusion

1.1. Hand or spray lamination

Hand lamination is the most common process, accounting for over 40% of composites production worldwide. This is due to its ease of use and flexibility, which allows all types of reinforcement to be utilized. Here, in the experimentation as well the hand lamination method is used.

III. FIBRE REINFORCED PLASTICS (FRP)

Fiber-reinforced polymers/plastics is a recently developed material for strengthening of RC and masonry structure. It has been found to be a replacement of steel plate bonding and is very effective in strengthening of columns by exterior wrapping. The main advantage of FRP is its high strength to weight ratio and high corrosion resistance. FRP plates can be 2 to 10 times stronger than steel plates, while their weight is just 20% of that of steel. However, at present, their cost is high. The commonly used fibers are Carbon fibers, Glass fibers and Aramid fibers and the commonly used resins are polyester, vinyl ester and epoxy.

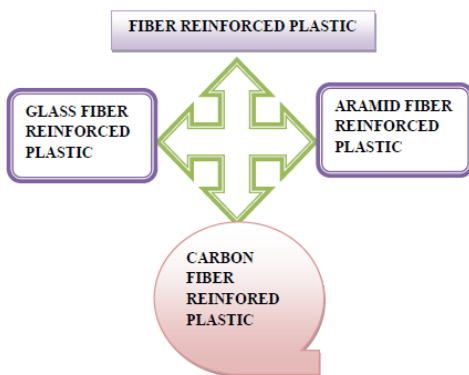


Fig. 1. Fiber Reinforced Plastic classification

A. 3.1 Machining on Carbon fiber reinforced plastics

Parts fabricated from FRP composites are normally laid in the near-net-shape, however cutting operations such as trimming, drilling, grinding and slotting are still required to remove excess material and meet dimensional tolerances and requirements. The use of laser machining for cutting composites is attractive due to its high cutting/travel speed, flexibility and ease of automation. However, it is not

uncommon that laser, as a thermally acting tool, may damage the matrix element in the composite, which reduce the composites mechanical properties [2]-[4].

B. 3.2 Heat affected zone (HAZ)

The heat-affected zone (HAZ) is the area of the base material, which is not melted and but has its properties altered by welding or heat intensive cutting operations in its microstructure[5]. The large differences in material properties of the carbon fiber and the epoxy resin in carbon fiber reinforced plastic (CFRP) composite make laser processing very challenging. It was found that laser parameters such as laser power, repetition rate, and work piece temperature determine the extent of HAZ[6].

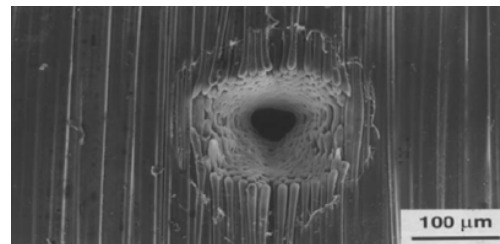


Fig. 2. Scanning Electron Microscope (SEM) image of a laser drilled hole

The figure is of SEM laser drilled hole in composite showing matrix volatilization and fiber swelling. When the carbon fiber composites are heated rapidly as in laser drilling the impurities evaporate creating high gas pressure. This high pressure leads to swelling of the fibers within the HAZ which are retained even when the material cools down and returns to normal pressure. Laser delivers high power-density beam which upon impact on the work piece is converted into heat. As the impact zone is very small very high temperature capable of melting or volatilizing the material can be attained. This leads to material removal. Laser drilling which is a non-contact process produce small holes in various materials having high degree of precision and reproducibility.

IV. METHODOLOGY

The following processes were followed: -

- Materials requirement
- Hand layup process
- Laser drilling
- Scanning electron microscope (SEM) Analysis

4.1 Materials used

- Carbon fabric
- Epoxy resin (LY545)
- Hardener (HY045)
- Wax

- Acetone
- Teflon sheet

4.2 Hand Lay-Up

Materials are purchased for making FRP laminates by Hand lay-up process. The carbon fiber fabric is usually trimmed to the appropriate size and laid down over a mold where it is formed to the desired shape[7]. Several layers may be required depending on the desired product. Fabric is positioned manually in the open mold, and resin is poured, brushed, or sprayed over and into the fabric[8]. Entrapped air is removed manually with rollers to complete the laminates structure. Laminates are usually left to cure under standard room temperatures.



Fig. 3. Hand Layup in progress



Fig. 4. Preparation of laminate by hand layup process

4.3 Laser drilling

Laser drilling is a process in which a laser is used to make holes, instead of conventional drilling[9]. Laser drilling of cylindrical holes generally occurs through melting and vaporization of the work piece material through absorption of energy from a focused laser beam. The energy required to remove material by melting is about 25% of that needed to vaporize the same volume, so a process that removes material by melting is often favoured[10].



Fig. 5. Laser drilling being carried out

The experimental trials were carried out on a state-of-art Marbach Compact CO2 laser cutting system (2115 DC-020). The machine is CNC controlled employing high-speed flatbed offering maximum cutting speed of 20,000 mm/min together with maximum cutting power of 2500 watt. CFRP work piece materials were manually laid up to provide nominally 3 mm thick symmetric UD CFRP laminates. The laminates were then cured according to the manufacturers' specifications to give a fiber weight fraction of ~ 65 % and subsequently cut into plates [11]-[15]. A scanning electron microscope (SEM) and a conventional optical microscope were employed to characterize the surface damage induced laser trimming[16]. Entry and exit Kerfs width for all work pieces were linearly measured using optical microscope and kerfs angle was subsequently calculated, as shown in figure 6.

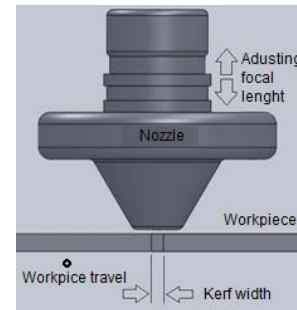


Fig. 6. The laser drilling process close up view

Figure 7 shows a schematic diagram of the structure of CFRP used in this study. CFRP with 3, 3.5, 4 mm thickness were used for laser processing. Figure 8 shows the optical setup of laser cutting of CFRP. In the experiments, a Q-switch Nd: YAG laser (Continuum, Minilite) was used. Figure 9 shows a schematic diagram of the laser cutting procedure. The laser beam was scanned with a constant speed on the surface[17]. The distance between the laser focus and the surface was kept constant during the scanning. Figure 10 shows the definition of focus positions of laser beam to the CFRP surface. The origin was defined on the CFRP surface and plus sign represented the focus inside of the CFRP, while minus sign represented that the focus located above the surface.

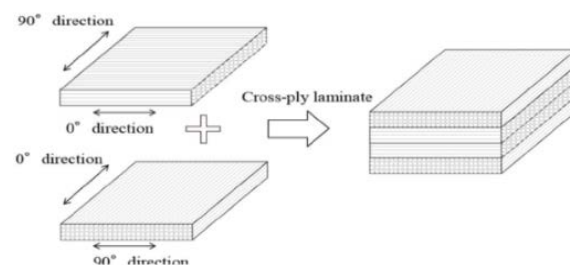


Fig. 7. A schematic diagram of the CFRP used in the experiments

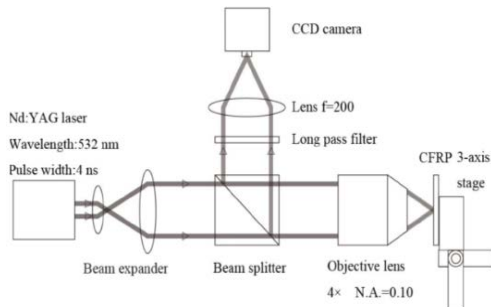


Fig. 8. Optical setup for the laser cutting of CFRP with nano-second pulse

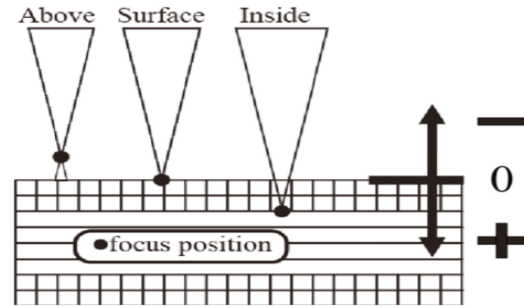


Fig. 10. The definition of focus positions of laser beam to the CFRP surface

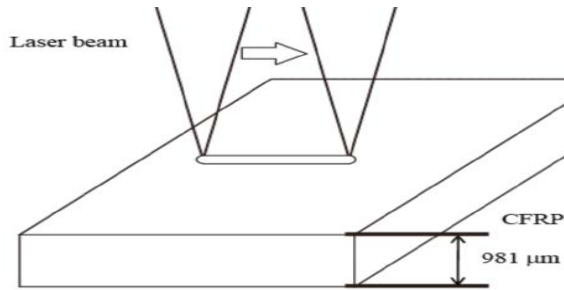


Fig. 9. A schematic diagram of laser processing procedure

V. RESULT AND DISCUSSION

Table 1.-Heat Affected Zone Values obtained after laser drilling

SL. NO.	Thickness (A)	Diameter of Hole (B)	Frequency (C)	Assist gas	HAZ
1	3.0	0.4	200	Ar	0.4022
2	3.5	0.4	200	Ar	0.4022
3	4.0	0.4	200	Ar	0.4022
4	3.0	0.6	200	Ar	0.6033
5	3.5	0.6	200	Ar	0.6033
6	4.0	0.6	200	Ar	0.6033
7	3.0	0.8	200	Ar	0.8044
8	3.5	0.8	200	Ar	0.8044
9	4.0	0.8	200	Ar	0.8044
10	3.0	0.4	400	Ar	0.4022
11	3.5	0.4	400	Ar	0.4022
12	4.0	0.4	400	Ar	0.4022
13	3.0	0.6	400	Ar	0.6033
14	3.5	0.6	400	Ar	0.6033
15	4.0	0.6	400	Ar	0.6033
16	3.0	0.8	400	Ar	0.8044
17	3.5	0.8	400	Ar	0.8044
18	4.0	0.8	400	Ar	0.8044

From the above table it is clear that the greater the diameter of the hole, the more the HAZ induced into the material.

5.1 Graphs and explanation

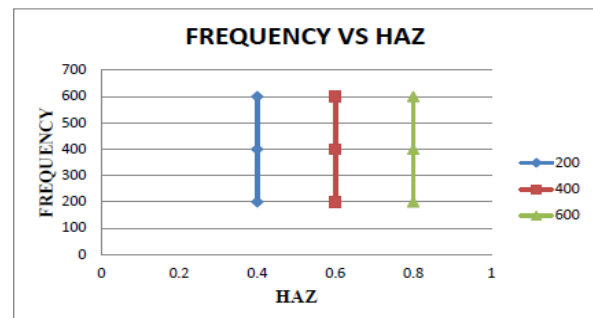


Fig. 11. Frequency v/s Heat Affected Zone

The frequency plays a major role in influencing the HAZ in a composite material, although there other factors also which influences the inducing of HAZ in the material.

The above graph is plotted between frequency and HAZ. In the graph for a constant frequency of LASER, HAZ is increasing, which implies that HAZ depends on some other parameter other than frequency.

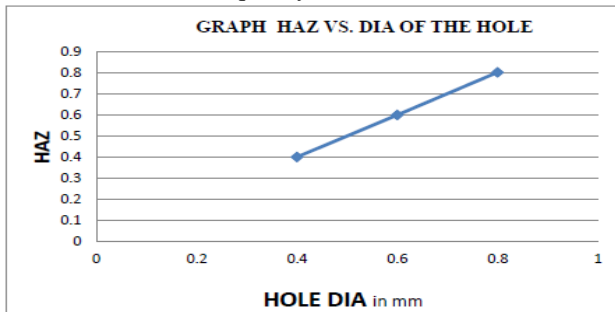
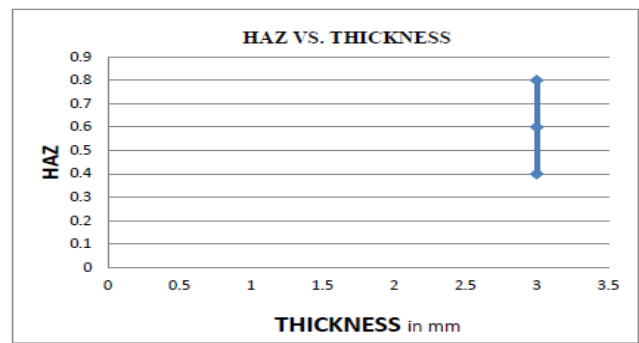


Fig. 12. Heat Affected Zone v/s Hole Diameter

This graph explains that for a constant thickness of laminate, with the increase in the hole diameter HAZ increases.



Graph 3-Heat Affected Zone v/s Thickness

The above graph explains that for a constant whole diameter of 0.4mm which is drilled over 3 laminates of different frequency, HAZ remains constant.

A. 5.2 Comparison among different laser drilled holes

Table 2.-laser Drilled Holes for 0.4 mm Diameter

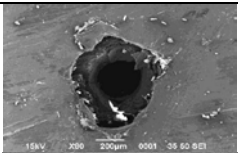
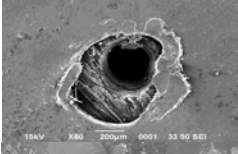
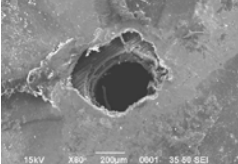
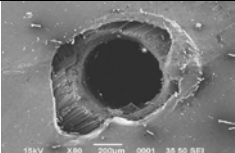
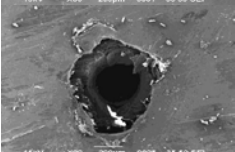
Sr. No.	Thickness	Diameter	HAZ	Broken Status	HAZ Effect
1	3.0	0.4		NO	LESS
2	3.5	0.4		YES	MORE
3	4.0	0.4		LESS	MODERATE

Table 3.-laser Drilled Holes for 0.6 mm Diameter

Sr. No.	Thickness	Diameter	HAZ	Broken Status	HAZ Effect
1	3.0	0.6		NO	LESS
2	3.5	0.6		YES	MORE

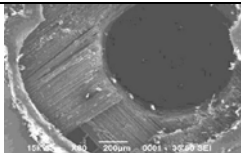
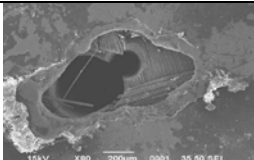
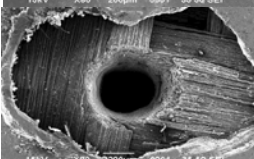
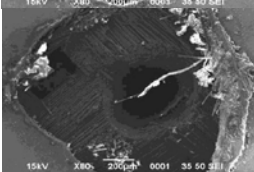
3	4.0	0.6		LESS	MODERATE
---	-----	-----	---	------	----------

Table 4.-laser Drilled Holes for 0.8 mm Diameter

Sr. No.	Thickness	Diameter	HAZ	Broken Status	HAZ Effect
1	3.0	0.8		YES	LESS
2	3.5	0.8		NO	MORE
3	4.0	0.8		YES	MORE

VI. CONCLUSION

1. Result shows that by careful control of Processing Parameters Laser Drilling of both Thin and Thicker composite materials is possible and the Scanning Electron Microscope Analysis shows that it is possible to micro-texture the surface of carbon composites to promote the bond strength.
2. Laser machining process induces heat in the composite material and may alter the properties of the material due to the creation of HAZ in the localized areas.
3. HAZ in the localized areas results in inducing of stress, thus the structural integrity of the material gets compromised due to improper machining.
4. Since the heat is accumulated in material during Laser processing especially in the case of carbon fibers, so minimum HAZ can be achieved in machining of CFRP composites by using short pulsed Lasers.
5. SEM analysis has enabled the proper visualization of the material and the stress induced in it due to improper machining technique and incorrect selection of parameters.
6. From the SEM analysis it is clear that the selection of the suitable parameters as well as proper bonding of the layers will result in a good finished micro hole and less material removal due to the thermal effect created by the Laser.

The optimum parameters for a good surface finish with less HAZ are as follows: -

1. Frequency Range: 200 to 250
2. Diameter of the Hole: 0.4
3. Drilling Speed: 200m/sec
4. Thickness of specimen: 3

ACKNOWLEDGEMENTS

All the authors would like to express their heartfelt thanks to Professor S.S. Sharma, Mechanical Engineering Department, Manipal Institute of Technology, who guided in the various stages of the experimentation and for pointing in the right direction. The Mechanical Laboratory of Manipal Institute of Technology, Manipal also helped in providing with all the useful resources for the successful fulfilment of the experimentation.

REFERENCES

- [1] http://www.ijammc-griet.com/attach/1402652848_14-08-03.pdf
- [2] M. H. El-Hofy, S. L. Soo, D. K. Aspinwall, W. M. Sim, D. Pearson, and P. Harden, "Factors Affecting Workpiece Surface Integrity in Slotting of CFRP," *Procedia Engineering*, vol. 19, pp. 94-99, 2011.
- [3] I. Shyha, S. L. Soo, D. Aspinwall, and S. Bradley, "Effect of laminate configuration and feed rate on cutting performance when drilling holes in carbon fibre reinforced plastic composites," *Journal of Materials Processing Technology*, vol. 210, pp. 1023-1034, 2010.
- [4] S. L. Soo, I. S. Shyha, T. Barnett, D. K. Aspinwall, and W.-M. Sim, "Grinding performance and workpiece integrity when superabrasive edge routing carbon fibre reinforced plastic (CFRP) composites," *CIRP Annals - Manufacturing Technology*, vol. 61, pp. 295-298, 2012.

- [5]. F. Abedin et al., Review On Heat Affected Zone (HAZ) In Laser Machining, 2010
- [6]. Pan & H. Hocheng et al., The Anisotropic Heat Affected Zone (HAZ) In The Laser Grooving Of Fiber-Reinforced Composite Material, 1995
- [7]. Engineers handbook, Manufacturing methods, hand layup method.
- [8] <http://www.carbonfiberguru.com/carbon-fiber-processing-part-1-wet-hand-lay-up/>
- [9] http://www.ijammc-griet.com/attach/1394181749_2014-03-11.pdf
- [10] Islam Shyha et al., An Investigation Into Co Laser Trimming Of CFRP & GFRP Composites, June 2013
- [11] William M. Steen, "Laser Material Processing", Springer-Verlag London Limited, p. 99, 1991.
- [12] Jose Mathew a & G.L. Goswami et al., Parametric Studies On Pulsed Nd: Yag Cutting Of CFRP Composites, Sept 1998
- [10] Keisuke Ushida & Wataru Inami et al., Characteristic analysis of CFRP cutting with nanosecond pulsed laser, 2012
- [11] Paul French & Mo Naeem et al., Macro And Micro Applications For Fiber Lasers In Laser Material Processing Of Aerospace Composite Material, 2007
- [12] Desh Bandhu, Sandeep Singh Sangwan & Mukesh Verma at el., A Review Of Drilling Of Carbon Fiber Reinforced Plastic Composite Material, 2006
- [13] T. Graf, R. Weber, V. Onuseit, M. Hafner, C. Freitag, A. Feuer; Laser Applications from Production to Machining of Composite Materials, EALA 2012.
- [14] R. Weber, M. Hafner, A. Michalowksi, T. Graf; Minimum damage in CFRP laser processing, Physics Proceedia 12(2), 2011, Pages 302-310.
- [15] A. Goeke and C. Emmelmann, Influence of Laser Cutting Parameters on CFRP Part Quality, Physics Proceedia 5 (2010), pp. 253-258.
- [16] H.Y. Zheng a, G.C. Lim a & P.L. Chu at el., Study On UV Laser Machining Quality Of Carbon Fiber Reinforced Composites, 2010
- [17] R. Weber, C. Freitag et al., Laser Processing Of CFRP, June 2012

3D biopolymer scaffolds for stem-cell culture in biomedical engineering

Q. T. Nguyen, E. Al Tawil, A. Monnier and B. Deschrevel

Abstract— Asymmetric three dimensional (3D) cell culture scaffolds with dual porosity were designed from bioresorbable poly(lactic acid) (PLA). The surface of these scaffolds is entirely functionalized with a nanolayer of hyaluronan (HA). The phase inversion process applied to PLA solutions of proprietary formula makes it possible to tune the scaffold architecture. The obtained functionalized scaffolds with interconnected macro- micro dual pores promote adhesion and proliferation of various human cell types, including mesenchymal stem cells (MSC). Interestingly, in the presence of a chondrogenic medium supplemented with transforming growth factor- beta 3 (TGF β 3), MSC differentiate on these dual-pore scaffolds into mature chondrocytes with deposition of a cartilaginous matrix revealed by glycosaminoglycan (GAG) secretion. This study indicates that such dual- pore scaffolds constitute strong candidates for cartilage tissue engineering.

Keywords—dual-pore, cell culture scaffolds, MSC, cartilage engineering

I. INTRODUCTION:

Regenerative medicine is a new domain of multidisciplinary research that has the potential revolution in the treatments of damaged tissues. Advances in the field of tissue engineering have been closely connected to biomaterials with improved performances as biocompatible and biodegradable scaffolds. A variety of polymer scaffolds have been proposed for in vitro culture of different cell types which create biological substitutes that restore and/or improve the function of damaged tissues. Articular cartilage is an avascular tissue whose ability to self-repair is extremely low. Even minor injuries may thus lead to painful osteoarthritic damages.

Cartilage tissue engineering is one of the most promising approaches for treatment of these damages. It is henceforth clear that this approach requires constructs associating at least a scaffold and cells [1]. Among the several cell sources, mesenchymal stem cells (MSC) have marked plasticity and potential for multiplication which make them an ideal cell source for musculoskeletal tissue engineering [1, 2]. The significant advances in cartilage tissue engineering, it remains

challenges to overcome such as deposition of a hyaline rather than a fibrocartilaginous matrix [3].

Scaffold for cartilage tissue engineering should satisfy many requirements including biocompatibility, bioresorbability, porosity, and bioactivity [2]. A broad range of natural and synthetic biomaterials in various forms are used to support chondrogenesis of MSCs in vitro and/or in vivo [4]. Poly(lactic acid) (PLA) scaffolds have been suitable carriers for high-density viable chondrogenic cells [5].

Scaffolds with macropores are considered to be the most promising ones for tissue engineering with MSC since they provide the three dimensional environment experienced by normal cells in the mammal body for normal differentiation, polarization, cell behavior and intercellular interactions with such scaffolds [6, 7]. Indeed, the third dimension of cell growth in macropores provides more contact space for mechanical inputs for cell adhesion, for integrin ligation, cell contraction and intracellular signaling [8]. In addition to macropores, micropores that connect them may bring about diffusion paths for nutrients, metabolites and gases to the macropore-adhering MSC.

For good adhesion and proliferation of cells on synthetic scaffolds, natural polymers extracted from the native extracellular matrix (ECM) have been used to modify the surface of PLA scaffolds [9]. Among them, hyaluronic acid (HA) which is an abundant glycosaminoglycan in ECM, can bind to MSC and chondrocytes via the trans-membrane receptor CD44 [10] and impart various signaling pathways to the surface localized MSC.

This paper deals with bioresorbable PLA scaffolds of dual porosity, i.e. with interconnected macropores and micropores, whose surface was modified by deposition of a nanolayer of hyaluronic acid *via* a simple surface treatment. Those PLA scaffolds were next studied in MSC cultures with differentiation induction into chondrocytes by TGF β 3.

II. MATERIALS AND METHODS

A. Materials

We used PLA from NatureWorks® LLC as raw material for scaffold fabrication. It has an average molecular weight of

The financial support of Seinari (Normandy Innovation Agency) for consumables and for A.M. post-doctoral fellowship, and that of the French Education and Research Ministry for E. A.Ph.D. fellowship are acknowledged. First author's e-mail: trong.nguyen@univ-rouen.fr).

All the authors are with PBS-UMR6270 Department, Rouen University, Mont St Aignan, 76821, France.

A. Monnier is now LAGEP, University of Lyon 1, 43 bd du 11 Novembre 1918, 69622 Villeurbanne Cedex

66 000 g.mol⁻¹ and 4 % D - 96 % L enantiomer contents. Its glass transition temperature and its melting temperature are 57 and 165 °C, respectively.

B. Preparation of asymmetric PLA membranes

The basis of dual pore PLA scaffolds were asymmetric membranes; they were prepared by the solvent-induced phase inversion technique which consists in immersing a polymer-solution film cast on a flat support in a coagulating liquid medium. The polymer solutions (casting dopes) were composed of PLA and a polymer additive, PEG (polyethylene glycol) used as porogen. They were obtained by dissolving polymers in appropriate weight ratios in DMF at 70 °C under a dry atmosphere for about 24 hours to ensure their complete dissolution. After bubble elimination, the cooled solutions were cast onto a glass plate into ca. 250 µm - thick films by means of a Gardner knife, and the glass plate was immediately immersed in a water bath at room temperature (25°C). After coagulation, the membrane was thoroughly washed with water. The final membrane thickness was ca 150- 200 µm, depending on the casting dope composition.

C. HA- nanolayer deposition on base membranes

PLA membranes were immersed in 1, 6 diamino-hexane (DAH) solutions in propanol-1 for 10 min at room temperature then abundantly rinsed with water. The DAH treated membranes were next immersed in an aqueous solution of HA at fixed pH for 10 min. at room temperature then again rinsed with water.

D. Characterization of scaffolds

The pore architecture of the asymmetric membranes was visualized by scanning electron microscopy (SEM). The scaffold cytotoxicity for dermal fibroblasts was measured via the activity of lactate dehydrogenase (LDH) (a stable cytosolic enzyme released upon cell lysis) with CytoTox kit (Promega, France). The liquid media from fibroblasts cultivated on different membrane samples were collected at 24- hr time and submitted to the enzymatic assay which results in a conversion of the tetrazolium salt into red formazan whose absorbance was measured. The toxicity was then calculated as: (culture medium absorbance measured for the sample - culture medium background absorbance)/ LDH absorbance of totally lysed cells of the culture medium by Triton X surfactant.

Cell seeding and induction of chondrogenic differentiation in vitro

PLA 3D porous functionalized scaffolds were carefully seeded in 12- well plates with 1 million cells suspended in 20 µL of medium. The constructs were kept in a 37°C incubator for 1 hr to allow the cells to diffuse into and attach to the scaffolds before addition of 2 mL of fresh medium containing DMEM, 10% FBS (ref), 2mM L-glutamine (Gibco, Invitrogen, France), 40 µg/mL L-proline (ref), 1% penicillin (100U/mL)-streptomycin (1000U/mL) solution, 100 nM dexamethasone, 50 µg/mL ascorbic acid, 1 mM sodium pyruvate, 1X ITS³⁺

(contains 1 mg/mL insulin from bovine pancreas, 0.55 mg/mL human transferrin), 0.5µg/mL sodium selenite, 470 µg/mL linoleic acid, 470 µg/mL oleic acid, 50 mg/mL human serum albumin and 10 ng/mL TGF β3 (Miltenyi Biotec, France). The medium was replaced twice in a week for the first two weeks then once until day 42.

E. Cell proliferation assay

Cell proliferation was carried out by adding Wst-1(Roche Applied Sciences, France) to the seeding well. The constructs were incubated at 37°C for up to 4 hrs. For each sample, 70 µL of supernatant (containing Wst-1 reagent and medium solution) were transferred to 96-well plate and were read at 420/600 nm using a micro plate spectrophotometer (Powerwave X, Bio-tek instruments, France). The absorbance directly correlates with the number of viable cells. Direct counting of histochemically- stained cell nuclei on slides in a confocal microscope PicoGreen assays (Invitrogen kit) for cell- DNA quantitation were also performed for comparison.

F. Cell flow cytometry analysis

Using our lab-developed enzymatic method to retrieve large numbers of viable cells for phenotypic analysis, the cell profiles were characterized by flow cytometry using the following fluorescent monoclonal antibodies: anti-CD 49_c – FITC, anti-CD 90 – PercpCy^{5.5} and anti-CD 105 – PE.

G. Biochemical assays

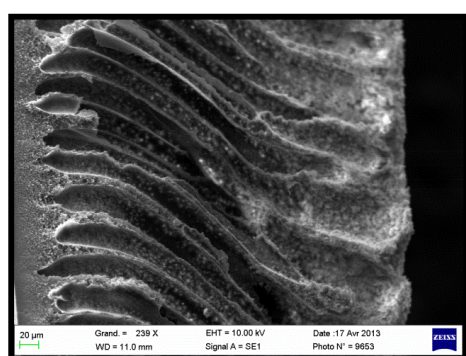
For determination of total glycosaminoglycan (GAGs) and DNA content, differentiated cells were collected at week 6 and were digested with papain (Sigma Aldrich, France) at 60° C overnight. For sulfated GAG quantification the 1,9-dimethylmethylene blue (DMMB) colorimetric assay was performed with chondroitin-6-sulfate as a standard.

III. RESULTS AND DISCUSSIONS

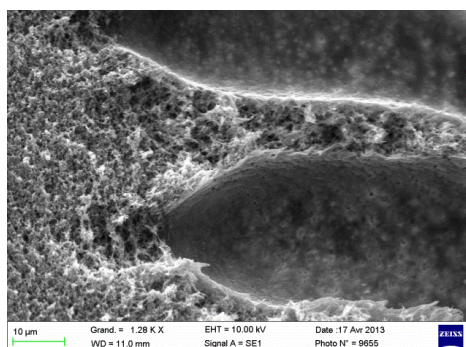
A. Scaffolds with interconnected macropores- micropores

The phase inversion technique that is widely used for industrial production of membranes [11], makes it possible to fabricate asymmetric membranes with reproducible architecture in the membrane section (Fig. 1). It provides a proven process for the fabrication of 3D PLA biomaterials that can be post- functionalized with bioactive molecules on the whole porous structure. We observed a decrease in pore size and porosity of the pristine membranes with an increase of PLA content, and a decreased of porogen content, in the casting dope solution. Such a behavior appears to be logical, and has been observed in the asymmetric membrane fabrication [11, 12].

However, there is a new effect of the porogen additive on the membrane structure. In addition to the increase in porosity [13] which is attributed to the extraction of the additive during the film coagulation step, we observed the formation of a dual-pore architecture with inter-twined and connected macropore - micropore network (Fig. 1). Such a behavior is quite different from the macropore suppression described by other authors [13]. We suggest that the dual pore architecture is generated by a double phase inversion in the nascent membrane. To the traditional separation into a polymer- rich and a polymer- lean phases, there would be a phase separation between two polymer (PLA- rich and PEG- rich) phases that occurs simultaneously. The latter phase separation is probably caused by the limited miscibility between PLA and PEG [14].



(a)



(b)

Fig. 1 SEM images of a PLA asymmetric membrane. (a) membrane section with parallel cigar- form macropores and (b) spongy membrane skin part with open micropores in- between the macropores. The membrane was prepared from a casting dope that contained 20 wt. % of PLA in DMF.

For the fabrication of membranes destined to human cell cultures, we chose the membrane casting solutions that contain less than 10 wt. % of PLA and 10 wt. % of PEG of molecular weight of ca. 8000 Daltons in DMF. Such dope formula gave membranes with macropore openings on the porous membranes in the range of 80- 200 µm (Fig. 2), and micropores of ca. 2- 8 µm size in the walls that separate the macropores (Fig. 1b) [15].

Compared with the other techniques [14], this technique offers the advantages of a simple preparation process while providing a special architecture. Such a dual-pore architecture makes the

prepared membranes more suitable for 3D scaffolds than classical ultrafiltration membranes which have much smaller pores. The larger number of big macropore openings on the porous membrane face (Fig. 2) must facilitate the seeding of cells inside the 3D scaffolds as well as their retrieval after proliferation at the end of the cell culture.

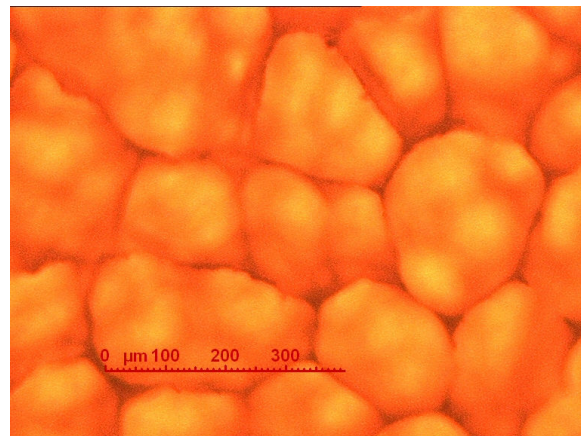


Fig. 2 : Optical microscopy image of the honeycomb-like macropore openings on the porous membrane face. The membrane was prepared from a casting dope that contained 6.7 wt. % of PLA and PEG of 8000 Daltons in DMF, respectively.

The macropore- micropore inter-twining (Fig. 1) must make easier the transport of oxygen, nutrients or metabolites *via* short the paths in pores filled with the culture medium, in both ways between the growing cells on the internal surface and the external medium. The dense skin on the other membrane face, which is not permeable to cells because of its small pores, prevents leakage of cells from the interior space but allows small solutes in the external medium to diffuse into it.

The whole fabrication process comprising the dual pore substrate preparation and the surface functionalization into bioactive 3-D scaffolds was described in a recent patent [15]. This process also makes it possible to tune the macroporous topography of biopolymer membranes to affect cellular responses, in a similar way as that proposed by Cheng *et al.* [16].

B. Biological behaviors of the dual- pore scaffolds

Concerning the scaffold cytotoxicity, the cell metabolic activity measured at 24 h after seeding on pristine PLA, DAH-treated PLA and HA- functionalized membranes showed no significant changes upon contact between their surface and the culture medium containing fibroblasts. In fact, the relative absorbances of the enzymatic assays fluctuated around 8 % of the level obtained with the plastic of the cell culture well.

The ability of the dual- pore HA- functionalized scaffolds to promote adhesion and proliferation is shown in the successful culture of various human cell lines over 14 days, confirming the non- toxicity of the scaffold (example on Fig. 3). The live/dead tests showed a high ratio of living cells (ca. 90 %) on the HA- functionalized scaffold. In contrast to this, the pristine

PLA scaffold showed very few adhering cells, and DAH-treated PLA adhering cells only in the first days.

In the case of fibroblast culture on the HA- functionalized scaffold, picogreen fluorescence-based DNA quantification showed that the living-cell DNA content was maximum at day 8 of culture (at 300 ng/mL level), then decreased slowly towards day 14. The same trend was observed in the monitoring of two other parameters, i.e. Wst-1 assays and living cell counting in optical microscopy. Moreover, fibroblasts spread with flattened morphology, forming a network with long filopodia, that is, a typical aspect of fibroblasts cultured in a friendly environment (Fig. 3).

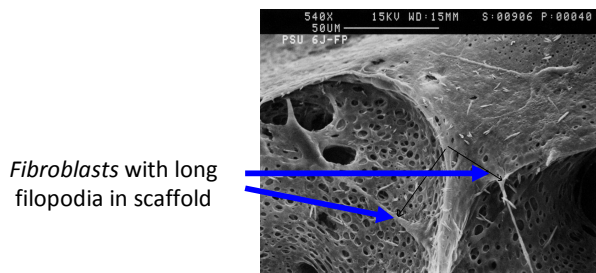


Fig.3: Proliferation of fibroblasts with long filopodia in macropores of the HA-functionalized scaffold at day 14 of cell cultivation

The versatility of such scaffolds can be explained by its special architecture that makes large macropore surface area available for cell adhesion and during the culture while promoting cell growth *via* the HA nanolayer that interacts naturally with the eukaryote HA receptors on the cell membranes: CD44, Rhamms...

C. Proliferation and differentiation of MSC on the scaffolds

MSC proliferation in 3D PLA scaffolds was observed till week 6 of cell culture (Fig. 4). Cells showed good proliferation with time. Nevertheless, cells continued to proliferate on scaffolds with a lower rate after 4 weeks, indicating a differentiation switch.

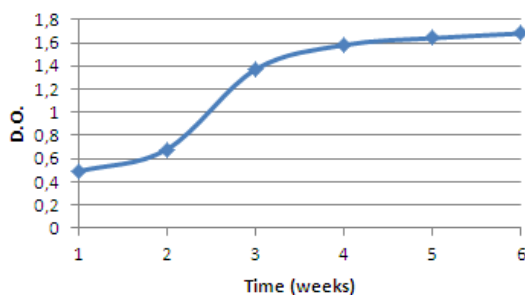


Fig.4: Proliferation rate of MSCs on HA- functionalized 3D PLA scaffolds in a 6- week cell culture (Wst-1 assays).

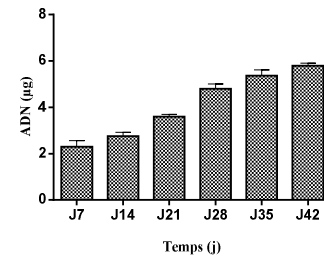
Change in DNA content

Cell numbers in the scaffolds were assessed through the measurement of DNA contents with Picogreen every week after seeding. The results showed that the number of cells

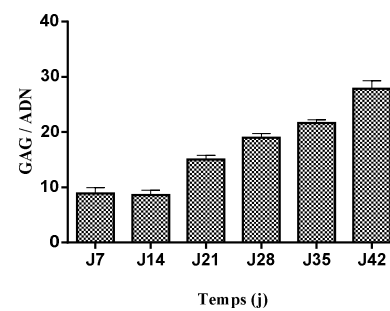
increase continuously in all scaffolds compared with the first week.

Change in GAG content

GAG content (normalized versus DNA content) was analyzed after 6 weeks of chondrogenic differentiation (Fig. 3a). Results showed increasing of GAG/DNA ratio in PLA scaffold functionalized with HA (Fig. 3b).



(a)



(b)

Fig. 5: Change in DNA mass and in GAG/ DNA mass ratio per 16 mm- diameter scaffolds *versus* time (day).

D. Phenotype characterization of MSC at different culture stages

The cell profile after living cell retrieval with trypsin contact was analyzed by immunophenotypic characterization (percentage of positive cells for the cell surface markers analyzed by flow cytometry), before (day 0) and after (day 42) chondrogenesis of MSC on our scaffolds. The results are shown in table 1. We observed a four- fold decrease in CD 90 and CD 166 markers per cell from day 7 to day 14 and progressive increase in CD 49_c et CD151 markers; this indicates a differentiation of CSM towards chondrocytes in long-term culture in the scaffolds.

Antibody (for marker detection)	Before scaffold seeding	After 42 days of culture
anti-CD 90	> 98 %	< 30 %
anti-CD 105	> 97 %	< 18 %
anti-CD 49 _c	< 8 %	> 95 %

Table 1 Changes in the percentage of positive cell membrane markers on initial MSCs and final chondrocytes after 42-day proliferation and differentiation on HA- functionalized 3D PLA scaffolds.

These results showed that MSCs grow and proliferate on our scaffolds, and express chondrogenic markers like CD49C and secrete a cartilaginous ECM. This could prove that our PLA scaffold functionalized with HA can be a valuable asset in terms of cartilage tissue engineering

IV CONCLUSION

HA-functionalized 3D PLA scaffolds appear to be appropriate for cell culture in general, and specifically for MSC cultures. They provide a more physiologically relevant surface, with 3D patterns that mimic tissues and HA bioactive surface. These features made it possible to obtain MSC proliferation and differentiation, in an appropriate environment, towards chondrocytes with correct cell phenotype. The phase inversion technique would offer a proven process for industrial fabrication of the base biomaterials for such scaffolds.

REFERENCES

- [1] B. Jhonstone. "New perspectives for articular cartilage repair treatment through tissue engineering: A contemporary review" *Eur Cell Mater* 25:248-267, 2013.
- [2] A. Matsiko. "Advanced strategies for articular cartilage defect repair". *Materials* 6:637-668, 2013
- [3] M. Demoor. *BBA* 1840:2414-2440, 2014
- [4] Y. Wang. "In vitro cartilage tissue engineering with 3D porous aqueous-derived silk scaffolds and mesenchymal stem cells". *Biomaterials* 2005;26:7082-7094
- [5] C.R. Chu; "In situ assessment of cell viability within biodegradable polylactic acid matrices". *Biomaterials* 1995;16:1381-1389.
- [6] F. Pampaloni, E. G. Reynaud, E. H. Stelzer, The third dimension bridges the gap between cell culture and live tissue, *Nat. Rev. Mol. Cell. Biol.*, 8 (10) 2007 839-45.
- [7] Y. Aizawa, S. C. Owen and M. S. Shoichet, "Polymers Used to Influence Cell Fate in 3D Geometry: New Trends," *Progress in Polymer Science*, Vol. 37, No. 5, 2012, pp. 645-658.
- [8] G. Y. Lee, P. A. Kenny, E. H. Lee and M. J. Bissell, "Three-Dimensional Culture Models of Normal and Malignant Breast Epithelial Cells," *Nature Methods*, Vol. 4, No. 4, 2007, pp. 359-365.
- [9] C.H. Lee, A. Singla and Y. Lee. "Biomedical Applications of Collagen". in *Int J Pharm* 221, 2001, pp 1-22.
- [10] C.B. Knudson and W. Knudson (2004) "Hyaluronan and CD44: modulators of chondrocyte metabolism". in *Clin Orthop Relat Res*, 2004 pp. 152-162.
- [11] M. K. Souhaimi, T. Matsuura, in *Membrane Distillation: Principles and Applications*, Amsterdam: Elsevier, 2011, ch. 3.
- [12] A. Ouradi, Q.T. Nguyen, A. Benaboura. "Polysulfone-AN69 blend membranes and its surface modification by polyelectrolyte- layer deposit-Preparation and characterization" in *J. Membr. Sci.*, 2014 vol. 454, pp. 20-35.
- [13] B. Bath, M. C. Goncalves, A. T. N. Pires, J. Roeder, B and A. Wolf "Effects of Polyethylene Glycol on the formation on the performance of Polysulfone membrane blend with silica", in *J. Membr. Sci.*, 2000 vol. 169, pp. 287-299.
- [14] I. Pillin, N. Montrelay, Y. Grohens. "Thermo-mechanical characterization of plasticized PLA. in *Polymer* 2006, vol. 47, pp. 4676-4682.
- [15] E Al Tawil, A. Monnier, Q. T. Nguyen, M. Stephane, Y. Kassum, E. Demange and B. Deschrevel. "Matériau pour la culture des cellules, procédé de préparation et ses utilisations" French Patent application n° 14 51478, 2014.
- [16] D. Cheng, X. Cao, H. Gao, J. Hou, W. Li, L. Hao and Y. Wang, Engineering poly(lactic-co-glycolic acid)/hydroxyapatite microspheres with diverse macropores patterns and the cellular responses, *RSC Adv.*, vol. 23, 17466-17473, 2015.

An Intelligent Diagnostic System for Lung Cancer based on Principle Component Analysis - Wavelet Support Vector Machines Classifiers

Derya AVCI

Firat University, Engineering Faculty, Department of Electrical and Electronic, 23119, Elazig, TURKEY

Abstract—in this study, an intelligent diagnosis system for lung cancer on Principle Component Analysis and Wavelet Support Vector Machine Classifier is presented. The structure of this intelligent system for diagnosis of lung cancer is composed by three phases: The attribute extraction and attribute reduction phase by using Principle Component Analysis method, classification phase by using Wavelet Support Vector Machine classifier phase, and the evaluation phase of this intelligent diagnosis system performance by using classification accuracy. In first phase, lung cancer dataset is obtained and dimension of this lung cancer dataset that has 24 attributes, is reduced to 10 attributes using Principle Component Analysis method. Then, in classification stage, these reduced attributes are given to Wavelet Support Vector Machine classifier. Finally, in third phase, the correct diagnosis performance of this intelligent system for diagnosis of lung cancer is calculated by using classification accuracy. The classification accuracy of this system was obtained about 91.66 % from results of these experimental studies.

Keywords— Principle Component Analysis; Wavelet Support Vector Machine Classifier; lung cancer data; intelligent system; classification accuracy.

I. INTRODUCTION

In world, many people die because of the lung cancers. Growth of abnormal cells in one or both lungs causes lung cancer. As they grow, the abnormal cell causes tumors and disturbs the lung function, which provides oxygen to the body via the blood. On medical research area, early diagnosis of lung cancer is very important issue. If early diagnosis of this lung cancer is not performed, this fatal disease may spread from lungs to the other organs [1], [2]. In medical literature, the cancer cells spread from one organ to another organ are called as metastases. There are many reasons of lung cancer but incidence of lung cancer is strongly correlated with cigarette smoking [1].

The diagnose of lung cancer is very trouble matter for a physician [2]. Moreover, there are several reasons why the

lung cancer diagnosis incorrectly by physicians. Therefore, an intelligent diagnostic system based on Principle Component Analysis (PCA) and WSVM classifier for diagnosis of lung cancer is proposed for physician to help on diagnose of lung cancer types. This intelligent system for diagnosis of lung cancer includes three phases: 1. The attribute extraction and attribute reduction phase by using PCA method, 2. classification phase by using WSVM classifier phase, and 3. the evaluation phase of this intelligent diagnosis system performance by using classification accuracy. In first phase, lung cancer dataset is obtained and with using PCA method 24 attributes of lung cancer dataset dimension is reduced 10 attributes dimension. Then, in classification phase, these reduced features are given to WSVM classifier. Finally, in third phase, the correct diagnosis performance of this intelligent system for diagnosis of lung cancer is calculated by using classification accuracy.

In this paper, the Wavelet Support WSVM classifier, which is a different type of SVM classifiers, is used. The WSVM has all advantages of SVM, such as high correct recognition rates, simple structure, small-sample-problem solving ability, good generalization, etc. [3]. Furthermore, by using combination of wavelet kernel the WSVM develops the SVM. For this reason, the WSVM acquires more accurate recognition rates and less computational load [3]. More information about WSVM classifiers will be given in Section 3.

II. PRINCIPLE COMPONENT ANALYSIS METHOD FOR FEATURE REDUCTION

Face detection and image compressions are some fields of PCA application [4]. The PCA method is a general technique for finding data patterns. This method is used to reduce the size of the high-dimensional feature vectors. It can be formulized as below:

The K is a t -dimensional data set [4]. Generally, M_1, M_2, \dots, M_n can be given by the n leading eigenvectors of the sample covariance matrix

$$C = \left(\frac{1}{R}\right) \sum_{i=1}^R (x_i - b)^T (x_i - b), \quad (1)$$

Where,

b is the mean of instances. R is the number of instances.

According to this:

$$UM_i = v_i M_i, \quad i \in 1, \dots, n, \quad (2)$$

In there, v_i is the i th largest eigenvalue of U and given observation vector are given as below:

$$j = [j_1, j_2, \dots, j_n] = [M_1^T x, M_2^T x, \dots, M_n^T x] = M^T x \quad (3)$$

here, j is the n principal components of x .

III. WAVELET SUPPORT VECTOR MACHINE CLASSIFIER

In this present study, WSVM classifier is used for experimental studies. WSVM classifier is consisting of Support Vector Machine classifier and wavelet kernel combination [5]. SVM classifier is used to find a hyper plane that separates the various classes [6-18]. This separated various classes are computed for training set by using maximum distance to the closest. This computations space is divided by ideal separated hyper plane as mentioned above. In [19], [20] references there are more information about SVM classifiers. The formulation of wavelet kernel is given as below:

$$K(x, x') = \prod_{i=1}^S d\left(\frac{x_k - c_k}{a}\right) d\left(\frac{x'_k - c'_k}{a}\right) \quad (4)$$

In there, $d(x)$ is a mother wavelet. a and c represent the dilation and translation, respectively. [5], [21]. Here, x is each of inputs.

Where, S is sample number. $x, x' \in R^S$ and this Eq(4) is named as dot-product wavelet kernels. So, the translation-invariant wavelet kernels [22] can be presented as below:

$$K(x, x') = \prod_{i=1}^S d\left(\frac{x_k - x'_k}{a}\right) \quad (5)$$

The Morlet mother wavelet function is explained in Eq(6).

$$d(x) = \cos(1.75x) \exp\left(-\frac{x^2}{2}\right) \quad (6)$$

Morlet mother wavelet is given in Eq(7).

$$K(x, x') = \prod_{i=1}^S d\left(\frac{x_i - x'_i}{a}\right) = \prod_{i=1}^S \left(\cos\left(1.75 \cdot \frac{(x_i - x'_i)}{a}\right) \exp\left(-\frac{\|x_i - x'_i\|^2}{2a^2}\right) \right) \quad (7)$$

here, . This equations is an acceptable SVM kernel function [21].

The WSVM contains wavelet kernel as Morlet kernel in these experimental studies. The readers can be found more

information about WSVM classifiers and proof of this WSVM based on kernel function in [5], [20], [21].

IV. THE STRUCTURE OF PROPOSED PCA-WSVM INTELLIGENT DIAGNOSIS SYSTEM IN THIS STUDY

In these experimental studies, an intelligent diagnosis system for lung cancer on PCA and WSVM (PCA-WSVM) classifier is introduced. This intelligent diagnosis system consists of three phases: 1. The attribute extraction and attribute reduction phase by using PCA method, 2. classification phase by using WSVM classifier phase, and 3. the performance evaluation part of this intelligent diagnosis system performance by using classification accuracy.

In Fig 1. Shows study of the PCA-WSVM intelligent diagnosis system for lung cancer.

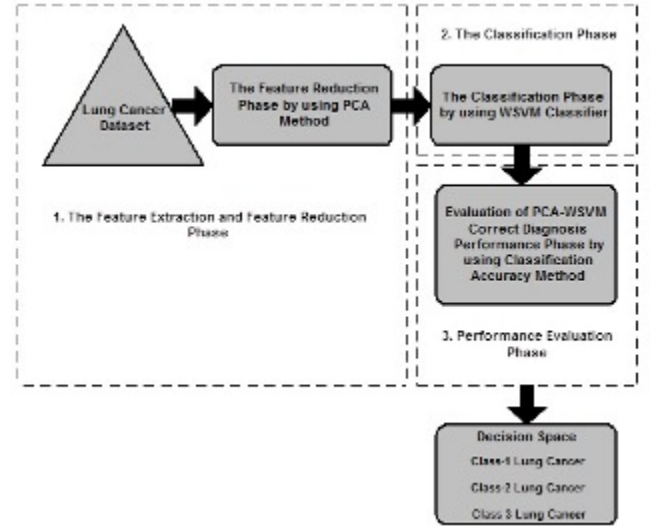


Fig 1. The blockdiagram of the PCA-WSVM intelligent diagnosis system for lung cancer used in this study.

These phases of PCA-WSVM intelligent diagnosis system for lung cancer can be given as below:

1) The Attribute Extraction and The Attribute Reduction Phase: Database of UCI machine learning respiratory and PCA-WSVM method for diagnosis of lung cancer is used for this study [23]. In this phase of PCA-WSVM intelligent diagnosis system for lung cancer, the dataset of lung cancer includes 24 attributes. In this study, database contains different kind of 160 lung cancer examples and those examples are separated three classes. Each of those classes has different kind of lung cancer types. The distribution of instances is given in Table 1.

Table 1. The distribution of instances in lung cancer dataset.

Classes of Lung Cancer	Number of Instances
Class-1 Lung Cancer	60
Class-2 Lung Cancer	50
Class-3 Lung Cancer	50

The size of this dataset is very extensive. By using PCA method 24 attributes is decreased to 10 attributes mentioned in Section 2.

2) The Classification Phase: Attribute extraction and the attribute reduction phase are given to WSVM classifier mentioned in Section 3.

The used WSVM classifier contains regularization factor (C) parameter, which can be optimized. For optimization of this parameter in these experimental studies parameter is changed between 0, 1 and 100000. These values are obtained from many experiments which are appropriate bottom and upper boundary values of C parameter respectively.

3) The Performance Evaluation Phase: In this phase of PCA-WSVM intelligent diagnosis system for lung cancer, the classification accuracy method is used for evaluating of performance of PCA-WSVM intelligent diagnosis system for lung cancer proposed in this study.

For PCA-WSVM diagnosis system 100 and 60 instances were used for testing and training set respectively. Table 2 shows the accuracy of classifications by using PCA-WSVM intelligent diagnosis system for lung cancer.

Table 2. The obtained classification accuracies by using PCA-WSVM intelligent diagnosis system for lung cancer.

	For C Regularization factor = 1	For C regularization factor = 10^2	For C Regularization factor = 10^3
Classification Accuracy (%)	88.33	91.66	90.00

As shown in Table 2, 91.66 % diagnosis rate is the highest correct rate for C = 102 which is obtained from proposed system.

V. DISCUSSIONS AND CONCLUSIONS

Our proposed system based on PCA-WSVM classifier was presented for diagnosis of lung cancer. In attribute extraction and attribute reduction phase of PCA-WSVM intelligent diagnosis system, PCA attribute method provides attributes reducing. Thus, lung cancer dataset which has 24 attributes is reduced 10 attributes.

These reduced attributes are given to WSVM classifier in classification phase of PCA-WSVM intelligent diagnosis system. The obtained 91.66 % ratio is very acceptable values for diagnosis lung cancer types. Therefore, this PCA-WSVM intelligent diagnosis system can be accepted as very successfully for diagnosis of the lung cancer types.

As shown from obtained results, the PCA attribute reduction method and WSVM classifier based learning method can assist in the diagnosis of lung cancer. The various attribute extraction and classifier methods will be used for increasing of correct accurate in future studies of lung cancer diagnostic.

REFERENCES

- [1] http://www.cdc.gov/lungcancer/basic_info/index.htm (last accessed: 07 April 2006).
- [2] K. Polat and S. Gunes, (2008), Principles component analysis, fuzzy weighting pre-processing and artificial immune recognition system based diagnostic system for diagnosis of lung cancer, Expert Systems with Applications, Volume 34, Issue 1, Pages 214-221.
- [3] Tolambiya, A. Kalra, P. K., WSVM with Morlet Wavelet Kernel for Image Compression, System of Systems Engineering, 2007. SoSE '07. IEEE International Conference on, 16-18 April 2007, On page(s): 1-5.
- [4] Polat, K., and Gunes, S. (2007). An expert system approach based on principal component analysis and adaptive neuro-fuzzy inference system to diagnosis of diabetes disease, Digital Signal Processing, Volume 17, Issue 4, Pages 702-710.
- [5] Zhang L., Zhou W. and Jiao L., (2004), Wavelet Support Vector Machine, IEEE TRANSACTIONS ON SYSTEMS, MAN, AND CYBERNETICS—PART B: CYBERNETICS, VOL. 34, NO. 1, Pages: 34-39.
- [6] Avci, E. and Turkoglu, I. (2003). Modelling of Tunnel Diode by Adaptive-Network-Based Fuzzy Inference System, International Journal of Computational Intelligence, Volume:1, Number:1, pp. 231-233.
- [7] Kosko, B., (1991), Neural Networks and Fuzzy Systems, A Dynamical Systems Approach, Englewood Cliffs, NJ: Prentice Hall.
- [8] Jang, J. S. R., Sun, C. T., (1995), Neuro-Fuzzy Modeling and Control, proceedings of the IEEE, vol. 3, No. 3.
- [9] Jang, J. S. R., May. (1993), "ANFIS: Adaptive network based fuzzy inference systems", IEEE Trans. Syst., Man. And Cybern., vol. 23, pp. 665-685.
- [10] Avci, E., Turkoglu I. and Poyraz M. (2005). Intelligent Target Recognition Based on Wavelet Adaptive Network Based Fuzzy Inference System, Lecture Notes in Computer Science, Springer-Verlag, vol. 3522 / 2005, pp. 594-601.
- [11] Comak, E., Arslan, A., & Turkoglu, I. (2006). A decision support system based on support vector machines for diagnosis of the heart valve diseases, Computers in Biology and Medicine, Volume 37, Issue 1, January 2007, Pages 21-27.
- [12] Avci, E. ve Akpolat, Z. H. (2006). Speech Recognition Using A Wavelet Packet Adaptive Network Based Fuzzy Inference System," Expert Systems with Applications, 31(3), 495-503.
- [13] Polat, K., and Gunes, S. (2007). An expert system approach based on principal component analysis and adaptive neuro-fuzzy inference system to diagnosis of diabetes disease, Digital Signal Processing, Volume 17, Issue 4, Pages 702-710.
- [14] Polat K. and Gunes, S. (2008), Principles component analysis, fuzzy weighting pre-Processing and artificial immune recognition system based diagnostic system for diagnosis of lung cancer, Expert Systems with Applications, Volume 34, Issue 1, Pages 214-221.
- [15] Watkins, A., (2001). AIRS: A resource limited artificial immune classifier, Master thesis, Mississippi State University.
- [16] Avci, E., (2007), A New Optimum Feature Extraction and Classification Method for Speaker Recognition: GWPNN, Expert Systems with Applications, 32(2), 485-498.
- [17] Avci, E., (2007). An Expert System Based on Wavelet Neural Network-Adaptive Norm Entropy For Scale Invariant Texture Classification," Expert Systems with Applications, 32(3), 919-926.

- [18] Avci, E., (2008). Comparison of Wavelet Families for Texture Classification By Using Wavelet Packet Entropy Adaptive Network Based Fuzzy Inference System”, *Applied Soft Computing*, 8 (1), 225-231.
- [19] W. M. Campbell, E. Singer, P. A. Torres-Carrasquillo and D. A. Reynolds, *Language Recognition with Support Vector Machines, Odyssey 2004*, May 31st -June 4th, Toledo, Spain, (2004).
- [20] Y. Yao, P. Frasconi, and M. Pontil, *Fingerprint Classification with Combinations of Support Vector Machines, AVBPA 2001, LNCS 2091*, pp. 253-258, (2001).
- [21] V. N. Vapnik. *Statistical Learning Theory*. Wiley, New York, (1998).
- [22] C. Cortes and V. Vapnik, “Support vector networks,” *Mach. Learn.*, vol. 20, pp. 273–297, 1995.
- [23] <ftp://ftp.ics.uci.edu/pub/machine-learning-databases>, Accessed 15.10.2014.
- [24] Watkins, A. (2001). *AIRS: A resource limited artificial immune classifier*, Master thesis, Mississippi State University.

Derya Avci – She was born in Malatya Turkey. She received a master's degree from Firat University Electronic and Computer Education. She received Ph.D. degree from Firat University Electrical and Electronic Engineering. Her interesting areas are pattern recognition, image processing, intelligent systems, and artificial intelligence systems.

Cytoplasmic Motion Visualization and Analysis of *C. elegans* Embryo

C. Atupelage*, K. Kyoda†, S. Onami††, H. Nagahashi*

*Imaging Science and Engineering Laboratory, Tokyo Institute of Technology, Japan.

†Laboratory for Developmental Dynamics, RIKEN Quantitative Biology Center, Japan.

††National Bioscience Database Center, Japan Science and Technology Agency, Japan.

Abstract—Cytoplasm is a semi-fluid substance that provides a medium to transport nutrients, proteins and organelles in between nuclear and cellular membrane. We observe different structural motions in the cytoplasm in three-dimensional (3D) space during the cell progression. Visual investigation of the dynamics of cytoplasm is important for interpreting cellular characteristics. This paper describes a technique for visualizing the cytoplasmic motion of *C. elegans* in 3D space. The motion vectors are computed by using optical flow estimation method and visualized in two different ways; velocity vector visualization in slice-images and velocity magnitude visualization as volume rendering. In addition, we performed an analytical experiment of velocity changes during mitotic cell division. The describing visualization methods will be significant for advanced biological investigations of cytoplasmic streaming.

Index Terms—Cytoplasmic streaming, Motion analysis, Optical flow, Lucas-Kanade, *C. elegans* embryo

I. INTRODUCTION

Cytoplasm's primary roles are providing a medium for cell's organelles and maintaining the cell's inner structure intact. Cytoplasm is a semi-fluid substance that contains proteins, enzymes, carbohydrates, lipids and so on. In a cell of living organism, cytoplasm occupies the space between cellular and nuclear membrane. During the cell progression, cytoplasm helps to exchange the materials between organelles, as well as between cells [1]. A number of biochemical reactions take place inside the cytoplasm during cell progression. We may visually observe movement of cytoplasmic particles such as cellular metabolites and this process is called cytoplasmic streaming. Physically, cytoplasm moves in three-dimensional (3D) space between cellular and nuclear membrane. Cytoplasmic streaming has been described in many research articles [1]–[3]. However, the physical motion of the cytoplasmic streaming in *Caenorhabditis elegans* (*C. elegans*) embryo has not been widely analyzed [4].

C. elegans is widely used for describing cellular dynamics in biology. *C. elegans* offers many advantages such as short life cycle, compact genome, stereotypical development, ease of propagation, transparent body, and so forth. The *C. elegans* embryo is an excellent tool for studying the cytoplasmic streaming because of its transparent body [5]. Using differential interference contrast (DIC) microscopic 3D time-lapse imaging of *C. elegans* embryo allows the examination of the spatiotemporal dynamics of cytoplasmic streaming. The 3D time-lapse DIC microscopy includes two parameters; distance

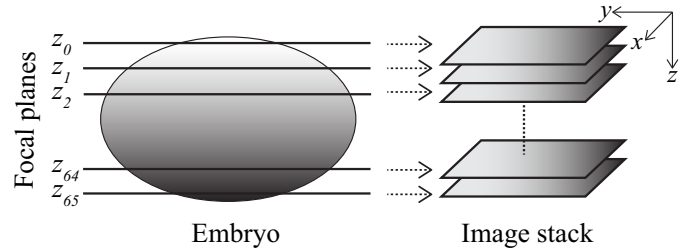


Fig. 1: DIC microscope imaging anatomy of *C. elegans* embryo.

between focal planes and duration between time-points. At every time-point, the microscope generates an image-stack that consist of 66 images of different focal plane as shown in Fig.1. An example of 3D time-lapse DIC microscope images of *C. elegans* embryo are shown in Fig.2. Focal plane moves from top to bottom and four neighbouring focal planes are shown. Three consequent time-points in early and later stages of cell division is presented from left to right.

Analyzing the dynamics of cytoplasmic streaming is important to understand many biological properties of the cell [3], [4], [6]. Most of the cytoplasmic streaming-based studies have used 2D motion of the cytoplasm. In fact, Cytoplasmic streaming takes place in 3D space and this motion can be observed by time-lapse image-stacks. Subjective analysis of this image data is a crucial task for the biologists. In general, image processing-based techniques are used to extract features of specific cellular organelle. The extracted features are used to describe the organelle's dynamics [7]. The cytoplasm is semi-fluid substance and it may have many unknowns. Therefore, it is necessary to have a user friendly visualization tool to examine the motion of cytoplasm in advance of its quantitative analysis.

This paper describes two forms of visualization of the motion of the cytoplasm. In particular, we compute the cytoplasmic motion in imaging domain by using optical flow (OF) estimation method and visualize the motion vectors in a user friendly manner. Inspired from our previous work [8], we advanced the visualization by incorporating volume rendering techniques for analyzing the spatiotemporal motion of cytoplasm. Visualizing the 3D motion of each slice in the image-stack provides clear picture to understand the motion of particular focal plane at given time-point. However, it does not

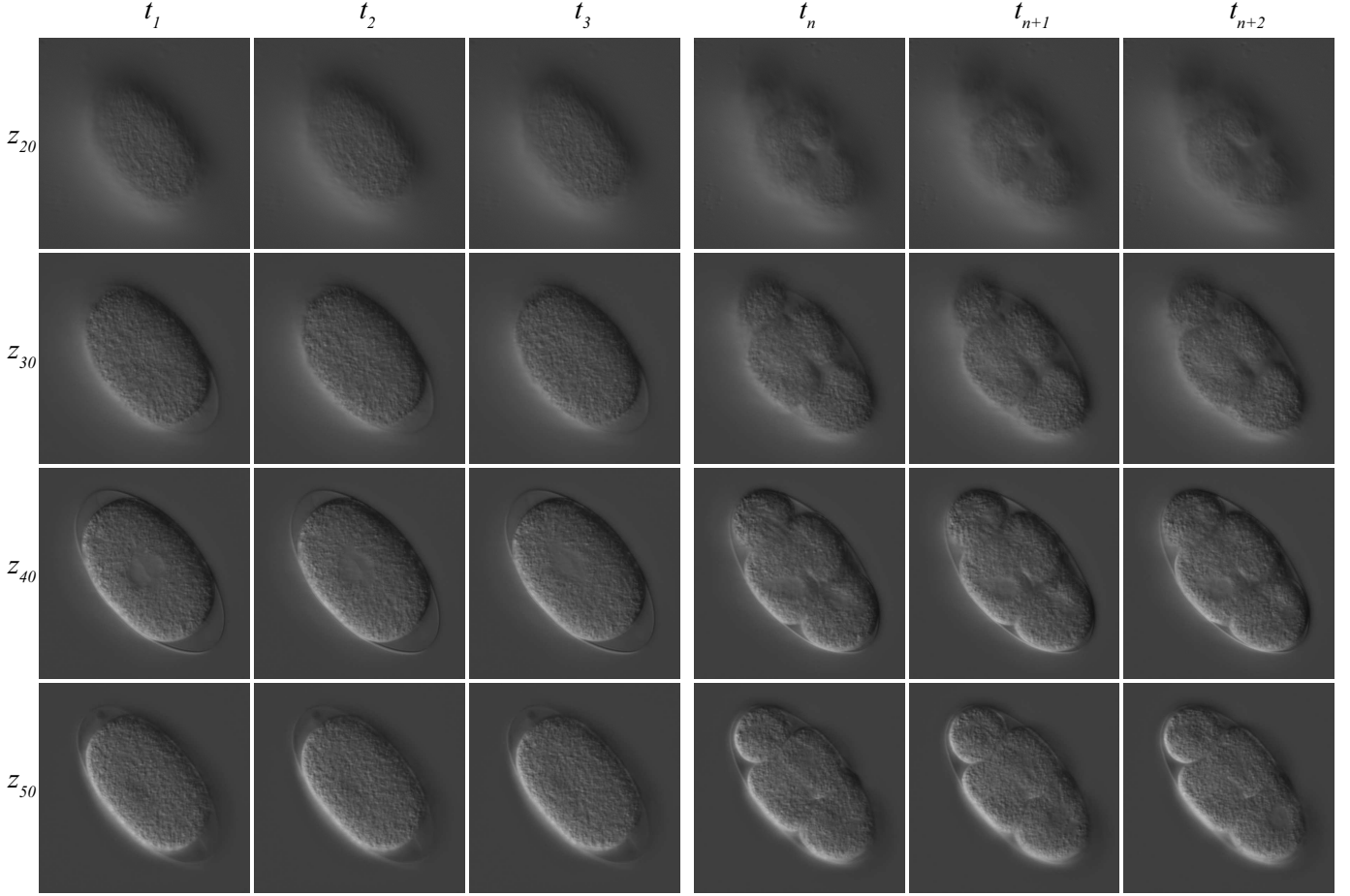


Fig. 2: DIC images of wild-type *C. elegans* embryo. Top to bottom: slice images of 20th, 30th, 40th and 50th focal planes (slice number is assigned along z axis as described in Fig.1). Left to right: Three consequent time-points in early and later stages of cell division. From t_1 to t_3 is one-cell stage and from t_n to t_{n+2} is 4-cells stage of the embryo.

enough to observe the motion inside the entire cell. As a result, observer cannot precisely grasp the entire physical motion of the cytoplasm. On the other hand, 3D vector fields can be visualized using different parameters such as magnitude, angle, divergence and curl. This paper describes volumetric visualization of velocity magnitudes of the cytoplasmic motion. This visualization method can be used in advanced biological investigations of cytoplasmic streaming.

Furthermore, we performed analytical experiments with respect to cell division. In particular, we compared the velocity magnitudes with manually determined cell division time-points. Examination of the velocities at local regions also important to determine the cellular structure and position of cleavage furrow at the division. We investigate the localized velocity magnitudes during cell progression. The results show that the position of cleavage furrow can be approximately observed by computing localized velocity magnitudes.

II. 3D MOTION ESTIMATION

A. Optical flow

OF describes the motion of the local window across any two consequent frames of an image sequence. In particular, it computes the distance of the movement of the pixels between

two adjacent images [9]. For 3D motion analysis, it estimates the distance of movement between adjacent voxels. OF estimation methods can be grouped into four categories: block-based methods, spatiotemporal differential methods, frequency-based methods, and correlation-based methods [10], [11]. Lucas-Kanade (KL) [12] OF estimation is a spatiotemporal differential method and it is well-known because of its accuracy for most of the natural phenomena. The basis for the spatiotemporal differential OF is the motion constraint equation. In the following, we describe the mathematical definitions of OF estimation for 3D volume images.

Let a volume at time t denote by $I(x, y, z)$. In time-interval δt , it moves by δx , δy and δz to $I(x + \delta x, y + \delta y, z + \delta z)$. Then we can write the basis for the 3D motion constraint equation as,

$$I(x, y, z, t) = I(x + \delta x, y + \delta y, z + \delta z, t + \delta t). \quad (1)$$

Assuming that δx , δy , δz and δt are very small, the right side of the equation is approximated by its Taylor expansion.

$$I(x + \delta x, y + \delta y, z + \delta z, t + \delta t) = I(x, y, z, t) + \frac{\partial I}{\partial x}\delta x + \frac{\partial I}{\partial y}\delta y + \frac{\partial I}{\partial z}\delta z + \frac{\partial I}{\partial t}\delta t + H.T.O., \quad (2)$$

where $H.T.O$ is Higher Order Term, which is very small.
Eq.1 and Eq.2 yield,

$$I_x v_x + I_y v_y + I_z v_z = -I_t, \quad (3)$$

where $v_x = \delta x / \delta t$, $v_y = \delta y / \delta t$, and $v_z = \delta z / \delta t$ are the optical flows (velocities) on x , y , and z directions, respectively. $I_x = \partial I / \partial x$, $I_y = \partial I / \partial y$, $I_z = \partial I / \partial z$, and $I_t = \partial I / \partial t$ are derivatives at (x, y, z, t) .

Eq.3 can be rewritten more compactly as,

$$(I_x, I_y, I_z) \cdot (v_x, v_y, v_z) = -I_t. \quad (4)$$

Then we obtain the motion constraint equation as,

$$\nabla I \cdot \vec{V} = -I_t, \quad (5)$$

where $\vec{V} = (v_x, v_y, v_z)$ is the 3D volume velocity (3D optical flow) and $\nabla I = (I_x, I_y, I_z)$ are spatial intensity gradients and I_t is the temporal intensity derivatives.

B. Lucas-Kanade (KL) method

The motion constraint equation in Eq.5 has three unknowns. LK method solved this problem by assuming that the local region has identical motion in between two consequent volumes.

For a n voxels of local region, we obtain a linear equation system from Eq.3 as,

$$\begin{aligned} \frac{\partial I_1}{\partial x_1}\delta x + \frac{\partial I_1}{\partial y_1}\delta y + \frac{\partial I_1}{\partial z_1}\delta z &= -\frac{\partial I_1}{\partial t} \\ \frac{\partial I_2}{\partial x_2}\delta x + \frac{\partial I_2}{\partial y_2}\delta y + \frac{\partial I_2}{\partial z_2}\delta z &= -\frac{\partial I_2}{\partial t} \\ &\dots \\ \frac{\partial I_n}{\partial x_n}\delta x + \frac{\partial I_n}{\partial y_n}\delta y + \frac{\partial I_n}{\partial z_n}\delta z &= -\frac{\partial I_n}{\partial t} \end{aligned} \quad (6)$$

We use the following notations and rewrite the above equation system in a matrix form.

$$A = \begin{bmatrix} \frac{\partial I_1}{\partial x_1} & \frac{\partial I_1}{\partial y_1} & \frac{\partial I_1}{\partial z_1} \\ \frac{\partial I_2}{\partial x_2} & \frac{\partial I_2}{\partial y_2} & \frac{\partial I_2}{\partial z_2} \\ \dots & \dots & \dots \\ \frac{\partial I_n}{\partial x_n} & \frac{\partial I_n}{\partial y_n} & \frac{\partial I_n}{\partial z_n} \end{bmatrix}, b = \begin{bmatrix} \frac{\partial I_1}{\partial t} \\ \frac{\partial I_2}{\partial t} \\ \dots \\ \frac{\partial I_n}{\partial t} \end{bmatrix}, v = \begin{bmatrix} v_x & v_y & v_z \end{bmatrix}^T$$

$$Av = b \quad (7)$$

By computing the pseudo-inverse of A , we can estimate optical flows: v_x , v_y and v_z ,

$$v = (A^T A)^{-1} b \quad (8)$$

C. Implementation optimization

Theoretical definitions of OF and LK method are based on two assumptions; 1) voxels' (or pixel) intensity is not changed within δt time interval, 2) Neighborhood voxels of a given point have identical motions within two volumes [13], [14]. Let a local volume W_t . We estimate its velocity according to Eq.8 and obtain corresponding local volume in subsequent frame as W_{t+1} . According to the definition in Eq.1, $W_t - W_{t+1} \approx 0$. In practice, $W_t - W_{t+1}$ is not always zero.

This problem can be minimized by computing and updating $\partial I / \partial t$ in Eq.6 iteratively k times as following,

$$I_{t+1}(x + v_i) - I_t(x) = v_{i+1}, \quad (9)$$

where $i = 0, 1, 2, \dots, k$, x and v present the voxel and velocities for each x , y and z directions.

In each iteration, the value v_{i+1} is getting lower. Setting appropriate value for k and threshold for v_{i+1} , we can obtain the motion vector as $\sum_{i=0}^k v_i$.

In addition, LK method assumes that the distance of the voxels movement is constrained to the maximum distance of the neighborhood. Therefore, it is unable to estimate the large motions that move beyond the neighborhood volume. However, large movement can be approximated by utilizing Gaussian pyramid approach into the computation.

Similar with the 2D Gaussian pyramids; we convoluted the entire volume with 3D Gaussian kernel and reduced the size to half. In practice, we obtain three levels of Gaussian pyramid. The OF computation starts from the top-level volume in the pyramid. The results are substitute to the computation in next level. Because the size of the next bottom level is twice as the upper level, results are interpolated by factor of two for each x , y and z directions. Finally, we estimate the motion from bottom-most level in the pyramid.

III. EXPERIMENTAL ANALYSIS

A. Data acquisition

A set of wild-type *C. elegans* embryos was captured using an automated 4D DIC microscope. It captures the embryo at 66 focal planes (spacing $0.5016 \mu m$) in 20 seconds time-interval. An image is 600×600 pixels and a one pixel is approximately equal to $0.1015 \mu m$. Therefore, we obtained image-stack of 66 images in each time-point. The image capturing was started before pronuclear meeting and continued about 30 minutes.

B. Visualization

In general, we can visually observe the positioning of nuclei and cellular membranes. However, visual analysis of cytoplasmic motion is an extremely difficult task. The 3D visualization of the motion vector enhances the capability of analyzing the cytoplasmic streaming. We describe two forms of motion vector visualizations; 1) Image slice-based motion vector visualization in 3D pane with the corresponding original image, 2) Visualizing motion vector magnitudes of every voxel in a single image-stack using volume rendering.

Looking at the motion vectors with corresponding image enhanced the observer's sensitivity of the motion of the

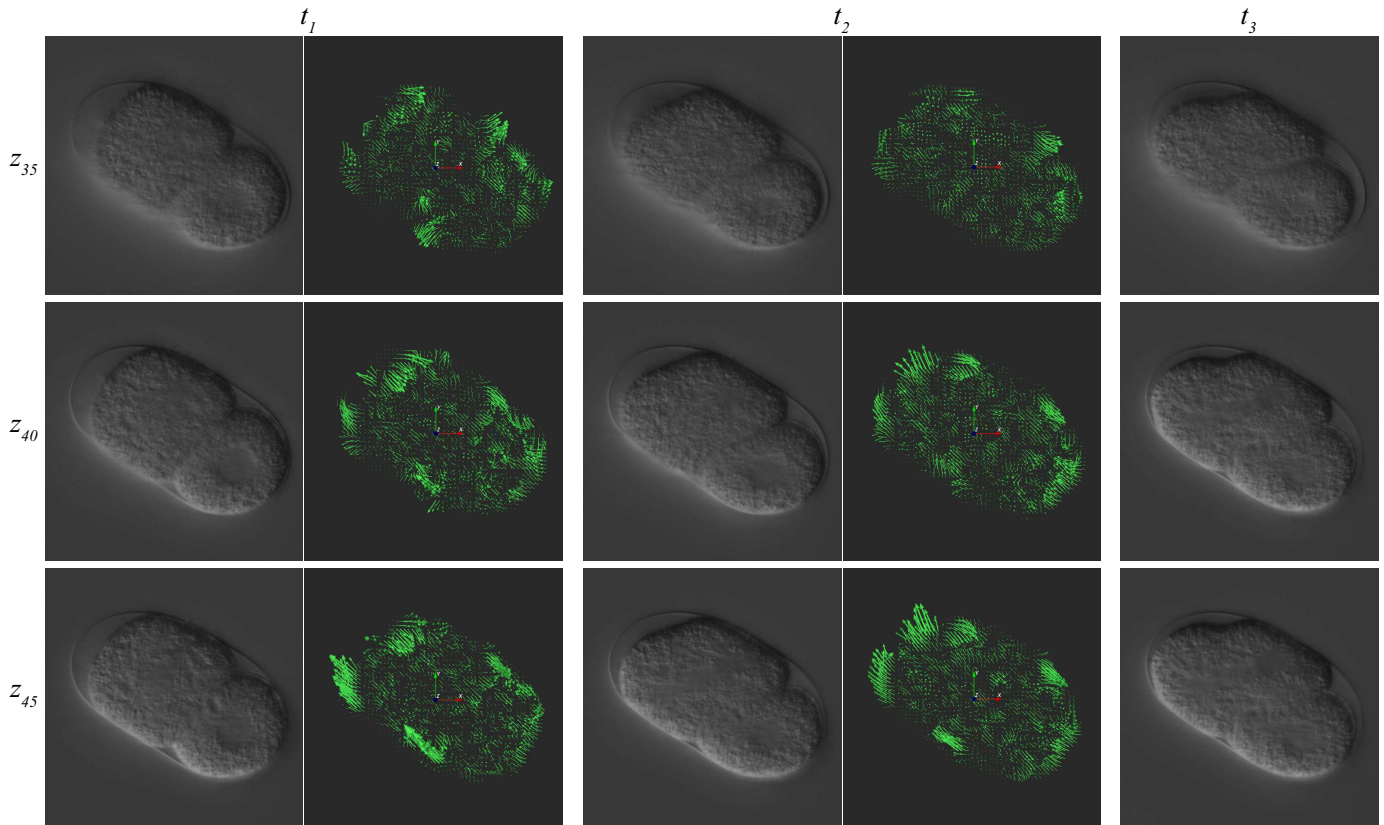


Fig. 3: Image slice-based motion vector visualization. Top to bottom: slice images of 35th, 40th and 45th confocal planes (slice number is assigned along z axis as described in Fig.1). Left to right: Three consequent time-points (t_1 to t_3) in early stage cell division. At t_1 and t_2 , slice images and corresponding motion vector panes are shown and at t_3 , only the slice image is given.

cytoplasm. Since the motion vectors are placed in 3D panel, observer can extend the visibility of velocities by looking through several angles. Slice-based motion vector visualization can be used to describe several cellular characteristics. In the following, we illustrate an example of utilizing slice-based motion vector visualization for describing particular cellular characteristic in spatiotemporal domain. Cytoplasmic streaming analyses may also be important for observing the cellular deformation during cell division. In particular, motions at a given time-point may help to describe the deformation of the cell at the next consequent time-point. In practice, examining consequent 2D image frames does not make clear understanding of the deformation, because the exact motion is occupied in 3D space. Therefore, it is important to visualize the consequent slice images with their motion vectors followed by images at next consequent time-point. Fig.3 shows an example; cytoplasmic motion of 35th, 40th and 45th slice images (slice number is assigned along z axis as described in Fig.1) at three consequent time-points. Second and 4th columns shows the 3D motion vectors of 1st and 3rd columns. Visual observation of Fig.3 indicates that there is a large motion towards up side around left region in the cytoplasm. Therefore, we may anticipate that the forthcoming daughter cell (result of AB cell division) in left-side will be placed slightly in a upper focal-plane in the embryo.

Visualizing 3D motion vectors in 2D space does not provide enough sensitivity of the cytoplasmic streaming through the entire cell. Therefore, we performed volumetric visualization of the motion vectors. The most straightforward visualization parameter is the magnitude of the vector. We used magnitudes of the motions vectors as voxels' intensities for volume rendering. We carried out few pre-processing over the volumetric data before the rendering. The major issue in our dataset is the space between image slices. There is a space, approximately five voxel, in between the two image slices. Therefore, we fill the space of two consequent image slices by performing bilinear interpolation. In addition, we performed smoothing by using 3D averaging filtering for the voxels. Example of the volumetric visualization of motion vector magnitudes are shown in Fig.4. Observing the volumetric data during cell progression rapidly improves the awareness of cytoplasmic streaming.

C. Motion analysis

In addition to the visualization, 3D motion vectors can be used for analytical investigations of cytoplasmic streaming. In 3D vector domain, the most straightforward analytical parameter is the velocity magnitudes. We investigated the average velocity magnitudes at each time point during early development of *C. elegans* embryo.

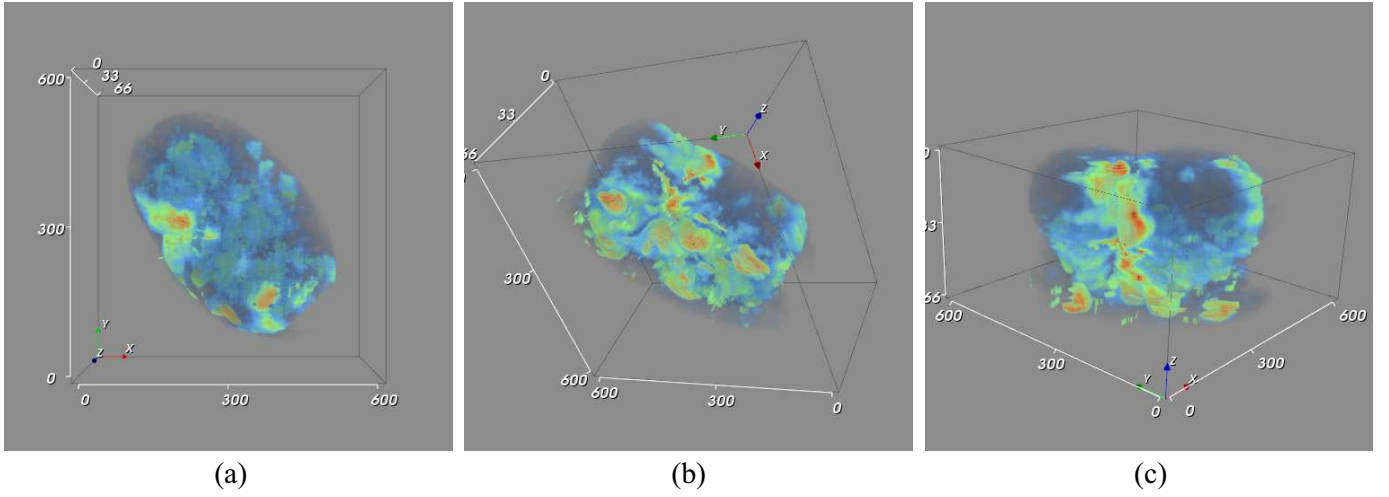


Fig. 4: 3D volumetric visualization of velocity magnitudes. (a), (b) and (c) shows a volume (fixed time-point) three different rotation angles.

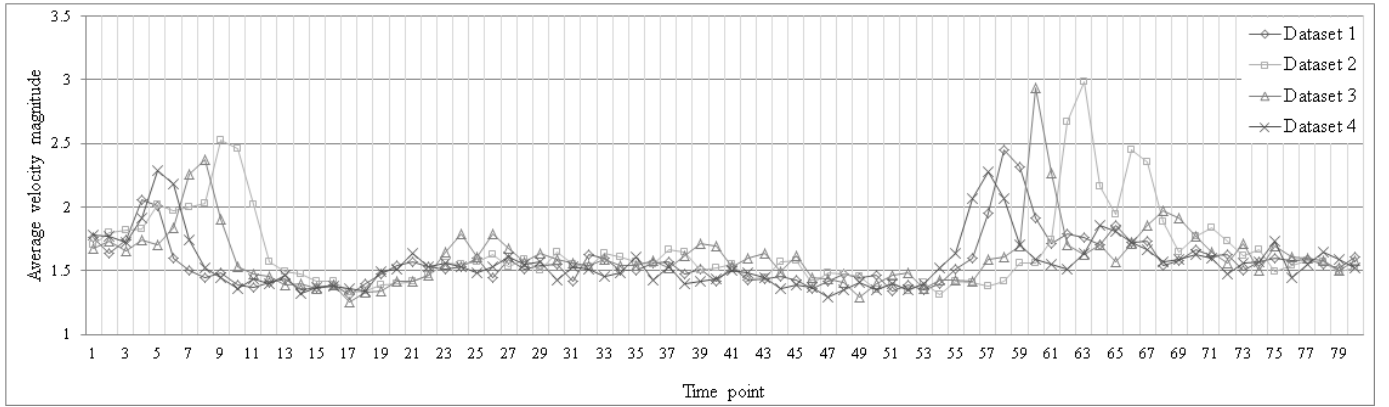


Fig. 5: Average velocity magnitudes of image stack during cell division.

In the early stage of *C. elegans* embryo, the male and female pronuclei migrate towards each other and fuse to become a one-cell stage embryo. This phase is called pronuclear meeting and the resulted cell is labelled as P_0 . During the early embryonic development, P_0 cell divides into two, AB and P_1 cells. This division process is continuously progressing individually on each cell, in which the number of cells in the embryo is increased. In this work, we utilized four datasets and visually examined the approximate time-points of three events; pronuclear meeting, P_0 cell division and AB cell division. Annotations are tabulated in Table I. Subsequently, we analyzed cytoplasmic motions of the entire cell up to AB cell division. Fig.5 shows averaged motion vector magnitudes of each image-stack up to 80 time-points.

Fig.5 shows that cytoplasmic motion is relatively larger during the pronuclear meeting and AB cell division. P_0 cell division shows relatively low acceleration in cytoplasmic streaming. In addition, Fig.5 indicates that cytoplasmic streaming accelerates after the time-point when cell division starts (as indicated in Table. I). Generally, the cell division starting time-point is determined by the nuclear shape. Nuclear shape change may not significantly affect (in terms of motion) the cytoplasm. During the cleavage furrow formation cytoplasm

is divided into two regions. As a consequence, we observe accelerations in cytoplasmic regions at the beginning of cellular membrane development.

Furthermore, localization of the motion vectors may be useful for pre-determination of position of cleavage furrow in the cell. For a given time-point and focal plane, we obtained the magnitudes of motion vectors and performed smoothing for enhancing the visualization. Subsequently, velocity magnitudes are visualized by using *Jet* color-map. Fig.6 shows the velocity magnitudes at P_0 and AB cell division of two *C. elegans* embryos. Fig.6(a) and (c) indicate that it is easy to identify the detaching points of P_0 cell division where two arrows are pointed. AB cell divisions are shown in Fig.6(b) and (d). We do not obtain precise detaching points from these images. However, geometrical computation using local-maxima points, locations of previous detaching points (at P_0 cell division) and domain specific information may be used to approximate the positions of cleavage furrow at AB cell division.

IV. DISCUSSION

Studying the cytoplasmic motion in 3D space is very difficult task for biologist. In fact, visual analysis of cytoplasmic

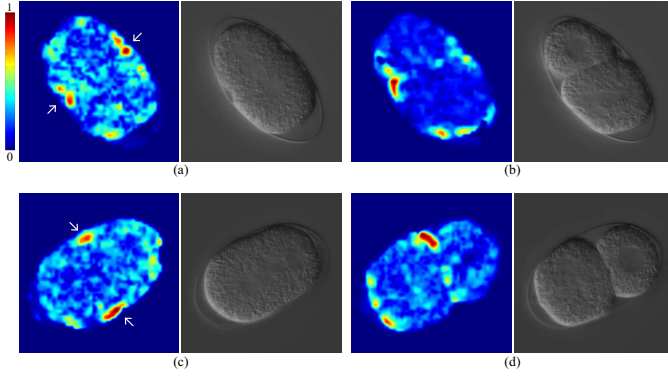


Fig. 6: Velocity magnitudes at P_0 and AB cell divisions of two *C. elegans* embryos. First and second rows present two embryos. (a) and (c) shows the velocity magnitudes at P_0 cell division. (b) and (d) shows the velocity magnitudes at AB cell division. Arrows in (a) and (c) point to the maximum velocities, where the cytoplasm detachment starting points of P_0 cell division. The image slice (focal plane) is selected for best visualization as large velocity magnitudes are localized in cell membrane.

TABLE I: Annotation of cell division starting time-points

Dataset	Pronuclear meeting	P_0 cell division	AB cell division
Dataset 1	2	17	55
Dataset 2	8	19	61
Dataset 3	8	18	57
Dataset 4	5	16	54

mic streaming is important for describing precise biological properties of the cell. This paper presents two cytoplasmic motion visualization methods based on OF computation.

Slice-based visualization is important for study the cytoplasmic behaviour while looking at the corresponding image sequence. In addition, slice-based motion velocities may be significant to estimate positions of cleavage furrow and approximate cell membrane. The presented volumetric visualization can be improved by including the boundary of egg shell. The presented work only utilized the vector magnitudes for volume rendering. Visualizing the vector field properties such as divergence and curl may benefit to localize specific motion patterns of cytoplasmic streaming.

The described motion estimation technique and visualization tool can also be used for both wild type and RNAi-treated *C. elegans* embryos. Four dimensional DIC microscope images of 136 RNAi-treated embryos against 72 genes are publicly available online at Worm Development Dynamics Database (WDDD) [15]. Utilizing motion analysis with these dataset may provide novel opportunity to explore gene function of cytoplasmic events.

V. CONCLUSION

During the cell progression, cytoplasmic particles move in between cellular and nuclear membrane. Visual analysis of

cytoplasmic motion in DIC time-lapse image-stacks is very challenging task. This paper described visualization methods for observing approximate physical motion of the cytoplasm in *C. elegans* embryo. OF motion estimation method is used for computing the motion vectors.

These motion vectors are visualized as a vector field in image slices. Volumetric visualization is used to present the magnitudes of entire image-stack. These visualizations methods are significant for studying the biological properties of cytoplasmic streaming. In addition, the motion vectors can be used to determine the significant turning points in the cell division such as cytoplasmic division.

REFERENCES

- [1] U. Wolke, E. A. Jezuit, and J. R. Priess, "Actin-dependent cytoplasmic streaming in *C. elegans* oogenesis," *Development*, vol. 134, no. 12, pp. 2227–2236, 2007.
- [2] J. A. Govindan, S. Nadarajan, S. Kim, T. A. Starich, and D. Greenstein, "Somatic cAMP signaling regulates MSP-dependent oocyte growth and meiotic maturation in *C. elegans*," *Development*, vol. 136, no. 13, pp. 2211–2221, 2009.
- [3] C. Resagk, E. Lobutova, L. Li, and D. Voges, "Micro PIV Measurements of the Internal Flow of an Amoeba proteus," in *16th Int Symp on Applications of Laser Techniques to Fluid Mechanics*, vol. 1, Lisbon, Portugal, Jul. 2012, pp. 1–4.
- [4] R. Niwayama, K. Shinohara, and A. Kimura, "Hydrodynamic property of the cytoplasm is sufficient to mediate cytoplasmic streaming in the *Caenorhabditis elegans* embryo," *Proceedings of the National Academy of Sciences*, vol. 108, no. 29, pp. 11 900–11 905, 2011.
- [5] P. Gönczy, C. Echeverri, K. Oegema, A. Coulson, S. J. Jones, R. R. Copley, J. Dupéron, J. Oegema, M. Brehm, E. Cassin, and others, "Functional genomic analysis of cell division in *C. elegans* using RNAi of genes on chromosome III," *Nature*, vol. 408, no. 6810, pp. 331–336, 2000.
- [6] J.-W. van de Meent, A. J. Sederman, L. F. Gladden, and R. E. Goldstein, "Measurement of cytoplasmic streaming in single plant cells by magnetic resonance velocimetry," *Journal of Fluid Mechanics*, vol. 642, pp. 5–14, 2010.
- [7] S. Hamahashi, H. Kitano, and S. Onami, "A system for measuring cell division patterns of early *Caenorhabditis elegans* embryos by using image processing and object tracking," *Systems and Computers in Japan*, vol. 38, no. 11, pp. 12–24, 2007.
- [8] A. Chamidu, N. Hiroshi, K. Kyoda, and S. Onami, "3d visualization of cytoplasmic streaming," in *Reports of the Technical Conference of The Institute of Image Electronics Engineers of Japan*, Wakayama, Japan, Feb. 2015, pp. 95–99.
- [9] B. McCane, K. Novins, D. Crannitch, and B. Galvin, "On benchmarking optical flow," *Computer Vision and Image Understanding*, vol. 84, no. 1, pp. 126–143, 2001.
- [10] D. J. Fleet and A. D. Jepson, "Computation of component image velocity from local phase information," *International journal of computer vision*, vol. 5, no. 1, pp. 77–104, 1990.
- [11] M. Ghanbari, "The cross-search algorithm for motion estimation [image coding]," *Communications, IEEE Transactions on*, vol. 38, no. 7, pp. 950–953, 1990.
- [12] B. D. Lucas and T. Kanade, "An iterative image registration technique with an application to stereo vision," in *Proceedings of the 7th International Joint Conference on Artificial Intelligence (IJCAI'81)*, April 1981, pp. 674–679.
- [13] B. Duvenhage, J. Delpont, and J. de Villiers, "Implementation of the Lucas-Kanade image registration algorithm on a GPU for 3d computational platform stabilisation," in *Proceedings of the 7th International Conference on Computer Graphics, Virtual Reality, Visualisation and Interaction in Africa*, 2010, pp. 83–90.
- [14] N. Sharmin and R. Brad, "Optimal Filter Estimation for Lucas-Kanade Optical Flow," *Sensors*, vol. 12, no. 9, pp. 12 694–12 709, 2012.
- [15] K. Kyoda, E. Adachi, E. Masuda, Y. Nagai, Y. Suzuki, T. Oguro, M. Urai, R. Arai, M. Furukawa, K. Shimada, and others, "WDDD: worm developmental dynamics database," *Nucleic acids research*, vol. 41, no. D1, pp. D732–D737, 2013.

Development of a portable system for vibration stimulation to improvement of walking stability

Min-Hwa Park and Dong-Wook Kim

Abstract—Postural equilibrium refers to the ability to maintain the balance of posture by supporting the weight of the body. Gait requires balance and the roles of visual senses, vestibular system and somatosensory system are important to maintain posture. Also gait is a voluntary movement that requires interactions between sensory, muscular and central nerve systems. Therefore, gait disorder may improve by using the external stimulus on sensory system. However, there have not been many studies on biomechanical changes of gait, a dynamic posture of body, when a somatosensory stimulation is applied. Gait experiment was performed to validate this hardware in actual situation with 3-dimensional motion analysis and gait analysis. The results showed changed ground reaction force and angle of joint, which was considered that local somatosensory stimulation gave immediate feedback and changed the characteristics of gait during the gait. This study used a real-time analysis of patient's movement and external stimulation applied at proper timing and its results would be usefully applied in patients who requires gait guidance and have gait abnormality due to lack of balance for rehabilitation.

Keywords—motion analysis, somatosensory, vibration stimulation.

I. INTRODUCTION

THE posture equilibrium and ability to control the posture is a must to perform various movements in everyday life. The postural equilibrium is particularly important in a gait, the movement to change the center of gravity of the body. Maintaining the postural equilibrium involves balancing all forces applied in the body to make the body stand at a desirable position or perform desirable movement or activities without losing the balance. In this process, the motor system of body is used.

Gait is a process of moving center of gravity of the body forward and for this moving, motion system of human body is utilized. One of the most significant elements of gaits is balance. The types of balance are composed mainly of static balance and dynamic balance. Static balance refers to the ability to maintain balance when we maintain a certain posture. Maintaining static

balance involves placing the center of gravity within the base of support, so that the body may not move helplessly. On the other hand, dynamic balance means the ability to maintain balance while the body is on the move, which involves maintaining the center of gravity within the base of support to maintain a desired posture [1].

Although gait treatment system of older operated by inflow of sensory stimulation from outside is taking medicine following doctor's prescription and physical therapy, it has a limitation.

Provided that somatosensory is the basic information to get the stable body position with visual, vestibular sense, we stimulate somatosensory in order to improve position stability of body.

Among the studies giving vibration stimulation to influence, there are a lot of studies that influence posture balance control when giving mechanical stimulation to lower limbs muscle of subjects [2, 3]. The strength put out by the muscles or the radius of joint movements is adjusted so that we can continue walking. A number of studies have been conducted to identify the relationship between stability in posture and stimulations on the somatosensory system. One of these studies include a study where electric stimulation was applied to the knee joint of a Parkinson patient through the stimulation of somatosensory system, which showed that such stimulations may result in reduction of agitation of the body [4]. A study reported that vibration stimulus applied to the soles of the feet of the elderly reduced the risk of falling by reducing gait variability [5]. Also, it was shown that electric stimuli applied to certain muscles on the left and right legs could help stabilize standing postures [6]. However, such electric stimuli have their limitations due to issues with stability [7].

From the study due to the vibration stimulus, when the vibration stimulation was applied to the tibialis anterior, the activity of the tibialis anterior and extensor digitorum longus increased, which showed that the activity of the muscles used for gait was changed according to the application site of vibration stimulation. And mechanical vibration stimulation that causes somatosensory stimulation affected the gait pattern via the adjustment of the characteristics of vibration stimulation, and even locally applied stimulation affected the broad part of the body [8].

In order to solve these problems, small sensors such as FSR sensor [9], acceleration sensor [10] and angular velocity sensor [11] are used for gait analysis.

This study shows the portable system which help distinguish

This work was supported by the National Research Foundation of Korea (NRF) grant funded by the Korea government (MSIP) (NRF-2012R1A2A2A01012599).

Min-Hwa Park is with the *Department of Healthcare Engineering, Chonbuk National University, Jeonju-si, Jeollabuk-do, Korea* (e-mail: pmh1004@jbnu.ac.kr)

Dong-Wook Kim is with the *Division of Biomedical Engineering, Chonbuk National University, Jeonju-si, Jeollabuk-do, Korea* (corresponding author to provide phone: +82-63-270-4060; fax: +82-63-270-2247; e-mail: biomed@jbnu.ac.kr).

types of gait abnormality applying gyro and acceleration signals which are get from small sensor and the portable system which cares gait abnormality system in normal life.

The Gait abnormality and treatment system showed in this system is produced to use in normal life and it is potable and can distinguish gait abnormality and decide the point of the external stimulation based on the information of the moving of patient, therefore this system can improve the effectiveness of treatment.

II. METHOD

In this study, we conceive the algorithm which gives proper stimulation when abnormality in order to develop somatosensory system using local vibration. We get the acceleration and gyro sensor signals from this sensor module, and output gyro and acceleration sensor signals which among the flexion of the ankle joint sagittal axis formed.

In this study, we stimulate tibialis anterior and triceps surae in order to inflow somatosensory handling extension ankle muscle which are in the category of proprioceptive sensibility during walking action.

The somatosensory senses related to the surface of various parts of the body that are affected by the somatosensory system require mechanical receptors. In this study, we designed the processes to apply stimulation onto the pacinian corpuscles, which re-acts to vibratory stimuli in a strong and fast manner. The receptor's sensitivity was highest at the tendons, while 200~300Hz frequencies resulted in the strongest reactions. In this study, therefore, we stimulated the tibialis anterior tendon and Achilles tendon in order to stimulate the tibialis anterior and triceps surae, which are responsible for flexion of the ankle muscles. Flexion of ankle muscles is one of the unique receptor sensors as a part of the somatosensory senses.

The software of the gait abnormality treatment system detects gait events by interpreting the peaks of gyro sensor signals received from the sensor module placed on the sole. The signal processor of the system receives gyro and acceleration signals from the sensor module in real time and extracts the pitch value of gyro signals. The gait events detected by gyro signals are heel strike and toe-off, which are used to distinguish the stance and swing phase and the system is controlled to output signals only during the stance phase.

The part applying into this stimulation produce output signal that operate vibration device part attached tibialis anterior tendon after detected dorsiflexion of ankle joint, when decreasing and detected plantar flexion of ankle joint, it produces output signal operating vibration device part attached achilles tendon.

Fig. 1 shows applied gait improvement algorithm. The gait improvement algorithm from this study is operated by sensor part which digitalize gyro and acceleration signals, control part which output the input signal of vibration stimulation by analyzing the input signal in this sensor, power supply part which supply power to motion sensor part and signals, hardware made by vibration device part producing vibration stimulation,

control part which detect gait event using gyro signals from sensor and firmware which control the input signal by gait event.

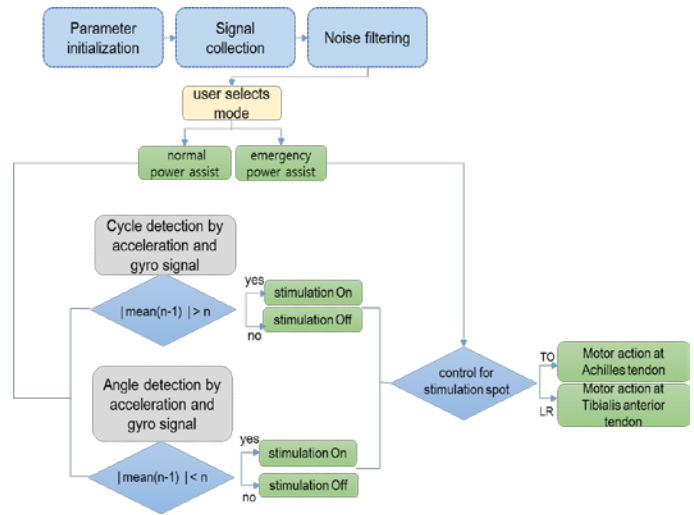


Fig. 1 The gait improvement algorithm.

Fig. 2 and 3 are the hardware of gait improvement algorithm based on vibration stimulation in this study. The hardware of gait improvement system consists of a sensor, signal processor, power supply and vibratory stimulation applicators. For this study, MPU-6050 sensor module consisting of triple-axis gyroscope, triple-axis accelerometer, and 32 bit MCU and ATmega128 (Atmel corporation, U.S.A.), low-power 8 bit microcontroller, were used. The sensitivity of gyro signals in the sensor module was set at 500 dps and sampling rate, 100Hz. The input port in the Atmega128 receives gyro signals from the sensor module and transmits them to signal processors. Its output port outputs the voltage signals that operate vibratory device upon the application timing and sites of vibratory stimulation after the gyro signals are processed in the signal processor.

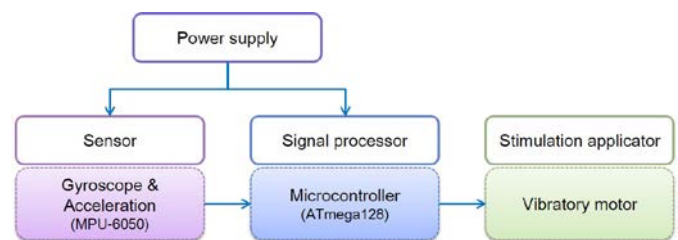


Fig. 2 Block diagram of vibration stimulation system

The vibratory stimulation applicator transmits the voltage signals from output port and activates the vibratory device to create vibratory stimulation. The vibratory device that creates mechanical vibratory stimulation controls the electronic signals and changes operation modules. In this study, the sensor of the

treatment system was placed beneath the arch of sole; the signal processor and power supply, the top of the foot; and vibratory stimulation applicator, the Achilles and tibialis anterior tendon.

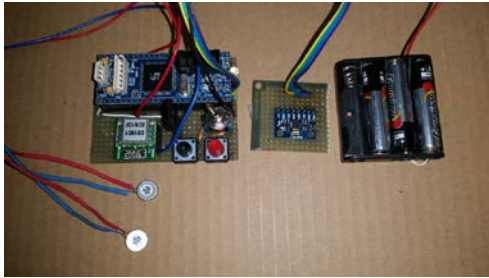


Fig. 3 The hardware of gait improvement algorithm based on vibration stimulation.

III. RESULT

The subjects in this study consisted of 5 young people do the study to analyze 3-dimensions motion analysis. The vibration stimulation system is equipped with control part, sensor part, power supply part and vibration device part on the subject's legs. The condition of this study is that we need normal power assist mode which input the signal when the signal attached on their leg over the permitted pattern and the flat walking to experiment with walking due to the emergence of obstacles to walking was performed by placing an event beyond the barriers of 10cm in height.

This study is to abstract GRF (ground reaction force) and 3dimensions motion analysis data, and the condition of this study is shown in Fig. 4.

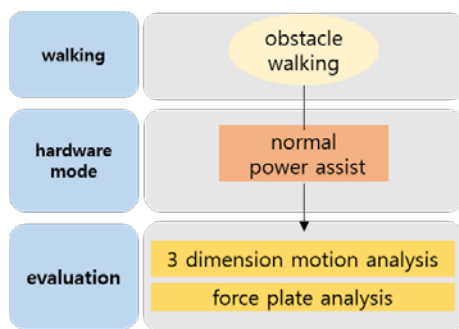


Fig. 4 Experiment conditions for measuring 3D motion analysis.

The experiment was carried out in a motion analysis laboratory equipped with a camera for motion analysis and a force platform. Four force platforms (Bertec Co., USA) were constructed under a 10m-footpath, and three infrared motion analysis cameras (Optotrak Certus, Northern Digital Inc., Canada) were installed around the footpath.

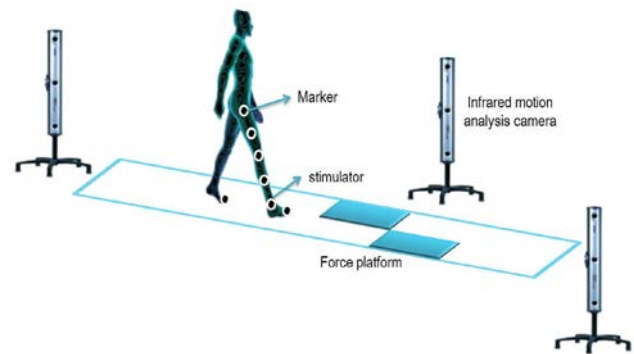


Fig. 5 Experiment environment for gait analysis by applying vibration stimulation.

The force platform collected ground reaction forces that arise in the course of gait, and the motion analysis camera collected three-dimensional information of 15 infrared lightening diode markers attached to the lower extremities of the subjects according to the Helen-Hayes marker set [12]. The sampling frequency was set at 100 Hz and 1000 Hz, respectively. The motion analysis camera and force platform were synchronized to analyze marker data and ground reaction force data by time and interval.

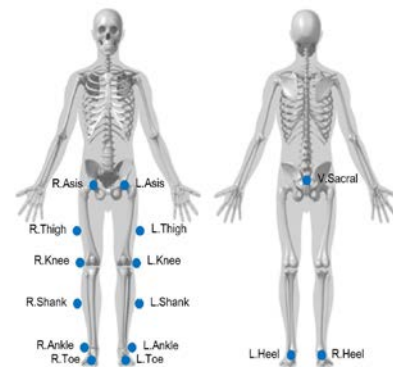


Fig. 6 Position of markers for motion analysis (Helen-Hayes marker set).

The somatosensory stimulation system that applied vibratory stimulation to the subjects was produced using the vibration motor that generates mechanical vibration. The somatosensory stimulation system was designed to adjust the intensity of somatosensory stimulation that is applied to the body by controlling the electrical characteristics of the input power that drives the vibration motor. In this study, stimulation with a vibration frequency of 250 Hz, which has the highest absolute sensitivity regardless of the contact area, was used [13-14]. The vibratory stimulation of 250 Hz accepted vibration from the Pacinian corpuscle receptor and was then transmitted to the central nervous system using the Pacinian corpuscle-associated fiber. As the tibialis anterior tendon and achilles tendon to which vibratory stimulation is applied have a relatively high density of the Pacinian corpuscle receptor, the optimum efficiency was expected to be achieved. In addition, to

change the application site, timing, and time of vibratory stimulation according to subject's gait cycle, a foot-switch was used at the bottom of the first metatarsal bone and the calcaneus. The vibratory stimulation was applied to the tibialis anterior tendon and Achilles tendon that play a major role in maintaining the balance of body posture.

A. Ground Reaction Force Analysis

Fig. 7 compare the moving with obstacle when operated by normal power assist mode and vertical GRF at the doing before jumping the obstacle without operating vibration stimulation systems.

It can be seen that peak 1 and peak 2 at the point just before jumping the obstacle is higher than when before giving stimulation and the difference in valley is seen prominently. The difference in two peaks is high. .

This is because of increasing the flexion in stance phase and because it helps driving force in swing phase to jump the obstacle.

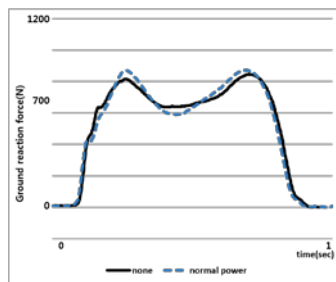


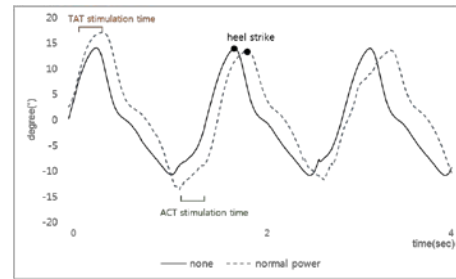
Fig. 7 Vertical GRF

B. Joint Angle Analysis

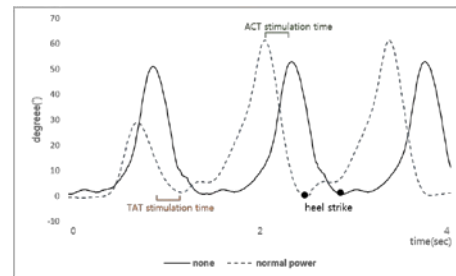
Fig. 8 shows the joint angle of ankle joint and knee joint when moving with giving vibration stimulation by normal power assist mode and without operating vibration stimulation systems. The angle of ankle joint is higher in HS (Heel-strike) and TO (Toe-off) without operation vibration hardware system, the part where vibration is not operated has no difference. The knee angle increases at Toe-off of PS (Pre-swing) phase. The knee joint that not using flexion had no difference comparing the ankle joint. There is no difference as well in the knee joint where stimulation is not operated. The point and the part that stimulation is given is different in normal power assist mode through gait event detection.

As a result of it, we assume that the fact that the angle ankle joint is high in LR (Loading-response) phase and stance phase leads input of vibration stimulation and activation and in Pre-swing phase, input of vibration stimulation leads activation to do plantar flexion.

That the angle of knee joint is high in Pre-swing phase leads strengthening in knee joint flexor.



Ankle joint



Knee joint

Fig. 8 Joint angle in normal power assist

IV. CONCLUSION

The evaluation related to somatosensory using vibration stimulation, systematic body response in dynamic posture is needed. The result of this study are expected to contribute in developing an effective means using vibration stimulation in apical applications to reduce the risk of walking disorder or falling injuries due to aging and compromised musculoskeletal functions. Findings can also be used in the rehabilitation treatment of patients with walking disorders since the efficiency of treatment by application of an appropriate external sensory stimulation can be facilitated.

ACKNOWLEDGMENT

This work was supported by the National Research Foundation of Korea (NRF) grant funded by the Korea government (MSIP) (NRF-2012R1A2A2A01012599).

REFERENCES

- [1] S.S. Bae, H.S. Gu and S.S. Kim, "Therapeutic exercise," Seoul: Daihak co., 1995.

- [2] Y.P. Ivanenko, V.L. Talis and O.V. Kazennikov, "Support stability influences postural responses to muscle vibration in humans," *European Journal of Neuroscience*, vol.11, no.2, pp.647–654, 1999.
- [3] Sabine M. P. Verschueren, Stephan P. Swinnen, Kaat Desloovere and Jacques Duysens, "Vibration-induced changes in EMG during human locomotion," *Journal of Neurophysiology*, vol.89, no.3, pp. 1299-1307, 2003.
- [4] A.M. Galica, H.G. Kang, A.A. Priplata, S.E. D'Andrea, O.V. Starobinets, F.A. Sorond, L.A. Cupples, L.A. Lipsitz, "Subsensory vibrations to the feet reduce gait variability in elderly fallers," *Gait and posture*, vol.30, no.3, pp.383-387, 2009.
- [5] D.C. Gravelle, C.A. Laughton, N.T. Dhruv, K.D. Datdare, J.B. Niemi, L.A. Lipsitz, and J.J. Collins, "Noise-enhanced balance control in older adults," *Neuroreport*, vol.13, pp.1123-1124, 2002.
- [6] R. Dickstein, Y. Laufer and M. Katz, "TENS to the posterior aspect of the legs decreases postural sway during stance," *Neuroscience letters*, vol.393, no.1, pp.51-55, 2006.
- [7] C. Mauter, T. Mergner, B. Bolha and F. Hlavackam, "Human balance control during cutaneous stimulation of the plantar soles," *Neuroscience letters*, vol.302, no.1, pp.45-48, 2001.
- [8] H.J. So, S.H. Kim and D.W. Kim, "The effects of application site and time of vibration stimulation: Changes in gait pattern and muscle activity," *Applied Mechanics and Materials*, vol.479, no.1, pp.475-480, 2014.
- [9] J.M. Hausdorff, "Gait dynamics, fractals and falls: finding meaning in the stride-to-stride fluctuations of human walking," *Human Movement Science* vol.26, no.4, pp.555-589, 2007.
- [10] J.M. Jasiewicz, J.H. Allum, J.W. Middleton, A. Barriskill, P. Condie, B. Purcell and R.C. Li, "Gait event detection using linear accelerometers or angular velocity transducers in able-bodied and spinal-cord injured individuals," *Gait and Posture*, vol.24, no.4, pp.502-509, 2006.
- [11] K. Tong and M.H. Granat, "A practical gait analysis system using gyroscopes," *Medical Engineering and Physics*, vol.21, no.2, pp.87-94, 1999.
- [12] <http://www.clinicalgaitanalysis.com/faq/sets/>
- [13] S. J. Bolanowski, G. A. Gescheider, R. T. Verrillo and C. M. Checkosky, "Four channels mediate the mechanical aspects of touch", *The Journal of the Acoustical Society of America*, Vol. 84, No. 5, pp. 1680-1694, 1988.
- [14] G. A. Gescheider, S. J. Bolanowski, J. V. Pope and R. T. Verrillo, "A four-channel analysis of the tactile sensitivity of the fingertip: frequency selectivity, spatial summation, and temporal summation", *Somatosensory and Motor Research*, Vol. 19, No. 2, pp. 114-124, 2002.

Min-Hwa Park received Master's degree in Healthcare Engineering from Chonbuk National University, Jeonju, South Korea in February of 2015. Her current research interests include sensory-motor integration, diagnosis and healthcare system.

Dong-Wook Kim received Ph.D. degree in Biomedical Engineering from Hokkaido University, Sapporo, Japan in 1995. Now he is a professor at Division of Biomedical Engineering and Vice President of Academic Affairs Office in Chonbuk National University, Jeonju, South Korea. His current research interests include biomedical engineering, rehabilitation engineering, sensory-motor integration, diagnosis and healthcare system.

An Automatic Diagnosis System for Hepatitis Diseases Based on Extreme Learning Machine

Derya AVCI

Firat University, Engineering Faculty, Department of Electrical and Electronic, 23119, Elazig, TURKEY

Abstract— Hepatitis is a major public health problem all around the world. This paper proposes an automatic disease diagnosis system for hepatitis using pattern recognition based on Extreme Learning Machines (ELM). The classifier used in this paper is single layer neural network (SLNN) and it is trained by ELM learning method. The hepatitis disease datasets are obtained from UCI machine learning database. The performance of proposed method is evaluated through statical methods such as classification accuracy, sensitivity and specivity analysis. The results of the proposed method are compared with the results of the previous hepatitis disease studies using same database as well as different database. When previous studies are investigated, it is clearly seen that the high classification accuracies have been obtained in case of reducing the feature vector to low dimension. However, proposed method gives satisfactory results without reducing the feature vector. The calculated highest classification accuracy of proposed method is found as 91.50 %.

Keywords— Hepatitis; Diagnosis Systems; Extreme Learning Machines (ELM).

I. INTRODUCTION

In medicine, the inflammation occurred in liver is called hepatitis. It can be caused by infections with viruses, bacteria, fungi, exposure to toxins such as alcohol and autoimmunity. The hepatitis damages to cells of liver and tenderness, swelling and inflammation in the liver are some symptoms of this disease. Commonly, the liver can handle significant amounts of damage, and the liver function is still effective. However, it will decline if the disease is not fully controlled at an early stage. The hepatitis can be acute or chronic and it is a common disease over the world. The different types of hepatitis are caused by different things, but they all produce inflammation of the liver [1]. Viral hepatitis refers to several common contagious diseases caused by viruses that attack the liver. The most important types of viral hepatitis are hepatitis-A, hepatitis-B, and hepatitis-C [2]. New forms of viral hepatitis such as D, E and G are also discovered. Hepatitis-A mainly infects by fecal contaminated substances taken by mouth. As a result of poor hygienic conditions, this results in epidemics based on water or food, especially in developing countries [1]. In infection of hepatitis A, any indication may be observed. Therefore, the patients could not become aware of the hepatitis-A.

Recently, a new learning algorithm called Extreme Learning Machine (ELM) which randomly selected all the hidden nodes parameters of generalized Single-hidden Layer Feedforward Networks (SLFNs) and analytically determines the output weights of SLFNs is proposed in [15-21]. Although output weights are analitically calculated, there is no rule in determination of number of hidden neurons and type of the activation function. To obtain a good classification performance of ELM, these parameters should be determined properly.

This study proposes ELM based an optimal intelligent system for diagnose of diabetes. The training and testing dataset for proposed method is obtained from UCI dataset. These dataset compose of 155 data. The randomly selected 100 of 155 data are used for training of classifier whereas remaining data is used for testing of classifier. For different activation function and number of hidden neurons, the results of proposed method are given. Further, a comparison is performed with previous studies to show validity of proposed method. From results, the proposed method is quite powerful tool for automatic diagnosis of hepatitis and may work in real-time systems.

II. METHODOLOGY

1. Pattern Recognition Concept

Pattern recognition could simply be defined as the process of categorizing the input signal. This process can be divided into two main groups as classification and regression. In the classification process, input signal is seperated into two or more classes while pattern recognition system tries to find the appropriate mapping between the input and the output variables in the regression process. Generally, regression problems are harder to solve than classification problems due to several reasons [22]. Figure 1 shows conventional pattern recognition concept for classification. As shown in Figure 1, the pattern recognition concept composes of two stages. They include feature extraction and classification stages. The feature extraction stage is the most important part of pattern diagnosis. The appropriate features are extracted by a feature extractor. If the appropriate features are not selected, the classification performance will be poor even though using the best classifier. Therefore, feature extractor should reduce the dimension of pattern vector to a lower. The reduced feature vector should also cover useful information of the original vector. In last stage, reduced feature vector is given to inputs of classifier for the classification [20-21].

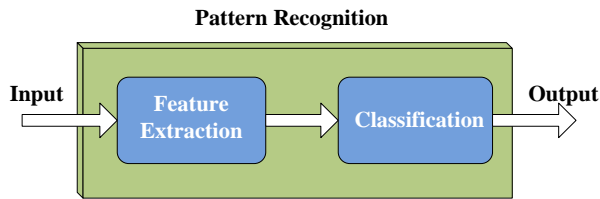


Figure 1. The block diagram of the pattern recognition concept

2. Extreme Learning Machine for Single Hidden Layer Feed Forward Networks

The NNs have been widely used in pattern recognition and regression problems. Commonly, the learning of NN has been performed by using gradient-based learning algorithms. However, such methods has several drawbacks such as difficult setting of learning parameters, slow convergence, slow learning and training failures [20-21].

To deal with the drawbacks of gradient-based learning methods, ELM was proposed by Huang, et al. [20]. In the ELM, the output weights of a single-hidden layer feedforward network (SLFN) are analytically computed by using the Moore-Penrose (MP) generalized inverse instead of iterative learning scheme. Figure 2 shows structure of a SLFN using ELM. In this figure, l_1m , l_2m and l_3m , are weights vector connecting the i th hidden neuron and the input neurons, and w is the weight vector connecting the i th hidden neuron and output neuron and $f(\cdot)$ is activation function.

The most important properties of ELM are given as follows:

- The learning speed of ELM is extremely fast. Therefore, SLFNs can be trained by ELM much faster than classical learning methods.
- The ELM tends to reach both the smallest training error and the smallest norm of weights. Thus, the ELM tends to have good performance for neural networks.
- The ELM learning algorithm can be used to train SLFNs with non-differentiable activation functions.
- The ELM tends to reach the solutions straightforward without such trivial issues [20].

4. Data Description

The hepatitis data is obtained from UCI machine learning database. It contains 20 attributes including the class attribute [26]. The output shows whether patients with hepatitis are die or alive. Hepatitis dataset contains 155 data belonging to two different target classes. There are 20 features, 13 binary and 6 attributes with 6–8 discrete values. Also, the class distribution contains 32 cases for die and 123 cases for alive. The attribute information of dataset is given in Table I.

Table I. Attribute informations and statistical analysis of dataset

	Attribute information	Values
1	Age	10-80 by step 10 years
2	Sex	Male and female
3	Steroid	No, yes

4	Antiviral	No, yes
5	Fatigue	No, yes
6	Malaise	No, yes
7	Anorexia	No, yes
8	Liver big	No, yes
9	Liver firm	No, yes
10	Spleen palpable	No, yes
11	Spiders	No, yes
12	Ascides	No, yes
13	Varices	No, yes
14	Bilirubin	0.39, 0.80, 1.20, 2.00, 3.00, 4.00
15	Alk phosphate	33, 80, 120, 160, 200, 250
16	Sgot	13, 100, 200, 300, 400, 500,
17	Albumin	2.1, 3.0, 3.8, 4.5, 5.0, 6.0
18	Prottime	10, 20, 30, 40, 50, 60, 70, 80, 90
19	Histology	No, yes
20	Class	Die, alive

5. Application of ELM for Diagnosis of Hepatitis

In these applications, a 3-fold cross-validation schema was applied where the two-fifth data were used for training the proposed ELM method and the remaining other data were used as the test data set. We applied this strategy for three times and we calculated the average values for determining the performance of proposed ELM method.

In the test process of ELM, the optimum parameters for the number of hidden layer neurons and type of activation function were used in ELM structure. As said previously, the dataset has 19 relevant features except for class attribute and includes a total of 155 cases. Thus, it is a matrix with dimension of 155 x 19. The type of activation function and the number of hidden neurons for ELM classifier are determined by doing many test in this study. The activation functions covers sigmoid, sinus, tangent sigmoid, sigmoid, radial basis, triangular, poly, hardlim. In addition, the numbers of hidden neurons are determined a value between 5 and 132. Performance of the proposed method is calculated by three evaluation methods as classification accuracy, sensitivity and specificity analysis. The classification accuracies for the datasets are found using the following equation.

$$\text{Correct accuracy } (C) = \frac{\sum_{k=1}^{|C|} \text{assess}(c_k)}{|C|}, \quad c_k \in C$$

$$\text{assess}(C) = \begin{cases} 1 & \text{if } \text{classify}(c) = c.m \\ 0 & \text{otherwise} \end{cases}$$

(1)

$$\text{assess}(c) = \begin{cases} 1, & \text{if } \text{classify}(c) = c.d \\ 0, & \text{otherwise} \end{cases}$$

(2)

Where, C is the set of hepatitis data to be classified (the test set), c.m is the class of item c and classify(c) returns the

classification of the by ELM. The sensitivity and specificity analysis are obtained as follows:

$$\begin{aligned} \text{sensitivity}(\%) &= \frac{TP}{TP + FN} \\ \text{specificity}(\%) &= \frac{TN}{FN + TN} \end{aligned} \quad (3)$$

Where; TP, TN, FP and FN are true positives, true negatives, false positives and false negatives, respectively.

6. Results and Discussion

In this study, an automatic intelligent system for diagnosis of hepatitis disease is presented. Performance of the proposed method is also evaluated by classification accuracy, sensitivity and specificity analysis. For different type of activation function and the number of hidden neurons, the classification accuracies of the proposed method are given in Table II. As shown in this table, the best classification accuracy of the proposed method is found as 91.50 % in case of activation function with tangent sigmoid and hidden neuron with 17. This table presents only the optimum results of proposed method. In addition, the worst classification accuracy of this method is also obtained as 61.7524% for radial basis activation function and hidden neuron with 240.

Table II. Some optimum results obtained from testing of the ELM for hepatitis diagnosis

Type of the activation function	The number of hidden neurons	Accuracy (%)
Sigmoid	87	89.0909
Poly	57	89.0909
Tangent sigmoid	259	90.7273
Sigmoid	143	90.9091
Poly	191	89.0909
Tangent sigmoid	17	91.50
Sigmoid	81	89.0909
Tangent sigmoid	204	92.7273

References

- [1] <http://www.hepcprimer.com/what.html>
- [2] Lale Ozyilmaz, Tulay Yildirim, Artificial Neural Networks for Diagnosis of Hepatitis Disease, International Joint Conference on Neural Networks, July 20-24, Portland, Oregon, USA, 2003.
- [3] Tahseen A. Jilani, Huda Yasin, Madiha Mohammad Yasin, PCA-ANN for Classification of Hepatitis-C Patients, International Journal of Computer Applications (0975 – 8887), Volume 14– No.7, February 2011.
- [4] Ultrasound and Magnetic Resonance Medical Images Textures Analysis Using Neural Networks, <http://www.intermag.kiev.ua/projects/neuraln.html>, (last accessed: 20 January 2012).
- [5] M. Serdar Bascil, Feyzullah Temurtas, A Study on Hepatitis Disease Diagnosis Using Multilayer Neural Network with Levenberg Marquardt Training Algorithm, J Med Syst (2011) 35:433 – 436.
- [6] Mahdieh Adeli, Hassan Zarabadipour, Automatic disease diagnosis systems using pattern recognition based genetic algorithm and neural networks, Recent Advances in Applied & Biomedical Informatics and Computational Engineering in Systems Applications,
- [7] Esin Dogantekin, Akif Dogantekin, Derya Avci, Automatic hepatitis diagnosis system based on Linear Discriminant Analysis and Adaptive Network based on Fuzzy Inference System, Expert Systems with Applications 36 (2009) 11282–11286.
- [8] Peng Guan, De-Sheng Huang, Bao-Sen Zhou, Forecasting model for the incidence of hepatitis A based on artificial neural network, China World Journal of Gastroenterol; 10(24), 2004, pp. 3579-3582.
- [9] Polat K., Gunes S., Hepatitis disease diagnosis using a new hybrid system based on feature selection (FS) and artificial immune recognition system with fuzzy resource allocation, Digital Signal Processing 16 (2006), pp. 889–901.
- [10] Duygu Çalışır, Esin Dogantekin, A new intelligent hepatitis diagnosis system: PCA–LSSVM, Expert Systems with Applications, Volume 38, Issue 8, pages: 10705-10708, 2011.
- [11] D. Rumelhart, and J. McClelland, "Parallel Distributed Processing", Vol. 1, MIT Press, 1986.
- [12] Suresh, S., Omkar, S.N., and Mani, V., Parallel Implementation of Back-propagation Algorithm in Networks of Workstations, IEEE Transactions on Parallel and Distributed Systems, 16, pp. 24-34, 2005.
- [13] Hsu, C.T. Kang, M.S. and Chen, C.S, Design of Adaptive Load Shedding by Artificial Neural Networks, IEE Proceed., Generation, Transmission and Distribution, 152, pp. 415-421, 2005.
- [14] Cho, J. H., Chun, M. G., Lee, D. J., Parameter Optimization of Extreme Learning Machine Using Bacterial Foraging Algorithm, EESRI, pp: 742-747, 2007.
- [15] G. B. Huang, H. Zhou, X. Ding, and R. Zhang, "[Extreme Learning Machine for Regression and Multiclass Classification](#)," (in press) IEEE Transactions on Systems, Man, and Cybernetics - Part B: Cybernetics, 2011.
- [16] G. B. Huang, D. H. Wang, and Y. Lan, "[Extreme Learning Machines: A Survey](#)," International Journal of Machine Learning and Cybernetics, 2 (2011) 107-1221.
- [17] G. B. Huang, X. Ding, and H. Zhou, "Optimization Method Based Extreme Learning Machine for Classification", Neurocomputing, 74 (2010) 155-163.
- [18] G. B. Huang, L. Chen and C. K. Siew, "Universal Approximation Using Incremental Constructive Feedforward Networks with Random Hidden Nodes", IEEE Transactions on Neural Networks, 17 (2006) 879-892.

- [19] G. B. Huang, Q.-Y. Zhu, and C.-K. Siew, "Extreme Learning Machine: A New Learning Scheme of Feedforward Neural Networks," 2004 International Joint Conference on Neural Networks ([IJCNN'2004](#)), (Budapest, Hungary), July 25-29, 2004.
- [20] G. B. Huang, Q.-Y. Zhu and C.-K. Siew, "Extreme Learning Machine: Theory and Applications", Neurocomputing, vol. 70, pp. 489-501, 2006.
- [21] N.-Y. Liang, G.-B. Huang, P. Saratchandran, and N. Sundararajan, "[A Fast and Accurate On-line Sequential Learning Algorithm for Feedforward Networks](#)", IEEE Transactions on Neural Networks, 17 (2006) 1411-1423.
- [22] L. Guo, D. Rivero, J. Dorado, C. R. Munteanu, A. Pazos, Automatic feature extraction using genetic programming: An application to epileptic EEG classification Expert Systems with Applications, Volume 38, Issue 8, August 2011, Pages 10425-10436.
- [23] B. Biswal, P.K. Dash, B.K. Panigrahi, Non-stationary power signal processing for pattern recognition using HS-transform, Applied Soft Computing, Volume 9, Issue 1, January 2009, Pages 107-117.
- [24] L. Jiang, Y. Liu, X. Li, S. Tang, Using bispectral distribution as a feature for rotating machinery fault diagnosis Measurement, Volume 44, Issue 7, August 2011, Pages 1284-1292.
- [25] Zhang, L. and Zhou, W. D., Density-induced margin support vector machines Pattern Recognition, 44, pp. 1448-1460, 2011.
- [26] UCI Machine Learning Repository. Available from: <http://www.ics.uci.edu/~mllearn/MLRepository.html> (last accessed: 20 January 2006).

Derya Avci – She was born in Malatya Turkey. She received a master's degree from Firat University Electronic and Computer Education. She received Ph.D. degree from Firat University Electrical and Electronic Engineering. Her interesting areas are pattern recognition, image processing, intelligent systems, artificial intelligence systems.

Agent Based Amino Acid Elongation Model: Influence of Ribosome Abundance on Polysome Formation

Anton Semchenko, Allbens Atman

Abstract—This article presents the agent based modeling approach to study the amino acid elongation process. Specifically, this modeling approach is applied to investigate the influence of the ribosome abundance on polysome formation and mRNA translation rates. The algorithm proposed here applies agent based model techniques to develop a computer simulation based on Markov chain representation of ribosome operation which is one of the most important steps of the protein synthesis process. The macromolecules involved in this process were treated as agents. The rules governing agents behavior were based on continuous-time Markov chain in order to reproduce the stochastic nature of the individual chemical reactions that are mediated by the ribosomes. This hybrid approach that combines the cellular automata and Monte Carlo techniques allowed for greater flexibility and closer representation of the complex biological processes with rigorous mathematical tools. This work integrates the most recent experimental finding on the ternary complex aa-tRNA:EF-Tu:GTP processing by the ribosome. Clear polysome formation was reproduced using visual and off-line data analysis tools. Observed saturation of the mRNA translation rate indicates that the model is able to carry-out the investigations concerning fast and flexible optimization of the operating regime of the protein synthesis.

Index Terms—Amino acid elongation, ribosome, agent based model, Markov chain, computer simulation, protein.

I. INTRODUCTION

THE FOCUS of the research effort presented here is the *in-silico* study of the amino acid elongation step of the protein synthesis process. The ultimate goal of the research project is to develop a computational model for performing in-depth studies of the protein synthesis. Biochemical reactions of the complete process of protein synthesis present enormous complexity and sheer number of the details if one would try to describe this process using the kinetics of basic chemical reactions. There has already been a number of modeling and simulation effort of the amino acid elongation step. In this work we present a hybrid approach that combines the agent based simulations (ABM) and continuous-time Markov chain mathematical model of individual amino elongation reactions.

One of the major advantages of ABM modeling approach, as it is presented here, is that it allows for consideration of the greater number of different factors and variables without going

through a great effort of reconstructing the complete model. In addition, consideration of spacial restrictions and space dependent interactions between macro molecules can be easily introduced into the model. In general we see that agent based modeling (ABM) serves as a viable alternative to traditional analytical methods of biochemical reactions modeling based on ordinary differential equations [1], [2] or using statistical analysis techniques [3].

After brief introduction into the agent based modeling we go over the essentials of the biochemical processes represented in our model. After that we describe the specific details of the ABM technique and how it represents the amino acid elongation reactions. Finally we present the observations of polysome formation simulation and analysis of the ribosome abundance influence on the mRNA translation rates.

A. Agent based modeling

Agent based modeling is based on an environment and objects that are called agents. This environment may or may not be supported by a grid which could be a one, two or three dimensional lattice. Independently of the grid presence, the agents can move and interact within the environment. The agents are individual elements that encapsulate many attributes as well as functional characteristics and that are adapted according to the nature and circumstances of the particular research project. They can be treated as objects possessing the information and exhibiting dynamic features within the computational environment. Behavior of the agents is determined by the interaction with the environment and neighbors. The dynamics of the model is controlled by the rules that the agent must obey. The rules can define the capability of agents to move, like, for example, random walk or directed by some force field. The intensity of interactions can be determined by the attributes of the agents. Figure 1 shows a simple example of the 3-D cells and two agents within these cells. Even though the modeler tries to keep the number of cells small in order to reduce the computational load it is common that the environment contains up to 10^6 cells. In our model, we relax the traditional cellular automata requirements that a cell within the grid be occupied by a single agent. We let the agent freely move at any point within the three dimensional environment. The location of an agent is thus defined by three continuous coordinates x , y , z . The topology of the environment is normally defined using three dimensional periodic boundary condition, but it is also possible to create borders, thus limiting the movement of the agents.

A. Semchenko is with the Physics and Mathematics Department, Centro Federal de Educação Tecnológica de Minas Gerais, Belo Horizonte, Brasil. e-mail: anton@aplasys.com.

A. Atman is with the Physics and Mathematics Department and National Institute of Science and Technology for Complex Systems, Centro Federal de Educação Tecnológica de Minas Gerais, Belo Horizonte, Brasil.

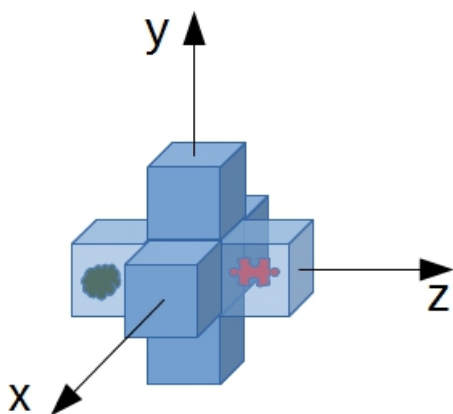


Fig. 1. Visualization of a simple three dimensional environment typically used in cellular automata ou agent based models.

Besides the first two components of any agent based model, which are the environment and the agents, the most important feature is the rules that govern all agent behavior and cell properties. For example, the modeler can define the movement speed of the agents or can configure the agents to perform a random walk. In addition to movement rules we can define how the agents interact with each other or how the environment affects their position or velocity. We can also define spacial features within the environment, for example, walls or obstacles. Agents can also occupy predetermined states and go through transitions between these states. Thus, statistical properties of natural phenomenas can be easily represented using this modeling approach.

This modeling technique is predominantly computational due to way the models are constructed and analyzed. However, certain agent behaviors and a number of necessary model features should be defined according to the basic laws of physics and expressed with mathematical formalism. Also ABM is closely related to complex systems research. The interaction between the individual elements of the modeled system is determined only by the functionality of the agents and, provided the system does not posses a central controlling unit within the model, we can study emergent behaviors by observing and measuring the attributes of the model as it evolves with time.

A typical scientific experiment with ABM would consist in executing the algorithms that aspire to represent the essential behavior of the natural phenomena and perform periodic measurement of the system properties. It is very common in this kind of experiments to observe certain features or attributes of the agent like their speed, position within the environment or some temporal characteristics like the time that it took for the agents to reach the specific state. For example, radioactive decay can be represented as a stochastic transition of agents representing a radioactive isotopes from one type into another. The experiment would measure the number of agents of each isotope within the environment and determine the half-life of the isotope.

Since computer simulation in general and agent based model as well are not a real-life experiment there is a need to

calibrate the temporal and spacial properties of the environment. Typically, some processes with experimentally measured characteristics and of the same class as the models phenomena are used to establish the real time and spacial dimensions of the agent based model. For example, we can use experimentally known average amino acid elongation speed in eukaryotes or prokaryotes in order determine the simulated time scale.

The ABM has already been applied to carry-out an investigation of biomedical research like, for example, when the models of acute inflammation were applied to obtain the insight into multiple organ failure [4]. In our work the ABM is constructed with granularity necessary to investigate the properties of macro-molecules involved in the chain of biochemical reactions of amino acid elongation process. The details of the ABM model are provided in the **Methods** section.

B. Overview of amino acid elongation

The subject of this study is the process of translation of the nucleotide sequence encoded within the mRNA molecule into the polypeptide structure of amino acids. This process is performed by the ribosome and a number of other biochemical elements. Together with EF-Tu elongation factor, tRNAs molecules are responsible to deliver the amino acids into the ribosome through its A site for peptide bond formation [5]. This process is composed of a sequence of biochemical reactions and conformational modifications. The principal component of this mechanism is, undoubtedly, the ribosome. It goes through a series of states and transitions during the assembly of the polypeptide chain starting from the translation initiation and finishing with translation termination. Below, we provide a brief summary of the individual steps of the elongation process that are represented in our study. Visual representation of the ribosomal states and transitions shown on Figure 2 facilitates the comprehension of the overall operation. Figure 3 and 4 provide condensed view of ribosomal states, transitions and the reaction rates.

It is reasonable to consider that the first step in open reading frame (ORF) translation by the ribosome is translation initiation. This is a complex process which results in ribosomal machinery coupled to first translated codon within the ORF and ready to receive the ternary complex. Under the condition of not ideal mixture within the live cell cytoplasm, which could easily occur due to the geometry of internal cell structure, the translation initiation could contribute to ribosome depletion in the vicinity of the mRNA, thus lowering the translation initiation rates. However for the purpose of our model we assume constant initiation rate k_{ini} .

After the ribosome initiates the translation of the open reading frame within the mRNA sequence, the first important step is to form the initial binding of the ternary complex composed of aminoacylated tRNA, EF-Tu elongation factor and GTP molecule with the open A-site of the ribosome. We assume that only one ternary complex at a time participates in the cycle of amino acid elongation reactions. Even though initial binding is performed through a complex biochemical mechanism we consider it as a single reaction with the rate

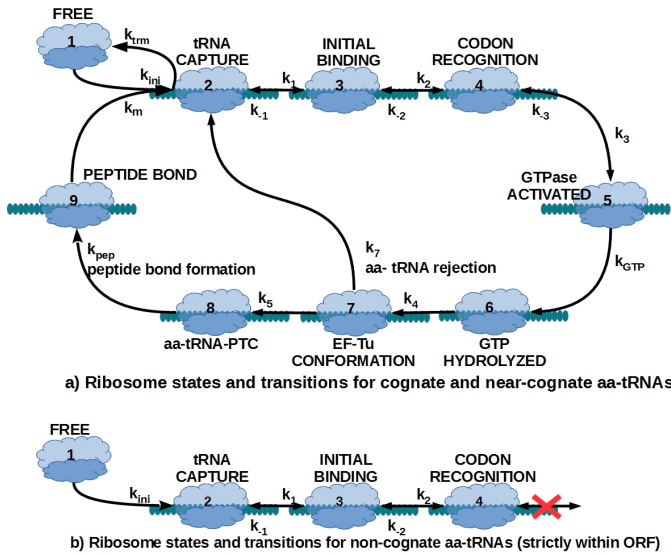


Fig. 2. This figure demonstrates how the most important chemical reactions of amino acid elongation are represented as stochastic state transitions. a) Both cognate and near-cognate aa-tRNA are considered. b) Only non-cognate aa-tRNAs.

#	State Name	Biological Interpretation
1	FREE	Ribosome is available for translation initiation, it is not yet translating the open reading frame of the mRNA.
2	tRNA CAPTURE	Ribosome is located on one of the codons within the open reading frame, which can be either start, stop codon or any other codon in between. No ternary complex is available for translation yet.
3	INITIAL BINDING	Ternary complex is bound to the ribosome.
4	CODON RECOGNITION	Sequence of reactions and events that lead to formation of the complex composed of tRNA anticodon and mRNA codon nucleotides.
5	GTPase ACTIVATED	Rearrangements within EF-Tu GTPase center caused by the correct codon-anticodon complex formation.
6	GTP HYDROLYZED	GTP hydrolysis is completed with assistance from EF-Tu and ribosomal elements.
7	EF-Tu CONFORMATION	EF-Tu completes the changes of its conformation from the GTP- to the GDP-bound form.
8	aa-tRNA-PTC	<i>Aminoacyl</i> -tRNA is dislocated into the peptidyl transferase center and becomes ready for the peptide bond formation.
9	PEPTIDE BOND	This states corresponds to the condition of the ribosome after formation of the peptide bond but when the ribosome is not yet ready to receive the next ternary complex.

Fig. 3. Summary of the states that the ribosome can assume within the model.

for the forward reaction k_1 and k_{-1} for the reverse process. The values of the initial binding and other reaction rates are provided in the Figure 4 and modeling aspects are discussed in more details in **Methods** section.

The following reaction is a sequence of steps that involve aa-tRNA entry into the decoding site of the ribosome, codon-anticodon complex formation and stabilization through tRNA and ribosome conformational changes and rearrangements. Experimental data is available for the overall reaction rate of codon recognition (forward direction k_2 and reverse direction k_{-2}) but not for the individual steps involved in this complex reaction. We assume that not only cognate and near-cognate aa-tRNAs participate in the reactions of codon recognition but also the non-cognate aa-tRNAs go through very similar set of reactions except for the final step of codon-anticodon complex formation. The overall rate of codon recognition set

Transition	Initial state	Final state	Transition Rates			
			Name	Cognate aa-tRNA	Near-cognate aa-tRNA	Non-cognate aa-tRNA
Translation initiation	FREE	tRNA CAPTURE	k_{ini} , [s ⁻¹]	2 ... 500	2 ... 500	2 ... 500
Initial binding	tRNA CAPTURE	INITIAL BINDING	k_1 , [M ⁻¹ s ⁻¹]	140-10 ⁶	140-10 ⁶	140-10 ⁶
Reverse initial binding	INITIAL BINDING	tRNA CAPTURE	k_{-1} , [s ⁻¹]	85	85	85
Codon recognition	INITIAL BINDING	CODON RECOGNITION	k_2 , [s ⁻¹]	180	180	180 (assumed)
Reverse codon recognition	CODON RECOGNITION	INITIAL BINDING	k_{-2} , [s ⁻¹]	0.2	140	98000 (assumed)
GTPase activation	CODON RECOGNITION	GTPase ACTIVATED	k_3 , [s ⁻¹]	190	0.6	No transition
Reverse GTPase activation	GTPase ACTIVATED	CODON RECOGNITION	k_{-3} , [s ⁻¹]	10 ⁶ (assumed)	10 ⁶ (assumed)	No transition
GTP hydrolysis	GTPase ACTIVATED	GTP HYDROLYZED	k_{gtp} , [s ⁻¹]	250	250	No transition
EF-Tu conformation	GTP HYDROLYZED	EF-Tu CONFORMATION	k_4 , [s ⁻¹]	50	50	No transition
aa-tRNA transfer into peptidyl transferase center	EF-Tu CONFORMATION	aa-tRNA	k_5 , [s ⁻¹]	22	0.06	No transition
aa-tRNA rejection	EF-Tu CONFORMATION	tRNA CAPTURE	k_7 , [s ⁻¹]	0.1	0.84	No transition
Peptide bond formation	aa-tRNA	PEPTIDE BOND	k_{pep} , [s ⁻¹]	3	3	No transition
Ribosome translocation	PEPTIDE BOND	tRNA CAPTURE	k_m , [s]	10 ⁶	10 ⁶	No transition
Translation termination	tRNA CAPTURE	FREE	k_{trms} , [s ⁻¹]	2 ... 500	2 ... 500	No transition

Fig. 4. Summary of the transitions that ribosome can go through between its states within the model.

of intermediate steps is determined by the aa-tRNA entry into the decoding site of the ribosome [5]. This behavior leads to similarity of codon recognition rates between different codons. In other words there is little codon dependence in codon recognition rates [6]. The dependence of the rate for the reverse codon recognition reaction on codon cognity is less clear. We assume that forward codon recognition reaction rate is the same for cognate, near- and non-cognate codons. Since non-cognate codons fail to form codon-anticodon complex within the decoding center on the 30S subunit of the ribosome this class of codons must move away from the decoding center and unbind from the ribosome leaving the A-site available for the next ternary complex.

Codon-anticodon complex is formed by binding the pairs of bases within the mRNA codon and tRNA anticodon. Standard base pairs are Adenine:Uracil (A:U) and Guanine:Cytosine (G:C). Wobble exists only for the pairing of the bases in the last 3' base position of the mRNA codon and the last 5' position of the tRNA anticodon as summarized in Figure 5. For example, Leucine amino acid may be coded by the 5'-UUG-3' codon. Its cognate anticodon would be 3'-AAC-5' if standard base pairing is observed. However, due to the wobble effect, Leucine codon 5'-UUG-3' must also be recognized by the tRNA anticodon 3'-AAU-5' because according to the Figure 5, 3'-end base of mRNA codon may bind to C or U base on the 5'-end of the tRNA anticodon.

Current experimental and modeling approaches [5]-[7] consider at least three types of ternary complexes from the point

tRNA Anticodon Base at 5' end	mRNA Codon Base at 3' end
G	U or C
C	G
A	U
U	A or G
I	A, U or C

Fig. 5. This table demonstrates the possibility for nucleotide base pair formation that generates ambiguity of tRNA anticodon and mRNA codon matching.

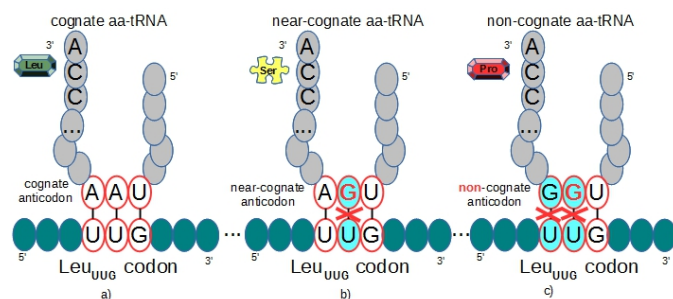


Fig. 6. This figure demonstrates the concept of codon and anticodon matching that occurs at the codon recognition step of amino acid elongation.

of view of tRNA anticodon match with the codon being translated. The aa-tRNA complexes is considered cognate when the anticodon nucleotides of the tRNA are in the perfect match with the codon under translation by the ribosome on the mRNA. The match of the nucleotides of the anticodon and nucleotides of the codon is defined by the standard pairing rule for the 1st and 2nd pair and wobble rule for the 3rd pair. However it is possible that either 1st or 2nd but not both base pairs are in mismatch according to the standard pairing. In such case the aa-tRNA is considered as near-cognate [8] given that the 3rd pair is formed according to the wobble binding. In other words, near-cognate aa-tRNA anticodon must always provide for wobble pair in the 3rd base. Clearly, if both 1st and 2nd base pairs are in mismatch then this aa-tRNA is non-cognate even if the third base is possible according to the wobble base bond formation. Also having a mismatch on the 3rd base makes the anticodon non-cognate no matter what happens at the first two base pairs since near-cognate codon must have wobble pairing on the 3rd base.

Modeling and simulation experiments are based on different reaction rates for each of this kind of aa-tRNAs. The details of the representation of ribosome operation for each of these aa-tRNA complexes is presented in the **Methods** section. Also some significant differences in modeling of cognate, near-cognate and non-cognate aa-tRNAs are mentioned below when we briefly introduce the state-of-the-art of the amino acid elongation *in-silico* studies.

GTPase activation can be viewed as specific changes in the positions of elements within EF-Tu bound to the ribosome.

Important insight into the possible mechanics involved in this step is that GTPases activation may be stimulated by formation of codon-anticodon complex [5], [9]. Since codon recognition reaction that may lead to codon-anticodon complex formation has low codon dependence and there is no apparent participation of anticodon nucleotides in GTPase activation process one can expect the rate of GTPase activation to have low codon dependence as well. However the rate values for this reaction (k_3) available in the published literature show much slower reactions for near-cognate than cognate tRNAs [6]. This can be explained by the differences in the strength of the signal from codon-anticodon complex formation in case of the near-cognate and cognate anticodons. Apparently the cognate anticodons form strong coupling to the mRNA codon [10] thus providing for the fast GTPase activation.

The major players in the GTP hydrolysis that follows the GTPase activation are the EF-Tu and ribosomal elements. Since there is little influence of anticodon sequence on the reaction, the rate of GTP hydrolysis (k_{GTP}) is assumed as independent of codon cognity.

The EF-Tu conformational change and P_i release that follows are considered as a single reaction which can be described with the same rate k_4 both for near-cognate and cognate anticodons. Also aa-tRNA is released from EF-Tu at this step. There is a possibility that this reaction is affected by the nature of amino acid bound to the tRNA [5] which opens an opportunity for further model development by including the amino acid dependence in the reaction rate.

Given the aa-tRNA has already been released from the EF-Tu, two reactions can occur. The first reaction happens when aa-tRNA completes the accommodation within the A-site of the ribosome and assures its correct position within the peptidyl transferase center. The rate of this reaction k_5 is strongly dependent on anticodon cognity. For example, near-cognate reaction rate k_5 could be smaller by three orders of magnitude than the rate for the cognate codons.

Alternatively, the tRNA rejection reaction can occur when aa-tRNA is detached from the ribosome into the cytoplasm leaving the ribosome in the state ready for the next ternary complex binding. In this case the cycle of the elongation reactions will run again depending on the cognity of the next tRNA that arrives to the open A-site. The above two reactions are part of the ribosome translation accuracy assurance. The rate of tRNA rejection reaction k_7 is much higher for the near-cognate anticodons than for cognates. Thus it is much more likely that cognate aa-tRNA will be given a chance to deliver its amino acid to the nascent polypeptide chain. We allow only for cognate and near-cognate aa-tRNAs into the peptidyl transferase center for peptide bond formation and we assume that all tRNA are correctly amino acylated.

Assuming that peptidyl-tRNA is present at the P-site and aminoacylated tRNA is correctly positioned at the A-site then the peptide bond formation reaction may occur within the peptidyl transferase center with the rate k_{pep} . In our model we assume that this reaction is not affected by the anticodon cognity, thus k_{pep} has the same value for near-cognate and cognate aa-tRNAs.

Peptide bond formation is accompanied by the translocation

of the ribosome along the mRNA chain of codons. The ribosome movement process deserves modeling attention as a separate project due to its complexity and a great number of intermediate steps and reactions. However, in an attempt to keep our model simple and focused, we will assume that translocation of the ribosome is just a stochastic reaction that occurs following the peptide bond formation. In order to avoid the impact of this assumption on the overall behavior of the system we keep the rate of the forward translocation k_m high thus making this reaction as not translation rate limiting.

II. METHODS

Earlier, we have outlined the essential elements of the complex process of amino acid elongation as it is facilitated by the ribosome with the help of a number of elongation factor. Clearly the reason that many researchers turn to mathematical modeling and computer simulation is the ability of this approach to capture the essence of the object of study with sufficient details that permit to obtain useful insights into the subject under scientific investigation. Here we provide the details on how our agent based model is constructed to investigate the behavior of this biochemical system.

A. Agent based environment and the agents

Based on the brief introduction of the agent based models earlier, we first define the environment of our model as three dimensional continuous space with x, y, z coordinates. The computer program that performs the simulations described here was built using NetLogo 3D tool [11]. The NetLogo 3D is an agent based environment with 3 dimensional grid world simulating cellular automata. In our simulations we do not impose any requirement on the number of agents within a single cell. The underlying mathematical model of the amino acid elongation Markov chain was implemented using NetLogo programming language. The 3D environment of cellular automata was used to simulate and visualize the spacial properties and movement of the macromolecules as shown on the simulation visualization snapshot on Figure 7.

Ribosome atomic structure and, even more so, the behavior of this biochemical phenomena is extremely complex. In our approach to model construction we abstracted the details of the ribosomal internal operations and focused on its states as it progresses from codon to codon, facilitating the formation of amino acid chain. Thus, having the goal of ribosomal states in mind, we can represent the ribosome as a simple single agent without any complex atomic structure. The ribosomal state is an attribute of the agent. We will present the rules that govern transitions between these states shortly. At the moment let us take a brief look at what other elements are represented and how.

Ternary complex is formed by one molecule of aminoacylated tRNA, one molecule of elongation factor EF-Tu with GTP bound to it. Formation of this complex occurs within the cellular environment prior to initial coupling with the ribosome. Undoubtedly this formation of ternary complexes is an important step of protein synthesis. However, based on our results, we can judge that in order to investigate

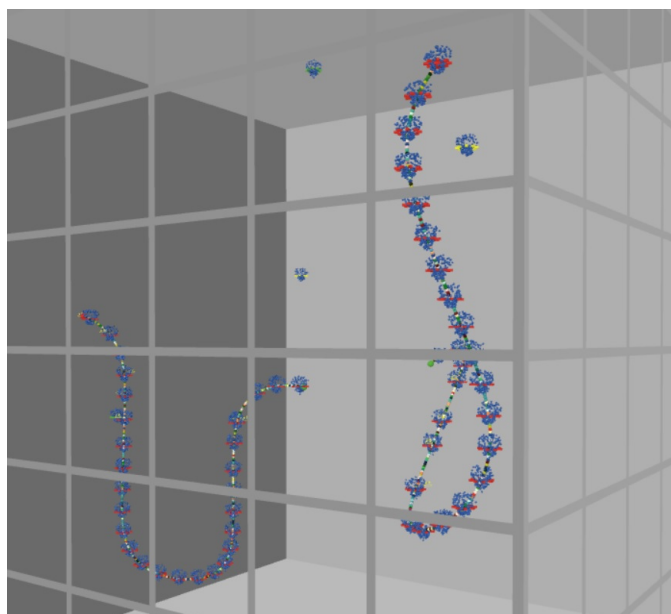


Fig. 7. Polysome formation in the agent based model. Ribosomes are blue colored agents and sequence of tiny colorful dots are the mRNAs.

the fundamental properties of polysome or single ribosome operation the set of chemical reactions required for ternary complex formation can be abstracted as a stochastic event at the ribosome location. We provide additional detail on initial binding below when we describe the agent behavioral rules. So far it is important to observe that ternary complex can be represented as a single agent. This assumption greatly reduces computational load during experimental runs. Even if the experiments were conducted to measure the concentrations and timing characteristic of such components as EF-Tu, GTP or phosphate liberated during amino acid elongation, the ternary complex could still be represented as a single agent. For example, the individual reaction of detachment of aa-tRNA:EF-Tu:GTP from the ribosome can be implemented as a transformation of a single agent representing the ternary complex into two new agents, one for aa-tRNA bound to the mRNA and secured by the ribosome and the other for the EF-Tu released into the cytoplasm. Agent birth, death and transformation are the important facilities available to the agent based model architect.

Codon is the building block of the mRNA sequence. Ribosome operates by facilitating the translation of one codon at a time by the aminoacylated tRNA which is delivered by the elongation factor EF-TU. In our algorithm, the reaction of codon recognition is represented as a single event with all three nucleotide composing a codon processed at the same time. We treat the triple nucleotide sequence as one single set of characters. This set is implemented as an attribute of the agent that represents a codon within mRNA sequence. Similarly, the anticodon is considered as a single set of three characters belonging to an agent that represents the tRNA. In order to represent the mRNA sequences that exist in the cytoplasm we populate our environment with the sequences of codon agents. Specifically, in NetLogo program, mRNA

sequence is implemented as a vector of codons. As any agent within the environment, each codon has three continuous coordinates x, y, z . As a consequence, the ribosome translocation is implemented as movement of the ribosomal agent from the coordinates of one codon to the coordinates of the next codon within the vector that represents the open reading frame (ORF) being translated.

At the moment we do not represent the amino acid chain as an agent. It is simply stored as a sequence of amino acids within the ribosome agent until the stop codon is reached. Amino acid chain data is stored in a permanent memory location at the end of translation termination for off-line data analysis.

B. Agent rules: amino acid elongation representation as Markov chain

As briefly outlined earlier, the ribosome facilitates synthesis of amino acid chains. This process is composed of a series of chemical reactions which are full of intricate details. The knowledge of all aspects of this phenomenon is going through active evolution with the help of various experimental and theoretical research techniques. The general approach to modeling the chemical reactions that make up the cycle of the amino acid elongation can be viewed as representing these chemical reactions as stochastic state transitions with firing time intervals exponentially distributed. The combination of these transitions and the states of the macro molecules involved in the reactions forms the Markov chain [13]. Specifically, the continuous-time Markov chain representation of the reactions involved in the amino acid elongation process, shown on the Figure 2, has been implemented in the computer program simulating translation initiation, individual codon translation, ribosomal translocation and translation termination.

Similar approach has been applied earlier to analyze, for example, *in-vitro* and *in-vivo* kinetics of the mRNA translation [6]. In this approach each step of amino acid elongation is represented as a stochastic transition between distinct Ribosomal states. We use the experimentally measured reaction rates [5], [6] of each step in order to calculate the firing times of the transitions that compose the Markov chain. Exponential distribution of the firing time intervals is assumed. The continuous-time Markov chain representing the set of chemical reactions that occur during amino acid elongation is assumed to have the states of the ribosome as presented in the Figure 3.

It is important to observe that the structure of Markov chain does depend on whether the ribosome is translating the codon with cognate (near-cognate) or non-cognate aa-tRNA complex bound to it. What changes in the process depending on the anticodon of tRNA is that non-cognate tRNAs terminate their life-span on the ribosome after an attempt to form the codon-anticodon complex during codon recognition process. The cognate of the aa-tRNA influences the rate of each transition with different degree. Figure 4 shows our assumptions regarding the behavior or the elongation mechanism for different anticodons participating in the amino acid elongation.

Apparently translation initiation is a rate limiting step of the protein synthesis and has been previously modeled in with

different level of details [14], [15]. For the purpose of our model we abstract from the intricate biochemical details of this process and consider it as a single stochastic transition. The firing time of the transition representing translation initiation is distributed exponentially with probability density function described by the Equation 1.

$$f_{ini}(\tau, T_{ini}) = \frac{1}{T_{ini}} e^{-\frac{\tau}{T_{ini}}} \quad (1)$$

where T_{ini} is the mean initiation wait time interval that represents the average time it takes for the ribosome that is not attached to the mRNA sequence to position itself onto the stop codon. Once the ribosome completes this transition it becomes ready to accept the ternary complex necessary for translation process. This transition takes the ribosome from the state that we call "FREE" to the state "tRNA CAPTURE". The mean wait firing time for this transition, T_{ini} , is calculated from the rate constant available experimentally.

$$T_{ini} = \frac{1}{k_{ini}} \quad (2)$$

Our model simplifies the representation of translation termination by considering this process as a single stochastic transition. The firing time of this event is described by the exponential probability density function according to the Equation 3.

$$f_{trm}(\tau, T_{trm}) = \frac{1}{T_{trm}} e^{-\frac{\tau}{T_{trm}}} \quad (3)$$

where T_{trm} is the model parameter, mean termination wait time interval. It represents the average time that the ribosome takes to complete the steps triggered when the ribosome arrives onto the stop codon. The rate k_{trm} of the overall reaction that represents the translation termination is used to calculate the mean firing time of this transition.

$$T_{trm} = \frac{1}{k_{trm}} \quad (4)$$

In this process the ribosome is influenced by the release factors and dissociates from the mRNA as the result. This transition takes the ribosome from the state "tRNA CAPTURE" to "FREE". Basically it means that the ribosome is no longer attached to the mRNA but it is available for translation initiation. This is the final step in the formation of the amino acid chain.

It is very important to consider the implementation of non-cognate aa:tRNA processing because most of the time the ribosome receives the non-cognate ternary complexes. Visual representation of the states and transitions of the Markov chain of the ribosome processing of aa-tRNAs during elongation set of reactions is shown on Figure 2. The frequency of cognate aa:tRNA arrival is much smaller than the frequency of non-cognates. It is common that when modeling elongation set of reactions executed by the ribosome, non-cognate aa-tRNAs are not included into the Markov chain representing the reactions. Non-cognates are discarded upon arrival onto the mRNA. According to the presently available experimental data

[5], the only mechanism for the ribosome to verify whether the anticodon of aa-tRNA is non-cognate is to let anticodon form a complex with mRNA codon located at the A-site of the ribosome. This verification is performed within the decoding center of the 30S subunit of the ribosome. From our understanding of the elongation cycle, the ribosome goes into the INITIAL BINDING state when ternary complex with non-cognate aa:tRNA attaches to it. Following this event the ribosome must execute a transition into some specific state in order to perform distinction between codons inside the decoding center of the ribosome. We consider this state to be CODON RECOGNITION which is the same state for all three kinds of anticodons, cognate, near-cognate and non-cognate.

Despite the codon reading that precedes codon recognition is very fast, codon recognition reaction rate is determined not as much by the codon-anticodon complex formation but by the speed of codon movement into decoding center of the ribosome. The speed of movement into this center for non-cognate codon is not likely to be faster than that of cognate or near-cognate. It may not depend on cognate of codon at all. Since the rate limiting step of this reaction is the movement of the aa-tRNA into the decoding center, the rate of the codon recognition reaction of non-cognate tRNA is determined the time necessary for this movement. Apparently this time interval does not show strong codon dependence. Thus, we assume that the rate of codon recognition in case of the non-cognate tRNA is the same as codon recognition rate for cognates and near-cognate aa-tRNAs. We assume, until more experimental data becomes available, that ribosome goes through codon recognition state for non-cognate codons even though it reverses its state into open A-site after codon recognition. Open A-site condition means the ribosome has its A-site open for the arrival of new ternary complexes. We call this state tRNA CAPTURE state.

The models that do not consider non-cognate tRNAs in the machinery of the ribosome operation represented by a formalism like, for example, the Markov chain fail to capture the tRNA selection mechanism. If a model discards non-cognate tRNA upon tRNA arrival then this model assumes that there is a mechanism within the modeled object that knows how to distinguish between non-cognate and cognate tRNA.

C. Codon translation and occupation time measurements

The measurements of two time intervals were performed during simulations. The codon translation time interval is the time that it takes for the ribosome to complete all chemical reactions involved in the connection of one amino acid to the nascent amino acid chain. The codon occupation time is the interval between ribosome translocation onto this codon and translocation onto the next codon.

In order to measure codon translation time interval, special counter is initialized for each codon, including the stop codon, only when the **ribosome translocates onto the codon**. In other words it is assumed that **codon translation starts as soon as the ribosome occupies the codon**. Our model does not have a specific translocation event in order to model the case of the start codon since translation initiation is represented

by a single stochastic transition. The codon translation time interval for start codon is initialized when translation initiation transition occurs. When ribosome rejects a non-cognate tRNA it goes back into the tRNA CAPTURE state. Codon translation time interval is not initialized at this moment since this event is just one of many attempts to select the cognate tRNA by the ribosome. Also the ribosome may reverse the initial binding as get back into the tRNA CAPTURE state. Neither in this case the codon translation time interval is initialized since this is a continuation of the elongation cycle for a given codon.

In case of the stop codon, translation time interval has a different meaning than in case of any other codon within the open reading frame. Stop codon is not translated by the ribosome and no tRNA exists in the cytoplasm for this codon. Codon translation time is used to track the time interval that it took for the ribosome to process the translation termination of the open reading frame. Thus codon translation time interval for the stop codon is initialized in the same manner as for any other codon but its analysis is specific for the translation termination modeling purposes. Most importantly, the **stop** codon translation time interval may be described by a statistical distribution different from the distribution of the codon translation time of the codons within the open reading frame. Thus in order to measure correctly all cases of codon translation and occupation time interval measurements it is necessary to consider separately start, stop and internal to ORF codons.

III. RESULTS AND DISCUSSION

A. Polysome formation upon mRNA sequence

Protein synthesis is composed of a number of steps. Amino acid elongation is just one intermediate task during this complex biological process. This task can be described in terms of the time that the ribosome takes to form one complete amino acid chain starting from Methionine encoded by the start codon until the ribosome is released from the mRNA after processing the stop codon at the end of the open reading frame (ORF). This time interval is a good choice when evaluating the protein production because it clearly represent one process without intermixing with separate activities, like folding or trigger factor processing. Given amino acid chain of length L_{orf} and the ORF translation duration t_{orf} , the protein production rate or sometimes it is called translation rate k_{orf} is given by the following formula.

$$k_{orf} = \frac{L_{orf}}{t_{orf}}, [aas/s] \quad (5)$$

We measured the time interval t_{orf} as a function of total number of ribosomes present in the environment which are available for translation. We also varied the translation initiation and termination rates in order to evaluate the formation and performance of the polysome in various dynamic regimes.

It is interesting to observe what happens with ORF translation duration t_{orf} from the very first amino acid chain synthesized from the mRNA with the evolution of the ribosomes-mRNA system. Figure 8 shows the changes in t_{orf} values starting from the 1st until the 300th amino acid that has

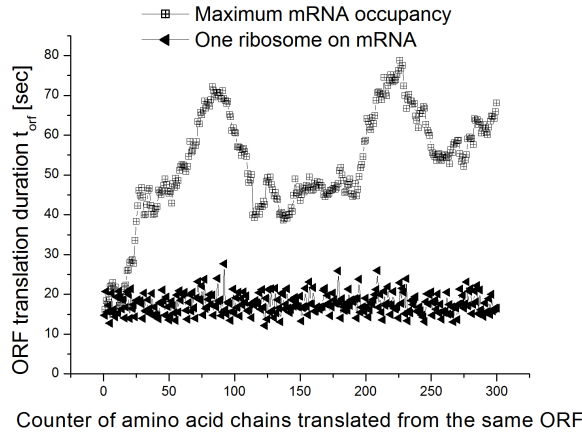


Fig. 8. This figure shows the dramatic difference in dynamic regimes of complete polysome (above) and single ribosome per mRNA (below).

been produced by the ribosomes from the same ORF. Two extreme conditions are shown, one with just a single ribosome occupying the mRNA and another when mRNA is completely filled with the ribosomes.

The regime of maximum mRNA occupancy occurs when the number of ribosomes translating the ORF at the same time is equal to the maximum number of the ribosomes that physically fit within the ORF. We assumed that the ribosome occupies $l_r = 12$ codons. In our experiments we used psbA1 gene which codes for Photosystem II protein D1 1 amino acid sequence of *Synechococcus* sp. (strain JA-3-3Ab) (Cyanobacteria bacterium Yellowstone A-Prime) [16] with $L_{orf} = 355$ codons. Thus maximum number of ribosomes that can form the polysome is $L_{orf}/l_r = 29$ in this case.

Maximum mRNA occupancy curve on Figure 8 was constructed from the t_{orf} measurements under fast translation initiation condition. This curve shows how the duration of the complete ORF translation gradually increases as grows the number of amino acid chains synthesized by the ribosomes from the same mRNA. The first amino acid chain is synthesized faster than any later chain because the first ribosome does not encounter any traffic jams along the ORF sequence. However the ribosomes that initiate translation shortly after the first ribosome will have a greater chance to experience the traffic jam. This effect is observed stronger under the condition of fast translation initiation and relatively slow termination. Traffic jams are easily observed on the agent based model presented on Figure 7.

B. Influence of ribosome abundance on polysome dynamics

Another interesting insight into the dynamics of the polysome formation upon mRNA can be obtained by studying the influence of the ribosome quantity on the characteristic ORF translation duration D_{orf} . This time interval is calculated from the set of t_{orf} measurements by simply averaging the t_{orf} values over a large number of amino acid chains synthesized from the same mRNA but discarding the initial amino acid chains until the polysome regime has been reached

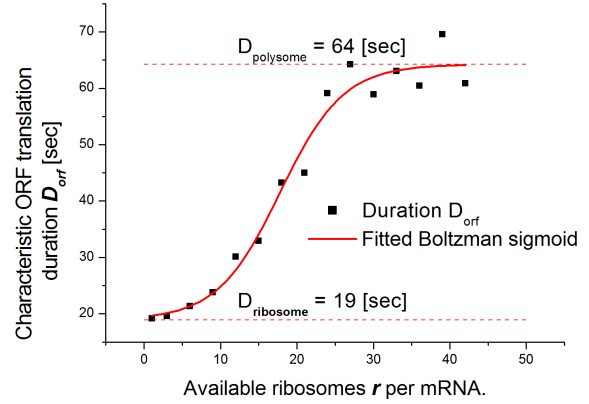


Fig. 9. The time interval that it takes for the ribosome to translate one single complete ORF (D_{orf}) grows with ribosome concentration until it saturates at the level corresponding to complete polysome formation on mRNA. Fitted Boltzmann sigmoid curve (in red) facilitates the visualization of exponential growth and saturation.

(approximately 50 initial amino acid chains). According to the Figure 9 the characteristic ORF translation duration D_{orf} initially grows exponentially with the number of ribosomes available for translation per mRNA. However the ribosome-mRNA system enters into polysomal regime when the number of available ribosomes per mRNA reaches the maximum physical capacity of one single ORF. As the consequence of this behavior, the characteristic ORF translation duration D_{orf} growth saturates and reaches its maximum when number of active ribosomes per mRNA is close to the mRNA capacity. We see the clear saturation behavior after the number of ribosomes per mRNA goes over the polysome capacity which is 29 ribosomes for the mRNA open reading frame with 355 codons encoded by psbA1 gene.

In silico experimental measurements of the characteristic ORF translation duration D_{orf} presented on Figure 9 are reasonably well described by fitting Boltzmann sigmoid according the following equation.

$$D_{orf} = \frac{D_{ribosome} - D_{polysome}}{1 + e^{(r-r_0)/dr}} + D_{polysome} \quad (6)$$

where:

- D_{orf} is the characteristic time necessary for the ribosome to translate one open reading frame averaged over the large number of amino acid chains synthesized from the same mRNA.
- $D_{ribosome}$ is the characteristic ORF translation time under the condition of only one single ribosome occupying the mRNA.
- $D_{polysome}$ is the characteristic ORF translation time under the condition of mRNA is occupied by the maximum possible number of ribosomes. Fitting resulted in $D_{ribosome} = 18,900 \pm 2,67$, $D_{polysome} = 64,239 \pm 1,85$ while $\chi^2/DoF = 11,29576$ and $R^2 = 0,97453$.
- r is the number of ribosomes per mRNA.
- r_0 and dr are fitting parameters.

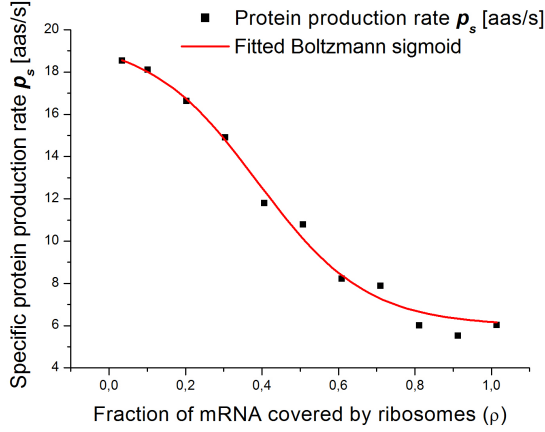


Fig. 10. Influence of mRNA coverage by the ribosomes (ρ) on specific protein production rate as calculated from the ORF translation time intervals (t_{orf}). $\rho \approx 0$ is equivalent to one single ribosome translating the ORF, $\rho = 1$ represents complete polysome. Fitted Boltzmann sigmoid curve (in red) makes it easier to visualize the gradual reduction trend.

Based on the D_{orf} experimental data from Figure 9 we calculate the specific protein production rate p_s according to the formula below.

$$p_s = \frac{L_{orf}}{D_{orf}} \quad (7)$$

where L_{orf} is the number of codons within one open reading frame and D_{orf} is the average time interval to translate one ORF.

Another important variable for analysis of polysome dynamics is the mRNA coverage ρ that is obtained using the following equation.

$$\rho = \frac{l_r \cdot r}{L_{orf}} \quad (8)$$

where l_r is the number of codons covered by one single ribosome and r is the number of ribosomes attached to mRNA inside the ORF. Basically, mRNA coverage shows how far is the polysome from its maximum ribosome capacity when $\rho = 1$.

If one would be interested to optimize the overall protein production rate from the mRNA then Figure 11 provides an interesting view of the effect of the ribosome occupation of the open reading frame. This figure shows the polysome protein production rate calculated as the product of the number of actively producing ribosomes r and specific protein production rate p_s from Figure 10.

$$P_y = r \cdot p_s, [aas/s] \quad (9)$$

Given the definition of the variables above, we can analyze and discuss the dependence of the specific protein production rate p_s (Figure 10) and the polysome protein production rate P_y (Figure 11) as a function of mRNA coverage ρ . One may expect that when number of ribosomes grows linearly then the rate of the protein production also grows since if more ribosomes are actively working then more amino acid chains would be produced. However, this amino acid chain production growth is limited by the rapid saturation of the

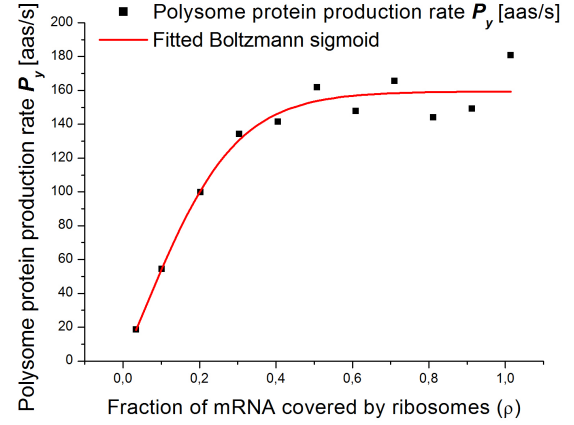


Fig. 11. Total protein production from a polysome. As number of ribosomes upon the mRNA grows the ability of the polysome to synthesize proteins saturates despite the growth of the number of actively producing ribosomes attached to the mRNA.

overall synthesis capacity even before complete polysome forms. From Figure 11 we can see that as mRNA coverage comes close to values of $\rho \approx 0.5$, or polysome is half-formed, the growth of polysome protein production P_y halts and P_y stays at the same level until the complete polysome is formed. In other words the half-filled ORF would produce proteins with the same rate as completely filled polysome.

Effect of mRNA occupancy has already been investigated before using flux analysis with differential equations [2]. The computational studies with that technique have shown that specific protein production rate p_s [aas/s] grows as mRNA coverage by the ribosomes ρ increases. In addition, it was also shown that after the growth of protein production rate, this rate sharply drops to zero after the mRNA becomes 95% covered by the ribosomes. In our work 95% coverage of the mRNA corresponds to ribosome quantity of 28 per mRNA. However we do not see any indication that protein production rate would drop sharply to almost zero values after mRNA coverage with the ribosomes reaches certain values. Even if we compare the polysome protein production rate P_y as a function of mRNA coverage ρ we do see the growth until $\rho \approx 0.5$ but we still do not observe any drop to zero presented in earlier research projects [2] for $\rho \approx 1$. One possible explanation of this difference is that our model takes into account ribosomal traffic jams and considers one single mRNA instead of the pool of mRNA producing a flux of proteins.

Also there are two more important details of our continuous-time Markov-chain model that represents the chain of amino acid elongation reactions. One is the treatment of non-cognate anticodons by letting them further downstream into the chain of states. We do allow for the non-cognate anticodon to reach past the INITIAL BINDING state. Even though from the biochemical point of view the state of the system ribosome:aa-tRNA(non-cognate):mRNA after codon reading and codon recognition reaction is different from the state for cognate anticodon this state is included into the Markov-chain of our model as CODON RECOGNITION state. It is different from

models when non-cognate anticodons are allowed only to form INITIAL BINDING state or not considered at all in the model.

Besides the above mentioned feature of our model related to non-cognate anticodon treatment another difference in our approach to Markov chain representation is in considering the ribosome translocation as a stochastic event as well. These specific properties of our model when integrated together into the agent based environment affect the dynamics of the whole system during simulations.

C. The ribosome pausing sites measured *in vivo* and model validation

Experimental studies of ribosome translation speed for the *psbA* gene that codes for Photosystem II protein D1 of *Hordeum vulgare* (Barley) [17] identified the following codon regions where ribosome experienced the most prominent pausing codons: 127 and 128 (region B), 236 and 240 (region D), 282, 289, 298 and 299 (region E). The regions are named according to the original publication that presented these results [17]. Remembering that the measurements were performed under polysomal regime we have to understand that ribosomes form clusters or patterns along the mRNA. Thus when comparing experimental ribosome distribution along the mRNA and *in silico* codon occupation time we have to look at the regions of codons in order to obtain fair evaluation of the simulation results. For example, region D from the *in vivo* experiments extends approximately from codon 228 until codon 253.

With the purpose of model validation we performed *in silico* measurements of codon occupation time for each codon along the mRNA sequence of the *psbA* gene of D1 protein (UniProt ID P05337). Since the *in vivo* experimental data were obtained under polysome regime we also chose to setup the simulation with ribosome abundance that guarantees the polysome formation. Codon occupation time is the time that ribosome spends upon each codon actively translating as well as passively waiting for the downstream ribosome to free up the room for translocation onto the next codon. The distribution of the codon occupation time obtained from *in silico* experiments based on our model for the mRNA of the *psbA* gene is presented on Figure 12. We can see that the region around codon position 245 in our results covers well the region D (positions 236 and 240) of ribosomal pausing identified from the *in vivo* experiments [17]. The extent of the ribosome pausing regions depends on the concentration of the ribosomes, translation initiation and termination time. The length of our region that corresponds to the region D is greater which can be explained by higher ribosome abundance in computer simulation experiments. It is much easier to fill up the environment with ribosomes in *in silico* experiments than *in vivo*.

In polysomal regime ribosomes do not act as a single agent. They form a system of interacting and cooperating elements. Region formation has strong statistical nature. This behavior can be grasped by the data analysis but it is much easier to visualize looking at the simulation in action. Formation of ribosome jams is dynamic, clusters may become longer

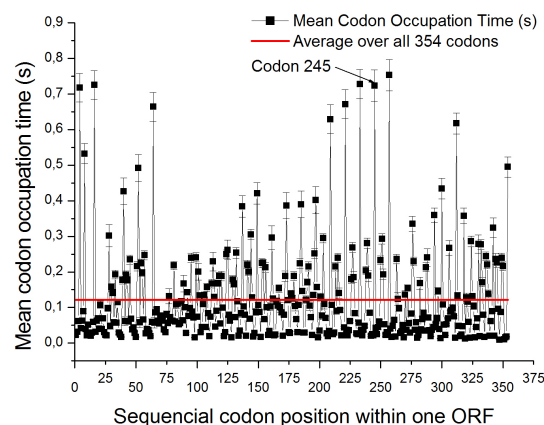


Fig. 12. The interval of time the ribosome spends on a codon along the open reading frame sequence as measured during *in silico* translation of *psbA* gene for Photosystem II protein D1 of *Hordeum vulgare* (Barley). The following *in vitro* experimentally detected [17] ribosome pausing sites were reproduced by *in silico* model in the vicinity of the codon clusters at the locations of codons 52-64, 257 and 312.

or shorter. Simulation approach compared to experimental technique [17] facilitates the evaluation of the statistical nature of ribosome clustering and polysome formation. For example, the mRNA signature on Figure 12 allows to easily estimate the length of the ribosome cluster around codon 245. The information on ribosome cluster size can be used to calculate the impact of clustering on co-translational folding. This particular feature of *in silico* experiments is hard to underestimate for membrane class of proteins.

Not all ribosome pausing sites identified by *in vivo* experiments were reproduced in our model. We can explain this difference by the fact that our model does not represent one important element that may influence the translation speed. It is the interaction of the nascent amino acid chain with the ribosomal exit tunnel as well as the role of the trigger factor and signal recognition particle in the synchronization of the ribosome operation with co-translational folding and protein targeting. It is important to observe that Photosystem II D1 protein is of transmembrane class for which targeting process strongly influences the translation rate. Additional factor that may contribute to the difference in codon positions of the pausing site locations measured in our *in silico* experiments and experimentally registered regions is the distribution of the tRNA concentrations. Our measurements were performed with generic tRNA concentrations equivalent to *E. Coli* tRNA abundance. This is similar to running experiments for heterologous expression of *psbA* gene.

We would like to observe the ease of agent based model construction and remarkable productivity gains of the researcher when working with NetLogo toolset. Combination of ABM and continuous-time Markov chain formalism presented here allowed us to gain valuable knowledge of polysome formation and obtain the characteristics of its dynamic regimes. The agent representation of macro molecules involved in the amino acid elongation process is an approach that facilitates model construction by the researchers with little specialization in

computing aspects of simulation techniques. In addition to that, ABM technique preserves the mathematical rigor of traditional models like, for example, differential equations. Construction of multi scale and distributed ABMs would allow for wider coverage of the modeled elements and integrate greater number of related processes into one synchronized simulation. The visualization resources offered specifically by NetLogo is the must-have feature for model verification. We have encountered and fixed a number of incorrectly operating elements within the model thanks to the ability to see the simulation and the model in execution.

IV. CONCLUSION

Application of agent based simulation to study the amino acid elongation proved to be a very convenient and precise tool for investigation of fundamental properties of ribosome operation during protein synthesis. It combines the flexibility, mathematical rigor and the power of visual model analysis. The proposed ABM model was able to reproduce the fundamental characteristics of amino acid elongation process as demonstrated by the polysome dynamic regime. Gradual translation rate degradation was observed until the lowest rate was reached. The analysis of the overall polysome production rate provided valuable knowledge about influence of the ribosome abundance per mRNA on the protein production rate. The presented agent based model can serve to perform the optimization procedures if one is interested to determine the best ribosome concentration for a given mRNA sequence.

ACKNOWLEDGMENT

The authors would like to thank the invaluable help with advice and consulting in the biochemical field besides the motivation to carry-out this research project that we received from Guilherme Oliveira from CEBio (FioCruz-MG).

REFERENCES

- [1] D. A. Drew, "A mathematical model for prokaryotic protein synthesis," *Bulletin of Mathematical Biology*, vol. 63, no. 2, pp. 329–351, 2001. [Online]. Available: <http://dx.doi.org/10.1006/bulm.2000.0225>
- [2] H. Zouridis and V. Hatzimanikatis, "A model for protein translation: Polysome self-organization leads to maximum protein synthesis rates," *Biophysical Journal*, vol. 92, pp. 717–730, 2007.
- [3] H. M. M. T. Eikelder, M. N. Steijaert, and E. P. D. Vink, "Stochastic analysis of amino acid substitution in protein synthesis," in *Proc. CMSB 2008*, 2008, pp. 367–386.
- [4] G. An, "Introduction of an agent-based multi-scale modular architecture for dynamic knowledge representation of acute inflammation," *Theoretical Biology and Medical Modelling*, vol. 5, p. 11, 2008.
- [5] M. V. Rodnina, "Mechanisms of decoding and peptide bond formation," in *Ribosomes: Structure, Function, and Dynamics*, 1st ed., M. V. Rodnina, Ed. Wien, Austria: Springer-Verlag, 2011, vol. 1, pp. 199–212.
- [6] S. Rudorf, M. Thommen, M. V. Rodnina, and R. Lipowsky, "Deducing the kinetics of protein synthesis *In Vivo* from the transition rates measured *In Vitro*," *PLoS Comput Biol*, vol. 10, p. e1003909, 2014.
- [7] P. Shah and M. A. Gilchrist, "Effect of correlated tRNA abundances on translation errors and evolution of codon usage bias," *PLoS Genet*, vol. 6, no. 9, p. e1001128, 09 2010.
- [8] P. Satpati and J. qvist, "Why base tautomerization does not cause errors in mRNA decoding on the ribosome," *Nucleic Acids Research*, vol. 42, no. 20, pp. 12 876–12 884, 2014.
- [9] M. V. Rodnina and W. Wintermeyer, "Fidelity of aminoacyl-tRNA selection on the ribosome: Kinetic and structural mechanisms," *Annual Review of Biochemistry*, vol. 70, no. 1, pp. 415–435, 2001, PMID: 11395413.

- [10] D. Bonaki, T. Pronk, and E. de Vink, "In silico modelling and analysis of ribosome kinetics and aa-tRNA competition," in *Transactions on Computational Systems Biology XI*, ser. Lecture Notes in Computer Science, C. Priami, R.-J. Back, and I. Petre, Eds. Springer Berlin Heidelberg, 2009, vol. 5750, pp. 69–89.
- [11] U. Wilensky. (1999) Netlogo. Center for Connected Learning and Computer-Based Modeling, Northwestern University, Evanston, IL, USA. [Online]. Available: <http://ccl.northwestern.edu/netlogo>
- [12] Electron micrograph of a polysome. [Online]. Available: http://www.nobelprize.org/educational/medicine/dna/a/translation/polysome_em.html
- [13] S. M. Ross, *Introduction to probability models*. San Diego: Academic Press, 2010.
- [14] D. Na, S. Lee, and D. Lee, "Mathematical modeling of translation initiation for the estimation of its efficiency to computationally design mRNA sequences with desired expression levels in prokaryotes," *BMC Systems Biology*, vol. 4, no. 1, p. 71, 2010.
- [15] F. Amman, C. Flamm, and I. Hofacker, "Modelling translation initiation under the influence of sRNA," *International Journal of Molecular Sciences*, vol. 13, pp. 16 223–40, 2012.
- [16] Photosystem ii protein d1 1. [Online]. Available: http://www.uniprot.org/uniprot/Q2J1J2#gene_name_table
- [17] J. Kim, P. G. Klein, and J. E. Mullet, "Ribosomes pause at specific sites during synthesis of membrane-bound chloroplast reaction center protein d1," *Journal of Biological Chemistry*, vol. 266, no. 23, pp. 14 931–14 938, 1991.

Anton Semchenko was born in St. Petersburg, Russia, where he earned his Master's degree in Nuclear Physics from St. Petersburg State Polytechnic University and later went on to earn Master's degree in Computer Science from Illinois Institute of Technology, Chicago, USA. Participated in a number of large scale industrial R&D and scientific international projects including high-energy research endeavor at Fermi National Accelerator Laboratory, Batavia, USA. Currently dedicates his time to research focused on mathematical modeling and theoretical studies of protein synthesis and developing computational approaches to novel protein design. Pursuing his PhD degree in Computational and Mathematical Modeling at CEFET-MG and teaches at the undergraduate courses as Assistant Professor of Newton Paiva Centro Universitário, Belo Horizonte, Brazil.

Allbens Atman completed his undergraduate studies in Physics at UFMG in Belo Horizonte, MG (1996), has Master's degree in Physics (UFMG-1998) and Ph.D. in Physics (UFMG - 2002), Post-Doc at Universit de Paris VII (2002/04) and UFMG (2004/05). Invited professor (ESPCI-Paris-2008) and laureate on the scope of the "Research in Paris" project (Mairie de Paris-2010). Currently holds Associate Professor position at Centro Federal de Educao Tecnolgica de Minas Gerais (CEFET-MG) and is fellow member of the National Institute of Science and Technology - Complex Systems (INCT-SC). Leader of the research group on Studies on Complex Systems at CEFET-MG, has interests on interdisciplinary subjects in Physics, including Statistical Mechanics, Complex Systems, Mechanics, Elasticity and Rheology, Biological Motivated Problems, Non-extensive Thermodynamics and Econophysics. Has expertise in advising graduate, Master and PhD students, and collaborations with tenths of researches in these areas. The bibliographic production spans over a wide range of different subjects such as fractals, roughness, percolation, cellular automata, self organized criticality, granular materials, jamming, simulation, mathematical modeling, econophysics and computational methods in physics.

Biological Impact of Certain Substituted Monoazo Thiazole-thiophene and Their Seleno Like Moieties: Part I

Mohamed E Khalifa^{1,2*} and Adil A Gobouri¹

Abstract— Thiophene and thiazole along with their seleno like nuclei are still of interest in organic chemistry due to their medicinal and valuable applications. In continuation of our interest in synthesis of S/N heterocyclic azo compounds, the synthesis of 3-amino-*N*-(4-aryl-5-arylo-2-thiazolyl)-thieno[2,3-*b*]pyridine-2-carboxamide) along with their seleno like derivatives of pyridine, pyridazine and quinolone, were accomplished. All the synthesized compounds were *in vitro* screening of their antioxidant activity, antitumor activity against Ehrlich ascites carcinoma cell EACC cell line and antimicrobial activity against various pathogenic microorganisms, such as Gram-positive bacteria (*Bacillus subtilis* and *Staphylococcus aureus*) and Gram-negative bacteria (*Escherichia coli* and *Salmonella typhimurium*) and fungi strains of *Aspergillus flavus* and *Candida albicans*. The structural–activity relationship was studied based on the obtained data.

Keywords—2- Aminothiazole, thiophene, Antioxidant, Antitumor agents, pathogenic microorganisms, Selenium

I. INTRODUCTION

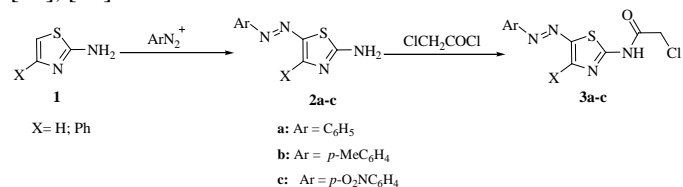
THE heterocyclic based mono azo compounds are not only important due to their excellent properties as dyes for polyester textiles but they also have been utilised in non-textile applications, such as photodynamic therapy, lasers, reprographic technology, functional dye applications and non-linear optical systems [1], [2]. The attraction interest in the field of thiazolyl azo compounds has grown, and these compounds have been extensively investigated to produce medicinal properties (i.e., antitumor activity, cytotoxic, antimicrobial, anti-inflammatory, mitodepressive, hypotensive, anti-HIV, hypoallergenic, tuberculosis, and agriculture pesticide action) [3]. Organo-selenium compounds have a wide range of unique properties, which include antimicrobial, antitumor and anticancer activities as well, where many medicinal preparations have been produced based on organic derivatives of selenium [4], [5]. In addition, organo-selenium compounds are capable of sensitizing processes in living organisms, and the selenium atom is also a primary constituent of four proteins, where its deficiency in human and animal organisms might be related to various

chronic diseases, especially necrosis of the liver [6]. In a continuation of our previous researches on the synthesis and important applications of S/N-Se heterocyclic compounds [7]-[11], we introduce an interesting biological study of their extensive activities as antitumor, antioxidant and antimicrobial compounds.

II. RESULTS AND DISCUSSION

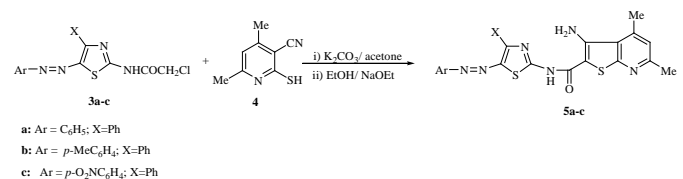
A. Chemistry

A set of 4-substituted-2-(*N*-chloroacetyl)-5-arylazothiazole derivatives **3a-c**, was prepared by azo coupling of 4-substituted-2-aminothiazole **1** with various diazotized aromatic amines to yield the 4-substituted-2-amino-5-arylazothiazole derivatives **2a-c**, followed by active condensation with chloroacetyl chloride as shown in scheme 1 [10], [11].



Scheme 1 Synthesis of 5-arylo-2-chloro-*N*-(thiazol-2-yl)acetamide derivatives **3a-c**.

The 2-(*N*-chloroacetyl)-5-arylo-4-substituted-thiazole derivatives **3a-c** were reacted with 4,6-dimethyl-2-mercaptopyridine-5-nitrile **4** by refluxing in acetone containing sodium carbonate, followed by cyclization upon heating in a solution of ethanol containing sodium ethoxide to afford the corresponding thieno-[2,3-*b*]pyridine derivatives **5a-c** (Scheme 2) [9].



Scheme 2 Synthesis of thieno-[2,3-*b*]pyridine derivatives **5a-c**

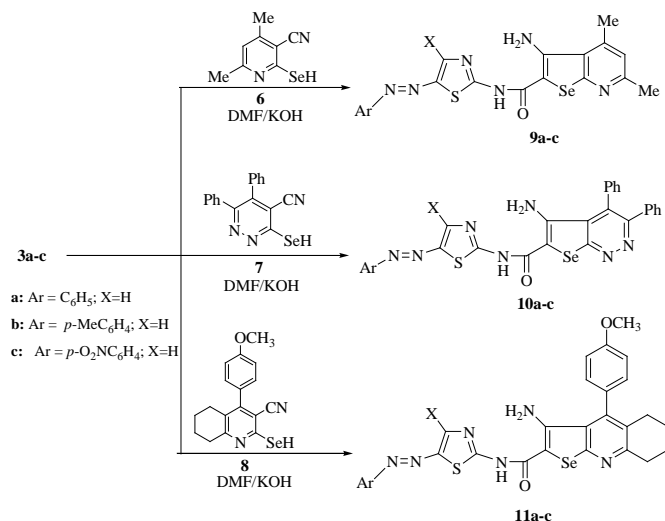
The chemical structures of **5a-c** were established on the basis of their elemental analyses and spectral data and in

M. E. Khalifa was with the Department of Chemical Engineering, Higher Institute for Engineering and Technology, New Dameitta, Egypt. He is now with the Department of Chemistry, Faculty of Science, Taif University, Taif 21974, Saudi Arabia (00966569846966; e-mail: mohamedezzat@tu.edu.sa).

A. A. Gobouri is with the Department of Chemistry, Faculty of Science, Taif University, Taif 21974, Saudi Arabia.

agreement with the literature. Where the IR spectrum of **5a** for example, clearly indicated the lack of cyano absorption band and revealed the characteristics of NH_2 absorption bands at $3177, 3280 \text{ cm}^{-1}$ in addition to the carbonyl absorption band at 1632 cm^{-1} . The strong decrease in the carbonyl absorption frequencies is attributed to the highly chelated intramolecular H-bond structure. The ^1H NMR spectrum of **5b** for example, confirmed the lack of the singlet signal that characterized the methylene protons and showed three singlet signals corresponding to the three methyl protons at δ 2.4, 2.8 and 3.0, in addition to the singlet signal at δ 7.3 for the pyridine $\text{C}_5\text{-H}$ proton and multiplet signal at δ 7.4-7.9 for the aromatic protons.

A one pot synthesis reaction of 4-substituted-5-arylaazo-2-chloro-*N*-(thiazol-2-yl)acetamide derivatives **3a-c** with selenol derivatives of pyridine **6**, pyridazine **7** and quinoline **8** in dimethyl formamide (DMF) containing 10 % aqueous potassium hydroxide, followed by Thorpe-Ziegler cyclization by treatment with an excess of 10% aqueous potassium hydroxide in (DMF), yield the corresponding 3-amino-4,6-dimethyl-*N*-(5-arylazothiazol-2-yl)selenopheno[2,3-*b*]pyridine-2-carboxamide derivatives **9a-c**, 3-amino-4,6-diphenyl-*N*-(5-arylazothiazol-2-yl)selenopheno[2,3-*b*]pyridazine-2-carboxamide derivatives **10a-c** and 3-amino-5,6,7,8-tetrahydro-4-(4-methoxyphenyl)-*N*-(5-arylazothiazol-2-yl)selenopheno[2,3-*b*]quinoline-2-carboxamide derivatives **11a-c** (Scheme 3) [11].



Scheme 3 Synthesis of 3-amino-*N*-(5-arylazothiazol-2-yl)selenopheno[2,3-*b*]pyridine, pyridazine and/or quinoline-2-carboxamide derivatives "**9a-c-11a-c**"

The chemical structures of selenol derivatives "**9a-c-11a-c**" were established based on their elemental analysis and spectral data and in agreement with the literature. The IR spectra of 3-amino-*N*-(5-arylazothiazol-2-yl)selenopheno[2,3-*b*]pyridine, pyridazine and/or quinoline-2-carboxamide derivatives "**9a-c-11a-c**" in common, clearly indicated the absence of the cyano group band and the appearance of characteristics absorption bands at 3177 and 3280 cm^{-1} corresponding to the NH_2 group as well as at 1652 cm^{-1} corresponding to the carbonyl group. The strong decrease in the carbonyl absorption frequencies

was due to the highly chelated intramolecular H-bonded structure. For example, the ^1H NMR spectrum of **9b** confirmed the absence of the characteristic signal of the methylene group. In addition, the results exhibited three singlet peaks corresponding to the three methyl protons at δ 2.44, 2.83, 3.09, a singlet peak at δ 7.33 corresponding to the pyridine $\text{C}_5\text{-H}$ proton and multiplet peaks at δ 7.47-7.95 corresponding to the aromatic protons. In addition, the peaks corresponding to the NH groups were absent due to the use of CF_3COOD as a solvent.

B. In vitro antioxidant potential of synthesized compounds

Antioxidant efficiency was performed using the DPPH free radical scavenging method (H-donor method) and hydroxyl radical scavenging assay, which based upon different mechanisms to provide complementary insight into the antioxidant activity of the synthesized compounds [12]. The results are indicated and listed in tables 1 and 2.

Table 1 Antioxidant activity percentage of synthesized compounds "**5a-c** and **9a-c-11a-c**" at different concentrations using the DPPH method

Compound #	% Antioxidant activity		
	100 μM	200 μM	300 μM
5a	18 ^{gh} ± 0.54	22 ^g ± 0.95	34 ⁱ ± 0.54
5b	19 ^f ± 0.74	34 ^f ± 0.42	33 ^g ± 0.23
5c	31 ^d ± 0.75	45 ^d ± 0.60	66 ^d ± 0.91
9a	21 ^{gh} ± 0.56	39 ^g ± 1.25	43 ⁱ ± 0.56
9b	25 ^f ± 0.79	46 ^f ± 0.46	57 ^g ± 0.30
9c	33 ^d ± 0.78	58 ^d ± 0.62	72 ^d ± 0.98
10a	28 ^e ± 0.30	52 ^e ± 1.32	74 ^c ± 0.70
10b	37 ^c ± 0.36	61 ^c ± 0.72	70 ^e ± 0.98
10c	49 ^b ± 0.46	70 ^b ± 1.59	78 ^b ± 0.72
11a	17 ⁱ ± 0.61	28 ⁱ ± 0.61	34 ^j ± 0.79
11b	20 ^h ± 0.44	34 ^h ± 0.89	46 ^h ± 0.50
11c	22 ^g ± 0.82	47 ^f ± 1.15	61 ^f ± 0.72
Ascorbic acid (standard)	53 ^a ± 0.50	78 ^a ± 0.52	95 ^a ± 0.53
LSD	1.002	1.678	1.208

Values are expressed as means \pm SD ($n = 3$).

Values with different superscript letters within the same column are significantly different ($P < 0.05$).

Table 2 Hydroxyl radical scavenging activity of synthesized compounds "5a-c and 10a-c -12a-c" at different concentrations

Compound #	% OH radical scavenging activity		
	100 μ M	200 μ M	300 μ M
5a	13 ^h ± 0.67	22 ^g ± 0.94	30 ^g ± 0.72
5b	16 ^f ± 0.35	29 ^f ± 0.95	33 ^e ± 1.32
5c	20 ^d ± 0.64	39 ^d ± 0.97	55 ^{cd} ± 0.60
9a	15 ^h ± 0.69	27 ^g ± 0.95	35 ^g ± 0.78
9b	19 ^f ± 0.35	38 ^f ± 0.95	49 ^e ± 1.32
9c	28 ^d ± 0.75	49 ^d ± 1.15	62 ^{cd} ± 0.61
10a	22 ^e ± 0.46	42 ^e ± 0.69	63 ^c ± 0.75
10b	32 ^c ± 0.96	54 ^c ± 0.56	61 ^d ± 1.06
10c	43 ^b ± 0.46	63 ^b ± 1.23	65 ^b ± 0.95
11a	13 ⁱ ± 0.36	23 ^h ± 0.35	26 ^h ± 0.26
11b	16 ^{gh} ± 0.75	27 ^g ± 0.53	35 ^g ± 0.36
11c	17 ^g ± 0.45	38 ^f ± 1.42	41 ^f ± 0.92
Ascorbic acid (standard)	49 ^a 2.10	73 ^a 0.89	84 ^a ± 0.30
LSD	1.508	1.584	1.369

Values are expressed as means \pm SD ($n = 3$).

Values with different superscript letters within the same column are significantly different ($P < 0.05$).

As shown in tables 1 and 2, the antioxidant and hydroxyl radical scavenging activities were increased when doubling the concentration of the tested compounds, and most of the synthesized compounds exhibited very good antioxidant activity (i.e., pyridazine > pyridine > quinoline analogues) relative to ascorbic acid, which was used as a standard due to its higher antioxidant activity. The high antioxidant and scavenging activities of the tested compounds may be due to the resonance phenomena of double bonds and lone pair electrons on nitrogen. This structure may lead to radical formation in more than one site, especially on the benzene ring attached to the nitro group, which is a highly electron withdrawing group that enables the benzene ring to convert to a radical form and forms a new covalent bond with another radical (e.g., 10c and 11a-c). In addition, protection against peroxides, peroxyxynitrite, glutathione, peroxidase-like activity and metal-binding capacity due to organoselenium analogues leads to antioxidant activity. This conclusion is also supported by previously reported results [13].

C. Acute toxicity and antitumor activity

The median lethal dose (LD50) of the selected compounds (9a and 10a-c) based on their *in vitro* antioxidant potential results, was measured in mice. The results indicated that the selected compounds were non-toxic at doses up to 500 mg kg⁻¹ B.wt (bodyweight of tested mice).

The tested compounds were evaluated *in vitro* for their cytotoxic activity against the Ehrlich Ascites Carcinoma Cell (EACC) line, and the viability percentages were determined and listed in table 3.

Table 3 Viability percentages of carcinoma cells treated with synthesized compounds "5a-c and 9a-c-11a-c" at different concentrations

Compound #	% Viability of carcinoma cells		
	100 μ M	200 μ M	300 μ M
5a	22 ^{bc} ± 0.72	12 ^c ± 0.51	11 ^c ± 0.74
5b	20 ^d ± 0.95	14 ^d ± 0.90	7 ^f ± 0.15
5c	21 ^e ± 0.63	16 ^e ± 0.94	6 ^g ± 0.24
9a	34 ^{bc} ± 0.62	24 ^c ± 0.53	17 ^c ± 0.78
9b	29 ^d ± 0.95	19 ^d ± 0.92	8 ^f ± 0.17
9c	25 ^e ± 0.66	17 ^e ± 0.98	5 ^g ± 0.26
10a	35 ^{ab} ± 0.95	24 ^c ± 0.52	16 ^d ± 0.62
10b	28 ^d ± 0.85	18 ^e ± 1.32	4 ^h ± 0.36
10c	23 ^f ± 0.79	13 ^f ± 0.44	0 ⁱ ± 0.00
11a	36 ^a ± 0.46	30 ^a ± 0.82	25 ^a ± 0.26
11b	33 ^c ± 0.26	28 ^b ± 0.46	18 ^b ± 0.44
11c	28 ^d ± 1.04	16 ^e ± 0.53	12 ^e ± 0.40
Control	100	100	100
LSD	1.325	1.336	0.734

Values are expressed as means \pm SD ($n = 3$).

Values with different superscript letters within the same column are significantly different ($P < 0.05$).

As shown in table 3, the tested compounds exhibited broad-spectrum antitumor activity in the following order: pyridazine > pyridine > quinoline analogues. The thieno-pyridine derivatives 5a-c in common, showed less activity than seleno derivatives. Compounds 9b,c and 10b,c exhibited higher antitumor activity compared to the other tested compounds, and compound 10c was the most active member in this study. The viability percentage of the treated EACC decreased from 100 % in the control sample to 0 %, 4 %, 5 % and 8 % at a concentration of 300 μ M for compounds 10c, 10b, 9c and 11b

respectively. However, compounds **9a**, **10a**, **11b** and **11c**, exhibited moderate cytotoxicity and a decrease in the viability percentage from 18 % to 12 % at a concentration of 300 μ M of each compound. The presence of the 4-phenyl function with a nitro group (e.g., **10c** and **9c**) and a methyl group (e.g., **11b** and **10b**) increased the antitumor activity due to their high antioxidant and free radical scavenging activities, as previously discussed and supported by previously reported results [14].

D. Antimicrobial performance

An antimicrobial screening of synthesized compounds "**5a-c** and **9a-c-11a-c**" against selected Gram-positive, Gram-negative bacteria and fungi compared to tetracycline, which is a standard antibacterial agent, and Amphotericin B, which is a standard antifungal agent, was performed, and the results are listed in table 4. All of the tested compounds exhibited high broad-spectrum antimicrobial activities against both gram-positive and gram-negative bacteria with inhibition percentages in the range of 50 % to 78 %. These compounds exhibited moderate activities against the studied fungi with inhibition percentages in the range of 24 % to 40 %. The presence of a strong electron-withdrawing group (e.g., compound **10c**) resulted in higher activity against the microorganisms under study.

Table 4 Inhibition zone diameter (mm) of synthesized compounds "**5a-c** and **9a-c-11a-c**"

Compounds #		Inhibition zone diameter (mm / μ g Sample)					
		Bs	Sa	Ec	St	Af	Ca
		(G ⁺)		(G ⁻)		Fungi	
Control (DMSO)		0	0	0	0	0	0
Standard	Tetracycline	22 ^a ± 0.46	24 ^a ± 0.53	20 ^a ± 0.26	19 ^a ± 0.30	-	-
	Amphotericin B	-	-	-	--	27 ^a ± 0.5 6	25 ^a ± 0.6 6
5a		10 ^f ± 0.35	12 ^e ± 0.50	8 ^d 0.41	11 ^f 0.09	6 ^{cd} ± 0.6 6	8 ^d ± 0.5 3
5b		12 ^e ± 0.53	11 ^{de} ± 0.40	10 ^d 0.42	11 ^d 0.35	7 ^{bc} ± 0.3 1	9 ^c ± 0.2 1
5c		13 ^c ± 0.41	16 ^{bc} ± 0.61	10 ^c 0.44	11 ^c 0.51	9 ^b ± 0.4 4	10 ^b ± 0.2 2
9a		11 ^f ± 0.36	14 ^e ± 0.52	10 ^d 0.44	11 ^f 0.10	8 ^{cd} ± 0.7 0	8 ^d ± 0.4 6
9b		14 ^e ± 0.56	15 ^{de} ± 0.44	11 ^d 0.40	13 ^d 0.35	9 ^{bc} ± 0.3 6	9 ^c ± 0.2 6
9c		16 ^c ± 0.44	17 ^{bc} ± 0.60	12 ^c 0.44	14 ^c 0.53	10 ^b ± 0.4 4	10 ^b ± 0.2 6
10a		14 ^e ± 0.26	15 ^{de} ± 0.85	10 ^d 0.46	11 ^f 0.10	8 ^{cd} ± 0.3 6	7 ^e ± 0.1 7
10b		14 ^e ± 0.36	16 ^{cd} ± 0.17	10 ^d 0.20	12 ^e 0.56	7 ^d ± 0.1 0	6 ^f ± 0.2 0
10c		17 ^b ± 0.17	18 ^b ± 0.36	13 ^b 0.50	15 ^b 0.46	10 ^b ± 0.8 7	8 ^d ± 0.1 0
11a		15 ^d ± 0.26	16 ^{cd} ± 0.60	11 ^d 0.00	13 ^d 0.20	9 ^{bc} ± 0.1	7 ^e ± 0.3

					0	0
11b	16 ^c ± 0.30	15 ^{de} ± 0.20	11 ^d 0.56	12 ^e 0.20	7 ^d ± 0.7 8	6 ^f ± 0.1 0
11c	17 ^b ± 0.56	18 ^b ± 0.17	12 ^c 0.50	14 ^c 0.20	9 ^{bc} ± 0.1 0	6 ^f ± 0.3 0
LSD	0.668	0.838	0.969	0.577	0.87 7	0.552

Values are expressed as means \pm SD (n = 3).

Values with different superscript letters within the same column are significantly different (P < 0.05).

Bs: *Bacillus subtilis*; Sa: *Staphylococcus aureus*; Ec: *Escherichia coli*; St: *Salmonella typhimurium*; Af: *Aspergillus Flavus*; Ca: *Candida albicans* G+: Gram-positive bacteria; G-: Gram-negative bacteria.

All of the tested compounds exhibited high broad-spectrum antimicrobial activities against both gram-positive and gram-negative bacteria with inhibition percentages in the range of 50 % to 78 %. These compounds exhibited moderate activities against the studied fungi with inhibition percentages in the range of 24 % to 40 %. The presence of a strong electron-withdrawing group (e.g., compound **11c**) resulted in higher activity against the microorganisms under study.

III. EXPERIMENTAL

A. Materials and instrumentation

The reagents were analytical grade or chemically pure. Elemental analyses (C, H, N, S) were conducted using the Perkin-Elmer 2400 Analyzer, series II (Perkin Elmer Co., Shelton, UK), their results were found to be in good agreement ($\pm 0.3\%$) with the calculated values. All of the corrected melting points were determined using a Stuart SMP 20 melting point apparatus (Bibby Scientific Limited, Staffordshire, UK). The infrared spectra were recorded on a Perkin Elmer Alpha platinum-ATR spectrometer, and the ¹H NMR spectra were measured on a Bruker WP 300 (Bruker, MA, USA) in CF₃COOD using TMS as an internal standard. All of the microanalyses and spectral analyses were performed at the Micro Analytical Centres of Taif (IR, CHN) and King Abdel-Aziz University (¹H NMR and ¹³C NMR analysis), Kingdom of Saudi Arabia. The biological tests were performed by the "Biotechnology Unit", Faculty of Agriculture, Cairo University, Egypt. The Ehrlich Ascites Carcinoma Cell (EACC) line was supplied by "The National Cancer Institute", Egypt. Biological statistical analysis was carried out according to Fisher, indicating the standard deviation "SD" and the standard error "SE" [15]. LSD (Least significant difference) test was used to compare the significant differences between means of treatment. The statistical package for social science S.P.S.S. (1999) program version was used for all analysis [16].

B. Synthesis and characterisation

General method for the synthesis of 5-aryl azo-2-aminothiazol derivatives **2a-c**

Coupling of molar ratio of 2-aminothiazole **1** with different diazotised aromatic amines (aniline, *p*-toluidine, *p*-nitroaniline) in ethanol/sodium acetate at -5 °C was performed to obtain the corresponding derivatives of 5-arylo-2-aminothiazol **2a-c**. The precipitate which formed was collected by filtration, dried and recrystallized from proper solvent. The IR and ¹H NMR spectra for the obtained compounds were recorded to characterise the structure of these compounds, and were found to be in agreement with the literature [10],[11], [17].

2-Amino-5-phenylazo-thiazole (**2a**). X=H: Reddish brown solid (EtOH), yield 84%, m.p. 270-271 °C, Lit. m.p. 270-271 °C; X= Ph: Red solid (EtOH), yield 83%, m.p. 278-279 °C, Lit. m.p. 280 °C.

2-Amino-5-(*p*-tolyl)azo-thiazole (**2b**). X=H: Brown solid (EtOH), yield 73%, m.p. 207-209 °C, Lit. m.p. 205 °C; X= Ph: Brown solid (EtOH), yield 94%, m.p. 204 °C, Lit. m.p. 203-205 °C.

2-Amino-5-(*p*-nitrophenyl)azo-thiazole (**2c**). X=H: Brown solid (EtOH), yield 80%; m.p. 167-169 °C, Lit. m.p. 167-169 °C; X= Ph: Brown solid (DMF), yield 76%, m.p. 261-262 °C, Lit. m.p. 261-262 °C.

General method for the synthesis of 2-[N-(chloroacetyl)amino]-5-arylo-2-thiazoles 3a-c

To a solution of 2-amino-5-arylo-2-thiazoles **2a-c** (10 mmol) in DMF (25 ml) containing 0.5 ml triethyl amine, chloroacetyl chloride (1.2 ml, 15 mmol) was added dropwise with stirring at room temperature. Stirring was continued for 2 hours and the reaction mixture was poured to ice cooled water. The precipitate which formed was collected by filtration, dried and recrystallized from the appropriate solvent. The structure of the synthesized compounds were characterised using IR and ¹H NMR spectra, and were found to be in agreement with previously reported [9], [10].

2-[N-(chloroacetyl)amino]-5-phenylazo-thiazole (**3a**). X= H: Greenish yellow solid (EtOH); yield 78%; m.p.: 220-222 °C; Lit. m.p.: 220-222 °C; X= Ph: Orange solid (EtOH); yield 79%; m.p.: 227-228 °C; Lit. m.p.: 229 °C.

2-[N-(chloroacetyl)amino]-5-(*p*-tolyl)azo-thiazole (**3b**). X= H: Yellowish brown solid (EtOH); yield 82%; m.p.: 235-237 °C; Lit. m.p.: 235-237 °C; X= Ph: Orange solid (EtOH); yield 77%; m.p.: 221 °C; Lit. m.p.: 222 °C.

2-[N-(chloroacetyl)amino]-5-(*p*-nitrophenyl)azo-thiazole (**3c**). X= H: Dark brown solid (EtOH-DMF), yield 85%, m.p. 186-187 °C; Lit. m.p. 186-187 °C; X= Ph: Brown solid (DMF), yield 82%, m.p. 215-216 °C, Lit. m.p. 216 °C.

*Synthesis of 3-amino-N-(4-phenyl-5-arylo-2-thiazolyl)-thieno[2,3-*b*]pyridine-2-carboxamide dyes 5a-c*

A mixture of 2-(N-chloroacetyl)-5-arylo-2-thiazole derivatives **3a-c** (0.01 mol), 4,6-dimethyl-2-mercaptopyridine-3-carbonitrile **4** (0.01 mol), and anhydrous potassium carbonate (0.01 mol) in acetone (30 ml) was refluxed for 4 hours. The thiazol-2-yl derivatives formed were added to a solution of sodium

ethoxide (from 0.005 mol sodium metal) in absolute ethanol (30 ml). The solution was refluxed for 2 hours, left to cool, and diluted with cooled water (50 ml). The solid obtained was filtered and recrystallized from ethanol [11].

5a; Red solid, yield 43%, mp >300 °C, Lit. m.p. >265 °C.

5b; Red solid, yield 50%, mp 298 °C, Lit. m.p. >265 °C.

8d; Greenish brown solid, yield 56%; mp >300 °C; Lit. m.p. >265 °C.

Synthesis of hydroseleno-(pyridine, pyridazine and quinoline)carbonitrile derivatives 6-8

2-hydroseleno-4,6-dimethylpyridine-3-carbonitrile **6**, 3-hydroseleno-5,6-diphenylpyridazine-4-carbonitrile **7** and 5,6,7,8-tetrahydro-2-hydroseleno-4-(4'-methoxyphenyl)quinoline-3-carbonitrile **8** were synthesized according to previously reported methods and their characterized data (m.p., IR and ¹H NMR) were in agreement with literature [11].

2-Hydroseleno-4,6-dimethylpyridine-3-carbonitrile (**6**). Brown solid (EtOH), yield 79%, m.p. 214-215 °C, Lit. 214-216 °C.

3-Hydroseleno-5,6-diphenylpyridazine-4-carbonitrile (**7**). Brown solid (EtOH), yield 90%, m.p. 219 °C, Lit. 218-220 °C.

5,6,7,8-Tetrahydro-2-hydroseleno-4-(4'-methoxyphenyl)quinoline-3-carbonitrile (**8**). Dark brown solid (EtOH), yield 67%, m.p. 171 °C, Lit. 170-172 °C.

General procedure for the synthesis of 3-amino substituted N-(5-arylo-2-thiazol-2-yl)selenopheno-pyridine, pyridazine and/or quinoline-2-carboxamide Derivatives 9a-c- 11a-c

The mixtures of 2-(N-chloroacetyl)-5-arylo-2-thiazole derivatives **3a-c** (10 mmol) with 2-hydroseleno-4,6-dimethylpyridine-3-carbonitrile **4** (2.12 g, 10 mmol), 3-hydroseleno-5,6-diphenylpyridazine-4-carbonitrile **5** (3.36 g, 10 mmol) and/or 5,6,7,8-tetrahydro-2-hydroseleno-4-(4'-methoxyphenyl)quinoline-3-carbonitrile **6** (3.43 g, 10 mmol) dissolved in DMF (30 ml) containing aqueous KOH (10 %, 5 ml), were stirred for 2 hrs. Treatment of reaction mixture with an excess amount of aqueous 10 % KOH (5 ml), and stirring for an additional 2 hrs., affording the corresponding derivatives "**9a-c-11a-c**". The precipitates formed were filtered and recrystallised from ethanol. The characterization for the products was in agreement with the literature [11].

3-Amino-4,6-dimethyl-N-(5-phenylazo-2-thiazol-2-yl)selenopheno[2,3-*b*]pyridine-2-acetamide (**9a**). Orange solid, yield 39 %, m.p. >300 °C, Lit. m.p. >300 °C.

3-Amino-4,6-dimethyl-N-[5-(4-tolylazo)thiazol-2-yl]selenopheno[2,3-*b*]pyridine-2-actamid (**9b**). Yellowish brown solid, yield 42 %, m.p. 156-157 °C, Lit. m.p. 156-157 °C.

3-Amino-4,6-dimethyl-N-[5-(4-nitrophenylazo)thiazol-2-yl]selenopheno[2,3-*b*]pyridine-2-actamid (**9c**). Dark brown solid, yield 62 %, m.p. 176-177 °C, Lit. m.p. 176 °C.

3-Amino-4,6-diphenyl-*N*-(5-phenylazothiazol-2-yl)selenopheno[2,3-*b*]pyridazine-2-acetamide (**10a**). Brown solid, yield 41 %, m.p. 167-168 °C, Lit. m.p. 168-169 °C.

3-Amino-4,6-diphenyl-*N*-[5-(4-tolylazo)thiazol-2-yl]selenopheno[2,3-*b*]pyridazine-2-acetamide (**10b**). Reddish brown solid, yield 57 %, m.p. 232 °C, Lit. m.p. 230-233 °C.

3-Amino-4,6-diphenyl-*N*-[5-(4-nitrophenylazo)thiazol-2-yl]selenopheno[2,3-*b*]pyridazine-2-acetamide (**10c**). Dark brown solid, yield 62 %, m.p. 180-181 °C, Lit. m.p. 180 °C.

3-Amino-5,6,7,8-tetrahydro-4-(4-methoxyphenyl)-*N*-(5-phenylazothiazol-2-yl)selenopheno[2,3-*b*]quinoline-2-acetamide (**12a**). Brown solid, yield 43 %, m.p. 142-143 °C, Lit. m.p. 142-144 °C.

3-Amino-5,6,7,8-tetrahydro-4-(4-methoxyphenyl)-*N*-[5-(4-tolylazo)thiazol-2-yl]selenopheno[2,3-*b*]quinoline-2-acetamide (**12b**). Reddish brown solid, yield 50 %, m.p. 155 °C, Lit. m.p. 154-155 °C.

3-Amino-5,6,7,8-tetrahydro-4-(4-methoxyphenyl)-*N*-[5-(4-nitrophenylazo)thiazol-2-yl]selenopheno[2,3-*b*]quinoline-2-acetamide (**12c**). Dark reddish brown solid, yield 58 %, m.p. 169-170 °C, Lit. m.p. 168-170 °C.

C. Screening of biological activities of the synthesized dyes

In vitro antioxidant potential of synthesized compounds

DPPH radical scavenging activity

The scavenging effect of the 2,2 diphenyl-1-picrylhydrazyl (DPPH) free radical was measured by the method reported by Chou et al. and is expressed in terms of the inhibition percentage (I %) [19]. Different concentrations of the synthesized compounds (100, 200 and 300 µM) with 0.1 ml of a 1 mM DPPH-methanol solution were incubated at room temperature for 30 min. The absorbance (A) of each solution was measured at 517 nm against a blank containing ascorbic acid using equation 1.

$$I\% = \frac{A_{\text{control}} - A_{\text{sample}}}{A_{\text{control}}} * 100 \quad (1)$$

Hydroxyl radical scavenging assay

The hydroxyl radical scavenging activity was measured according to Nagai et al., [12] where mixtures of various concentrations of the synthesized compounds (100, 200, 300 µM) with 0.45 ml of a sodium phosphate buffer solution (0.2M), 0.15 ml of a 2-deoxyribose solution (10 mM), 0.15 ml of an FeSO₄-EDTA solution (10 mM) and 0.15 ml of H₂O₂ (10 mM) were prepared and filled to the final volume (1.5 ml) with distilled water. The solutions were incubated at 37 °C for 4 hours, and the reaction was terminated by adding 0.75 ml of a trichloroacetic acid solution (70 % w/v) and 0.75 ml of a thiobarbituric acid solution (50 mM). The absorbance (A) was measured at 520 nm, and the inhibition of deoxyribose degradation as a percentage (I %) was calculated according to equation 1.

In vitro acute toxicity and antitumor activity

Acute toxicity (LD₅₀)

The median lethal dosage (LD₅₀) values of selected compounds (**9c**, **10a**, **10b** and **10c**) based on *in vitro* antioxidant potential results were determined in mice. LD₅₀ represents the individual dose required to kill 50 % of a population of tested animals (e.g., rats, fish, mice, cockroaches). A group of five female adult albino mice (25-30g) was injected intraperitoneally (I.P) with graded doses of 100-1000 mg Kg⁻¹ of body weight for each selected compound suspended in DMSO. The percentage of mortality was determined 72 hours after injection. The LD₅₀ calculation was processed using a graphical method [18].

In vitro antitumor activity

Female Swiss albino mice (25-30g) were housed at a constant temperature (24±2 °C) with alternating 12 hours of light and dark cycles and were fed standard laboratory food (Milad Co) along with ad libitum water. The care and handling of the animals were performed according to the guidelines of "The World Health Organization, Geneva, Switzerland". A strain of Ehrlich Ascites Carcinoma Cells (EACC) was supplied by "The National Cancer Institute", Egypt. The tumour cell line was maintained in female Swiss albino mice through serial intraperitoneal inoculation at 7 or 8 day intervals in the form of ascites.

In vitro cytotoxicity

The EACC cells were obtained by needle aspiration of the ascitic from preinoculated mice under aseptic conditions according to the method reported by Uma Dev et al. [19]. The tumour cell suspension (2×10⁶ cells per ml) was prepared in RPMI-1640 media, 10 % Foetal bovine serum and L-glutamine. The tested compounds with different concentrations (i.e., 100, 200, 300 µM) in DMSO were incubated overnight with 2 ml of suspended tumour cells under 5 % CO₂ at 37 °C. The trypan blue exclusion method reported by Bennett et al. was used to calculate the viability percentage of tumour cells using equation 2 [20].

$$I\% = \frac{\text{No. of variables}}{\text{Total no. of cells}} * 100 \quad (2)$$

The antioxidant and hydroxyl radical scavenging activities increased when the concentration of the tested compounds was doubled, and most of the synthesized compounds exhibited very good antioxidant activity (i.e., pyridazine > pyridine > quinoline analogues) relative to ascorbic acid, which was used as a standard. The high antioxidant and scavenging activities of the tested compounds may be due to the resonance phenomena of double bonds and lone pair electrons on nitrogen. This structure may lead to radical formation in more than one site, especially on the benzene ring attached to the nitro group, which is a highly electron withdrawing group that enables the benzene ring to convert to a radical form and forms a new covalent bond with another radical (e.g., **9c** and **10a-c**). In addition, protection against peroxides, peroxyxynitrite, glutathione, peroxidase-like activity and metal-binding capacity due to organoselenium analogues leads to antioxidant

activity. This conclusion is also supported by previously reported results [13].

Antibacterial and antifungal activities

The antibacterial activity of novel synthesized compounds "5a-c and 9a-c – 11a-c" (100 µg/ml in DMSO) was determined *in vitro* using the disc diffusion method [21], against a variety of pathogenic microorganisms, such as Gram-positive bacteria (i.e., *Bacillus subtilis* and *Staphylococcus aureus*) and Gram-negative bacteria (i.e., *Escherichia coli* and *Salmonella typhimurium*), in nutrient agar media by measuring the zone of inhibition in mm. The antifungal screening of the synthesized compounds was also carried out *in vitro* using the same method against two fungi strains of *Aspergillus flavus* and *Candida albicans*. In addition, *Tetracycline* and *Amphotericin B* served as standard antibacterial and antifungal agents, respectively, and both served as positive controls for antimicrobial activity.

IV. CONCLUSION

A series of monoazo compounds based on 4-substituted-3-amino-*N*-(4-aryl-5-arylaazo-2-thiazolyl)-thieno[2,3-*b*]pyridine-2-carboxamide) along with their seleno like derivatives of pyridine, pyridazine and quinolone was synthesized and *in vitro* tested for their biological activity. They exhibited variable antioxidant activity due to the protection against peroxide and peroxy nitrite radicals, as well as antitumor activity. In addition, these compounds are emerging as promising downstream candidates for cancer therapy due to their ability to modulate multiple physiological functions implicated in cancer development due to their antioxidant and anticancer chemo preventive or apoptotic activities while being nontoxic. These compounds also have the potential for use as antibacterial agents against different pathogenic bacteria and fungi.

ACKNOWLEDGMENT

The authors want to dedicate this work with great honor and attitude to their master, Prof. Dr. Mohamed A. Metwally (May God bless and rest his soul) for his fabulous efforts as long as his life, serving the human beings in the field of teaching and scientific research. All cordial gratitude presented to our research team, Faculty of Science, Taif University (KSA) for their great support.

REFERENCES

- [1] J. H. Choi, S. H. Hong, E. J. Lee, and A. D. Towns, "Structure-wet fastness relationships of some blue disperse dyes for polyester," *Color Technol.*, vol. 116, pp. 273-278, Sept. 2000.
- [2] P. Gregory, "Modern reprographics," *Rev. Prog. Color.*, vol. 24, pp. 1-16, June 1994.
- [3] A. Rao, A. Carbone, A. Chimirri, E. De Clercq, A. Monforte, P. Monforte, C. Pannecouque, and M. Zappal, "Synthesis and anti-HIV activity of 2,3-diaryl-1,3-thiazolidin-4-ones," *II Farmaco*, vol. 58, pp. 115-120, Feb. 2003.
- [4] A. Dari, L. E. Christiaens, and M. J. Renson, "Synthesis of a Selenium Analogue of Ellipticine: 5,11-dimethyl[1]benzoselenolo[2,3-*g*]isoquinoline," *Acta Chem. Scand.*, vol. 47, pp. 208-211, 1993.
- [5] N. Furukawa, "Formation of Unusual Valent Organic Sulfur and Selenium Compounds via Transannular Interaction," *Phosphorus Sulfur*, vol. 74, pp. 261-278, 1993.
- [6] D. E. Metzler, *The chemical reactions of living cells*. in Biochemistry, 2nd ed. vol. 2, New York: 2003, pp. 425-430.
- [7] E. Abdel-Latif, M. A. Metwally, F. A. Amer, and M. E. Khalifa, "Synthesis of 5-arylaazo-2-(arylidenehydrazino)-thiazole disperse dyes for dyeing polyester fibres," *Pigm. Resin Technol.*, vol. 38, pp. 105-110, 2009.
- [8] M. A. Metwally, M. E. Khalifa, Abdel-Latif, E., and F. A. Amer, "New arylhydrazonothiazolidin-5-one disperse dyes for dyeing polyester fibers," *Pol. J. Chem. Technol.*, vol. 12, pp. 1-6, 2010.
- [9] M. E. Khalifa, M. A. Metwally, E. Abdel-Latif, and F. A. Amer, "Synthesis of Some New 5-Arylazothiazole Derivatives as Disperse Dyes for Dyeing Polyester Fibers," *Inter. J. Textile Science.*, vol. 1, pp. 62-68, 2012.
- [10] M. E. Khalifa, E. Abdel-Latif, and A. A. Gobouri, "Disperse Dyes Based on 5-Arylaazo-thiazol-2-ylcarbamoyl-thiophenes: Synthesis, Antimicrobial Activity and Their Application on Polyester," *J. Heterocycl. Chem.*, 2014, under press DOI 10.1002/jhet.2153
- [11] M. E. Khalifa, S. H. Abdel-hafez, A. A. Gobouri, and M. I. Kobeasy, "Synthesis and biological activity of novel arylazothiazole disperse dyes containing selenium for dyeing polyester fibers (accepted for publication)," *Phosphorus Sulfur* doi: 10.1080/10426507.2014.948622
- [12] T. Nagai, H. Inoue, N. Suzuki, T. Muoda, and T. Nagashima, "Antioxidative ability in a linoleic acid oxidation system and scavenging abilities against active oxygen species of enzymatic hydrolysates from pollen *Cistus ladaniferus*," *Int. J. Mol. Med.*, vol. 15, pp. 259-263, Feb. 2005.
- [13] F. Sztaricskai, I. E. Takacs, F. Pusztai, G. Szabo, and I. Csipo, "Antiulcer Effect of the N- and O-β-D-Glucopyranosides of 5-Aminosalicylic Acid," *Arch. Pharm.*, vol. 332, pp. 321-326, Sept. 1999.
- [14] S. M. M. Shanab, E. A. Shalaby, and E. A. El Fayoumy, "Enteromorpha compressa Exhibits Potent Antioxidant Activity," *J. Biomed. Biotechnol.* Vol. 2011, pp. 1-11, June 2011.
- [15] R. A. Fisher, *Statistical method for research workers Edinburgh*, In Classics in the history of psychology, 14th ed., Oliver and Boyd, 1970, pp. 140.
- [16] S.P.S.S., 1999. *Statistical Package for the Social Science*, Inc. Chicago.
- [17] A. S. Shawali, and A. O. Abdelhamid, "New routes to aroylthiadiazolines and arylazothiazoles from phenylglyoxalyl bromide arylhydrazones and phenacyl thiocyanate," *J. Heterocycl. Chem.*, vol. 13, pp. 45-49, 1976.
- [18] P. Litvinov, V. Yu. Mortikov, Yu. A. Sharanin, and A. M. Shestopalov, "Condensed Pyridines; 1. A Convenient Method for Synthesis of Novel 3-Cyanopyridine-2(1H)-selenones and 3-Aminoselenolo [2,3-*b*]pyridines," *Synthesis*, vol. 1985, pp. 98-99, 1985.
- [19] P. Uma Devi, F. E. Soloman, and A. C. Sharada, "Plumbagin, A Plant Naphthoquinone with Antitumor and Radiomodifying Properties," *Pharm. Biol.*, vol. 37, pp. 231-236, Jan. 1999.
- [20] J. M. Bennett, D. Catovsky, , M. T. Danniel, D. A. G. Galton, H. R. Graanlink, and C. Sultan, "Proposals for the Classification of the Acute Leukaemias," *Brit. J. Hematol.*, vol. 33, pp. 451-458, Aug. 1976.
- [21] I. L. Martins, J. P. Miranda, N. G. Oliveira, A. S. Fernandes, S. Goncalves, and A. M. M. Antunes, "synthesis and biological activity of 6-selenocaffeine: potential modulator of chemotherapeutic drugs in breast cancer cells," *Molecules*, vol. 18, pp. 5251-5264, May 2013.

Grayscale and binary image enhancement of hand vein images to aid peripheral intravenous access

Marlina Yakno, Junita Mohamad-Saleh, Bakhtiar Affendi Rosdi

Abstract—Difficulty in achieving a peripheral intravenous (IV) access in pediatric and some adult's patient is a clinical problem. The use of near-infrared imaging device to aid visualization of an IV access usually suffers from low contrast and noise due to non-illumination and thickness of hand skin. This further complicates subsequent processing such as image segmentation. In this work, two methods are proposed in two different stages; grayscale enhancement and binary enhancement for correction of low contrast and noisy images. For grayscale enhancement, a combination of histogram-based and fuzzy-based contrast enhancement algorithms are applied on hand vein images. For binary enhancement, a combination of three techniques; Artificial Neural Network pixel corrector, Binary Median Filter and Massive Noise Removal, are applied on the binary hand vein images. Comparative analysis on test images using different contrast enhancement methods has shown superior results from the proposed method in comparison to its counterparts.

Keywords—Image enhancement, neural network, fuzzy, hand vein imaging, peripheral intravenous access.

I. INTRODUCTION

A peripheral IV access is a process of obtaining blood vessel for the purpose of blood drawing, intravenous fluid feeding or administration of medicine in patient's blood vessels by inserting a needle or catheter through the skin and into an underlying vein. It is often performed by medical laboratory scientists, medical practitioners, paramedics, phlebotomists and other nursing staff.

A catheter is a small tube, but is most often difficult to be placed into blood vessel, especially if a patient is at an extreme age, with chronic disease or has dark skin color [1-3, 5]. It was reported that worldwide, 10% (i.e. more than 1 million per year) of attempts to establish an IV line has failed [4]. The failure, although a small percentage, has led to various negative impacts during IV access such as fainting or feeling

lightheaded, hematoma (blood accumulating under the skin) and pain associated with multiple punctures to locate a vein. In addition, the frightful and stressful moments faced particularly by children patients during IV may lead to the development of severe psychological problems such as needle phobia or worse still, hospital phobia.

Near-infrared (NIR) imaging offers a solution for veins visualization as it can penetrate up to several millimeters into a tissue (i.e. skin) with a specific wavelength between 700 and 1000nm [5-7]. However, its image acquisition most often resulted in vein images with poor contrast, non-uniform gray level and noises because the acquisition is affected by luminous intensity and thickness of the back of hand skin. Several methods have been used to solve these imaging problems, focusing at grayscale or binary image enhancement.

Image enhancement process usually produces a better-quality image for the next imaging process such as separation or segmentation of vein from its background. A classical grayscale enhancement technique is based on histogram equalization (HE) [8]. Although HE is suitable for an overall contrast enhancement, practically HE usually causes level saturation, an effect which degrades the appearance of an image leading to loss of information [9]. To overcome this limitation, Kumar and Prathyusha have employed an extension of HE known as Contrast Limited Adaptive Histogram Equalization (CLAHE) into vein imaging [10]. By applying an appropriate value of clipping level, CLAHE method does not only enhance the contrast, but it is also able to solve the illumination problem. This method has been reported to be suitable for most medical imaging purposes [11-13]. However, if the chosen clipping level is inappropriate, CLAHE can degrade the quality of an image significantly.

Simplest methods such as unsharp masking (UM) [14-15] have also been proposed to enhance image contrast. Recently, Zhao et al. presented a method to enhance hand vein images based on Butterworth High Pass Filter and HE [16]. However, the methods may have poor performance at improving the contrast of some hand vein images due to the two main drawbacks. At first, it enhances high-contrast areas more than areas that do not exhibit high image dynamics. Second, the presence of linear highpass filter makes the system extremely sensitive to noise. Consequently, some unpleasant overshoot artifacts may appear in the output image.

Marlina Yakno. Author is with the Faculty of Electrical & Electronics Engineering, University Malaysia Pahang, Pahang, Malaysia (corresponding author to provide phone: 609-424 6032; fax: 609-424 6111; e-mail: marlinayakno@ump.edu.my).

Junita Mohamed-Saleh. Author, is with the School of Electrical & Electronics Engineering, University Sains Malaysia, Pulau Pinang, Malaysia. (e-mail: jms@usm.my).

Bakhtiar Affendi Rosdi. Author is with the School of Electrical & Electronics Engineering, University Sains Malaysia. (e-mail: eebakhtiar@usm.my).

When dealing with binary images, the contrasts of vein patterns vary depending on the illumination of an image. A binary hand vein normally contains some noise and un-sharp edges. Thus, the quality of the image needs to be enhanced to expose the vein structures. Shahin et al. have employed Binary Median Filter (BMF) [17] and Kumar and Prathyusha applied Massive Noise Removal (MNR) [10] to eliminate noise regions with small amount of connectivity. Work by Ding et al. utilized the advantages of MNR and BMF into their work for the same purpose [18].

Image enhancement using fuzzy techniques have been used extensively in medical applications especially in digital mammogram [19-20]. Fuzzy Histogram Hyperbolization (FHH) is an example of fuzzy technique which promises good enhancement results in various applications. However, very few researchers have explored this approach for hand vein image enhancement. Also, to the best of our knowledge, no researchers have combined CLAHE with FHH for any application.

Aside from the conventional techniques, a more sophisticated technique like Artificial Neural Network (ANN) has also been employed in hand vein imaging. However, the ANN approach for hand vein imaging is mostly applied to vein recognition for biometric purposes [21-22]. To the best of our knowledge, no researcher has ever applied ANN technique onto binary hand vein image enhancement for medical purposes.

This paper proposes the application of CLAHE with FHH for grayscale enhancement of hand vein image. Then, using local threshold method the enhanced image is converted into binary. Finally, a combination of ANN pixel corrector, BMF and MNR techniques are applied in binary enhancement stage. With this method, the contrast of binary images can be increased and subsequently a more accurate hand vein patterns can be obtained to aid peripheral IV access. The proposed approach is compared with various existing image enhancement methods at exposing binary hand vein patterns.

II. HAND VEIN IMAGE ACQUISITION

In this work, a Sony CCD TV camera is used to capture the vein patterns at the back of a hand. The subject's hand is illuminated by 48-near-infrared light emitting diodes (LEDs) with wavelength of 890nm. The LEDs are equi-distantly mounted around the camera lens to ensure an even illumination on the hand skin. The current level of the LEDs can be manually adjusted according to the environment. Subjects were asked to place their hands on a small platform with back of the hand facing the camera. The CCD TV camera was connected to a computer to capture the images as shown in Fig. 1. A captured hand vein image is then filtered from impulse noise [23] and extracted into a region of interest [24] based on modification on the image size at a pre-processing stage.

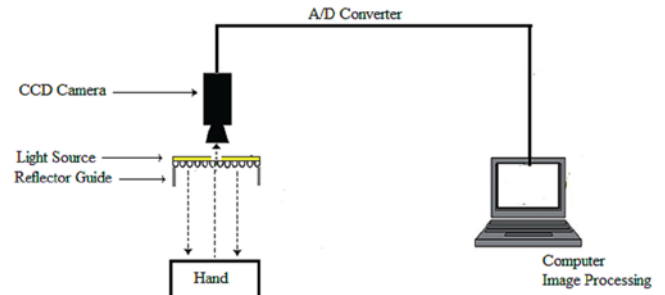


Fig. 1 Schematic of hand vein image acquisition

III. HAND VEIN PATTERNS IMAGING

In general, the proposed enhancement method for hand vein imaging in this work consists of grayscale enhancement, segmentation, binary enhancement and image evaluation stages. This process is illustrated in Fig. 2. Each of these stages are discussed.

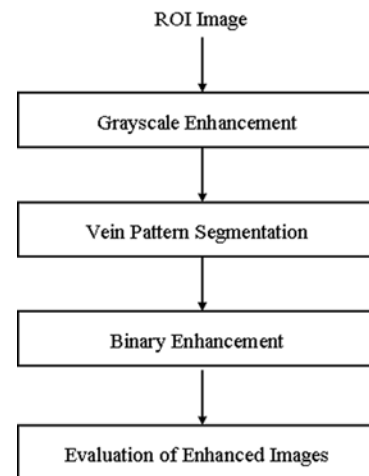


Fig. 2 Process flow diagram of proposed hand vein exposure system development

A. Grayscale Enhancement

Grayscale enhancement is employed to simplify the separation of veins and its background within an image. This work considers CLAHE method to take advantages of its capability at enhancing image contrast. Then, it applies FHH to further sharpen the vein patterns. Image enhancement methods considered in this work are discussed.

1) Contrast Limited Adaptive Histogram Equalization

As already stated, CLAHE method is an improvement over standard HE. While HE considers the entire image, CLAHE algorithm operates by partitioning the image into a number of non-overlapping contextual regions. A histogram is calculated and constructed separately according to the size of contextual regions. Then, a clip limit value for clipping histograms is determined as a threshold. Next, the histogram is clipped according to the predefined clipping limit. The access clipped

pixels are then distributed back to the clipped histogram. Finally, the gray level mappings were combined using bilinear interpolation in order to assemble the final enhanced image .

2) Fuzzy Histogram Hyperbolazation

It has been reported that CLAHE method may result in loss of image information [25]. Hence, after employing CLAHE, FHH is applied for further enhancement of the vein image. FHH combines the concepts of histogram hyperbolization and fuzzy hyperbolization [26]. Basically, the algorithm works in the following sequence:

- **Gray Level Fuzzification:** The image fuzzification transforms a gray level image into the range of [0, 1]. Here, a non-linear function is applied as a membership function [27]:

$$\mu(g_{ij}) = \frac{g_{ij} - g_{\min}}{g_{\max} - g_{\min}} \quad (1)$$

where g_{\min} and g_{\max} are the minimum and maximum value of the gray level in the image.

- **Modification of Membership Function:** A membership modification is carried out using [27]:

$$\mu'(g_{ij}) = [\mu(g_{ij})]^\beta \quad (2)$$

where fuzzifier, β is a parameter used to modify the meaning of a fuzzy set. Applying fuzzifier may result in either reducing image contrast or increasing image contrast, depending on the value of β , obtained based on trial-and-error.

- **Gray Level Defuzzification:** A new set of gray level is generated as follows [27]:

$$g'_{ij} = \left(\frac{L-1}{e^{-1}-1} \right) \times \left[e^{-\mu'(g_{ij})^\beta} - 1 \right] \quad (3)$$

where $\mu(g_{ij})$ is the gray level in the fuzzy membership values, β is the fuzzifier parameter, g'_{ij} is the new gray level values and L is the maximum number of gray levels in the original image.

B. Segmentation

Segmentation is a process which partitions a digital image into multiple regions or sets of pixels that have similar characteristics to each other [28]. A simple segmentation process involves thresholding which can be categorized into global or local threshold. In global threshold, a distinct peak in the histogram is expected for determining the global threshold for the entire image. For hand vein images however, such peaks do not exist, and thus, it is unlikely that global thresholding can produce good results [19]. Therefore, local thresholding method is adopted in this work as it has been reported to perform better and produce more satisfactory results than global threshold [29].

To find local threshold value, the intensity values of the

local neighbourhood of each pixel are first statistically examined to determine the most suitable statistical function. This is necessary as suitable statistical function is dependent upon the input image. For hand vein images used in this work, mean of local intensity has been found to be the most appropriate statistical function. It is also simple in implementation and has fast execution.

For image window $W(i,j)$ of size $N \times N$, the mean value is calculated as follows [30].

$$\mu = \frac{1}{N \times N} \sum_{i=0, j=0}^{i=N-1, j=N-1} W(i, j) \quad (4)$$

On the whole, mean of local area alone is not suitable as a threshold, because the range of intensity values within a local neighbourhood is very small and their mean values are close to the centre pixel [29]. The situation has been improved by employing a proposed threshold value ($mean - C$), where C is a constant. C is determined based on trial-and-error as it is dependent upon the image.

The local threshold $T_L(i,j)$ for each centre pixel of window $W(i,j)$ is selected as [29].

$$T_L(i, j) = (\mu - C) \quad (5)$$

where μ is a mean and C is a constant. Window $W(i,j)$ is then thresholded as [30]:

$$W_L(i, j) = \begin{cases} 1 & \text{if } W(i, j) > T_L(i, j) \\ 0 & \text{otherwise} \end{cases} \quad (6)$$

All pixels with value above the threshold, T_L are assumed to belong to the object of the interest while all pixels with values below the threshold level are assumed to be the background.

C. Binary Enhancement

A segmentation result normally contains some noise and unsharp edges which affect the structure of vein images. Thus, the quality of an image needs to be enhanced to expose the vein structures. To achieve this, a proposed binary enhancement algorithm consisting of three stages; correction of selected pixels using ANN pixel corrector, smoothing of vein edges using BMF and elimination of unwanted noise using MNR, are tested. After a series of trial-and-error process, a sequence of the three components is employed.

1) ANN Pixel Corrector

An ANN pixel corrector has been designed and trained to classify a pixel as background or vein based on the position of the pixel in a vein image. Outputs from the ANN pixel corrector are either 1 for vein or 0 for background.

For ANN training in general, it is necessary to gather sample data containing various features that can possibly appear in a vein image so that the ANN learns to map specially adapted parameters of these features. For this reason, a set of 3 x 3 window of binary image are used as training patterns for

binary vein image (see Figure 3), whereby x_1 refers to the pixel of interest, and x_2 until x_9 are the neighbouring pixels. The window acts as a template to determine the correction for pixel x_1 .

A total of 256 sets of training pattern have been generated from a hand vein image. These input patterns are then randomly divided into three subsets namely the training, validation, and test set with a ratio of 40:20:40 respectively. These datasets are used in ANN training.

In ANN training process, the binary values of each 3 x 3 window together with their corresponding desired binary output are fed into a Multilayer Perception (MLP), a variant of ANN model. The proposed MLP is a three layer feed-forward ANN with one hidden layer as shown in Figure 4. Each layer consists of a number of processing elements which do the computation. The feed-forward MLP neural network is trained by supervised learning using the Levenberg-Marquardt iterative back-propagation algorithm, from one to ten hidden layer neurons. For each specified number of hidden neurons, an MLP is trained 30 times to avoid local minima traps. After each iteration, the mean square errors (MSE) of the training and validation datasets are calculated. The training process terminates when there is no further reduction in the validation MSE for 5 consecutive training iterations. The best MLP is

x_2	x_5	x_7
x_3	x_1	x_8
x_4	x_6	x_9

Fig. 3 A 3 x 3 window of binary image pixels

selected from each of the 30 trains runs of each specified number of hidden neurons.

2) Binary Median Filter (BMF)

At this stage, the output of ANN pixel corrector is scanned uniformly using 5 x 5 sliding windows to eliminate burrs and make the vein edges smooth. This is done by using a median value. The median is calculated by first sorting all the pixel values from the surrounding neighborhood into numerical order and then replaces the value of the center pixel by the median value as given by:

$$m(i, j) = \text{median}(w(i, j)) \quad (7)$$

3) Massive Noise Removal (MNR)

Massive noise removal technique involves a conversion of the white pixel value of '1' (foreground) to black which is '0' (background) if the total value of white pixels in each object in an image is less than the minimum number of white pixels set for a connected component. The minimum number of the white

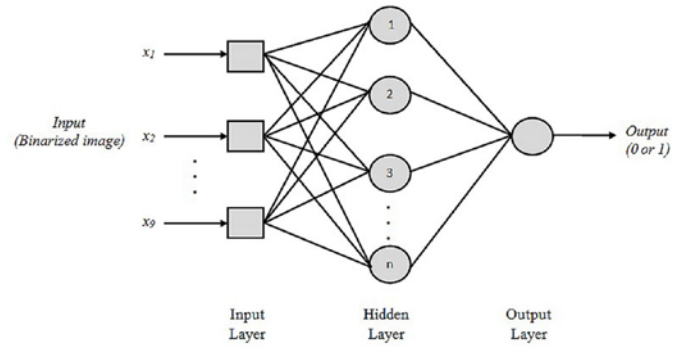


Fig. 4 Structure of a three-layer-feed-forward MLP-pixel corrector

pixels for connected components is also known as threshold value. In general, this technique is carried out based on four stages; connected component labeling area, component labeling area computation, threshold value determination and small objects removal.

It begins by assigning a unique label (*i.e.* $L=1, 2, 3, \dots, n$) to each object (a group of connected pixels with intensity of 1) in a binary image by scanning the image pixel-by-pixel using 4-connectivity, from left to right and top to bottom. The area of each labeled component is then calculated. This is followed with the threshold value determination. Before the threshold value can be determined, the maximum size of connected components is defined using:

$$C_{L_{\max}} = \max(C_L) \quad (8)$$

where C_L is the connected components with a unique label and $C_{L_{\max}}$ is the maximum size of connected components.

Then, threshold value T is calculated as follows:

$$T = C_{L_{\max}} / m \quad (9)$$

Where m is determined based on trial-on-error as it is dependent upon the image.

Finally, MNR is represented as:

$$Y(i, j) = \begin{cases} 0 & \text{if } C_L < T \\ 1 & \text{otherwise} \end{cases} \quad (10)$$

Based on Eq. (10), such connected component, C_L which is less than the minimum threshold value is converted to background and the others remained unchanged. This process ends the image enhancement process.

D. Evaluation of Enhancement Image

The performance of proposed grayscale and binary enhancement approaches have been quantitatively evaluated by examining an image's sensitivity. Sensitivity is often used to evaluate a clinical test [31]. For an enhanced binary image, sensitivity measures the proportion of positives or foregrounds (*i.e.* vein pixels) which are correctly identified against the entire region of the truth image. Each truth image is generated based on the grayscale image. In this case, background pixels are the false negatives. Sensitivity is calculated as follows

[31]:

$$\text{Sensitivity} = \frac{\text{True Positives}}{\text{True Positives} + \text{False Negatives}} \quad (11)$$

where true positive is the number of foreground pixels correctly classified as foreground and false negative is the number of foreground pixels incorrectly classified as background. Sensitivity has a range of [0, 1]. Higher sensitivity values signify good accuracy of classification.

Sensitivity is used to evaluate the two proposed work stages, grayscale enhancement (i.e. CLAHE with FHH) against four commonly used contrast enhancement methods: LCS, HE, and CLAHE and binary enhancement compared to the existing binarization methods; BMF, MNR and a combination of both.

I. RESULTS AND DISCUSSION

The performance of grayscale enhancement evaluates the ability of a method to provide high contrast between vein patterns and the background. Figure 5(b) to Figure 5(e) show the performance of the LCS, HE, CLAHE, and CLAHE with FHH over a low contrast hand vein image. Visually, it can be seen that the output image from CLAHE with FHH (Figure 5(e)) has the best enhancement throughout all vein regions as the contrast of vein texture and background is the largest. The

vein outlines are the clearest and continuous for the proposed method. By producing higher contrast fluctuation with minimum unwanted artifacts, the proposed method is capable of strong contrast enhancement around vein patterns present in the input image. Hence, it allows easier and more effective vein segmentation.

In order to verify effective segmentation from grayscale enhancement image, local threshold has been applied onto the images. As depicted in Figure 5(f) to Figure 5(i), it seems that vein patterns imaged by the proposed method (see Figure 5(i)) reveal clearest vein patterns. However, there is still much noise in these binarized images and thus, binary enhancement has been employed.

The performance of binary enhancement is analyzed both quantitatively and qualitatively, by comparing binarized image from the proposed method, ANN+BMF+MNR to BMF, MNR, BMF+MNR and MNR+BMF. The results are as shown in Figure 6. Based on visual perception, the proposed method produces the clearest vein patterns than other methods because it is able to reveal the vein patterns more accurately for most graylevel enhancement images.

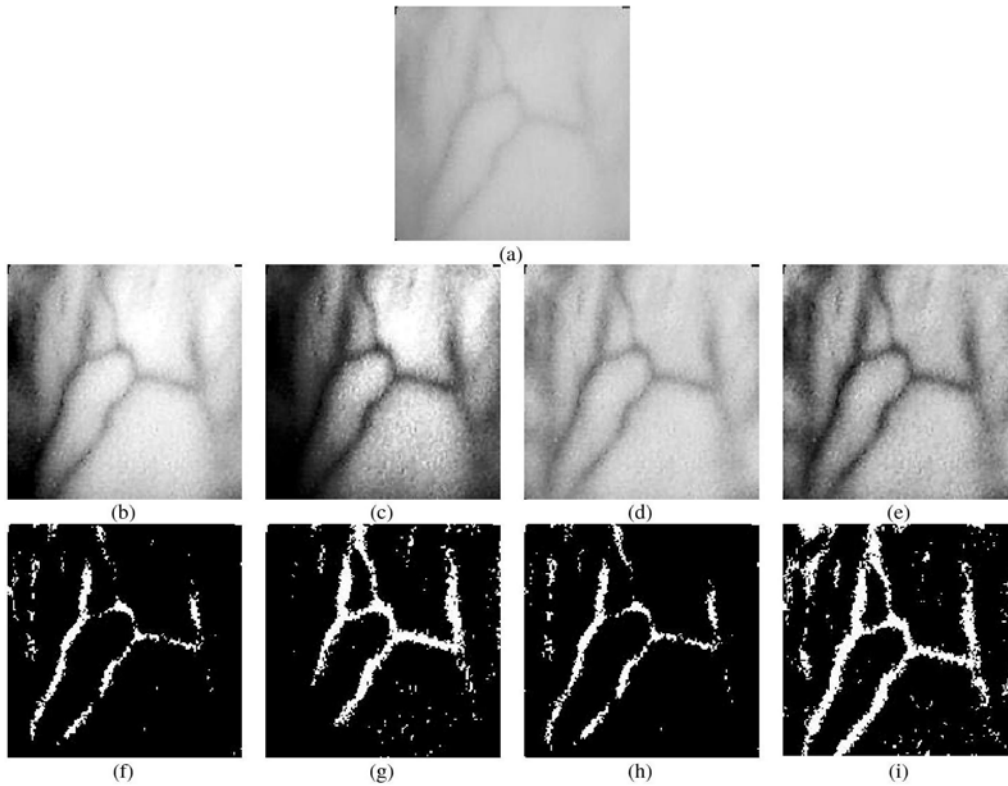


Fig. 5 Results of a grayscale image enhancement over (a) the original hand vein image using (b) LCS, (c) HE, (d) CLAHE and (e) proposed method, CLAHE with FHH. Binarized image using local threshold on the enhanced images of (f) LCS, (g) HE, (h) CLAHE and (i) proposed method, CLAHE with FHH

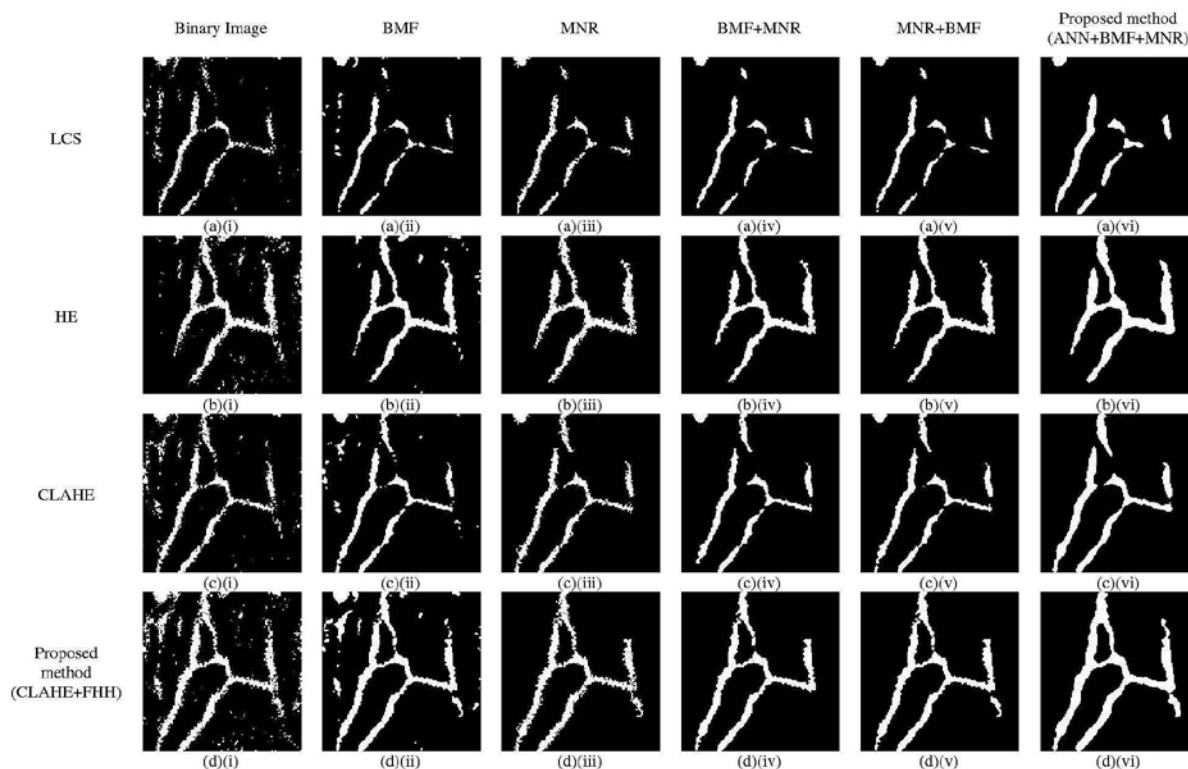


Fig. 6 Results of gray and binary image enhancement over (i) the original binary image on grayscale enhancement using (a) LCS, (b) HE, (c) CLAHE and (d) CLAHE +FHH and binary enhancement using (ii) BMF, (iii) MNR, (iv) BMF+MNR, (v) MNR+BMF and (vi) proposed method, ANN+BMF+MNR

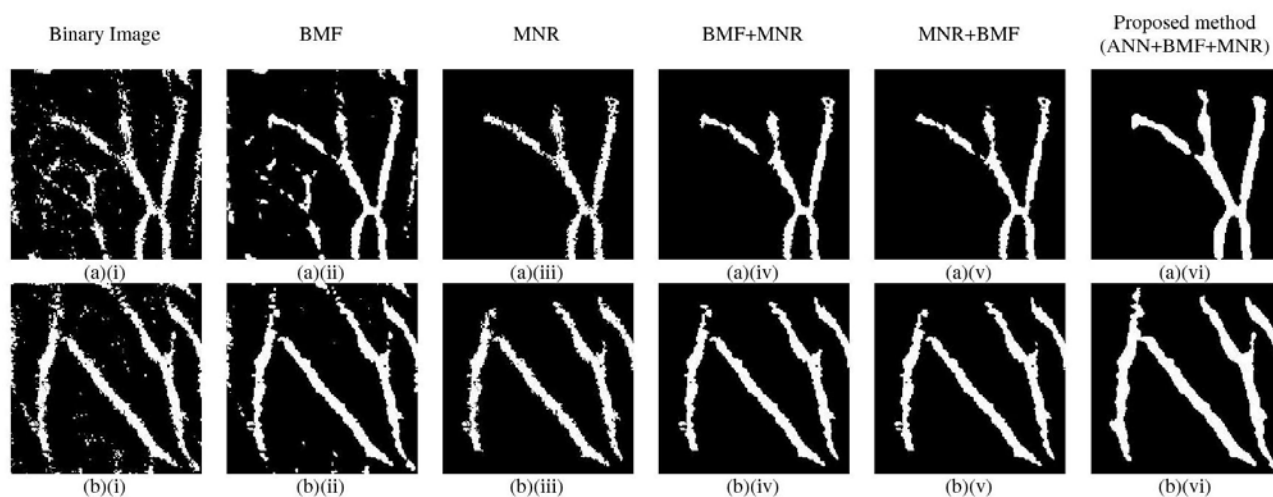


Fig. 7 Results of binary enhancement using (ii) BMF, (iii) MNR, (iv) BMF+MNR, (v) MNR+BMF and (vi) proposed method, ANN+BMF+MNR

The results of Figure 6 are also supported by the sensitivity values in Table 1. The sensitivity values for all binary enhancement methods show some increments after application of the proposed method compared to a binary image. Nevertheless, as can be seen, after applying the proposed three-level binary enhancement, CLAHE with FHH has the highest sensitivity value compared to the other enhancement methods. Figure 8 are additional result of CLAHE+FHH using different methods of binary enhancement.

TABLE 1. COMPARISON OF SENSITIVITY VALUE AMONG THE PROPOSED METHOD AND OTHER BINARY ENHANCEMENT METHODS

Binary	BMF	MNR	BMF+ MNR	MNR+ BMF	ANN+B MF+MNR
LCS	0.4647	0.4336	0.4233	0.4131	0.4171
HE	0.6762	0.6926	0.6553	0.6817	0.6824
CLAHE	0.6700	0.6723	0.6396	0.6484	0.6572
CLAHE+FHH	0.8485	0.8899	0.8427	0.8584	0.8844
					0.9627

Table 2 shows the average sensitivity value obtained from 10 test images. This table clearly shows that the proposed method is able to produce highest sensitivity for all tested images as compared to the other binary enhancement methods. As can be observed also, the proposed method has increased the sensitivity value of the original image up to 10.66%. These results complement the findings obtained graphically in Figure 6.

TABLE 2. COMPARISON OF SENSITIVITY VALUE AMONG THE PROPOSED METHOD AND OTHER BINARY ENHANCEMENT METHODS

Original Binary image	BMF	MNR	BMF+ MNR	MNR+ BMF	ANN+B MF+MNR
1	0.8485	0.8899	0.8427	0.8584	0.8844
2	0.7704	0.7973	0.7447	0.7761	0.7752
3	0.7422	0.7479	0.7002	0.7163	0.7151
4	0.7004	0.6990	0.6634	0.6737	0.6718
5	0.6730	0.6899	0.6263	0.6477	0.6492
6	0.7807	0.7988	0.7552	0.7751	0.7551
7	0.7715	0.7749	0.7152	0.7273	0.7239
8	0.7644	0.7781	0.7464	0.7650	0.7650
9	0.7317	0.7297	0.7593	0.7159	0.7798
10	0.6585	0.6566	0.6069	0.5745	0.6196
Average	0.7441	0.7562	0.7158	0.7230	0.7339
					0.8508

Table 3 shows the average standard deviation values obtained from 10 test images. This table shows that all binary enhancement methods are able to maintain the standard deviation values closer to the truth image. However, the proposed method produced the lowest average of standard deviation values. This means that the proposed method does not deviate far from the truth image.

TABLE 3. COMPARISON OF STANDARD DEVIATION VALUES AMONG THE PROPOSED METHOD AND OTHER BINARY ENHANCEMENT METHODS

	Truth image	BMF	MNR	BMF+ MNR	MNR+ BMF	ANN+BM F+MNR
1	0.3088	0.3440	0.3099	0.3060	0.3107	0.3480
2	0.2936	0.3262	0.2728	0.2733	0.2731	0.3099
3	0.3759	0.3586	0.3370	0.3371	0.3366	0.3735
4	0.2929	0.2818	0.2736	0.2712	0.2712	0.2913
5	0.3508	0.3793	0.3221	0.3227	0.3229	0.3624
6	0.3275	0.3561	0.3022	0.3034	0.3034	0.3384
7	0.3549	0.3603	0.3381	0.3301	0.3369	0.3620
8	0.2458	0.3000	0.2825	0.2817	0.2817	0.3197
9	0.2818	0.2905	0.2973	0.2757	0.2950	0.3101
10	0.4276	0.3927	0.3700	0.3587	0.3690	0.4128
Average						
Difference (%)		2.5200	2.652	2.7600	2.7470	2.0160

I. CONCLUSION

This paper presents a CLAHE with FHH method for grayscale vein image enhancement. It also presents a combination of three approaches; ANN pixel corrector, BMF and MNR, for binary image enhancement. The numerical results explicate that the proposed grayscale image enhancement and binary image enhancement methods are able to successfully increase the binary hand vein image contrast. The clearly exposed vein patterns, when projected back onto patient's hand is able to aid peripheral IV access.

ACKNOWLEDGEMENT

This work is funded by the Universiti Sains Malaysia Research University (RU) grant with number: 1001/PELECT/814092.

REFERENCES

- [1] M. Stovroff, and W. G. Teague, "Intravenous access in infants and children," *Pediatric Surgery for the Pharmacy Care Pediatrician*, vol. 45, pp. 1737-1793, 1998.
- [2] L. L. Kuenstin, S. DeBoer, R. Hollera, B. L. Shultz, R. A. Steinmann, and J. Venell, "Difficult venous access in children: taking control," *Journal of Emergency Nursing*, vol. 35, pp. 419-424, 2009.
- [3] D. Mbamalu, and A. Banerjee, "Method of obtaining peripheral venous access in difficult situations," *Postgrad. Med. J.*, vol. 75, pp. 459-462, 1999.
- [4] Medical Encyclopedia, available on: <http://www.nlm.nih.gov/medlineplus/ency/article/007245.htm>. Assessed 1 July 2009
- [5] J. Simon, F. Vojko, D. Matjaz, H. Andreas, and Z. Borut, "Towards a low-cost mobile subcutaneous vein detection solution using near-infrared spectroscopy," *The Scientific World Journal*, vol. 2014, pp. 1-15, 2014.
- [6] M. Wolf, M. Ferrari, and V. Quaresima, "Progress of near-infrared spectroscopy and topography for brain and muscle and clinical applications," *J. Biomed. Opt.*, vol. 12, pp. 062104, 2007.
- [7] M. A. Calfon, C. Vinegoni, V. Ntziachristo and F. A. Jaffer, "Intravascular near-infrared fluorescence molecular imaging of atherosclerosis: towards coronary arterial visualization of biologically high-risk plaques," *J. Biomed. Opt.*, vol. 15, pp. 011107, 2010.
- [8] P. C. Eng, and M. Khalil-Hani, "FPGA-based embedded hand vein biometric authentication system," in *Conf. IEEE Region 10*, 2009, pp. 1-5.
- [9] G. Hong-Seng, T. S. Tan, A. K. Ahmad Helmy, K. A. Sayuti, A. K. Rafiq, T. Weng-Kit, W. Liang-Xuan, K. T. Chaudhary, J. Ali and P. P. Yupapin, "Medical image visual appearance improvement using bihistogram bezier curve contrast enhancement: data from the osteoarthritis initiative," *The Scientific World Journal*, vol. 2014, pp. 1-13, 2014.
- [10] A. Kumar, and K. V. Prathyusha, "Personal authentication using hand vein triangulation and knuckle shape," *IEEE Trans. Image Process.*, vol. 18, pp. 2127-2136, 2009.
- [11] E. D. Pisano, S. Zong, B. M. Hemminger, M. DeLuca, R. E. Johnston, K. Muller, M. Braeuning, and S. M. Pizer, "contrast limited adaptive histogram equalization image processing to improve the detection of simulated speculations in dense mammograms," *Journal of Digital Imaging*, vol. 11, pp. 193-100, 1998.
- [12] S. M. Pizer, R. E. Johnston, J. P. Ericksen, B. C. Yankaskas, and K. E. Muller, "Contrast limited adaptive histogram equalization: speed and effectiveness," in *Proc. of the First Conference on Visualization in Biomedical Computing*, 1990, pp. 337-345.
- [13] A. Papadopoulos, D. I. Fotiadis, and L. Costaridou, "Improvement of microcalcification cluster detection in mammography utilizing image enhancement techniques," *Comput. Biol. Med.*, vol. 38, pp. 1045-1055, 2008.
- [14] H. D. Zeman, G. Lovhoiden, C. Vrancken, and R. K. Danish, "Prototype vein contrast enhancer," *Opt. Eng.*, vol. 44, pp. 086401, 2005.
- [15] T. Tanaka and N. Kubo, "Biometric authentication by hand vein patterns," in *SICE Annual Conference*, 2004, pp. 249-253.
- [16] J. Zhao, H. Tian, W. Xu and X. Li, "A new approach to hand vein image enhancement," in *Second International Conference on Intelligent Computation Technology and Automation*, 2009, pp. 499-501.
- [17] M. Shahin, A. Badawi, and M. Kamel, "Biometric authentication using fast correlation of near infrared hand vein patterns," *International Journal of Biological and Medical Sciences*, vol. 2, pp. 141-148, 2007.
- [18] Y. Ding, D. Zhuang and K. Wang, "A study of hand vein recognition method," in *Proceedings of the IEEE International Conference on Mechatronics & Automation*, 2005, pp. 2106-2110.
- [19] A. E. Hassanien, J. M. H. Ali, and H. Nobuhara, "Detection of spiculated masses in mammograms based on fuzzy image processing," in *Proceedings of the Artificial Intelligence and Soft Computing*, 2004, pp. 1002-1007.
- [20] A. Hassanien, and A. Bader, "A comparative study on digital mammography: Enhancement algorithms based on Fuzzy Theory", *International Journal of Studies in Informatics and Control*, vol. 2, pp. 21-31, 2003.
- [21] X. Yan, Y. Song, and X. Wei, "Parallel sub-neural network system for hand vein pattern recognition," *Chinese Optics Letters*, vol. 9, pp. 051002, 2011.
- [22] Z. Zhang, S. Ma, and X. Han, "Multiscale feature extraction of finger-vein patterns based on curvelets and local interconnection structure neural network," *The 18th International Conference on Pattern Recognition*, 2006, pp. 145-148.
- [23] M. Yakno, J. Mohamad-Saleh, and B. A. Rosdi, "Impulse noise detector for vein images based on feed-forward neural network," *Opt. Eng.*, vol. 50, pp. 093202, 2011.
- [24] C. L. Lin, and K. C. Fan, "Biometric verification using thermal images of palm-dorsa vein patterns," *IEEE Transactions on Circuits and Systems for Video Technology*, vol. 14, pp. 199-213, 2004.
- [25] E. D. Pisano, E. B. Cole, B. M. Hemminger, M. J. Yaffe, S. R. Aylward, A. D. A. Maidment, R. E. Johnston, W. B. Williams, L. T. Niklason, E. F. Conant, L. L. Fajardo, D. B. Kopans, M. E. Brown, and S. M. Pizer, "Image processing algorithms for digital mammography: a pictorial essay," *Radiographics*, vol. 20, pp. 1479-1491, 2000.
- [26] H. R. Tizhoosh and M. Fochem, "Image enhancement with fuzzy histogram hyperbolization," *Proceeding of EUFIT*, 3, 1995, pp. 1695-1698.
- [27] H. R. Tizhoosh, G. Krel and B. Muchaelis, "Locally adaptive fuzzy image enhancement," *Proceedings of the International Conference on Computational Intelligence, Theory and Applications*, 1997, pp. 272-276.
- [28] R. C. Gonzalez, and R. E. Woods, *Digital Image Processing*, Prentice Hall, Upper Saddle River, NJ, USA, 2010.
- [29] A. Yuksel, L. Akarun and B. Sankur, "Biometric identification through hand vein patterns," *International Workshop in Emerging Techniques and Challenges for Hand-Based Biometrics (ETCHB)*, 2010, pp. 1-6.
- [30] R. Fisher, S. Perkins, A. Walker and E. Wolfart. (2003) Adaptive Thresholding. [Online]. Available: <http://homepages.inf.ed.ac.uk/rbf/HIPR2/adpthrsh.htm>
- [31] A. G. Lalkhen and A. McCluskey, "Clinical tests: sensitivity and specificity," *British Journal Anaesthesia*, vol. 8, pp. 221-223, 2008.

Marlina Yakno received her BEng in Electrical and Electronic Engineering from the Universiti Tenaga Nasional, Malaysia in 2007 and MSc from the Universiti Sains Malaysia in 2013. She is currently a lecturer in the Faculty of Electrical and Electronic Engineering, Universiti Malaysia Pahang. Her research interests include image processing and computational intelligence.

Junita Mohamad-Saleh received her BSc in Computer Engineering from the Case Western Reserve University, Ohio, USA in 1994, MSc from the University of Sheffield, UK, in 1996, and PhD from the University of Leeds, UK, in 2002. She is currently an associate professor in the School of Electrical and Electronic Engineering, Universiti Sains Malaysia. Her research interests include computational intelligence, tomographic imaging, and soft computing.

Bakhtiar Affendi Rosdi received his BEng, MEng, and DEng in Electrical and Electronic Engineering from Tokyo Institute of Technology, Tokyo, Japan in 1999, 2004, and 2007, respectively. He is currently a senior lecturer in the School of Electrical and Electronic Engineering, Universiti Sains Malaysia. His research interests are LSI implementation of pattern recognition and image processing algorithms.

Photocatalytic oxidation and morphology control of TiO₂ film

Jinshu Wang , Bingxin Zhao, Hongyi Li

Abstract—TiO₂ films were in-situ synthesized on Al substrate by Liquid Phase Deposition (LPD) with Anodic Aluminum Oxide (AAO). It was found that the growth of TiO₂ nanotubes and nanorods could be controlled by the electrolytes using during the preparation of AAO templates. The morphology control mechanism was discussed. The effects of experimental conditions such as solution composition, deposition temperature were investigated. The results showed that the deposition temperature in the range of 30-40°C was favorable for the formation of TiO₂ nanoarrays. TiO₂ nanotube film exhibited a certain photocatalytic oxidation performance which could be improved by SiO₂ modification.

Keywords—Anodization, Liquid Phase Deposition, Anodic Aluminum Oxide, Photocatalytic oxidation.

I. INTRODUCTION

PHOTOELECTROCHEMICAL processes at semiconductor colloid-electrolyte interfaces have been received special attention because of their possible applications in the conversion of solar energy into chemical energy and pollution control[1-6]. Photocatalytic reaction systems have been commercially supplied to conduct self-cleaning, deodorant, anti-bacteria, etc., and are expected to be applied to the pollution control to decompose toxic materials in air and waste water using sun light and indoor light. Among all the photocatalysts, only TiO₂ has been commercially used because of the excellent photocatalytic activity and chemical stability. In view points of its utility in such a field, compared with TiO₂ powder, processing TiO₂ as thin films or coatings with high crystallinity, high specific surface area is favorable for easy separation, recovery and high recycle rate. Crystalline TiO₂ has many morphologies such as nanofibers, nanoparticles, nanorods, nanospheres, nanotubes and nanowires[7-9]. TiO₂ nanotubes are highly efficient in photocatalysis since they have a relatively higher interfacial charge transfer rate and surface area compared with spherical TiO₂ particles[10].

Many approaches have been developed for the preparation of TiO₂ nanotubes, i.e., chemical vapor deposition (CVD), anodic oxidation, seeded growth, the wet chemical

(hydrothermal method, the sol-gel method)[11, 12] and liquid phase deposition (LPD) of templates. Among all these approaches, LPD of template method is one of the simplest and most practical one to fabricate TiO₂ nanotubes, since it has so many advantages such as low cost, mild reaction condition, simple equipment requirement and allows TiO₂ films to be deposited over large areas. Anodic aluminum oxide is one of the commonly used templates due to its unique structure, such as controllable pore diameter, extremely narrow pore size distribution, and ideally cylindrical pore shape[13]. TiO₂ nanohole arrays by LPD method using anodic alumina disk have been reported[14-16]. However, the diameter of AAO templates prepared with different electrolytes and the corresponding morphology of TiO₂ nanoarrays have seldom been systematically studied. It was found that the morphology of particles affected the electric properties and photoreactivity of the materials [17,18]. In this work, we studied the morphology control of TiO₂ nanoarrays prepared with different AAO templates and discussed morphology change mechanism of TiO₂ nanotube. Dyes are important industrial pollutants and methylene blue is famous for its good stability as dye materials. The degradation of methylene blue aqueous solution is usually used to evaluate the performances of photocatalysts under UV and visible light irradiation[19-21]. Therefore, the photodegradation of methylene blue by the TiO₂ nanotube films have been studied.

II. EXPERIMENTAL

A. Preparation of AAO template

The aluminum sheets were cut into samples with size of 30 × 30 × 0.1 mm, and the organic impurity and oxides on the surface of samples were removed by ultrasonically washing in de-ionized water, ethanol, acetone, respectively. Then the washed samples were annealed in vacuum at 400 °C for 2 h. The oriented AAO templates were synthesized via a two-step anodic oxidation approach. The aluminum plates were firstly anodized in aqueous solution of oxalic acid, sulfuric acid and phosphoric acid or mixed electrolytes with outer voltage of 100 V at 10 °C for 4 h, respectively. Then the anodized samples were immersed into 1.8 vol. % H₂CrO₄:6 vol. % H₃PO₄ aqueous solution to remove anodized oxide film on the aluminum surface. The final AAO template was secondly anodized at the same condition as the first step.

B. The preparation of TiO₂ nanotube

The AAO template was immersed into 0.5 M (NH₄)₂TiF₆ at 20 °C for 10 min. With the aqueous flowing along the wall of the

This work was supported by the National Natural Science Foundation of China(no. 51225402, 51471006) and Beijing Natural Science Foundation(2151001)”,Guangxi Natural Science Foundation (no.2014GXNSFBA118039)

Jinshu Wang is with School of Materials Science & Engineering, Beijing University of Technology, China (phone & fax:86-10-67391101; e-mail:wangjsh@bjut.edu.cn). A

AAO template, TiO₂ nanoarrays could be in-situ formed in the inner side of AAO template. The deposited TiO₂ arrayed film was calcined in air at 400 °C for 4h.

C. Photocatalytic activity

The photocatalytic activities of the samples were measured by the degradation of methylene blue. The samples immersed in 100 mg/L methylene blue solution for 24 h in the dark. Saturation of methylene blue adsorption was confirmed to be reached after 24 h from the fact that no change in the reflectance of the film occurred between the solutions kept for 24 and 25 h in the dark. Then the samples were removed from the solution with the methylene blue on the surface. Under the Hg lamp irradiation (CMH-250, 10 mW/cm²), the degradation of methylene blue on samples' surface was began. Methylene blue decomposition was estimated by the degradation fraction (Eq.1), where the wavelength of 580 nm was monitored by UV-Vis spectrometer (UV2550).

$$\eta = \frac{REF_t - REF_{initial}}{REF_0 - REF_{initial}} \quad (1)$$

REF_{initial}: the reflectivity of the samples with adsorption of methylene blue without light irradiation;

REF_t: the reflectivity of the samples with adsorption of methylene blue under light irradiation for various time;

REF₀: the reflectivity of the samples without adsorption of methylene blue.

III. RESULTS AND DISCUSSION

A. Morphology of AAO templates

AAO templates were prepared by anodic oxidation method using different electrolytes. **Figure 1** shows the morphology of AAO templates prepared with oxalic acid, sulfuric acid and phosphoric acid or mixed electrolytes. All the AAO templates have hexagonal shape which was caused by high electric field squeezing[22]. The outside diameters of AAO obtained in different electrolytes were in the order: AAO prepared with phosphoric acid > That with mixed electrolytes of oxalic acid and phosphoric acid > That with oxalic acid > That with mixed

electrolytes of sulfuric acid and phosphoric acid ≈ That with sulfuric acid. The AAO prepared with phosphoric acid had the largest pore size, i.e., the mean outside diameter of the tubule and inside diameter were about 250 nm and 150 nm, respectively, as shown in **Figure 1(a)**. On the other hand, the AAO prepared with sulfuric acid has the smallest pore size(**Figure 1(d)**). The mean outside diameter and inside diameter of that prepared with oxalic acid are about 50 nm and 20 nm, respectively. The mean diameter of the AAO templates prepared with mixed electrolytes of oxalic acid and phosphoric acid was in the middle place with the outside diameter of 200 nm and inside diameter of 100 nm, as shown in **Figure 1(c)**. **Figure 1** also showed that although the AAO templates prepared with mixed electrolytes of oxalic acid and sulfuric acid had smaller pore size, the pores existed orderly and uniformly. On the other hand, the large pores had been obtained in the phosphoric acid, but the pores had different diameters. The results showed that the pore size was correlated with the kind of electrolyte. Sulfuric acid had good dissolving capability, therefore, under the lower voltage, Al which located at underneath layer dissolved first and the initial cavity could be formed in the oxide film. Phosphoric acid had a weak oxidizing ability, therefore, Al could only be dissolved under higher voltage. It was reported that the highest anodizing voltage applied in the electrolyte was in the order of phosphoric acid > oxalic acid [23]. It was deduced that the highest anodizing voltage applied in the electrolyte of phosphoric acid was the largest among those applied in all five electrolytes. The pore size formed in the templates was related to the anodizing voltage applied in the electrolyte. To obtain the templates with large pores, high anodizing voltage should be applied in the electrolyte. Therefore, AAO templates prepared with phosphoric acid had the largest pore size.

B. Morphology of TiO₂ nanoarray

By immersing the AAO templates obtained with different electrolytes into (NH₄)₂TiF₆ solution, TiO₂ nanoarray films were prepared and the morphologies were shown in **Figure 2**. As shown in **Figure 2(a)**, TiO₂ prepared with AAO template using oxalic acid exhibited as the nanorods with the mean

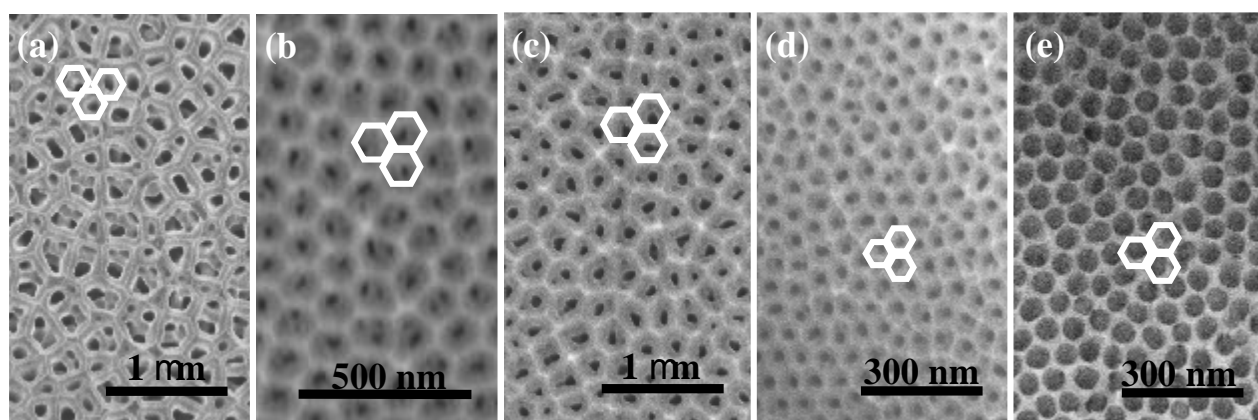
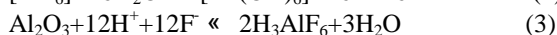
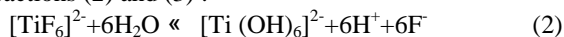


Fig. 1. SEM images of the AAO template anodized with different electrolytes. (a) H₃PO₄, (b) H₂C₂O₄, (c) Mixed electrolytes of H₂C₂O₄ and H₃PO₄, (d) H₂SO₄ and (e) Mixed electrolytes of H₂SO₄ and H₃PO₄

diameter about 100 nm. The uniform and well aligned TiO_2 nanorods were perpendicular to Al substrates. Furthermore, this structure was similar to that of anodic alumina as comparing **Figure 2 (a)** to **Figure 1(b)**. The pore diameter of AAO template was also about 100nm, indicating that hydrous TiO_2 deposited in-situ on anodic alumina template and filled in the tubule. However, TiO_2 prepared with the AAO templates using sulfuric acid which had small tubule was covered by a thick deposited substance on the surface after LPD

process. After ultrasonic treatment, it was clear to see in **Figure 2 (c)** that TiO_2 existed as nanorods with the diameter of 50 nm, whereas using the AAO templates obtained with phosphoric acid, mixed electrolytes of phosphoric acid and oxalic acid, or mixed electrolytes of phosphoric acid and sulfuric acid, all TiO_2 existed as nanotubes, but the nanotube diameter varied with the electrolyte, which were summarized in **Table 1**. TiO_2 prepared with AAO obtained with phosphoric acid had the largest diameter with the outside diameter of 200 nm and inside diameter of 180 nm, as displayed in **Figure 2(d)**, since the pore size of AAO templates obtained with phosphoric acid was the largest among all the electrolytes. By comparing the morphology of TiO_2 nanotube obtained with different electrolytes, TiO_2 nanotubes prepared with the mixed electrolytes of sulfuric acid and phosphoric acid had ordered and uniform structure with the smaller outside diameter of 50 nm and was nearly free of scratches on the surface, as shown in **Figure 2(e)**. From **Figure 2**, it was evident that the formation of TiO_2 nanorod or nanotube was correlated with the pore size of the AAO templates.

The formation mechanism of nanotube and nanorod would be discussed based on the formation of hydrous TiO_2 as illustrated in reactions (2) and (3).



The above chemical reactions indicated that the production of 2 mol TiO_2 needed to consume 1 mol Al_2O_3 . TiO_2 prepared after LPD existed as hydrous titania and would transform into anatase phase after heat treatment. Al_2O_3 in anodic alumina template had the phase of $\gamma\text{-Al}_2\text{O}_3$ ^[24]. It could be calculated that 1 mol Al_2O_3 with the volume of 29.14 cm^3 would be consumed

for the formation of 2 mol TiO_2 with the volume of 41.67 cm^3 based on the density of $\gamma\text{-Al}_2\text{O}_3$ (3.5 g/cm^3) [24] and anatase (3.84 g/cm^3) [25]. So the volume ratio of $V_{\text{Al}_2\text{O}_3} / V_{\text{TiO}_2}$ was 0.71, indicating that TiO_2 produced by the in-situ synthesis would cover all the template surface when the ratio of volume of Al_2O_3 to the total volume of the template ($V_{\text{Al}_2\text{O}_3}$ and V_{pores}) was equal to 0.71.

Figure 3 shows the Schematic diagram of different AAO templates. We supposed that the template cell was composed of hexagon outside and circle inside. The shadowed part was anodic alumina. According to the hexagon area and circle area shown in **Figure 3**, the volume ratios of Al_2O_3 in different templates were calculated and summarized in **Table 1**.

As shown in **Figure 3** and **Table 1**, the volume ratios of Al_2O_3 in the AAO templates prepared with oxalic acid and sulfuric acid were larger than 0.71, therefore, TiO_2 existed as nanorod and the excess amount of TiO_2 was dissolved into the solution or existed on the container wall since the volume of TiO_2 exceeded the total volume of the templates. Especially for TiO_2 prepared with AAO templates using sulfuric acid, we found a titanium oxide layer on the film surface which might be caused by the deposition of the excess TiO_2 , but this deposited layer could be easily removed by ultrasonic treatment. On the other hand, the volume ratio of Al_2O_3 in the AAO templates prepared with phosphoric acid and mixed electrolytes were smaller than 0.71, therefore, TiO_2 existed as nanotubes since TiO_2 would not cover all the AAO templates.

C. The effect of deposition temperature on the morphology of TiO_2 film

When AAO templates were immersed in $(\text{NH}_4)_2\text{TiF}_6$, the reaction would take place and the reaction velocity was affected by the temperature. **Figure 4** displays the morphology of TiO_2 prepared with the AAO templates obtained with phosphoric acid but deposited at different temperatures with the same deposition time of 20 min. As described above, TiO_2 grew in-situ with the depletion of alumina. When the temperature was low, the reaction rate was low, therefore, alumina was left, which is shown in **Figure 4(a)**. When the temperature was increased to 35 °C, it was hard to find the remained alumina and only TiO_2 nanotube was observed, as shown in **Figure 4(b)**.

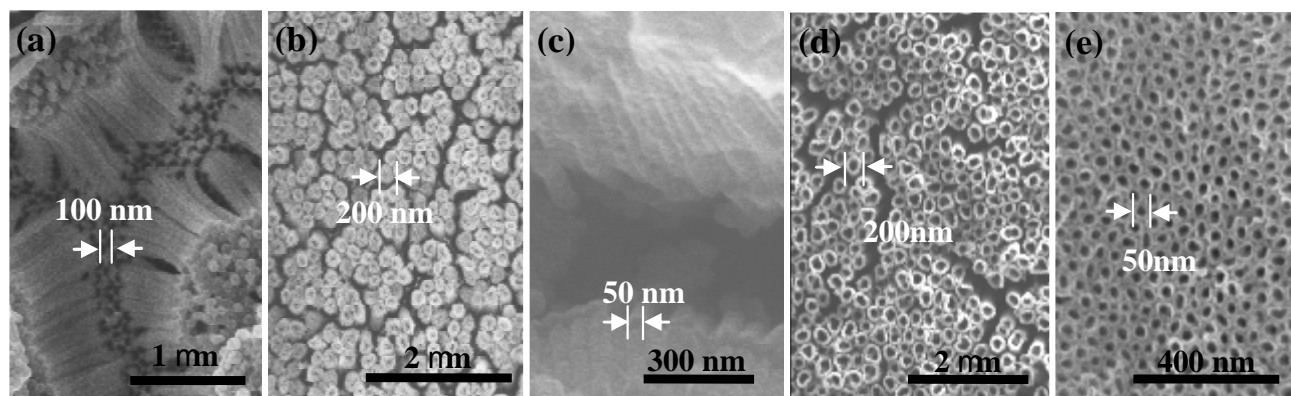


Fig. 2. SEM images of the AAO template anodized with different electrolytes. (a) $\text{H}_2\text{C}_2\text{O}_4$, (b) Mixed electrolytes of $\text{H}_2\text{C}_2\text{O}_4$ and H_3PO_4 , (c) H_2SO_4 , (d) H_3PO_4 and (e) Mixed electrolytes of H_2SO_4 and H_3PO_4 .

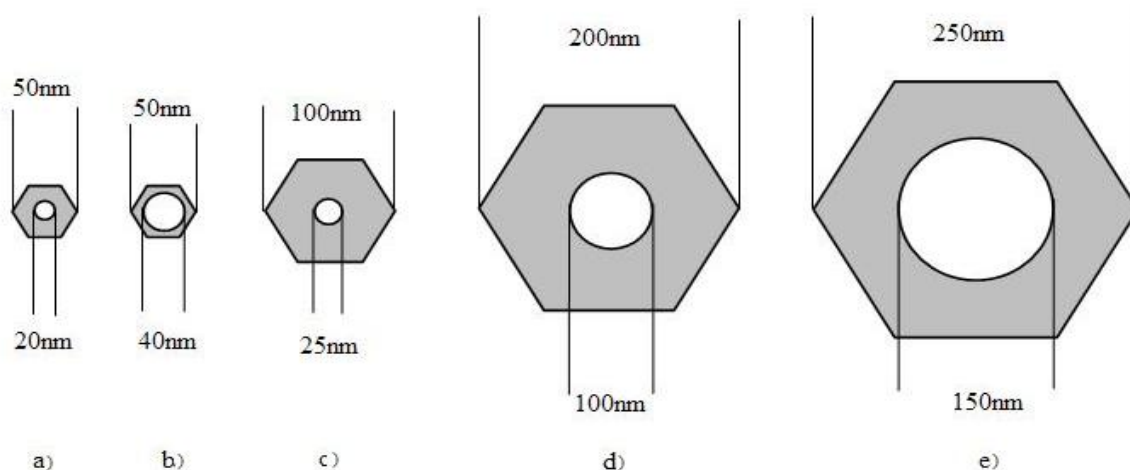


Fig. 3. Schematic diagram of AAO templates prepared with different electrolytes. (a) H_2SO_4 , (b) Mixed electrolytes of H_2SO_4 and H_3PO_4 , (c) $\text{H}_2\text{C}_2\text{O}_4$, (d) Mixed electrolytes of $\text{H}_2\text{C}_2\text{O}_4$ and H_3PO_4 and (e) H_3PO_4 .

Table 1 Volume ratio of alumina in different AAO membranes

Electrolyte	H_2SO_4	$\text{H}_2\text{SO}_4, \text{H}_3\text{PO}_4$	$\text{H}_2\text{C}_2\text{O}_4$	$\text{H}_2\text{C}_2\text{O}_4, \text{H}_3\text{PO}_4$	H_3PO_4
Area of hexagon (nm^2)	1623.8	1623.8	6495.19	25980.76	40594.94
Area of circle (nm^2)	314	1256	490.63	7850	17662.5
Volume ratio	0.81	0.23	0.92	0.70	0.56
Morphology of TiO_2	Nanorod	Nanotube	Nanorod	Nanotube	Nanotube

Increasing the temperature to 40 °C and 45 °C, as shown in **Figure 4(c)** and **(d)**, the fast reaction rate led to the production of an excess amount of titanium compound which covered on the surface of TiO_2 nanotube. The higher the temperature, the larger the amount of titanium compound. But the covered compound could be removed from the surface after ultrasonic treatment.

C. Photocatalytic oxidation property of TiO_2 nanotube and modified TiO_2 nanotube with SiO_2

It is found that $\text{SiO}_2/\text{TiO}_2$ composite had a higher photocatalytic activity than pure TiO_2 [26-29]. Therefore, in this work, SiO_2 - TiO_2 nanotubes with different silica contents were prepared. The AAO templates were immersed into mixed $(\text{NH}_4)_2\text{SiF}_6$ and $(\text{NH}_4)_2\text{TiF}_6$ solution with different atomic ratios of Si/Ti at 40 °C for 30 min. During the liquid phase deposition, apart from the chemical reaction described in equations (2) and (3), the following reaction also might take place.

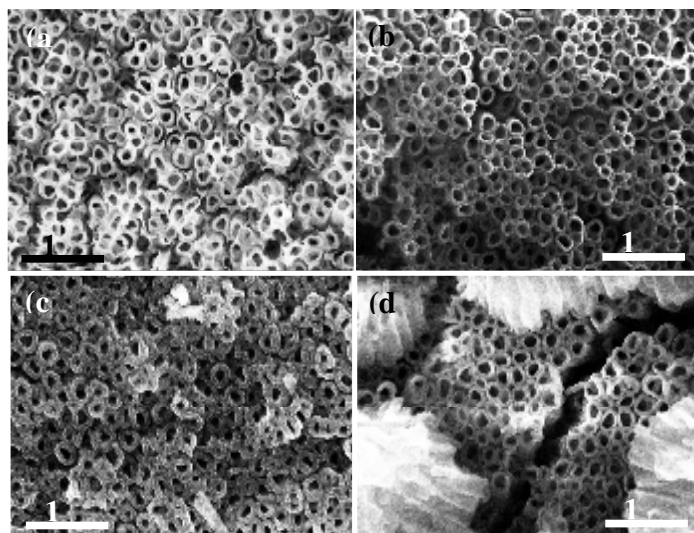
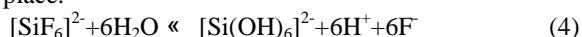


Fig. 4. SEM images of TiO_2 nanotubes prepared at different LPD temperature. (a) 30 °C, (b) 35 °C, (c) 40 °C, (d) 45 °C.

Al_2O_3 was taken as scavenger for F^- . The equilibrium reaction (4) was shifted to the right side by the reaction of Al_2O_3 , H^+ and F^- , since Al_2O_3 reacted readily with F^- and H^+ ions to form water soluble H_3AlF_6 , as described by equation (3). The product hydrous silica and titania deposited in-situ on AAO template. After heat treatment, SiO_2 modified TiO_2 could be formed.

Figure 5 shows the morphology of SiO_2 modified TiO_2 prepared with different atomic ratios of Si/Ti. The nanotube wall thickness increased with the atomic ratio of Si/Ti. When the atomic ratio of Si/Ti exceeded 0.5, SiO_2 were modified by TiO_2 . However, SiO_2 might be eroded by the F^- ions which were produced by chemical reactions (2) and (4) to form SiF_4 . We found that the number of nanotube decreased with the increase of amount of $(\text{NH}_4)_2\text{SiF}_6$, and almost no SiO_2 nanotubes were formed when pure $(\text{NH}_4)_2\text{SiF}_6$ solution was used. Therefore, during the preparation, the atomic ratio of Si/Ti and the deposition time are two crucial factors for the preparation of SiO_2 - TiO_2 composite nanotubes.

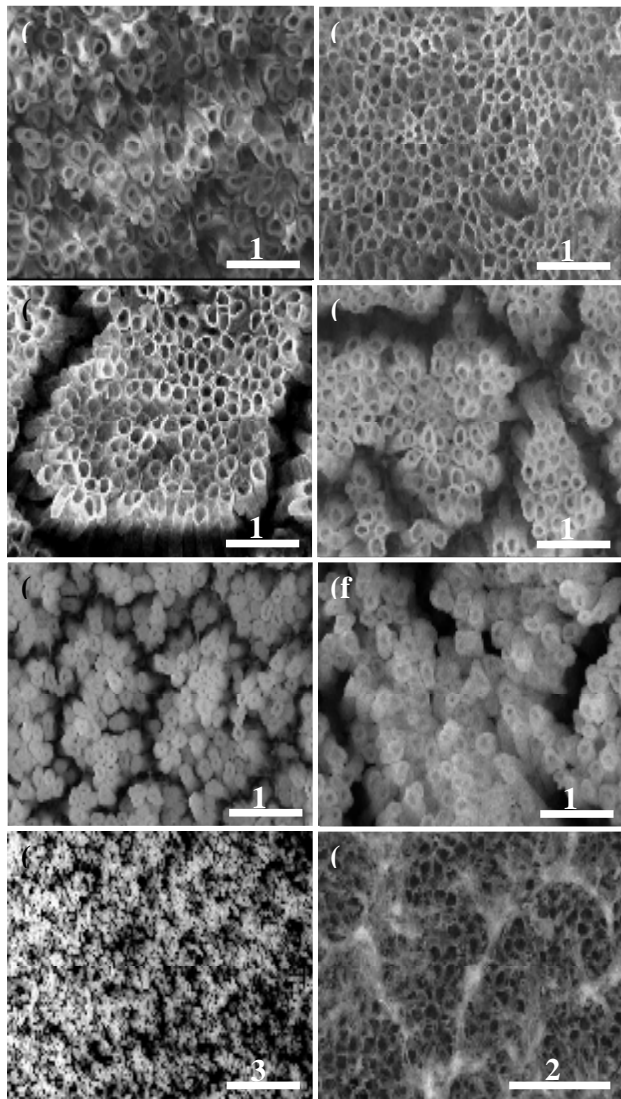


Fig.5. SEM photos of SiO_2 modified TiO_2 prepared with different atomic ratio of Si/Ti. (a) 0.1, (b) 0.2, (c) 0.3, (d) 0.4, (e) 0.5, (f) 0.6, (g) 0.95, (h) 1.0.

The photocatalytic activities of TiO_2 nanotube and TiO_2 - SiO_2 composite nanotube with different Si/Ti atomic ratios had been measured, which is shown in **Figure 6**. As expected, the concentration of SiO_2 in TiO_2 affected the photocatalytic activity of the catalysts. It was found that the sample prepared with 50% SiO_2 exhibited the highest photocatalytic

performance. The photocatalytic activities of the obtained catalysts were in the order of SiO_2 50%- TiO_2 > SiO_2 40%- TiO_2 > SiO_2 10%- TiO_2 ≈ TiO_2 after being irradiated for 4 h. The highest percentage of degradation was about 82% for TiO_2 - SiO_2 composite nanotubes, about 1.3 times higher than pure TiO_2 nanotubes.

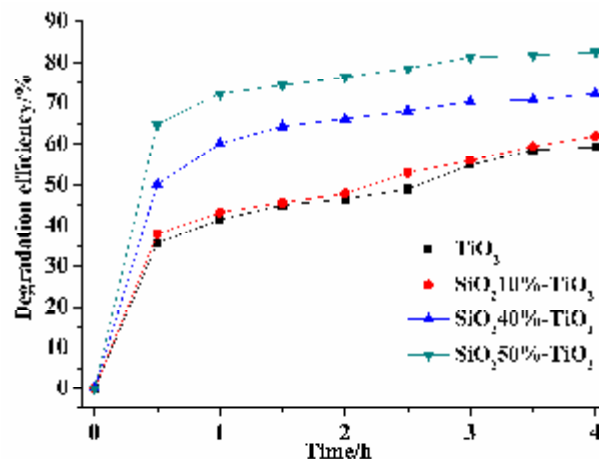


Fig.6. The photocatalytic activities of the obtained TiO_2 - SiO_2 composite photocatalysts after being UV light irradiated for 4 h.

IV CONCLUSION

- (1) The pore diameter of AAO template could be controlled by electrolytes. The outside diameters of AAO obtained in different electrolytes were in the order: AAO prepared with phosphoric acid > That with mixed electrolytes of oxalic acid and phosphoric acid > That with oxalic acid > That with mixed electrolytes of sulfuric and phosphoric acid ≈ That with sulfuric acid.
- (2) TiO_2 nanoarray films were prepared in-situ using anodic alumina template by LPD method. The formation of TiO_2 nanotube or nanorod was depended on the volume fraction of Al_2O_3 to AAO template. TiO_2 nanotubes would be formed when the fraction was smaller than 0.71. Otherwise, TiO_2 would exist as nanorods.
- (3) TiO_2 nanotube arrayed film exhibited a certain photocatalytic activity. The photocatalytic oxidation capability of TiO_2 could be improved by modification of SiO_2 under UV light irradiation.

REFERENCES

- [1] A. Fujishima and K. Honda, *nature*, 238, 37 (1972).
- [2] J.S.Wang, H. Li, H.Y. Li, C.Zhou, H. Wng, *ACS Appl. Mater. Interfaces* 6, 1623–1631(2014)
- [3] N.M. Mahmoodi and M. Arami, *J. Photochem. Photobiol. B*, 94, 20 (2009).
- [4] J. S. Wang, H. Li, H. Y. Li, and H.Wang, *J. Phys. Chem. C*, 116, 9517(2012).
- [5] M. N. Ghazzala, H. Kebailib, M. Josepha, D. P. Debeckera, P. Eloya, J. D. Coninckb, and E. M. Gaigneauxa, *Applied Catalysis B: Environ.* 115– 116, 276 (2012).
- [6] J. S. Wang, H. Li, H. Y. Li, S. Yin, and T. Sato, *Solid State Sci.* 11, 988 (2009).
- [7] L. L. Costa and A.G. S. Prado, *J. Photochem. Photobiol. A* 201, 45 (2009).
- [8] M. H. Seo, M. Yuasa, T. Kida, J. S. Huh, K. Shimanoe and N. Yamazoe, *Sens. Actuators, B*, 137, 513 (2009).
- [9] F. M. Wang, Z. S. Shi, F. Gong, J. T. Jiu and M. Adachi, *Chin. J. Chem. Eng.* 15, 754 (2007).

- [10] C. Colmenares, R. Luque, J. M. Campelo, F. Colmenares, Z. Karpiński and A. A. Romero, *Mater.* 2, 2228 (2009).
- [11] Y. P. Guo, N. H. Lee, H. J. Oh, C. R. Yoon, K. S. Park, W. H. Lee, Y. Z. Li, H. G. Lee, K. S. Lee and S. J. Kim, *Thin Solid Films*. 516, 8363 (2008).
- [12] D. L. Morgan, H. Y. Zhu, R. L. Frost and E. R. Waclawik, *Chem. Mater.* 20, 3800 (2008).
- [13] F. Wang, H. B. Huang, and S. G. Yang, *J. Eur. Ceram. Soc.* 29, 1387 (2009).
- [14] S. Yamanaka, T. Hamaguchi, H. Muta, K. Kurosaki, and M. Uno, *J. Alloys Compd.* 373, 312 (2004).
- [15] T. Hamaguchi, M. Uno, and S. Yamanaka, *J. Alloys Compd.* 386, 265 (2005).
- [16] J. S. Wang, Z. Z. Wang, H. Li, and Y. T. Cui, *J. Alloys Compd.* 494, 372 (2010).
- [17] J. Wang, S. Yin, and T. Sato, *J. Photoch. Photobio. A*. 187, 72 (2007).
- [18] A. Yourdkhani and G. Caruntu, *J. Mater. Chem.* 21, 7145 (2011).
- [19] Z. H. Ai, Y. Cheng, L. Z. Zhang, and J. R. Qiu, *Environ. Sci. Technol.* 42, 6955 (2008).
- [20] L. Wang, X. L. Wu, W. H. Xu, X. J. Huang, J. H. Liu, and A. W. Xu, *ACS Appl. Mater. Interfaces*. 4, 2686 (2012).
- [21] P. Kampalanonwat, and P. Supaphol, *ACS Appl. Mater. Interfaces*. 2, 3619(2010).
- [22] S. Ono, M. Satio, and H. Asho, *Electrochimica Acta*. 51, 827 (2005).
- [23] M. Lu, D. Qin, and H. Li, *J. Lanzhou Univ.* 4, 47 (2002).
- [24] Z. F. Zhu, Editor, *Anodic oxidation of aluminium alloy and surface treatment technology*, Chemical industry press, Beijing (2004).
- [25] L. Gao, S. Zheng, Q. Zhang, *TiO₂ nanophotocatalyst and its application*, Chemical industry press, Beijing, 2002, 26.
- [26] Carl Anderson, Allen J. Bard, *J. Phys. Chem.*, 99 (24), 9882(1995)
- [27] M. Bellardita, M. Addamo, A. Di Paola, G. Marci, L. Palmisano, L. Cassar, M. Borsa, *J. Hazard. Mater.*, 174(1–3), 707(2010)
- [28] Z. Z. Wang, J. S. Wang, H. Y. Li, G. S. Sun, and K. L. Huang, *Res. Chem. Intermediat.* 37, 541 (2011).
- [29] S. Z. Hu, F. Y. Li, Z. P. Fan, *Bull. Korean Chem. Soc.*, 33 (6), 985(2012)

Jinshu Wang Ph. D, Professor and Dean of the School of Materials Science and Engineering, Beijing University of Technology. She obtained her Bachelor majoring in Physical Chemistry of Metallurgy and Master degree majoring in Inorganic Nonmetallic Materials from University of Science & Technology, Beijing, respectively in 1990 and 1993. She received her Ph. D degree majoring in Materials Science from Beijing University of Technology in 1999. From 2002 to 2004, she has been worked in Tohoku University, Japan, as a post-doctor. Her current research mainly covered rare earth doped W/Mo electronic emission materials, nano-semiconductor materials and applied electrochemistry. She received China Youth Science and Technology Award and National Science Fund for Distinguished Young Scholars. She is the senior committee member of Vacuum Electron Society, Chinese Electronics Society; the committee member of Manufacturing Technology Society, Chinese Electronics Society, and the committee member of Energy & Source Society, Chinese Corrosion & Protection Society.

Nanomaterials synthesis in combustion

Z.A. Mansurov

Abstract— This paper presents original results in the area of synthesis of fullerenes, carbon nanotubes, graphene, and superhydrophobic soot in hydrocarbon flames and data on the self-propagating high-temperature synthesis of nanomaterials obtained in recent years at the Institute of Combustion Problems.

Keywords— carbon nanotubes, fullerenes, graphene, nanomaterials.

I. INTRODUCTION

The practical use of combustion processes can be divided into two areas: energetic and chemical-technological. In the first case, use is made of the heat of combustion and very often, but not always, the energy of expanding gaseous products. In the second case, of interest is the combustion product itself, which is the target material of the chemical-technological process [1]-[5].

As regards the chemical-technological area, it has been developed in isolation from the theory of combustion, mostly by chemical engineers and metallurgists, and has reduced to the development of individual processes. Unfortunately, the scope and level of research are not high enough and are not adequate to the importance and relevance of this problem [4], [5].

The main feature of technological combustion processes is that the desired product is produced by a combustion reaction which proceeds spontaneously at high temperatures, at a high rate, without energy expenditure from outside, i.e., due to its own heat release.

Considerable interest of researchers and technical experts in methods of producing, structure and properties of nanoscale systems is due to the diversity and uniqueness of their practical applications. The small size of the structural components – usually up to 100 nm – determines the difference between the properties of nanomaterials and their analogs with larger particle sizes [6]-[8].

The scientific and engineering area “Nanoparticles – materials, technologies, and devices has emerged in the last

This work was supported in part by the state order for the budget program “Grant funding for research” for 2012-2014 y. on “Formation of layered graphene films in the flame”, “Obtaining of nanosized superhydrophobic carbon materials in mode pyrolysis and combustion of hydrocarbons”, “Improving of the efficiency solar cells using metal oxide nanoparticles and layered graphene films synthesized in the flame”

Zulkhair Aimukhametovich Mansurov, the Institute of Combustion Problems, 172 Bogenbai Batyr, 050012, Almaty, Kazakhstan (corresponding author to provide phone: +7 727 292 43 46; fax: +7 727 292 58 11; e-mail: zmansurov@kaznu.kz).

decade in many industrial countries, and its funding is the fastest growing in the world. National and multinational companies are engaged in the production of nanomaterials and large-scale studies in this area [7], [8].

The formation of carbon fibers were observed in the pyrolysis of benzene in 1976 [9]. In 1991, carbon nanotubes in an arc discharge of graphite were discovered [10], followed by the rapid development of this field. Due to a unique combination of different properties, carbon nanotubes are of interest for both basic and applied research [11].

Over the past few years, more than 150 papers on self-propagating high-temperature synthesis of nanomaterials were published, a review of which is given in [12]. In SHS, as in powder metallurgy, the particle sizes of reactants significantly affect both the process and the properties of the materials produced [12]. In this regard, the SHS is closely related to nanotechnologies.

This paper presents original results on the development of a technology for producing carbon nanomaterials for various applications obtained at the Institute of Combustion Problems:

- synthesis of fullerenes in flames;
- synthesis of carbon nanotubes in flames;
- synthesis of a superhydrophobic carbon surface in the combustion regime;
- synthesis of graphene in flames;
- SHS of nanoscale materials;
- formation of Al_2O_3 whiskers during SHS in the $\text{Al}-\text{B}_2\text{O}_3-\text{Cr}_2\text{O}_3$ system;
- synthesis of nanoscale catalysts for carbon dioxide reforming of methane to synthesis gas.

Fullerene synthesis in flame

The structure of fullerene C_{60} proposed by R. Smalley resembles a football, so it is sometimes called footballene, and that of C_{70} resembles a rugby ball. Fullerenes C_{60} and C_{70} were identified in 1985 and prepared in macroscopic quantities in 1990, both by evaporation of graphite in an arc discharge [13]. In flames, fullerene ions were found in 1987, and in 1991, C_{60} and C_{70} were extracted in large quantities from laminar sooting flames of premixed mixtures of benzene and oxygen at low pressures [14], [15] and then spectroscopically identified.

It is known that the formation and synthesis of fullerenes in the traditional method of arc evaporation of graphite is performed at pressures $p < 40$ Torr [16].

As noted in [17], nano- and subnanosize particles are formed by gas-phase condensation in asymptotic giant branched stars. Experiments were carried out at pressures of 0.1-2.6 and 7 mbar, close to the values of p in the

astrophysical atmosphere at temperatures $T < 1\,700\text{ K}$, at which the formation of fullerenes was observed.

Because fullerenes are formed at low pressures, the corresponding spatial orientation is important, which requires a consideration of the steric factor. For a molecule of C_{60} to form, a spatial orientation of two molecules of C_{30} is required. There are various models of formation of fullerenes C_{60} , one of which is the zip mechanism [18] (Fig. 1).

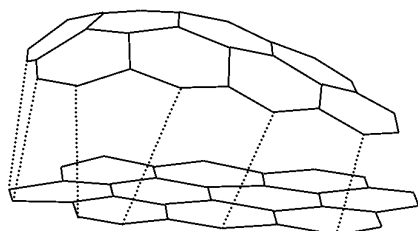


Fig. 1 model of five- and six-membered rings through the connection of two PCAHs by the zip mechanism [18]

A necessary condition for this mechanism is low pressure. As the pressure increases, i.e., with transition to atmospheric pressure or above, where triple collisions dominate, PCAHs coagulate to form soot clusters. It has been shown [15] that the maximum of fullerene formation is shifted to the right relative to the maximum of soot formation. In a detailed study of fullerene formation from benzene flames, the second maximum at 70 mm from the burner matrix was detected [19] (Fig. 2). These data have provided the basis for the development of an alternative method of producing fullerenes in the hydrocarbon combustion regime.

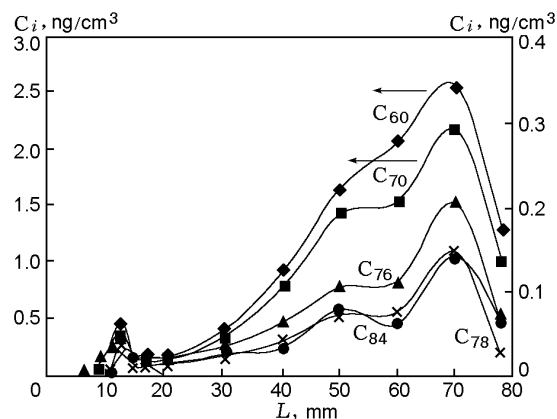


Fig. 2 concentrations profile of fullerenes on the axis of a premixed benzene-oxygen-argon flame [19]

The influence of gas discharge, the type of electrode, and the inter electrode spacing on the yield of fullerenes in combustion was studied in [20]. The experimental conditions were as follows: $C/O = 1$, $p = 40\text{ Torr}$, flow rate of benzene $250\text{ cm}^3/\text{min}$, oxygen $758\text{ cm}^3/\text{min}$, argon $101\text{ cm}^3/\text{min}$, $v = 18.4\text{ cm/s}$, $T = 1200\text{ K}$, and $\delta = 0.5\text{--}0.8\text{ cm}$; electrode systems are the needle- plane, plane-plane, and ring-plane with an inter electrode spacing of 4-21 cm; voltage $U = 0.5\text{--}$

20 kV. A premixed $C_6H_6/O_2/Ar$ flame under conditions corresponding to the maximum yield of fullerenes was studied [20].

Processing of the experimental data revealed the advantage of the ring electrode over the electrode in the form of a needle and showed that the yield of fullerene C_{60} ($\approx 15\%$) was the highest when the electrode was placed in the middle of the flame ($L = 4\text{ cm}$).

It has been found [20] that if the peripheral zone of the benzene flame is heated by some external source, such as a laser beam, which not just burns the soot but also creates the same conditions as in the middle of the flame, the concentration of fullerenes increases.

The effect of acetylene-oxygen flames on the different zones along the height of the benzene-oxygen flame have been studied using a ring burner. It has been found that fullerene formation is activated at the boundary of contact of the acetylene-oxygen and benzene-oxygen flames. The positive effect of the acetylene flame consists of increasing the temperature in the upper part of the reaction zone of the main benzene-oxygen flame by $50\text{ }^\circ\text{C}$, increasing the degree of ionization, and intense conversion of PCAHs present in the benzene-oxygen flame to fullerenes [21].

Formation of carbon nanotubes in flames

The most promising way to produce carbon nanotubes, according to Merchan-Merchan et al. [22], is the flame method. In the synthesis of carbon nanoparticles using flames, part of the fuel is consumed in heating of the mixture, and part is used as a reactant, which makes this method more cost-effective than methods based on the use of electricity, pyrolysis of hydrocarbons or arc evaporation of graphite.

Results of a study of flat diffusion propane – oxygen flame stabilized on an opposed-jet burner at atmospheric pressure are presented in [23]. Two opposed flows formed the flat flame. The flame was surrounded by an external nitrogen flow supplied from the burner matrices. A solution of catalyst $[Fe(CO)_5]$ or an alcoholic solution of nickel nitrate] was sprayed by an ultrasonic nebulizer and delivered through a metal nozzle into the flame from the side of the fuel. The conditions of the experiment are shown in Table 1.

Table 1. Experimental conditions

Catalyst	Flow of catalyst, cm^3/min	Gas flow rate, cm^3/min				Flame temperature, $^\circ\text{C}$
		C_2H_2	O_2	N_2	C_3H_8	
$Fe(CO)_5$	0.05	130-210	100-170	50-200	-	1700-1850
$Ni(NO_3)_2 \cdot 6H_2O$	0.05	-	160-210	50-200	70-160	900-1150

The resulting products were deposited on the walls of the reactor and collected in traps with liquid nitrogen. The temperature in the reactor was measured by a thermocouple, and in the flame by an Iron Ultrimax pyrometer. It is evident that the samples contain soot agglomerates, among which metal particles are encountered. It was found that under certain

experimental conditions, well-ordered bundles of carbon nanotubes 20-30 nm in diameter formed. It is evident from Fig. 3 that the samples contain soot agglomerates, among which metal particles are encountered. It was found that under certain experimental conditions, well-ordered bundles of carbon.

The flame synthesis of carbon nanomaterials is mainly determined by carbon atoms serving as sources of graphite layers, the catalytic metals providing the transformation of the gas-phase carbon atoms into solid graphite layers, and the heat sources activating the catalytic metals.

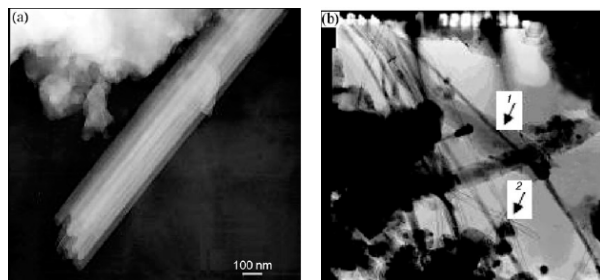


Fig. 3 electron micrographs of samples: (1) carbon nanotube; (2) Ni in a carbon shell

In [24], the synthesis of carbon nanotubes and nanofibres on a $\text{Ni}(\text{NO}_3)_2$ film deposited on a metal substrate with the use of a counter-flow ethylene flame as a heat source was investigated. Puri et al. have developed, on the basis of numerous experimental data on synthesis of carbon nanotubes in a flame, a model of formation of these nanotubes with participation of nanoparticles of the catalysts (Fe, Ni, Co) [25], [26], [27]. Fig. 4, a schematically described of the CNT formation process and in Fig. 4, b are shown schematic diagram of the CNT growth model by Puri and et al [25]. In this article [25] was underlined that the chemistry includes PAH species but soot was not modeled, since it has negligible presence in the flame.

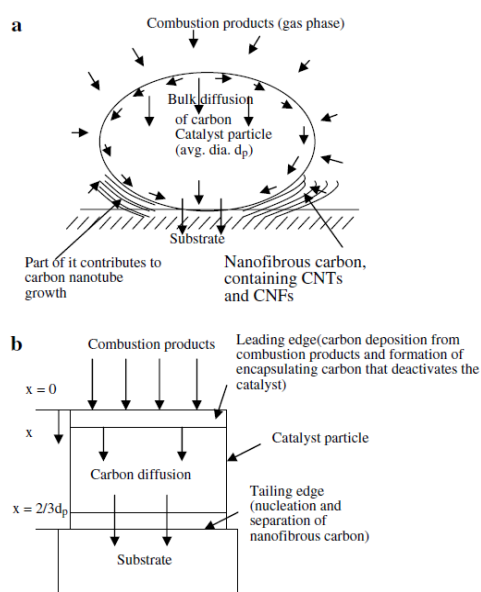


Fig. 4 (a) schematic diagram of the CNT formation process; (b) Schematic diagram of the CNT growth model [25]

In accordance with this model, nucleation of carbon nanotubes begins when the density of carbon atoms on the surface of the catalyst particles increases due to the addition of the indicated atoms from the outer shell of these particles. However, once the nucleation and growth of carbon nanotubes begins, carbon atoms are transported through the nanoparticles mainly due to their diffusion. This diffusion decreases with time because of the decrease in the concentration of the carbon atoms.

Formation of hydrophobic soot in hydrocarbon flames

Low surface-energy materials like amorphous carbon (a-C) films are frequently used to modify surfaces in order to control their wettability. The nanobeads are morphologically similar to the carbon nanopearls synthesized by Levesque and co-workers [28] by acetylene dissociation at 700°C on nickel catalyst nanoclusters. Puri et al. [27] have determined new ways of synthesis of carbon nanotubes in the fuel-rich diffusion flames, exposed to an electric field during 2-10 min, on superhydrophobic surfaces representing nanodimensional round amorphous carbon particles deposited on a silicon substrate.

A silicon (Si) disk is placed 2 cm above the burner, as shown in Fig. 5, and exposed to the flame for 4, 6 and 10 minutes. The nonpremixed flame is established using propane and oxygen flow rates of $50\text{-}150\text{ cm}^3/\text{min}$ and $260\text{-}310\text{ cm}^3/\text{min}$.

Si disc with a carbon nano-bead coating after a 4 min exposure to the flame showing the three deposition zones are shown in Fig. 5, b. The deposited carbonaceous material was examined using Raman spectroscopy. The Raman spectra for the middle zone indicate the presence of several modifications of carbon. Raman peaks near 1350 cm^{-1} (D - amorphous) and 1590 cm^{-1} (G - graphite) in all three zones (1-3). The peaks near 1470 cm^{-1} for Zones 1 and 2 are typical of fullerenes [29].

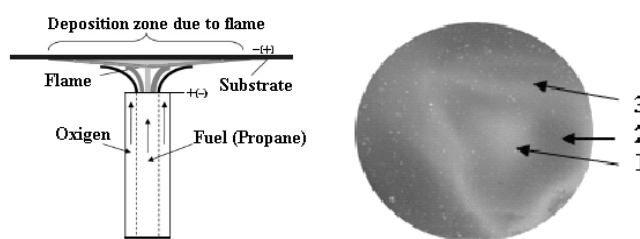


Fig. 5 schematic representation of the burning experimental setup (a) and Si disc with a carbon nanobead coating after a 4 min exposure to the flame showing the deposition zones (b)

The formation of hydrophobic soot surface on silicon and nickel substrates during combustion of propane-oxygen flame was studied [29]. It is stated that the hydrophobic properties are due to the presence of soot particles in the form of nanobeads.

Fig. 8 shows a drop water on a hydrophobic surface, and, as we found, the hydrophobicity of the surface was very stable. The outer contact angle θ is in the range of $152.4\text{--}157.1^\circ$ in all cases.

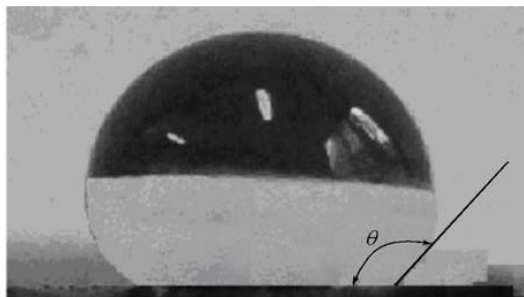


Fig. 8 a liquid drop on the superhydrophobic surface

It was investigated the influence of an electric field of 1 kV applied between the substrate and the burner rim. For studies the substrates were exposed with and without the applied field, in both cases for 10 minutes, to a flame established at propane and oxygen flow rates of 50 and 260 cm³/min. For this flame, shown schematically in Fig. 5, middle zone contained carbon nano-bead chains that were 15 - 30 nm long in the absence of an electric field. The chain length was increased to 40-50 nm in middle zone when the electrical field was applied. In the outer zone, regardless of the conditions of combustion, there are coagulated aggregates of soot particles with sizes 30-50 nm.

The results for the exploration of the soot formation of hydrophobic surfaces on silicon and nickel substrates during combustion of propane oxygen flame are listed. The distance from the matrix burner and the substrate was varied, the exposure time and the influence of an electric field of different polarity and voltage. It is shown that at the exposure of more than 4 minutes the soot with hydrophobic properties is formed and division of the soot surface area is occurred. The applying of an electric field narrows the soot deposition on the substrate and in diameter of 2.5-3 cm from the center, the soot super hydrophobic surface with a wetting angle of more than 170° is formed [30], [31].

Formation of a layered graphene films in the flames [32]

Synthesis graphene in the flame was conducted at a pressure of 40-100 Torr by combustion premixed butane-oxygen mixture with the addition of benzene on a nickel substrate. For this purpose, the burner was placed in a quartz reactor (Fig. 6, a), which created initial low pressure of 5 Torr. The experiments were performed in the following conditions: butane flow rate of 450 cm³/min, oxygen flow rate of 740 cm³/min and benzene flow rate of 70 - 120 cm³/min corresponding to the C/O ratio = 0.8-0.9. Nickel plate was used as the catalyst substrate. The flame temperature in the experiments was in the range of 900-950 °C. The residence time of the plate in the flame was 3 min. Fig. 6 shows the photograph of quartz reactor (a) and photo of the flame with the insert of a nickel substrate (b).

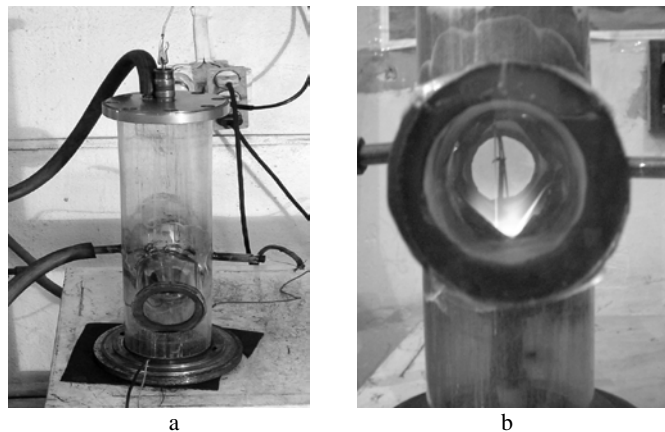


Fig. 6 the photograph of the burner used for low-pressure synthesis of graphene layers in the flame: a – general view, b – with the substrate placed in the flame

Investigations on synthesis of graphene layers in hydrocarbon flame at low pressure have shown that the formation of graphene layers is occurred in sooting zone as well as at atmospheric pressure, as was shown in [32]. Fig. 7 shows the Raman spectra (a) that characterizing the carbon structures are formed on nickel plate in areas 0, 1, 2, 3 (b). In zones 0, 1 and 2 (Fig. 7, a, b) the amorphous carbon structure is observed, but in zone 3 the graphene layers are synthesized. At that, an area of graphene formation at low pressure is more expanded than at atmospheric pressure. Above zone 3 there is soot structure is formed (Fig. 7, b).

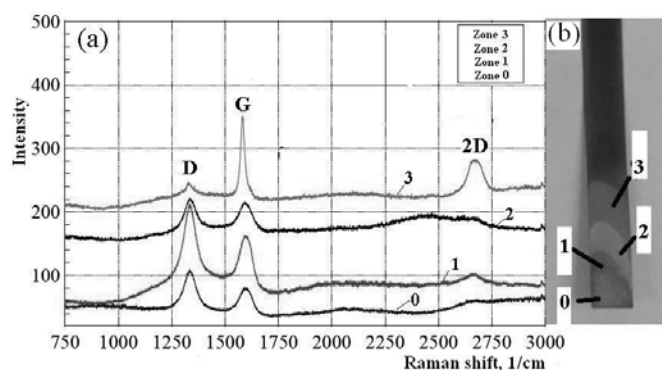


Fig. 7 the Raman-Spectra of carbon structures in accordance with (a) zones; and photo of nickel substrate (b) with an indication of formed carbon structure zones

(P = 90 Torr, C/O = 0.8, T = 900 °C, t = 30 sec) [33]

Analysis of the results of synthesis of graphene layers in the flame at low pressure and with addition of benzene showed that in the pressure range of 40-100 Torr one- to three-layer graphene sheets on nickel substrate are formed, which is characterized by the intensity ratio $I_G/I_{2D} \leq 1.3$. At a pressure of 55 Torr preferential formation of a single layer graphene is observed, its characteristic Raman spectra was shown in Fig. 8.

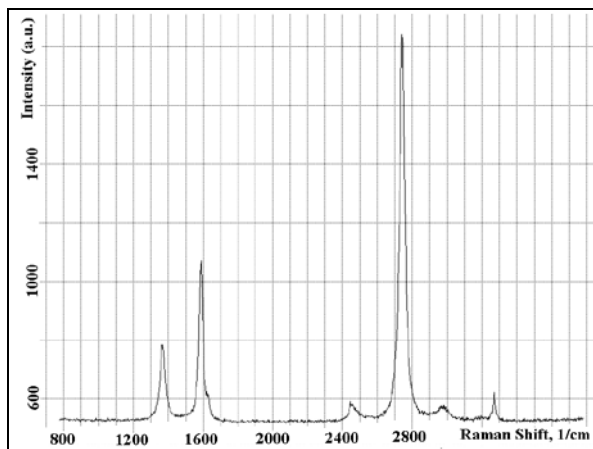


Fig. 8 raman spectra of single-layer graphene samples obtained with the addition of benzene to C_4H_{10}/O_2 flame on a nickel substrate at a pressure of: 55 Torr ($I_G/I_{2D}=0.58$) [34]

Mechanism of soot formation in rich flames [35]

The flame front structure of soot formation flames can be considered in close connection with mechanism of fuel conversion. A scheme that suggested by Bockhorn [36] in 1994 is known, where polycyclic aromatic hydrocarbon (PAH) are precursors of soot particles. Since then, in rich fuel flames the nanosized particles such as fullerenes and graphenes are found.

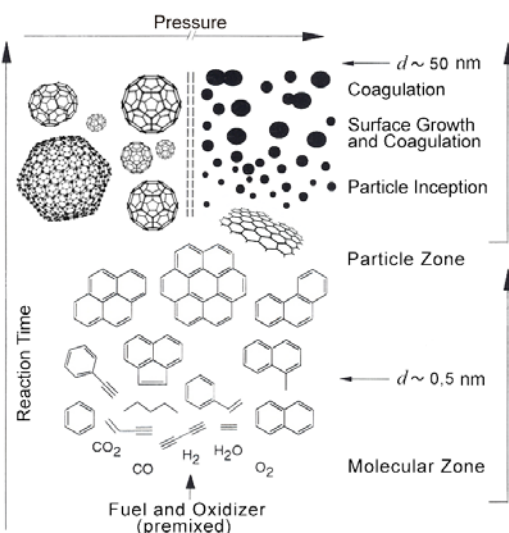


Fig. 9 modified scheme for soot, fullerenes and graphene formation process in flame [35]

The fullerenes formation is generally observed at pressures below 60 Torr, because for fullerenes formation is necessary an adherence of steric spatial factor, but in flames at atmospheric pressure this factor is prevented by triple collisions. Therefore, the pressure coordinate can be introduced to the general scheme for soot formation. At low pressure the formation of fullerenes from polycyclic aromatic hydrocarbon (PAH) is occurred, but with pressure increase the polycyclic aromatic hydrocarbon (PAH) is coagulates to soot

particles. From (PAH) follows the graphene formation as intermediate product between PAH and soot particles, which is confirmed by the formation of multi-layered graphene films at atmospheric pressure and single-layered at the pressures below 60 Torr. On the basis of the data on synthesis of fullerenes, carbon nanotubes, superhydrophobic soot and graphene in the flame it is possible to modify the general scheme proposed by H. Bockhorn [36] for rich fuel flames, namely to make a pressure-coordinate, which allows the formation of fullerenes at low pressures, and soot at high pressures. In addition the scheme was completed by graphene formation as an intermediate product stage of graphene formation (Fig. 9) [35].

Increase of the power of solar cells coating by nanoparticles of nickel oxides synthesized in flame

The work present the investigations results on synthesis of nickel oxide nanoparticles in propane-oxygen flame in counter jets which subsequently are used to increase the efficiency of light conversion in the solar cells.

The reactor of the burner is a hollow cylinder with a diameter of 150 mm and a height of 82 mm is made of stainless steel. Two burners are installed on the axis of this cylinder opposite each other. Nichromic wire with a diameter of 0.3 mm was used as a substrate for the growth of nickel oxide nanoparticles. X-ray fluorescent analysis of nichromic wire shows that the main composition wire is Ni-60.27 %. The wire before its using for synthesis of nanoparticles was preliminary treated with 25 % solution of nitric acid for 20 minutes [37].

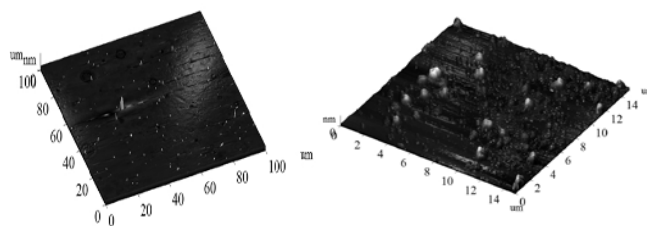


Fig. 10 photo of nickel oxide nanoparticles on the surface of the solar cell, 5sec (a) 2 min (b) [37]

The obtained results of electron-microscopic investigations show that the treatment of nichromic wire with flame for 2 minutes leads to the formation of nickel oxides with an average size of 300 nm on its surface. High temperature and active radicals formed in propane-oxygen flame interact with nickel surface promoting the growth of nickel nanoparticles. After coating of nickel oxide nanoparticle were on the surface of solar cell on atomic power microscope. The resulting image (Fig. 10) shows that the size of metal oxide nanoparticles on the surface of a solar cell depends on the residence time in the flame [38].

To study output characteristics silicon solar cells with an active region of 1 cm² were used. To obtain uniform coating based on nanoparticles on the surface of the solar cell suspension of nanoparticles was preliminary created in ethanol

in ultrasonic bath. To coat one solar element up to 0.1 ml of suspension was necessary. Primordially the measurement of short – circuit current and voltage of non-load running of the solar element without applying a coating was carried out. Not changing the conditions of the experiment short-circuits current and open circuit voltage with applied nanooxide film was measured.

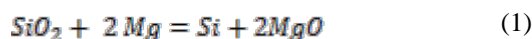
The applying of silicon solar cells of nickel oxide nanoparticles to the surface caused the increase of output open circuit voltage of 4-7 %, the increase of short – circuit current of 2-8 %, that in total caused the increase of efficiency of the solar cells by 2-3 % [38].

SHS of nanoscale materials

Producing a silicon nanopowder is an important problem for various applications, including microelectronics, solar power engineering, and rocket propellants. In [39], a silicon nanopowder was produced by SHS, which is a simple and cost-and power-effective technology for producing various materials. The principal possibility of producing a pure silicon powder with a high surface area is shown, and a comparative analysis of the products obtained using three different silicon oxides was made.

The method is based on the well-known process of magnesium-thermic reduction of silica but which is carried out in the regime of a self-propagating combustion reaction. The starting material was silicon oxide powders differing in particle size and purity: quartz of the Erken Kazakhstan field (hereinafter in the text, quartz KZ) with a purity 98.8% and a particle size $d \leq 100 \mu\text{m}$; Cerac quartz (WI, USA) with a purity 99.9% and a particle size of $d < 44 \mu\text{m}$; untreated fumed silica (UFS) quartz (Cabot Corporation, MA, USA) with a purity of 99.9% and a specific surface of $\approx 200 \text{ m}^2/\text{g}$.

Synthesis was carried out by the following reaction:



The synthesized samples were treated with 36 % hydrochloric acid for 3 hours under normal conditions to produce pure silica. It is evident from Fig. 11 that the typical microstructure (morphology and size) of the synthesized silicon powder depends weakly on the morphology and particle size of the initial quartz. In all cases, the powder has a very porous microstructure with a particle size of the components (pores and separate crystallites) not less than $1 \mu\text{m}$.

Due to rapid cooling, the microstructure of the product consists of small ($\leq 1 \mu\text{m}$) MgO grains a silicon matrix. Chemical removal of MgO yielded a very porous silicon skeleton with a typical size of the microstructure comparable to the scale of the grain size of magnesium oxide crystals. The size of these grains is determined solely by the rate of crystallization and temperature conditions in the combustion wave (most likely, the rate of cooling of the product). A weak

dependence of the microstructure of the synthesized silicon on the size of SiO_2 was observed.

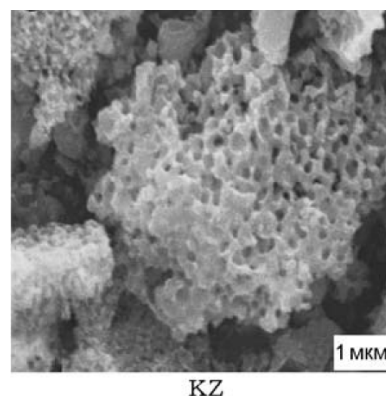


Fig. 11 particles of synthesized silicon after chemical treatment with hydrochloric acid

Since the silicon produced in all cases has a highly porous, sponge-like structure with high surface area, it is reasonable to assume that a fine (submicron or nanosized) silicon powder can be obtained by mechanically destroying the thin bridges of the skeleton. Treatment in a high-energy mill (Glen Mills Inc., USA) for 5 min resulted in a submicron silicon powder with a particle size of 300 nm.

SHS of Al_2O_3 whiskers in the $\text{Al}-\text{B}_2\text{O}_3-\text{Cr}_2\text{O}_3$ system

In [40], SHS was performed in the $\text{Cr}_2\text{O}_3-\text{B}_2\text{O}_3-\text{Al}$ and $\text{Cr}_2\text{O}_3-\text{B}_2\text{O}_3-\text{Mg}$ systems.

Borides of chromium and aluminum oxide were identified by x-ray diffraction analysis. It is seen that a small portion of aluminum interacted with air to give AlN .

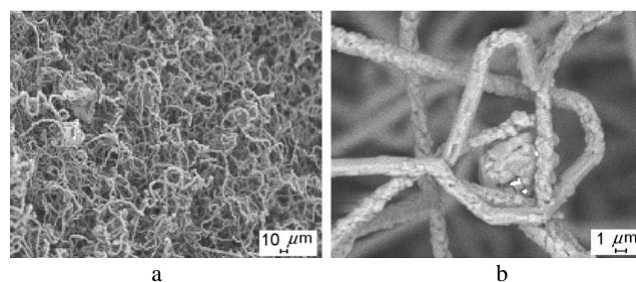


Fig. 12 sem images of the $\text{Cr}_2\text{O}_3-\text{B}_2\text{O}_3-\text{Al}$ system: (a) straight, wavy, and twisted forms of whiskers; (b) branching of several crystals

Results of an electron microscopic study of the combustion products of $\text{Cr}_2\text{O}_3-\text{B}_2\text{O}_3-\text{Al}$ indicate the formation of whiskers of different sizes and shapes from aluminum oxide in a boride matrix (Fig. 12). Fig. 12 a shows fibers of straight, twisted, and wavy forms, and Fig. 12 b shows whiskers with a branched structure. Analysis on a scanning electron microscope (SEM) revealed the formation of $\alpha\text{-Al}_2\text{O}_3$ fibers with a length $l \approx 10\text{-}25 \mu\text{m}$ and a diameter $d = 200\text{-}500 \text{ nm}$. The fibers are not ordered. Different fiber diameters are

due to self-turbulence in the growth of the system, namely, in the growth in temperature, diffusion, and chemical reaction rate [39]. The process of formation and the mechanism of growth of aluminum oxide whiskers and fibers were studied in [41]–[43]. Aluminum, as follows from the literature, can serve as a concentrator of whisker growth by the vapor–liquid–crystal mechanism.

Synthesis of nanoscale catalysts for carbon dioxide reforming of methane to synthesis gas

Fiber glass-based metal oxide (CoO and NiO) catalysts were developed. Use was made of KS-11-LA (88) Na–Si fiberglass (the working temperature range of this fiber glass is 1000–1200 °C). Oxides of metallic Ni and Co were deposited on its surface by solution combustion (SC) [44] which is a version of self-propagating high-temperature synthesis [45], [46].

Samples with a low content of oxides – not more than 1% by weight were synthesized (IK1–IK5 in Table 2).

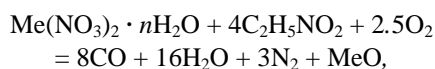
A fiber-glass sample of size 5 × 5 cm was impregnated with a solution of nitrate salts of cobalt, nickel, and glycine taking into account its water capacity, and the sample was then dried for 30 min in air at 100 °C.

Table 2. Synthesis conditions of fiberglass catalysts

Sample number	Ccat, %	Co/Ni, %	Glycine, mol
IK1	1.0	100/0	4.0
IK2	1.0	70/30	4.0
IK3	1.0	50/50	4.0
IK4	1.0	30/70	4.0
IK5	1.0	0/100	4.0

As shown by physicochemical studies, the formation of 10–50 nm nanoparticles occurred during heating of samples in a thermostatic oven at 400–450 °C for 1 h, followed (in the case of using a ≥1% concentration of the active ingredient) by weak bluish glow.

The method of SC between the starting components corresponds to the reaction:



where $\text{C}_2\text{H}_5\text{NO}_2$ is glycine, which acts as a reducing agent. Additional missing oxygen comes from the air.

Investigation of the surface of the fiber-glass sample by SEM and TEM (transmission electron microscope) revealed that the active component is dispersed mainly in the form of individual particles with a size of about 10 nm or less, which form an oxide film.

Fig. 13 (a) shows a three-dimensional image of individual particles of the 1.0-KS-0/100 catalyst taken from the substrate using an ultrasonic disperser.

A TEM image of the 0.8-KT-60/40 catalyst Fig. 13 (b) showed the presence of cobalt and nickel particles with a size of 5–20 nm on the fiber-glass surface.

In connection with the annual decline of oil reserves in the world, there is an urgent need for new sources of alternative clean fuel. Such a fuel can be dimethyl ether produced from synthesis gas by carbon dioxide reforming of methane. Among the investigated catalytic systems used in the carbon dioxide reforming of methane and other hydrocarbons are deposited nickel ($\text{Ni}/\text{Al}_2\text{O}_3$, Ni/SiO_2 , and Ni_3Al) and cobalt-nickel catalysts, codeposited Ni–Mg contacts ($\text{Ni}0.03\text{Mg}0.97\text{O}$), and catalysts based on precious metals.

Dependences of the conversion of the starting substances, methane, carbon dioxide, and the yield of the desired reaction products (hydrogen and carbon monoxide) on the temperature and time of catalysis have been studied. The IK1 catalyst showed rather high activity: the yield of synthesis gas reaches 32 % H_2 and 46 % CO at 745 °C. The conversion of CH_4 is 30 %, and that of CO_2 is 80 % at the same temperature.

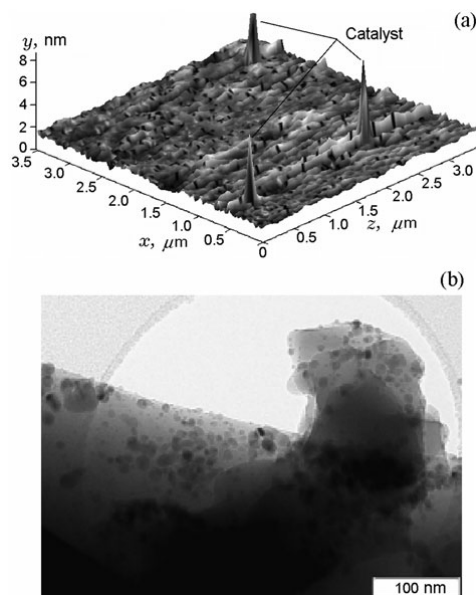


Fig. 13 three-dimensional image of particles of the 1.0-KC-0/100 catalyst (a) obtained in an atomic force microscope and a TEM image of the 0.8-KT-60/40 catalyst (b)

Samples of catalysts coated with cobalt oxide exhibit high activity in the carbon dioxide reforming of methane. It should be noted that compared to the GIAP-18 commercial catalyst, the IK1 fiber-glass catalyst is carbonized much slower, and after 3 h of operation, the degree of carbonization of IK1 did not exceed 0.5%.

CONCLUSIONS

It was established the formation of fullerenes and carbon nanotubes as well as soot with the superhydrophobic surface,

obtained on nickel and silicon supports in benzene-oxygen and propane-oxygen diffusion flames. New results regarding the synthesis of superhydrophobic surface with a contact angle 135-175 ° have great practical interest as anti-corrosion additives to various materials. Graphene sheets with 1-3 layers are mainly formed in the range of 40-100 Torr on nickel substrate in butane-oxygen flame with the addition of benzene. At pressure of 45-55 Torr preferential formation of a single layer graphene is observed.

The photovoltaic properties of solar cells coated by nickel oxide nanoparticles synthesized in counter flow propane-air flame. It is revealed that coated the surface of a silicon solar cell by nickel oxide nanoparticles results in the increase in solar cell efficiency by 3%.

SHS of nanopowders of metal oxides and catalysts is an alternative to the conventional technology of producing inorganic substances and materials.

All these processes are characterized by the use of the chemical energy of combustion instead of electric energy; ease of equipment due to the absence of external sources of heat; and a high rate of the process.

REFERENCES

1. N. N. Semenov, *Some Problems of Chemical Kinetics and Reactivity* (Izd. Akad. Nauk SSSR, Moscow, 1954 [in Russian]).
2. Ya. B. Zel'dovich, G. I. Barenblatt, V. B. Librovich, and G. M. Makhviladze, *Mathematical Theory of Combustion and Explosion* (Nauka, Moscow, 1980; Plenum, New York, 1985).
3. D. A. Frank-Kamenetskii, *Diffusion and Heat Transfer in Chemical Kinetics* (Nauka, Moscow, 1967; Plenum, New York, 1969).
4. G. I. Ksandopulo and V. V. Dubinin, *Gas-Phase Chemistry of Combustion* (Khimiya, Moscow, 1987) [in Russian].
5. A. G. Merzhanov, "Combustion and Explosion in Physical Chemistry and Technology of Inorganic Materials," *Usp. Khim.* 72 (4), 323-345 (2003).
6. K. E. Drexler, *Nanosystems: Molecular Machinery, Manufacturing and Computation* (John Wiley and Sons, New York, 1992). *Nanotechnologies. Nanomaterials. Nanosystem Equipment.* Global Progress Ed. by P. P. Mal'tsev (Tekhnosfera, Moscow, 2008 [in Russian]).
7. W. F. Smith and J. Hashemi, *Foundations of Materials Science and Engineering* (McGraw-Hill, 2010).
8. A. Oberlin, M. Endo, and T. Koyama, "Filamentous Growth of Carbon Through Benzene Decomposition," *Cryst. Growth* 32 (3), 335-349 (1976).
9. S. Iijima, "Helical Microtubules of Graphitic Carbon," *Nature* 354, 56-58 (1991).
10. M. Endo, M. S. Strano, and P. M. Ajayan, *Potential Applications of Carbon Nanotubes*, Eds. by A. Jorio, G. Dresselhaus, M. S. Dresselhaus (2008), pp. 13-61. (*Topics in Appl. Phys.*, Vol. 11.)
11. Z. A. Mansurov, "Some Applications of Nanocarbon Materials for Novel Devices," in *Nonoscale-Devices—Fundamentals*, Ed. by R. Gross et al. (Springer, 2006), pp. 355-368.
12. A. E. Sychev and A. G. Merzhanov, "Self-Propagating High-Temperature Synthesis of Nanomaterials," *Usp. Khim.* 73 (2), 157-170 (2004).
13. H. W. Kroto, J. R. Heath, S. C. O'Brien, R. F. Curl, and R. F. Smalley, "C₆₀: Buckminsterfullerene," *Nature* 318 (6042), 162-164 (1985).
14. J. B. Howard, "Fullerenes Formation in Flames," in *24th Symp. (Int.) on Combustion* (1992), pp. 933-946.
15. W. Kra'tschmer, L. Lamb, K. Fostiropoulos, D. Huffman, "Solid C: A New Form of Carbon," *Nature* 347, 354-358 (1990).
16. C. Jäger, F. Huisken, Jansa I. Lamas, Th. Henning, "Formation of Polycyclic Aromatic Hydrocarbons and Carbonaceous Solids in Gas-Phase Condensation Experiments," *Astrophys.*, No 696, 706-712 (2009).
17. J. Ahrens, M. Bachmann, Th. Baum, J. Griesheimer, R. Kovacs, P. Weilmu'nster, K.-H. Homann, "Fullerenes and Their Ions in Hydrocarbon Flames," *Int. J. Mass Spectrom. Ion Proc.* 138, 133-148 (1994).
18. W. J. Grieco, A. L. Lafleur, K. C. Swallow, et al. "Fullerenes and PAH in Low-Pressure Premixed Benzene/Oxygen Flames," in *Symp. (Int.) on Combustion* 27 (2), 1669-1675 (1998).
19. Z. A. Mansurov, N. G. Prikhodko, T. T. Mashan, and B. T. Lesbaev, "The Study of Influence of Electric Field on Soot Formation at Low Pressure," *Chem. Physics* 25 (10), 18-22 (2006).
20. M. Bachman, W. Wiese, and K.-H. Homann, "Thermal and Chemical Influences on the Soot Mass Growth," in *Symp. (Int.) on Combustion* 25 (1), 635-643 (1994).
21. N. G. Prikhod'ko, "Features of Formation of Fullerenes and Nanotubes in Combustion of Hydrocarbons in an Electric Field," *Doct. Dissertation in Chem. Sci.* (Al-Farabi Kazakh National University, Almaty, 2010).
22. W. Merchan-Merchan, A. V. Saveliev, L. A. Kennedy, "High-Rate Flame Synthesis of Vertically Aligned Carbon Nanotubes using Electric Field Control," *Carbon* 42, 599-608 (2004).
23. D. I. Chenchik, Z. A. Mansurov, T. A. Shabanova, and T. Orynsaikh, "Producing Carbon Nanotubes in an Opposed-Jet Burner," in *Int. Symp. Combustion and Plasma Chemistry* (Almaty, 2007), pp. 288-290.
24. G. W. Lee, J. Jurng, and J. Hwang, "Formation of Ni-catalyzed multiwalled carbon nanotubes and nanofibers on a substrate using an ethylene inverse diffusion flame," *J. Combust. Flame*, 139, 167-175 (2004).
25. S. Naha, S. Sen, A. K. De, and I. K. Puri, "A detailed model for the flame synthesis of carbon nanotubes and nanofibers," *Proc. Combust. Inst.*, 31, Issue 2, 1821-1829 (2007).
26. S. Naha and I. K. Puri, "A model for catalytic growth of carbon nanotubes," *J. Phys. D: Appl. Phys.*, 41, No. 065304, 6

(2008).

27. S. Naha, S. Sen, and I. K. Puri, Flame synthesis of superhydrophobic amorphous carbon surfaces, *J. Carbon*, 45, Issue 8, 1702–1706 (2007).
28. A. Levesque, V. T. Binh, V. Semet, D. Guillot, R. Y. Filit, M. D. Brookes, et al., “Mono Disperse Carbon Nanoparticles in a Foam-Like Arrangement: A New Carbon Nano-Compound for Cold Cathodes,” *Thin Solid Films*, Nos. 464 and 465, 308–314 (2004)
29. M. Nazhipkyzy, Z. A. Mansurov, I. K. Puri, T. A. Shabanova, and I. A. Tsyganova, “Producing a Superhydrophobic Carbon Surface during Propane Combustion,” *Neft Gaz* 5 (59), 27–33 (2010)
30. Mansurov Z.A. Soot and nanomaterials synthesis in the flame// *Journal of Materials Science and Chemical Engineering*. 2014, 2, P.1-6
31. Innovative patent of the Republic of Kazakhstan № 26912. Method for producing a hydrophobic carbon black. Published in BI 2013, № 5.
32. Prikhodko, N.G., Lesbayev, B.T., Auyelkhankyzy, M., Mansurov, Z.A. Synthesis of Graphene Films in a Flame//*Rus. J. of Phys. Chem. B*, 2014, 8, 1. P. 61–64.
33. Prikhodko N.G., Auyelkhankyzy M., Lesbayev B.T., Mansurov Z.A. Combustion synthesis of graphene films // 35th Intern. Symposium on Combustion 2014. – San Francisco, California, USA, 2014.
34. Prikhodko N.G., Auyelkhankyzy M., Lesbayev B.T., Mansurov Z.A. The Effect of Pressure on the Synthesis of Graphene Layers in the Flame // *Journal of Materials Science and Chemical Engineering*. - 2014. – V. 2, № 1 – P. 13-19.
35. Zel'dovich Memorial: Accomplishments in the combustion science in the last decade / [Edited by A.A. Borisov and S.M. Fialkov]. – Moscow: TORUS PRESS, 2014. – Vol. 1. 196 p. (Mansurov Z.A. From cool flame to nanomaterials synthesis in flames, PP. 17-25)
36. H. Bockhorn (ed). Soot formation in Combustion. Springer-Verlag, Berlin, Heidelberg. 1994. P.4.
37. Innovative patent Republic of Kazakhstan № 27091. Method manufacturing a solar cell. Published in BI 2013, № 6.
38. Lesbayev B.T., Prikhodko N.G., Mansurov Z.A., Auyelkhankyzy M., Chenchik D.I., Dikhanbayev K., Taurbayev T.I., Saveliev A.V. Increase of the Power of Solar Elements Based on Nanoparticles of Nickel Oxides Synthesized in Flame // *Advanced Materials Research*. 2012. Vol. 486. pp. 140-144.
39. Zh. Yermekova, Z. Mansurov, A. S. Mukasyan, “Combustion Synthesis of Silicon Nanopowders,” *Int. J. Self-Propag. High-Temp. Syn.* 19 (2), 96–103 (2010)
40. D. C. Abdulkarimova, I. M. Vongai, Z. A. Mansurov, and O. Odavara, “Producing Boride Composites by SHS,” in *Int. Symp. Physics and Chemistry of Carbon Materials/Nanoengineering* (Almaty, 2010), pp. 116–118
41. H. Chen, Y. Cao, X. Xiang, J. Li, C. Ge, “Fabrication of β -Si₃N₄ Nano-Fibers,” *J. Alloys Compounds* 325 (1, 2), L1–L3 (2001)
42. P. L. Longland, A. I. Moulson, “The growth of α - and β -Si₃N₄ Accompanying the Nitriding of Silicon Powder Compacts,” *J. Mater. Sci* 13 (10), 2279–2280 (1978)
43. V. Valcárcel, A. Souto, F. Guitián, “Development of Single-Crystal α -Al₂O₃ Fibers by Vapor–Liquid–Solid Deposition (VLS) from Aluminum and Powder Silica,” *Adv. Mater* 10 (2), 138–140 (1998)
44. G. G. Aldashukurova, N. V. Shikina, A. V. Mironenko, Z. A. Mansurov, Z. R. Ismagilov, “Catalysts for Processing Light Hydrocarbon Raw Stock: Combustion Synthesis and Characterization,” *Int. J. Self-Propag. High-Temp. Syn.* 20 (2), 124(4) (2011)
45. A. S. Mykasyan, P. Dinka, “Novel Approaches to Solution–Combustion Synthesis,” *Int. J. Self-Propag. High-Temp. Syn.* 16 (1), 23–35 (2007)
46. B. M. Reddy, G. K. Reddy, I. Ganesh, M. F. Ferreira Jose, “Single Step Synthesis of Nanosized CeO₂—M_xO_y Mixed Oxides (M_xO_y = SiO₂, TiO₂, ZrO₂, and Al₂O₃) by Microwave Induced Solution Combustion Synthesis: Characterization and CO Oxidation,” *J. Mater. Sci. Lett.* 44 (11), 2743–2751 (2009)

Rapid screening 73 antibiotic drugs in animal feeds using ultra-performance liquid chromatography coupled to FT-Orbitrap high resolution mass spectrometry

Yu-an Sun, Qiuxia Zhang, Wei Ke, Zhenxing Li, Ke Wang, and Guoqing Wang

Abstract—In this paper, we proposed a rapid screening method for the determination and confirmation of 73 antibiotic drugs in multiclass animal feeds, including 7 β -lactams, 3 lincosamides, 11 macrolides, 23 sulfonamides, 18 quinolones, 3 quinoxalines, 5 tetracyclines, and 3 amphenicols, using ultra-high performance liquid chromatography coupled to FT-Orbitrap high resolution mass spectrometry (UHPLC—Orbitrap HRMS). Feed samples were extracted with 6 mL water-acetonitrile (1:1, v/v), and then extracted with 4 mL acetonitrile. The extracts were purified by an $-NH_2$ cartridge, concentrated by N_2 , and filtrated prior to analysis by C18 column. The method was validated in fortified samples, including pre-mixture, concentrates and compound feeds. The results show that the recoveries are in the range of 34.51%-129.64% with relative standard deviations (RSD) 0.1%-24.4%, and all of the drugs analyzed can be detected at 0.3-156.3 ng/g.

Keywords—Antibiotics drugs, animal feeds, ultra-performance liquid chromatography, high resolution mass spectrometry.

I. INTRODUCTION

As feed additives, antibiotics are used mainly for three purposes, *i.e.*, therapeutic use to treat sick animals, prophylactic use to prevent infection in animals, and as growth promoters to improve feed utilization and production [1]. The frequent but regulated use of antibiotics may leave residues in edible tissues that can lead to an allergic reaction, disorder of intestinal flora or emergence of resistant strains of bacteria [2]. The majority of the recently developed methods for the analysis

of antibiotics in feed are simultaneously analyses within a single class of compounds [3]-[10]. There are a few multiclass/multiresidue liquid chromatography tandem mass spectrometry (LC-MS/MS) methods for the determination of antibiotics in various food matrices, such as meat, egg, milk, and honey, etc. [11]-[14]. It is obvious need for multiclass analytical methods for monitor of antibiotics in animal feeds.

Multiclass residue rapid screening methods require low selectivity and simple preparation procedure, no sample discrimination, high flux and high precision. However, there are problems lead by the strong ion suppression and the matrix interference. The high resolution mass spectrometry (HRMS) instruments, such as Orbitrap MS, which can operate in the full scan mode, theoretically, there is no limitations in number of monitored compounds [15], can provide accurate mass measurements. Since Orbitrap MS was first introduced in 2000 [16] and commercially used in 2005, it was incorporated in hybrid-MS systems and typically used in proteomics [17],[18], metabolomics [19],[20], drug monitor [21],[22], environmental monitor [23],[24], and food security [25],[26]. With the introduction of a single stage mass spectrometer, Orbitrap technology has become an attractive option for full scan screening in the field of food safety [27]. Gómez-Pérez *et al.* [28] created a database for the simultaneous analysis of more than 350 pesticides and veterinary drugs in honey using UHPLC—Orbitrap HRMS. Kaufmann *et al.* [29] validated the multi-residue methods for veterinary drugs or pesticides in food using TOF and Orbitrap MS, the results showed that because of the higher resolution and the superior mass stability, the method using Orbitrap instruments had significantly better performance parameters, *e.g.*, linearity, reproducibility, and detection limits.

This study reported the development of an exact mass database for determination of 73 antibiotics drugs by UHPLC—Orbitrap HRMS, and it was applied to multiclass analysis of animal feeds using generic extraction and chromatographic conditions.

II. MATERIALS AND METHODS

A. Reagents and chemicals

The following sources of antibiotics were used in this study:

This work was supported by the National Natural Science Foundation of China (21075113).

Yu-an Sun is with School of Materials and Chemical Engineering, Zhengzhou University of Light Industry, Zhengzhou 450000, China (e-mail: sya@zzuli.edu.cn).

Qiuxia Zhang is with School of Food and Biological Engineering, Zhengzhou University of Light Industry, Zhengzhou 450000, China; School of Chemistry and Chemical Engineering, Pingdingshan University, Pingdingshan 467000, China (e-mail: zqx@pdsu.edu.cn).

Wei Ke is with China National Tobacco Quality Supervision and Test Center, Zhengzhou 450000, China (e-mail: yamei0926@163.com).

Zhenxing Li is with School of Materials and Chemical Engineering, Zhengzhou University of Light Industry, Zhengzhou 450000, China (e-mail: 279170556@qq.com).

Guoqing Wang is with School of Materials and Chemical Engineering, Zhengzhou University of Light Industry, Zhengzhou 450000, China (corresponding author to provide phone: +86-371-63556063; fax: +86-371-63556320; e-mail: gqwang@zzuli.edu.cn).

β -lactams, lincosamides, macrolides, quinoxalines, tetracyclines, amphenicols (National institutes for food and drug control, China); sulfonamides and quinolones (Dr.Ehrenstorfer, Augsburg, Germany). HPLC grade methanol (MeOH) and acetonitrile (ACN) were purchased from J.T. Baker (Deventer, Holland). Formic acid (ACS grade) was purchased from Amethyst Chemicals (J&K Scientific, Beijing). LC-MS water was generated in-house from a Milli-Q Advantage water system. For accurate mass calibration, a mixture of caffeine, Met-Arg-Phe-Ala acetate salt (MRFA) and Ultramark 1600 (ProteoMass LTQ/FT-Hybrid ESI positive mode calibration mix) from Sigma-Aldrich was used in the Orbitrap analyzer.

Oasis HLB, MCX and MAX (60 mg, 3 mL), Sep-Pak Alumina (500 mg, 3 mL) solid phase extraction (SPE) columns were obtained from Waters (Manchester, UK); Supelclean SCX (500 mg, 3 mL) and Supelclean ENVI-Carb (500 mg, 6 mL) SPE columns were obtained from Supelco (Bellefonte, PA); MEGA BE-NH2 cartridges (500 mg, 6 mL) were purchased from Agilent cooperation, USA.

B. Apparatus

A refrigerated centrifuge (Sigma 30K, Osterede am Harz, Germany), a vortexer (IKA MS 3 basic; IKA Werke GmbH & Co. KG, Staufen, Germany), a multitube vortexer (VX-III; Beijing Targin Technology Co. Ltd, China), a nitrogen evaporator (N-EVAP-112; Organomation Associates Inc., Berlin, MA), and the adjustable pipettes, range: 10–100 μ L, 20–200 μ L, 100–1000 μ L, 500–5000 μ L (Eppendorf Research, Hamburg, Germany) were also used in this study.

C. Preparation of Standard Stock Solutions

Between 9.5 and 10.5 mg of antibiotics in the same class were weighed into 10 mL volumetric flask. Macrolides, sulfonamides, quinolones and tetracyclines were filled up to the mark with MeOH, β -lactams, lincosamides and quinoxalines fill up to the mark with 50% MeOH (MeOH:H₂O, v/v), amphenicols were filled up to the mark with ACN. And then, approximately 1.5 mL aliquots were transferred into amber autosampler vials and stored below 0°C.

Working standard solutions were prepared on the day of analysis by successive dilutions of the mixed-standard stock solution using 50% ACN (ACN:H₂O, v/v).

D. Sample preparation

2 g homogenized feed was weighed into a 35 mL centrifuge tube, added 6 mL 50% ACN (ACN: H₂O=1:1, v/v), and vortexed 30 s. The mixture was shaken by a multitube vortexer for 10 min and centrifuged at 8000 r/min for 5 min. After centrifugation, the remaining supernatant was removed to a 10 mL centrifuge tube, and the residue was extracted by 4 mL ACN in the same steps. Then the supernatant were combined and loaded onto a MEGA BE-NH2 cartridge previously conditional with 6 mL ACN. The extraction passed through the cartridge was evaporated under a stream of nitrogen and redissolved with 1 mL of a mixture of ACN/ H₂O (50:50 v/v). Finally, 5 μ L of the sample extract that filtered through a 0.2

μ m Pall GHP Acrodisc filter (Pall Corporation, East Hill, NY, USA) were injected into the UPLC system.

E. Feed samples

Three different feed matrices (including pre-mixture, concentrates and compound feed) and 15 different commodities used in this work were supported by Henan Institute of Veterinary Drug Control. In these feed matrices used as blank samples during the optimization and validation of the method, the target compounds can not be detected.

F. UPLC-Orbitrap MS analysis

For detection of multiclass veterinary drugs, a method developed by Gómez-Pérez *et al.* [28] was modified. The separation of the analytes was carried out using an Accela UPLC (Thermo Fisher Scientific, San Jose, CA, USA) equipped with a Hypersil GOLD Q C18 column (100 mm \times 2.1 mm, 1.9 μ m particle size) from Thermo (Thermo Fisher Scientific, San Jose, CA, USA). The mobile phase consisted of 0.1% (v/v) formic acid in water (eluent A) and ACN (eluent B). The analysis started with 98% of eluent A. After 0.5 min, this percentage was linearly decreased up to 5% in 8.5 min. This composition was held during 1.5 min and increased again up to 98% in 1.5 min, followed by a re-equilibration time of 3 min (total running time = 15.0 min). The flow rate was 0.45 mL/min and the column temperature was set at 20 °C.

The UHPLC system was coupled to a single stage Orbitrap mass spectrometer (ExactiveTM, Thermo Fisher Scientific, Bremen, Germany) operating with a heated electrospray interface (HESI^{III}, Thermo Fisher Scientific, San Jose, CA, USA), in positive (ESI⁺) and negative ionization mode (ESI[−]) using the following operational parameters: spray voltage, 3.0 kV (−2.5 kV in ESI[−]); skimmer voltage, 20 V (−20 V in ESI[−]); capillary voltage, 60 V (−60 V in ESI[−]); tube lens voltage, 120 V (−120 V in ESI[−]); sheath gas (N₂, >95%), 35 (a dimensional); auxiliary gas (N₂, >95%), 10 (a dimensional); heater temperature, 300 °C; and capillary temperature, 350 °C.

The mass spectra were acquired using two independent acquisition functions: (1) full MS, ESI⁺, without fragmentation (the higher collisional dissociation (HCD) collision cell was switched off), mass resolving power is 25,000 FWHM; scan time is 0.25 s; (2) full MS, ESI[−] using the aforementioned settings. All the analyses were performed without lock mass. Mass accuracy was carefully monitored as follows: checked everyday with multi-compound standards; evaluated (once a week) and calibrated when necessary (every two weeks at least) with mass accuracy standards. External calibration mode was adopted.

All data were processed using XcaliburTM version 2.2.1 (Thermo Fisher Scientific, Les Ulis, France) with Qual and Quanbrowser. Genesis peak detection was applied. ToxIDTM 2.1.1 (automated compound screening software, Thermo Scientific) was used for screening and LCQuanTM 2.6 software (Thermo Scientific) was used for quantification during method validation and sample analysis.

III. RESULTS AND DISCUSSION

A. Database development

A good UPLC-MS method can separate the isomer drugs and less affected by matrix effects. To verify this, a comparative study was provided. The standard solutions were mixed by ACN/H₂O (50:50 v/v) to 1 µg/mL, and then injected in the system with the extracted ion chromatogram of m/z at 311.07990 shown as Fig.1a. It shows that sulfadimoxine and sulfadimethoxine can be separated completely. Every individual class standard solution was mixed by blank matrix extraction to 1 µg/mL and then injected in the system. Compared to the extracted ion chromatogram in Fig.1, it can be seen that the response value and retention time were affected less by matrix effects. Therefore, retention time obtained by detected by the standard solutions in this method can be used to recognized target drugs.

The isotopic pattern was used to investigate the matrix effects on mass spectrometry analysis. Clindamycin that has characteristic atoms Cl and S was selected. Comparison of the blank matrix sample added with mixed standards, mixed standard solution and theoretical isotopic mass was shown in Table 1. It can be seen that the single Orbitrap mass analyzer

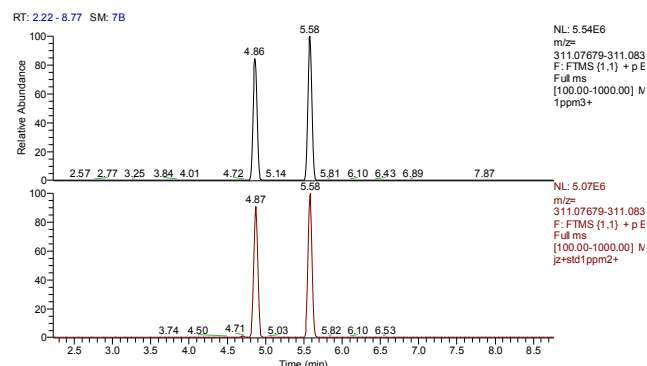


Fig. 1 Extracted ion chromatogram of m/z at 311.07990: (a) standard solution; (b) standard solution was mixed by blank matrix extraction. RT 4.86 min is sulfadimoxine and RT 5.58 min is sulfadimethoxine.

can identify the target compounds.

The information used to build the database such as retention time (RT), ionization mode (including polarity), characteristic ions and possible adducts with Na⁺ or H₃O⁺ can be obtained by the UHPLC-MS system. Furthermore, the automatic screening method was developed by ToxID software. The information of the database was shown in Table 2.

Table 1 Comparing of isotopic pattern

Sample type	Isotopic patterns (m/z)			Relative abundance		
Theoretical	425.18715	426.19050	427.18420	100.00	19.47	31.96
Standard	425.18706	426.19055	427.18403	100.00	19.57	36.52
Matrix added standard	425.18701	426.19050	427.18395	100.00	19.59	36.18

Table 2 The information of the database

Compound Name	Formula	[M+H] ⁺ Theoretical	Detected (m/z)	Delta (ppm)	RT
Benzylpenicillin G	C ₁₆ H ₁₈ N ₂ O ₄ S	335.10600	335.10516	-2.51	5.48
Ampicillin	C ₁₆ H ₁₉ N ₃ O ₄ S	350.11690	350.11658	-0.93	3.67
Oxacillin	C ₁₉ H ₁₉ N ₃ O ₅ S	402.11182	402.11148	-0.84	6.02
Flucloxacillin	C ₁₉ H ₁₇ ClFN ₃ O ₅ S	454.06342	454.06302	-0.89	6.48
Cephalexin	C ₁₆ H ₁₇ N ₃ O ₄ S	348.10125	348.10089	-1.04	3.72
Cefradine	C ₁₆ H ₁₉ N ₃ O ₄ S	350.11690	350.11658	-0.93	3.90
Ceftiofur	C ₁₉ H ₁₇ N ₅ O ₇ S ₃	524.03629	524.03564	-1.22	4.93
Lincomycin	C ₁₈ H ₃₄ N ₂ O ₆ S	407.22103	407.22028	-1.86	3.45
Clindamycin	C ₁₈ H ₃₃ ClN ₂ O ₅ S	425.18715	425.18665	-1.18	4.56
Pirlimycin	C ₁₇ H ₃₁ ClN ₂ O ₅ S	411.17150	411.17102	-1.16	4.16
Tiamulin	C ₂₈ H ₄₇ NO ₄ S	494.32985	494.32830	-1.55	5.76
Tylosin	C ₄₆ H ₇₇ NO ₁₇	916.52643	916.52478	-1.80	5.22
Tilmicosin	C ₄₆ H ₈₀ N ₂ O ₁₃	869.57332	869.57208	-1.42	4.68
Azithromycin	C ₃₈ H ₇₂ N ₂ O ₁₂	749.51580	749.51447	-1.78	4.31
Clarithromycin	C ₃₈ H ₆₉ NO ₁₃	748.48417	748.48230	-2.50	5.68
Erythromycin	C ₃₇ H ₆₇ NO ₁₃	734.46852	734.46692	-2.18	5.08
Roxithromycin	C ₄₁ H ₇₆ N ₂ O ₁₅	837.53185	837.52966	-2.61	5.76
Josamycin	C ₄₂ H ₆₉ NO ₁₅	828.47400	828.47357	-0.51	6.12
Natamycin	C ₃₃ H ₄₇ NO ₁₃	666.31202	666.31158	-0.65	5.25
Spiramycin I	C ₄₃ H ₇₄ N ₂ O ₁₄	843.52128	843.51770	-4.24	5.76

Table 2 *Continued.*

Compound Name	Formula	[M+H] ⁺ Theoretical	Detected (m/z)	Delta (ppm)	RT
Kitasamycin A5	C ₃₉ H ₆₅ NO ₁₄	772.44778	772.44666	-1.46	5.64
Sulfamonomethoxine	C ₁₁ H ₁₂ N ₄ O ₃ S	281.07029	281.06979	-1.76	4.54
Sulfamethoxazole	C ₁₀ H ₁₁ N ₃ O ₃ S	254.05939	254.05907	-1.27	4.84
Sulfadimethoxine	C ₁₂ H ₁₄ N ₄ O ₄ S	311.08085	311.08038	-1.51	5.29
Sulfaquinoxaline	C ₁₄ H ₁₂ N ₄ O ₂ S	301.07537	301.07501	-1.20	5.25
Sulfadimidine	C ₁₂ H ₁₄ N ₄ O ₂ S	279.09102	279.09079	-0.84	4.09
Sulfachlorpyridazine	C ₁₀ H ₉ ClN ₄ O ₂ S	285.02075	285.02039	-1.28	4.69
Sulfapyridine	C ₁₁ H ₁₁ N ₃ O ₂ S	250.06447	250.06425	-0.88	3.69
Sulfaguanidine	C ₇ H ₁₀ N ₄ O ₂ S	215.05972	215.05949	-1.06	1.70
Sulfamoxol	C ₁₁ H ₁₃ N ₃ O ₃ S	268.07504	268.07468	-1.35	4.05
Sulfamethizole	C ₉ H ₁₀ N ₄ O ₂ S ₂	271.03179	271.03140	-1.44	4.18
Sulfisomidine	C ₁₂ H ₁₄ N ₄ O ₂ S	279.09102	279.09079	-0.84	3.4
Sulfamethoxypyridazine	C ₁₁ H ₁₂ N ₄ O ₃ S	281.07029	281.06979	-1.76	4.33
Sulfachloropyrazine	C ₁₀ H ₉ ClN ₄ O ₂ S	285.02075	285.02039	-1.28	5.30
Sulfadimoxine	C ₁₂ H ₁₄ N ₄ O ₄ S	311.07990	311.08038	-1.51	4.75
Sulfadiazine	C ₁₀ H ₁₀ N ₄ O ₂ S	251.05972	251.05940	-1.28	3.49
Sulfacetamide	C ₈ H ₁₀ N ₂ O ₃ S	215.04849	215.04825	-1.12	3.31
Sulfamerazine	C ₁₁ H ₁₂ N ₄ O ₂ S	265.07537	265.07465	-2.72	4.15
Sulfafurazole	C ₁₁ H ₁₃ N ₃ O ₃ S	268.07504	268.07468	-1.35	5.04
Sulfanitran	C ₁₄ H ₁₃ N ₃ O ₅ S	336.06487	336.06451	-1.05	5.93
Sulfametoxydiazine	C ₁₁ H ₁₂ N ₄ O ₃ S	281.07029	281.06979	-1.76	4.27
Sulfathiazole	C ₉ H ₉ N ₃ O ₂ S ₂	256.02089	256.02057	-1.27	3.70
Trimethoprim	C ₁₄ H ₁₈ N ₄ O ₃	291.14517	291.14468	-1.66	3.77
Enrofloxacin	C ₁₉ H ₂₂ FN ₃ O ₃	360.17180	360.17133	-1.31	4.01
Ciprofloxacin	C ₁₇ H ₁₈ FN ₃ O ₃	332.14050	332.14005	-1.36	3.86
Sarafloxacin	C ₂₀ H ₁₇ F ₂ N ₃ O ₃	386.13107	386.13031	-1.98	4.29
Danofloxacin	C ₁₉ H ₂₀ FN ₃ O ₃	358.15615	358.15509	-2.95	5.16
Difloxacin	C ₂₁ H ₁₉ F ₂ N ₃ O ₃	400.14672	400.14594	-1.97	4.34
Nadifloxacin	C ₁₉ H ₂₁ FN ₂ O ₄	361.15581	361.15527	-1.49	5.48
Sparfloxacin	C ₁₉ H ₂₂ F ₂ N ₄ O ₃	393.17327	393.17233	-2.39	4.28
Norfloxacin	C ₁₆ H ₁₈ FN ₃ O ₃	320.14050	320.14001	-1.50	3.81
Oxilinic acid	C ₁₃ H ₁₁ NO ₅	262.07100	262.07074	-0.99	4.98
Pefloxacin	C ₁₇ H ₂₀ FN ₃ O ₃	334.15615	334.15570	-1.33	3.84
Marbofloxacin	C ₁₇ H ₁₉ FN ₄ O ₄	363.14631	363.14518	-1.14	3.68
Orbifloxacin	C ₁₉ H ₂₀ F ₃ N ₃ O ₃	396.15295	396.15157	-1.40	4.03
Flumequine	C ₁₄ H ₁₂ FNO ₃	262.08740	262.07021	1.27	5.04
Nalidixic acid	C ₁₂ H ₁₂ N ₂ O ₃	233.09207	233.09175	-1.36	5.66
Cinoxacin	C ₁₂ H ₁₀ N ₂ O ₅	263.06625	263.06552	-2.77	4.69
Lomefloxacin	C ₁₇ H ₁₉ F ₂ N ₃ O ₃	352.14672	352.14621	-1.46	3.93
Ofloxacin	C ₁₈ H ₂₀ FN ₃ O ₄	362.15106	362.15045	-1.68	3.82
Fleroxacin	C ₁₇ H ₁₈ F ₃ N ₃ O ₃	370.13730	370.13618	-3.03	3.78
Mequindox	C ₁₁ H ₁₀ N ₂ O ₃	219.07642	219.07617	-1.13	4.00
Olaquindox	C ₁₂ H ₁₃ N ₃ O ₄	264.09788	264.09750	-1.43	3.01
Quinocetone	C ₁₈ H ₁₄ N ₂ O ₃	307.10772	307.10690	-2.73	6.01
Oxytetracycline	C ₂₂ H ₂₄ N ₂ O ₉	461.15546	461.15485	-1.32	3.83

Table 2 *Continued.*

Compound Name	Formula	[M+H] ⁺ Theoretical	Detected (m/z)	Delta (ppm)	RT
Tetracycline	C ₂₂ H ₂₄ N ₂ O ₈	445.16054	445.16003	-1.14	4.02
Chlortetracycline	C ₂₂ H ₂₃ ClN ₂ O ₈	479.12157	479.12106	-1.06	4.18
Doxycycline	C ₂₂ H ₂₄ N ₂ O ₈	445.16054	445.16003	-1.14	4.78
Metacycline	C ₂₂ H ₂₂ N ₂ O ₈	443.14489	443.14417	-1.64	4.65
Chloramphenicol	C ₁₁ H ₁₂ Cl ₂ N ₂ O ₅	321.00395[M-H] ⁻	321.00534	0.90	4.90
Thiamphenicol	C ₁₂ H ₁₅ Cl ₂ NO ₅ S	353.99643[M-H] ⁻	353.99786	0.97	3.87
Florfenicol	C ₁₂ H ₁₄ Cl ₂ FNO ₄ S	355.99209[M-H] ⁻	355.99472	3.45	4.75

B. Extraction procedure optimization

For a screening method, the generic extraction method that allowed the determination of multiclass compounds needed to establish at first. Depending on the nature of the feed sample and the target compounds, the extraction solution was selected according to the “Like Dissolves Like” principle. Hydrophilic solvents such as MeOH, ACN and H₂O were tested for the extraction procedure, and the hydrophilic solvents had three advantages: 1) feed samples mixed easily and extracted acceleratedly; 2) can effectively reduce the loss of adsorption of polar analytes; 3) can deproteinized and defatted. Method A: 6 mL MeOH/H₂O (50:50, v/v) extracted and 4 mL MeOH secondary extracted. Method B: ACN was used to extract like method A. The recoveries of method A and B were compared as shown as Fig. 2. It can be seen that program B shows better recoveries of 73 drugs.

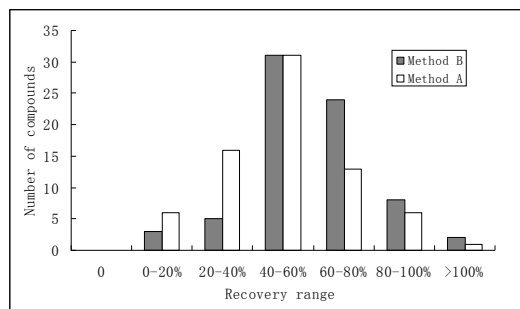


Fig. 2 Recovery results at different extraction method

C. Purification procedure optimization

In order to establish a generic purification method, two different program based on SPE were used to study with the workflows shown as Fig. 3. The blank matrix sample added concentration 1 µg/g was used in the two different purification programs to compare the recoveries.

In program A, four type cartridges were used to compare, such as SCX, MAX, MCX, and HLB. The recovery profile was shown in Fig. 4. The results of recoveries show that different cartridges have different selectivity. For example, after purified by SCX cartridge, the recoveries of macrolides are in range of 64% to 92%, but sulfonamides are not retained. Therefore, this purification method can't meet the requirement for multiclass drugs analysis.

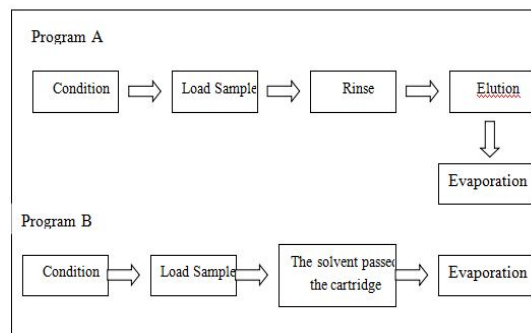


Fig. 3 Workflow of purification SPE programs

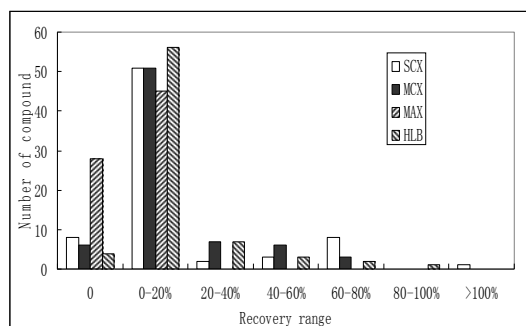


Fig. 4 Recovery results of program A

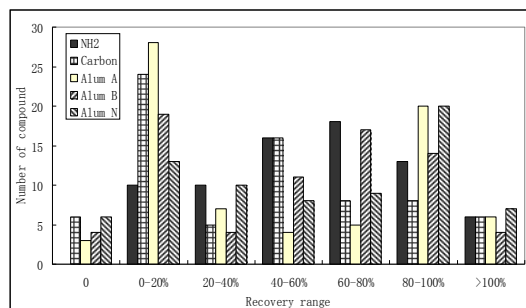


Fig. 5 Recovery results of program B

In program B, five type cartridges were used to compare, such as Alumina cartridges (Neutral, Acidic and Alkaline), NH₂ and Carbon cartridges. The recovery profile was shown in Fig. 5. The experimental results show that, for Alumina cartridges, the recoveries of tetracyclines and quinolones are extremely low; and for Carbon cartridges, the recoveries of quinolones are poor. However, for NH₂ cartridges, the recoveries of 73 drugs are

satisfying. Therefore NH₂ cartridges can be used to establish multiclass antibiotics analysis.

D. Method validation

The validation procedure for the developed method was carried out in order to ensure the adequate identification and quantification of the target compounds. Several parameters such as linearity, intra-day precision and limits of detection (LODs) were studied.

Three different blank feed matrices, including pre-mixture, concentrates, and compound feed, were added equal volumes of different concentrations of mixed standard solution with added in an amount of 100, 250, 500 ng/g feed, and then carried out according to the preparation method. The concentration of inject into the UPLC-MS were 40, 100, 200 ng/mL. LODs for the 73 antibacterials were calculated as ten times signal to noise ratio, respectively. The results were shown in Table 3. It can be seen that this proved method can meet the requirement of multiclass screening of animal feed.

Intra-day precision, or within-day reproducibility, is expressed as the average of the relative standard deviation (RSD%) of the areas obtained for each analyte after the replicate (n=6) analysis, and three different blank feed matrices fortified at the level (2.5 µg/g) with all 73 analytes during the same day. The results were shown in Table 3. The recoveries of different class feed prove that the combined capability of different component feeds and different drugs is obvious distinction.

For internal standard based quantification, six point calibration curves, were constructed using least-squares linear regression analysis based on peak areas, from application of the overall method to blank matrix extraction containing the standard antibiotic mixture at concentrations ranging from 10 to 1000 ng/mL. The data proved that validation linearity range of macrolides, tetracyclines, β—lactams, quinoxalines is 50-1000 ng/mL, and sulfonamides, quinolones, lincosamides, amphenicols are 10-1000 ng/mL. The correlation coefficients (r^2) were shown in Table 3.

Table 3 Summary of validation results (part of drugs)

Compound Name	Correlation Coefficient (r^2)	Recovery/%(n=6)			RSD/%(n=3)			LOD (ng/g)		
		A	B	C	A	B	C	A	B	C
Cephalexin	0.9946	14.07	38.20	30.62	5.6	16.6	22.0	6.0	9.8	17.5
Oxacillin	0.9981	45.68	71.10	24.28	1.7	12.3	5.5	10.9	18.5	26.3
Flucloxacillin	0.9980	48.04	52.90	19.36	5.5	11.0	10.4	131.6	156.3	119.0
Cefradine	0.9992	46.93	59.17	50.30	3.2	7.9	7.6	8.4	6.4	8.7
Lincomycin	0.9966	75.64	127.69	108.52	7.4	4.2	7.2	2.3	1.5	9.2
Clindamycin	0.9980	58.83	75.46	75.76	8.8	2.6	8.1	2.1	1.2	1.3
Tylosin	0.9999	50.50	50.84	35.77	4.5	5.1	5.6	6.1	7.9	11.5
Tiamulin	0.9989	69.64	65.31	59.29	6.1	5.4	34.4	0.5	0.8	0.9
Tilmicosin	0.9993	111.48	125.81	94.05	4.5	12.0	12.7	5.5	5.8	3.8
Azithromycin	0.9857	109.09	114.17	98.44	6.2	4.0	8.6	2.4	1.8	3.6
Erythromycin	0.9996	65.78	66.82	50.61	0.3	5.1	10.4	0.4	1.3	0.7
Natamycin	0.9995	20.54	27.18	29.30	4.1	10.0	21.7	23.8	55.6	13.9
Sulfamonomethoxine	0.9994	54.47	74.90	68.33	6.7	3.5	12.4	0.7	0.7	0.8
Sulfamethoxazole	0.9996	49.34	70.14	74.62	5.3	8.0	15.7	1.5	1.2	0.9
Sulfadimethoxine	0.9980	73.76	76.06	67.62	4.5	9.4	10.2	1.4	1.2	1.5
Sulfaquinoxaline	0.9992	56.66	72.84	70.24	5.9	4.9	10.5	1.0	0.7	1.0
Sulfachlorpyridazine	0.9991	49.13	63.42	72.82	10.2	12.5	15.5	5.0	4.2	4.7
Sulfapyridine	0.9980	48.03	61.05	62.96	7.2	7.6	2.3	0.4	0.3	1.5
Sulfamoxol	0.9997	70.12	75.81	24.06	1.8	3.8	10.0	0.9	1.0	5.0
Sulfamethizole	0.9996	48.30	69.34	65.28	5.0	6.0	10.6	2.0	3.0	2.2
Sulfadimoxine	0.9968	81.63	70.59	57.55	3.3	6.7	12.9	1.5	1.0	1.5
Enrofloxacin	0.9962	24.48	36.14	19.15	3.2	5.9	13.2	14.7	3.0	3.8
Ciprofloxacin	0.9986	8.84	25.44	11.22	5.3	14.0	24.4	14.3	4.3	90.9

Table 3 *Continued.*

Compound Name	Correlation Coefficient (r^2)	Recovery/%(n=6)			RSD/%(n=3)			LOD (ng/g)		
		A ^a	B ^b	C ^c	A	B	C	A	B	C
Sarafloxacin	0.9983	29.53	34.51	14.27	4.2	5.7	19.7	3.1	5.1	5.5
Difloxacin	0.9993	42.56	51.62	18.60	2.9	1.7	15.7	90.9	8.5	10.4
Nadifloxacin	0.9993	61.54	0.85	57.10	16.1	7.3	3.5	2.5	78.1	2.2
Pefloxacin	0.9998	13.80	23.20	23.47	4.9	3.0	23.7	6.0	8.5	76.9
Mequindox	0.9960	68.96	82.29	78.44	5.8	3.5	5.7	3.0	11.0	32.3
Olaquindox	0.9982	73.66	117.40	73.46	11.5	10.2	17.5	4.7	2.5	2.7
Quinocetone	0.9880	57.38	71.60	51.89	0.1	4.6	9.2	2.0	1.8	2.1
Oxytetracycline	0.9894	2.68	10.03	0.34	14.5	7.4	/ ^d	11.6	35.7	27.0
Tetracycline	0.9978	10.66	29.32	0.97	14.7	12.4	/	14.1	2.4	45.5
Chlortetracycline	0.9822	6.01	99.22	0.04	15.0	19.1	/	58.5	1.3	/
Doxycycline	0.9964	11.97	27.22	2.23	5.9	4.9	17.3	29.4	8.6	47.2
Chloramphenicol	0.9864	87.55	96.82	88.89	9.9	11.5	19.1	0.7	5.2	0.8
Thiamphenicol	0.9929	100.76	99.04	129.64	11.0	10.5	9.5	2.5	3.3	1.2
Florfenicol	0.9971	98.99	99.23	129.08	6.2	11.1	8.1	2.8	8.3	2.1

^a Concentrate feed; ^b Compound feed; ^c Pre-mixture feed; ^d not detected.

E. Sample analysis

The method applicability was assessed by analyzing 15 feed commodities, including 5 pre-mixtures, 5 concentrates, and 5 compound feeds. Chlortetracycline was detected in one pig compound feed at 8.5 µg/g feed.

The extracted ion chromatogram was shown in Fig. 6. It can be seen the peak width of the standard is less than that the real feed sample, and the real sample can be identified by the retention time.

The isotopic abundance was shown in Table 4. It is noteworthy that the results obtained by using ToxID automated screening have some false positives. Therefore, the manual confirmation is necessary.

Table 4 Comparing of isotopic pattern about chlortetracycline in a real feed sample

Sample type	Isotopic patterns (m/z)			Relative abundance		
Theoretical	479.12157	480.12492	481.11862	100.00	23.79	31.96
Standard	479.12096	480.12450	481.11767	100.00	24.78	30.60
Matrix added standard	479.12071	480.12432	481.11771	100.00	25.81	29.86

The proposed method was compared to that of reference [12] and [15]. It shows that the recovery, RSD, LOD of the proposed method are comparable to the reported results with automated screening based on the developed database.

IV. CONCLUSION

A multiclass analytical method was developed for determination of 73 antibacterials with 8 families in feed by

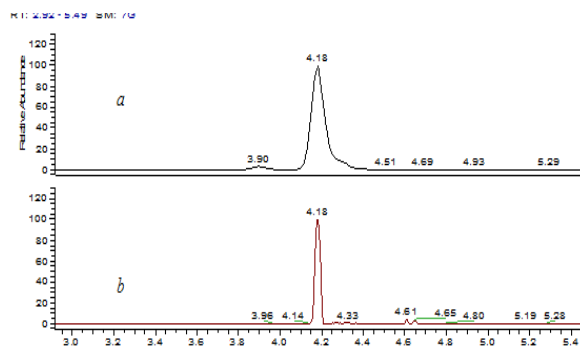


Fig. 6 Extraction ion chromatograms of real feed sample (a) and standard solution (b)

UPLC–Orbitrap–MS. The generic methods of instrumental analysis and pretreatment can facilitate the determination of a wide range of compounds. And the database including retention time, characteristic ions and accurate mass information of the target compounds can be used to automate screening of the analytes through ToxID. The proposed method is practical with the recoveries 34.51%-129.64%, RSD 0.1%-24.4% and LODs 0.3-156.3 ng/g.

ACKNOWLEDGMENT

The authors are grateful to the experts from Henan Institute of Veterinary Drug Control of China for their assistance of providing some antibiotics drugs standards.

REFERENCES

- [1] M.D. Barton MD, "Antibiotic use in animal feed and its impact on human health," *Nutr. Res. Rev.*, vol. 13, no. 2, pp. 279-300, Feb. 2000.
- [2] M. Gaugain-Juhel, B. Delépine, S. Gautier, M-P Fourmond, V. Gaudin, D. Hurtaud-Pessel, E. Verdon, and P. Sanders, "Validation of a liquid chromatography-tandem mass spectrometry screening method to monitor 58 antibiotics in milk: a qualitative approach," *Food Add. Contam.*, vol. 26, no. 11, pp. 1459-1471, Nov. 2009.
- [3] L. Kantiani, M. Farré, and D. Barceló, "Development and validation of a pressurized liquid extraction liquid chromatography-electrospray-tandem mass spectrometry method for β -lactams and sulfonamides in animal feed," *J. Chromat. A*, vol. 1217, no. 26, pp. 4247-4254, Mar. 2010.
- [4] I. Pecorelli, R. Galarini, R. Bibi, A. I. Floridi, E. Casciarri, and A. Floridi, "Simultaneous determination of 13 quinolones from feeds using accelerated solvent extraction and liquid chromatography," *Anal. Chim. Acta*, vol. 483, no. 1, pp. 81-89, Apr. 2003.
- [5] S. Croubels, P. Wassink, and P. DeBacker, "Simultaneous determination of sulfadiazine and trimethoprim in animal feed by liquid chromatography with UV and tandem mass spectrometric detection," *Anal. Chim. Acta*, vol. 473, no. 1, pp. 183-194, Aug. 2002.
- [6] C. Van Poucke, K. DeKeyser, A. Baltusnikiene, J. McEvoy, and C. Van Peteghem, "Liquid chromatographic-tandem mass spectrometric detection of banned antibacterial growth promoters in animal feed," *Anal. Chim. Acta*, vol. 483, no. 1, pp. 99-109, May 2003.
- [7] V. Jimenez, J. Adrian, J. Guiteras, M-P Marco, and R. Companyo, "Validation of an enzyme-linked immunosorbent assay for detecting sulfonamides in feed resources," *J. Agr. Food Chem.*, vol. 58, no. 13, pp. 7526-7531, Jun. 2010.
- [8] L. Kantiani, M. Farré, J. M. G. Freixedas, and D. Barceló, "Determination of antibacterials in animal feed by pressurized liquid extraction followed by online purification and liquid chromatography-electrospray tandem mass spectrometry," *Anal. Bioanal. Chem.*, vol. 398, no. 3, pp. 1195-1205, Mar. 2010.
- [9] R. Liu, P. He, Z. Li, and R. Li R, "Simultaneous Determination of 16 Sulfonamides in Animal Feeds by UHPLC-MS-MS," *J. Chromat. Sci.*, vol. 49, no. 8, pp. 640-646, Aug. 2011.
- [10] T. MingChih, and S. BorLing, "Determination of tetracyclines in feed, chicken blood, muscle and liver by liquid chromatography tandem mass spectrometry," *J. Taiwan Livestock Res.*, vol. 42, no. 4, pp. 351-360, Apr. 2009.
- [11] R. Peters, Y. Bolck, P. Rutgers, A. Stolker, and M. Nielen, "Multi-residue screening of veterinary drugs in egg, fish and meat using high-resolution liquid chromatography accurate mass time-of-flight mass spectrometry," *J. Chromat. A*, vol. 1216, no. 46, pp. 8206-8216, Oct. 2009.
- [12] M. I. Lopez, J. S. Pettis, I. B. Smith, and P-S Chu, "Multiclass determination and confirmation of antibiotic residues in honey using LC-MS/MS," *J. Agr. Food Chem.*, vol. 56, no. 5, pp. 1553-1559, May 2009.
- [13] C. ChiaoChan, U. Koesukkiwat, S. Yudthavorasit, and N. Leepipatpiboon, "Efficient hydrophilic interaction liquid chromatography-tandem mass spectrometry for the multiclass analysis of veterinary drugs in chicken muscle," *Anal. Chim. Acta*, vol. 682, no. 1, pp. 117-129, Aug. 2010.
- [14] A. Stolker, P. Rutgers, E. Oosterink, J. Lasaroms, R. Peters, J. Van Rhijn, and M. Nielen, "Comprehensive screening and quantification of veterinary drugs in milk using UPLC-ToF-MS," *Anal. Bioanal. Chem.*, vol. 391, no. 6, pp. 2309-2322, Mar. 2008.
- [15] E. Van der Heeft, Y. Bolck, B. Beumer, A. Nijrolder, A. Stolker, and M. Nielen M, "Full-scan accurate mass selectivity of ultra-performance liquid chromatography combined with time-of-flight and orbitrap mass spectrometry in hormone and veterinary drug residue analysis," *J. Am. Soc. Mass Spectr.*, vol. 20, no. 3, pp. 451-463, Feb. 2009.
- [16] A. Makarov, "Electrostatic axially harmonic orbital trapping: a high-performance technique of mass analysis," *Anal. Chem.*, vol. 72, no. 6, pp. 1156-1162, Mar. 2000.
- [17] Y. Luo, T. Li, F. Yu, T. Kramer, and I. M. Cristea, "Resolving the composition of protein complexes using a MALDI LTQ Orbitrap," *J. Am. Soc. Mass Spectr.*, vol. 21, no. 1, pp. 34-46, Jan. 2010.
- [18] S. A. Müller, T. Kohajda, S. Findeß, P. F. Stadler, S. Washietl, M. Kellis, M. vonBergen, and S. Kalkhof S, "Optimization of parameters for coverage of low molecular weight proteins," *Anal. Bioanal. Chemistry*, vol. 398, no. 7-8, pp. 2867-2881, Apr. 2010.
- [19] L. Van Meulebroek, J. V. Bussche, K. Steppe, and L. Vanhaecke, "Ultra-high performance liquid chromatography coupled to high resolution Orbitrap mass spectrometry for metabolomic profiling of the endogenous phytohormonal status of the tomato plant," *J. Chromat. A*, vol. 1260, no. 19, pp. 67-80, Oct. 2012.
- [20] L. MacIntyre, L. Zheng, P. Scullion, P. Keating, and D. G. Watson, "Metabolomic profiling of biomarkers of liver X receptor-induced toxicity in mouse liver tissue," *Metabolomics*, vol. 7, no. 1, pp. 54-70, Apr. 2011.
- [21] E. Viryus, T. Sobolevskii, and G. Rodchenkov, "Detection of oxandrolone and its metabolite in urine by high-performance liquid chromatography-high-resolution mass spectrometry with atmospheric pressure chemical ionization and orbitrap detection after ceasing drug administration," *J. Anal. Chem.*, vol. 64, no. 1pp. 31-35, Jan. 2009.
- [22] A. Thomas, H. Geyer, W. Schänzer, C. Crone, M. Kellmann, T. Moehring, and M. Thevis, "Sensitive determination of prohibited drugs in dried blood spots (DBS) for doping controls by means of a benchtop quadrupole/Orbitrap mass spectrometer," *Anal. Bioanal. Chem.*, vol. 403, no. 5, pp. 1279-1289, Mar. 2012.
- [23] A. Hogenboom, J. Van Leerdam, and P. de Voogt, "Accurate mass screening and identification of emerging contaminants in environmental samples by liquid chromatography-hybrid linear ion trap Orbitrap mass spectrometry," *J. Chromat. A*, vol. 1216, no. 3, pp. 510-519, Jan. 2009.
- [24] J. A. van Leerdam, A. C. Hogenboom, M. M. van der Kooi, and P. de Voogt, "Determination of polar 1H-benzotriazoles and benzothiazoles in water by solid-phase extraction and liquid chromatography LTQ FT Orbitrap mass spectrometry," *Int. J. Mass Spectr.*, vol. 282, no. 3, pp. 99-107, Mar. 2009.
- [25] M. Nielen, M. Van Engelen, R. Zuiderent, and R. Ramaker, "Screening and confirmation criteria for hormone residue analysis using liquid chromatography accurate mass time-of-flight, Fourier transform ion cyclotron resonance and orbitrap mass spectrometry techniques," *Anal. Chim. Acta*, vol. 586, no. 1, Nov. 122-129, Spt. 2007.
- [26] S. E. Edison, A. Lin, and L. Parrales, "Practical considerations for the rapid screening for pesticides using ambient pressure desorption ionisation with high-resolution mass spectrometry," *Food Add. Contam. A*, vol. 28, no. 10, pp.1393-1404, Oct. 2011.
- [27] M. Kellmann, H. Muenster, P. Zomer, and H. Mol, "Full scan MS in comprehensive qualitative and quantitative residue analysis in food and feed matrices: how much resolving power is required?" *J. Am. Soc. Mass Spectr.*, vol. 20, no. 8, pp. 1464-1476, Aug. 2009.
- [28] M. L. Gómez-Pérez, P. Plaza-Bolaños, R. Romero-González, J. L. Martínez-Vidal, and A. Garrido-Frenich, "Comprehensive qualitative and quantitative determination of pesticides and veterinary drugs in honey using liquid chromatography-Orbitrap high resolution mass spectrometry," *J. Chromat. A*, vol. 1248, no. 27, pp. 130-138, Jul. 2012.
- [29] A. Kaufmann, P. Butcher, K. Maden, S. Walker, and M. Widmer, "Development of an improved high resolution mass spectrometry based multi-residue method for veterinary drugs in various food matrices," *Anal. Chim. Acta*, vol. 700, no. 1-2, pp. 86-94, Aug. 2011.

Scaling-Up Liquid-Liquid Extraction Experiments with Deep Eutectic Solvents

Emad Ali, Sarwono Mulyono, Mohamed Hadj-Kali

Abstract—New generation of green solvents, known as Deep Eutectic Solvents, have emerged as potential alternatives to conventional solvents in many industrial applications. Among these applications, removing sulfuric compounds from fuel oil is receiving much interest because organic sulfides becoming a serious source of pollution. The separation of aromatic and aliphatic hydrocarbons having the same number of carbon atoms is also a challenging process especially at low aromatic concentration. Deep Eutectic Solvents were utilized for the separation of aromatics using liquid-liquid extraction method and both the distribution ratio and selectivity were higher than that for sulfolane which is the most used solvent in industry. Laboratory scale results demonstrated the benefits of DESs in this separation operation. In this work the use of a pilot plant scale centrifugal extraction multi-stage unit is studied for the separation of thiophene from a mixture of thiophene and heptane. The pilot plant is being used for the validation of previous laboratory scale results. This could constitute a very important step towards the implementation of this method in industrial scale.

Keywords— Liquid-Liquid Extraction, Deep Eutectic Solvents, Scale Up.

I. Introduction

In recent years, many petrochemical transformation companies embarked in building refineries with special interests on aromatics production. In fact, these companies are investigating the possibility of adding aromatics as a key component in the existing refineries. The produced aromatics would be processed into downstream products, and then exported. In order to economically and technically utilize aromatics they must be separated from aliphatic compounds that are usually present in the refinery mixture.

The type of process used for the separation of aromatics from their mixture of corresponding aliphatic hydrocarbons depends on the concentration of the aromatic in the feed. For example, extraction is used when the concentration is in the range of 20–65 wt.%, while extractive distillation is used for the range of 65–90 wt.%. In addition, azeotropic distillation is used when the concentration of aromatics is higher than 90 wt.% [1,2]. However, when the concentration of aromatics is small, i.e. less than about 20 wt.%, there is no separation process that can be used efficiently and economically [3].

The difference in solubility of the components to be separated is the basis for the well known liquid-liquid extraction (LLE) process. In this case a solvent is added to original solution and the whole mixture is splitted into two immiscible phases. The added solvent should have the ability to extract the desired component from the original solution. Examples of solvents used in LLE include sulfolane, ethylene glycol, n-methyl pyrrolidone, and n-formylmorpholine. However, it was found that an additional step is needed to separate the solvent from both phases. This in turn will increase the cost of investments and the energy consumption [2]. The use of solvent especially ionic liquids (ILs) for LLE process has received attention due to its successful application in removal of sulfur-containing compounds in gasoline fuel. The technology is known as deep extractive desulfurization of fissile fuel which became an urgent object in refinery and petrochemical industries in order to meet the stringent regulations in Europe and USA [4,5]. Under this context, many researchers have been developing new innovative methods. Among all these new processes, extractive desulfurization appears to be especially promising because it is clean, cheap due to low energy demand, requires mild operation conditions and simplistic operation option. Hence, researching efforts over the last years are being focused on finding the most suitable solvent for deep desulfurization purposes [6].

Maria et al [7] reviewed the role of Ionic Liquids on desulfurization of fuel oils. Among these salts, the pyridiniums delivered the most promising results on sulfur reduction by simple liquid-liquid extraction. Liquid-liquid equilibrium data for ternary system was developed. The phase equilibrium can help to design and simulate multistage separation process. Chu et al. [8] studied the extraction of sulfur from diesel fuel using [BF₄] based IL. They showed that the absorption capacity depends on the size and structure of the IL. They showed the best rate of desulfurization can reach up to around 40%. Wang et al. [9] tested several ILs from the removal of sulfur-containing compounds from gasoline at room temperature. They found that [BPy]BF₄ had the best selective extraction rate of 45.5% in one cycle and up to 96% in six cycles. They also reported that the anion, cation structure and size of IL are important factors affecting the recovery rate. Yi et al. [10] show that the alkylimidazole solvent and/or its mixture with an IL can be used as a potential extractant for the extractive desulfurization of fuel oils. The used S-containing solvent can be regenerated by a water diluting process followed by simple distillation. Luisa et al. [11] analyzed the use of IL [C8mim][BF₄], as solvent for desulfurization of gasoline by liquid-liquid extraction. Results showed that solvent extraction of thiophene and dibenzothiophene is possible. After three stages the composition of thiophene is reduced by 79 wt % and that of dibenzothiophene is reduced by 87 wt %.

Emad Ali, Sarwono Mulyono, Mohamed Hadj Kali
Chemical Engineering Department/King Saud University
Riyadh, Saudi Arabia, P.O.box 800, 11421
amkamal@ksu.edu.sa, smulyoprayitno@ksu.edu.sa, mhadjkali@ksu.edu.sa

Jiang and co-workers [12] demonstrated the effectiveness of few ILs on the removal of aromatic sulfur compounds in fuel oil. The results suggest that [EEIM][DEP] might be used as a promising solvent for the extractive desulfurization of fuel. The preference is based on its higher sulfur extractive ability, lower solubility for fuel and thus negligible influence on the constituent of fuel, and the ease of regeneration for the spent IL via water dilution process. Lusia et al. [13] tested the ionic liquid 1-ethyl-3-methylimidazolium ethylsulfate as solvent for the separation of thiophene from aliphatic hydrocarbons. The phase diagrams for the ternary mixtures including both the experimental and calculated tie-lines have been presented.

In the past decade, ILs analogues, called deep eutectic solvents (DESs), have emerged as alternatives to conventional solvents and ILs themselves [14-16]. A DES is a mixture of two or more components that has a melting point less than that of any of its components. DESs are usually composed of salts, a hydrogen-bond donor (HBD), or a complexing agent. DESs have many advantageous over ILs. They are easily synthesized and thus the purity of the DES is not an issue. Their cost depends on the cost of used components. By a carefully choosing the components of the DES we can get non-toxic and biodegradable solvents. In addition, most DESs do not react with water. Some applications that used DESs as solvents include but are not limited to electrochemical processes, purification of palm [16], enzyme catalysis [17], and electrochemical applications [18].

Recently, we showed that low cost DESs can be used for the separation of aromatics using liquid-liquid extraction method. Both the distribution ratio and selectivity were higher than that for sulfolane which is the most used solvent in industry. The results were published in high esteemed journals [19-21]. Similarly, Changping et al. [22] investigated the use of DES in deep desulfurization of fuel. In optimal conditions, the extraction efficiency can reach as high as 82.83% for one cycle and 99.8% in five cycles. Despite, the solvent type, e.g. IL or Des, all previous research work focused on LLE at the lab scale. To our knowledge no effort, at least for the DES, of using extractive desulfurization on pilot plant scale was reported. In fact, in order to industrially implement the use of DES for LLE processes and particularly in deep desulfurization, pilot plant scale experiments must be conducted and the operational parameters should be optimized.

II. Experimental Protocol

A. Chemicals

Pure grade compounds thiophene, n-heptane, tetrabutylammonium bromide, choline chloride were purchased from Acros Organics (Belgium), ethylene glycol and pyridine from Panreac (Spain). All chemicals were of high purity (>99%) and used without any further purification. The DESs was prepared according to the method described by Abbott et al [14].

B. Lab Scale Protocol

DES1 was prepared using tetrabutylammonium bromide salt and pyridine with a molar ratio of 1:8 while DES2 was prepared using choline chloride : ethylene glycol with a molar ratio of 1:4. The mixture was put in screw-capped bottles and then stirred in an incubating-shaker equipped with temperature (± 0.1 °C) and speed control at a temperature of 100°C with a rotational speed of 200 rpm until a clear liquid was formed. In the other hand, feed mixture containing 10 wt% of thiophene in n-heptane was prepared by mixing weighed amounts of the chemicals using an analytical balance (± 0.0001 g).

The feed was then mixed with the DESs in a mass ratio of 1:1. Each set of experiments was conducted at 25°C. The vials were placed in the incubator shaker. The shaking time was six hours followed by a settling time of about 12 hours to guarantee that the equilibrium state was completely attained. Samples were taken from the top and bottom layers and analyzed using a HPLC.

C. Analysis

Samples from the top and bottom layers were withdrawn using a syringe and then diluted using 2-propanol. The samples were analyzed using a HPLC Agilent 1100 series with a zorbax eclipse xdb-c8 column. The temperature of the column oven was set to 30 °C. The mobile phase was acetonitrile and distilled water with a volume ratio of 3 : 1. The flow rate of the mobile phase was 1.4 ml min^{-1} with a pressure of 120 bars. The uncertainty in the reported concentrations was estimated to be 0.001 wt% (10 ppm). The measured composition at equilibrium in both liquid phases is shown in Table 1 and the ternary phase diagram is given in Fig. 1. The reliability of the experimental data have been ascertained by using Othmer-Tobias and Hand correlations where the regression coefficients R^2 obtained was close to unity indicating the degree of consistency.

The distribution (D) and selectivity (S) of thiophene at equilibrium is given Table 2, which indicate that DES has higher selectivity at small thiophene mole fraction. Therefore, the solvent is more effective for fuel with traces of and/or diluted thiophene mixture.

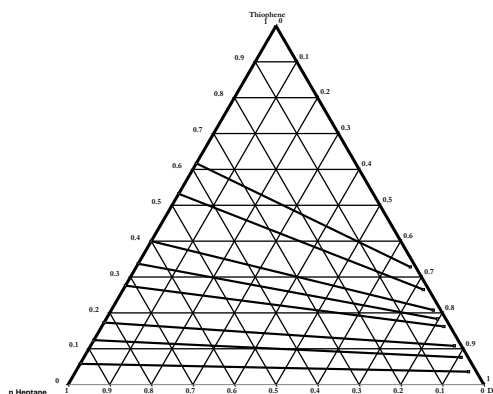


Figure 1: Ternary phase diagram for thiophen-DES-heptane system

TABLE 1: Composition of the experimental tie lines for the ternary system thiophene-DES-n-heptane

Feed			Top Layer			Bottom Layer			D	S
Thiophene	Heptane	DES	Thiophene	Heptane	DES	Thiophene	Heptane	DES		
0.050	0.452	0.498	0.058	0.942	0.000	0.036	0.019	0.945	0.625	30.660
0.103	0.399	0.498	0.124	0.876	0.000	0.076	0.017	0.907	0.619	32.580
0.152	0.349	0.500	0.173	0.827	0.000	0.108	0.017	0.875	0.622	29.772
0.205	0.299	0.496	0.276	0.724	0.000	0.162	0.015	0.823	0.587	28.287
0.252	0.252	0.496	0.337	0.663	0.000	0.183	0.020	0.797	0.544	18.287
0.300	0.202	0.499	0.400	0.600	0.000	0.208	0.018	0.774	0.519	16.832
0.349	0.151	0.500	0.532	0.468	0.000	0.265	0.014	0.722	0.497	16.755
0.402	0.100	0.498	0.617	0.383	0.000	0.328	0.013	0.659	0.531	15.597

III. Pilot Plant Description and Methodology

A. Unit description and nomenclature

The pilot plant setup under consideration for the study of liquid-liquid extraction (LLE), is a 3-stage LLE unit (BP 17-3) designed and built in collaboration with SOLTEQ® (Malaysia). It is an intermediate size unit that is destined for research purposes and which may take up to 10liters of both heavy and light liquids.

The unit consists of mainly three sets of liquid-liquid centrifugal separators, two storage tanks for placing the heavy and light liquid phases, and a pumping and heating circuit (see Fig. 2 and the components nomenclature Table 2). The unit is also supplied with suitable instruments for process monitoring. A data acquisition system is furnished for automatic and continuous recording of operating parameters.

This pilot plant unit has been built after collaborative design work between university and an engineering constructor; it is intended for research work dealing with the optimization of the different operating process parameters such as flow rates, temperatures, number of stages, etc... It is the result of several years of research dealing with liquid-liquid extraction studies particularly with the use of deep eutectic solvents (DESs). As typical liquid-liquid extraction equipment, this pilot plant is schematically shown in Fig. 2 and described in Table 1. In addition, not shown in diagram, the unit contains Thermostat circuit for temperature control using a bath and 2 heat exchangers and an acquisition/control computerized system.

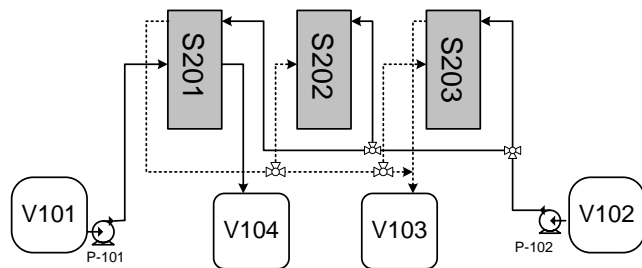


Figure 2: Simplified schematic of the pilot plant

TABLE 2: NOMENCLATURE OF PILOT PLANT UNIT

unit	Description
S-201	Stainless steel Motorized Centrifugal extractors :
S-202	Max flowrate 1.9Lpm; hold-up vol 0.2L; motor 1/8hp and
S-203	max 3450rpm
V-101	Light Phase Feed Tank :
	Stainless steel cylindrical vessel, max. capacity 10L
V-102	Heavy Phase Feed Tank :
	Stainless steel cylindrical vessel, max. capacity 10L
V-103	Light Phase Collection Tank :
	Stainless steel cylindrical vessel
V-104	Heavy Phase Collection Tank :
	Stainless steel cylindrical vessel
P-101	Light Phase Pump :Motor 0.05kW, capacity 2.5Lpm, 3bar
P-102	Heavy Phase Pump :Motor 0.15kW, capacity 2.5Lpm, 8bar

The pilot plant comprises a number of pumps and valves which allow circulating fluid phases through 1-, 2- or 3-stage scenarios. For instance, only S201 should be used for the 1-stage operation by setting valves directions in the correct manner (preventing flows through the S-202 and S-203 centrifugal extractors); also, the S-202 and S-203 may be included for 2- or 3- stage operation. To optimize the extraction operation, the centrifugal speed may be adjusted by acting on the motor controls via the acquisition/control system.

B. Experimental procedure

1. Set all valves on the correct directions (for the 1-, 2- or 3-stage operations)
2. Fill tank V101 with light phase, V102 with heavy phase
3. Turn on unit machine
4. Turn on computer and run the solteq software
5. Turn on extractors (S201, S202 and S203) depending on the flow scenario and set the speed
6. Turn on the pumps and set the speed
7. Let the operation run until the solutions are completely transferred from the supply tanks to the collection ones.
8. After stopping the pumping, turn off the solteq machine
9. Analysis the collected solutions in V103 for light phase and V104 for heavy phase
10. Save data temperatures and flow rate from the acquisition software.

C. Experimental methodology

During this preliminary scale-up study, it is intended to reproduce previous typical laboratory scale results on much larger scale. Experiments were performed for a given DES with the same components molar ratio for three scales runs, i.e.:

- 10g,
- 100g, and
- 1000 ~2000g scales.

So, for the extraction experiments, the percentage recovery (i.e. extracted thiophene) is targeted in different scales studied. The pilot plant is operated at atmospheric pressure and room temperature. One stage is used with centrifugal pump runs at 3000rpm. The experiment lasted 30 minutes. At the end of the experiment, samples were taken from the heavy and light phase tanks and analyzed by HPLC, screen capture of the analysis is shown in Figs. 3 and 4. The peak corresponding to thiophene is zoomed inside each figure. The weight percentage of thiophene in both phases is determined by fitting its HPLC magnitude in the pre-designed calibration diagram. Consequently, the weight percent extraction of thiophene is calculated using the following correlation:

$$E\% = \frac{\text{thiophene wt\% in heavy phase}}{\text{thiophene wt\% in heavy phase} + \text{thiophene wt\% in light phase}}$$

IV. Preliminary Scale-Up Results

Scale-up is an important stage for the passage from laboratory apparatus to industrial installation. Various process parameters and long term effects have to be investigated in order to optimize the operating condition. The preliminary runs performed concern the extraction of thiophene from heptane. This mixture mimics the gasoline fuel which usually contains thiophene, heptane and other heavy hydrocarbons. Starting from the same initial weight percent (10 wt%) and DES molar ratio (1:8), typical results are summarized in table 3. The first four runs in Table 3 are based on lab scale tests, among them three repeated ones at 10gm scale denoted as A, B, and C. The condition of the model oil and solvent is exactly the same for that used in the lab scale for fair comparison. The result of the pilot plant scale, which is also based on 1000g is listed at the bottom of the table. Shortage of raw materials availability limited the results at this initial stage of the study.

It can be seen from table 3, that the % extraction of thiophene from lab scale runs (triplicate values) had an average value of about 46 (with a standard deviation 1 %).

TABLE 3: SUMMARY OF LAB AND PILOT PLANT TESTS

Run No	System	% of thiophene extracted
1	DES1_10_A	47.5
2	DES1_10_B	47.6
3	DES1_10_C	45.2
4	DES1_100	53.7
5	Pilot plant DES1	41.1

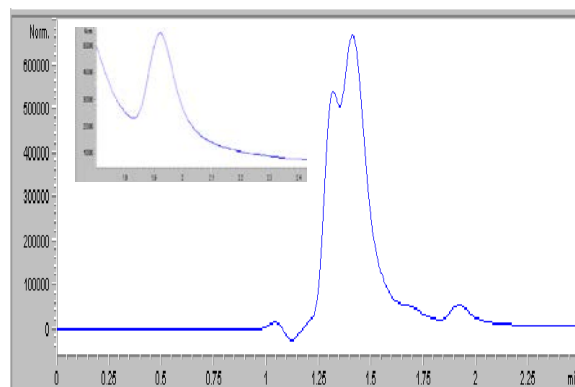


Figure 3: HPLC diagram for heavy phase showing DES and thiophene

The 100 g scale resulted in value of 54%, while that of the pilot scale was about 41%. The results show that thiophene recovery is increased as weight of solution is increased from 10 g to 100 g. Moreover, the pilot plant result confirms the percentage recovery obtained at lab scale.

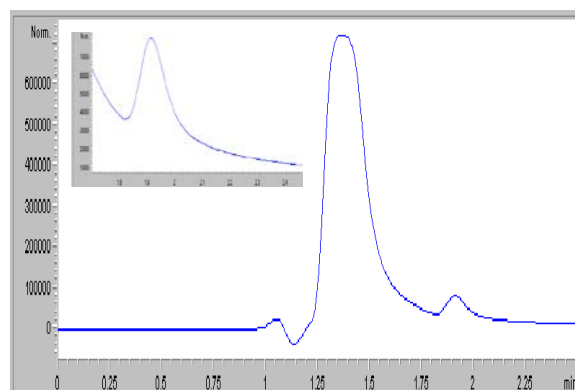


Figure 4: HPLC diagram for light phase showing DES and thiophene

Despite lack of repetitions for the last two scales, results are somewhat comparable and the same order of magnitude. Our extraction results are very comparable with those in the literature for them type of oil mixture. For example, Wang et al. [9] studied the extraction of thiophene from thiophene, n-heptane, xylol mixture. The reported sulfur removal percentage, with IL to oil mass ratio is 1:1, ranges from 21.8% to 45.5% depending on the type of IL used. This means the proposed DES in this work has slightly better extraction ability. However, we used binary oil mixture while ternary oil mixture is utilized in [9]. They have found that increasing the ratio of oil to IL, i.e. using less IL, the extracting ability reduces. Moreover, the extraction efficiency increases slightly with temperature. These parameter need to be assessed using pilot scale operations. Luisa et [11,13] showed that using [C8mim][BF4] IL, thiophene recovery can reach 79 wt% when three cycles are used. However, they used somehow different oil mixture. For example, they tested oil solution containing, thiophene in i-octane, in n-hexan, or in toluene. Changping et al. [22] has investigated the effect of the separation parameter such as temperature, extraction time,

phase ratio of model oil to DES, and initial concentration of sulfur compounds in the oil. However, the effect of parameters needs to be further assessed during upscale stage because continuous operation involve other factors such as feed flow rate, impurities, recycle, deactivation, etc. Therefore, in out next steps, more runs are scheduled for this scale up work during which optimization aforementioned parameters will be conducted.

v. Conclusions

The use of Deep Eutectic Solvents for Liquid-Liquid Aromatic/Aliphatic Hydrocarbon using a pilot plant Separation has been tackled in this work. In particular, scale up from 10g to more than 1000g has been explored; preliminary results showed that extraction efficiencies (here %extraction of thiophene) are comparable between the different scale up magnitudes (10g, 100g, and 1000g, respectively). Despite lack of repetitions especially for the 100g and the pilot scales, results are encouraging. Nevertheless, DES used here is proven to be a good solvent to separate Hydrocarbon mixture that is difficult to separate using conventional methods such as distillation. More elaborate work is scheduled for the near future particularly for the optimization of process parameters which will enhance the liquid-liquid separation of Aromatic/Aliphatic Hydrocarbon.

vi. References

- [1] V.A. Dukhande, T. S. Choksi, S. U. Sabnis, A. W. Patwardhan and A. V. Patwardhan. "Separation of toluene from n-heptane using monocationic and dicationic ionic liquids." *Fluid Phase Equilibria* 342(0): 75-81, 2013.
- [2] Y. Hou, Y. Gu, S. Zhang, F. Yang, H. Ding, Y. Shan, "Novel binary eutectic mixtures based onimidazole", *Journal of Molecular Liquids*, 143, 154-159, 2008.
- [3] Z. Chen, W. Zhu, Z. Zheng and X. Zou. "One-pot α -nucleophilic fluorination of acetophenones in a deep eutectic solvent." *Journal of Fluorine Chemistry* 131(3): 340-344, 2010.
- [4] Directive of the European Parliament and of the Council, Brussels COM (11.05.2001) 241 final (BS EN 590-2004/DIN EN 590-2004) Automotive fuels, Diesel, Requirements and test methods; and 2003/17/EC OJ L 76, 22.3.2003, p.10.
- [5] EPA-Diesel RIA, United States Environmental Protection Agency, Air and Radiation,
- [6] EPA 420-R-00-026, December 2000, Clean Air Act Tier 2, 1999.4.
- [7] F. Maria, Alberto A., Ana S., "Ionic Liquids on Desulfurization of fuel Oils", *Fluid Phase Equilibria*, in press.
- [8] X. Chu, Hu Y., Li J., Liang Q., Liu Y., Zhang X., Peng X., Yue W., "Desulfurization of Diesel Fuel by Extraction with $[\text{BF}_4]$ based Ionic Liquids", *Chinese Journal of Chemical Engineering*, 16(6) 881-884, 2008.
- [9] J. Wang, Zhad D., Zhou E., Dong Z., "Desulfurization of Gasoline by Extraction with N-alkyl-pyridinium-based Ionic Liquids", *Journal of Fuel Chemistry and Technology*, 35(3) 2930296, 2007.
- [10] N. Yi, Chun X., Zi W., "Extractive Desulfurization o Fuel Oil Using alkylimidazol and Dialkylphosphate Ionic Liquids", *Industrial Engineering and Chemistry Research*, 46, 5108-5112, 2007.
- [11] A. Luisa, Alberin A., Maria F., Oscar R., Ana S., "Gasoline Desulfurization Using Extraction with $[\text{C}_{8}\text{mim}][\text{BF}_4]$ Ionic Liquid", *AIChE*, 53(12), 3108-3115, 2007.
- [12] X. Jiang, Yi, N., Chunxi L., Zihao W., "Imidazolium-based alkylphosphate Ionic Liquids – A potential Solvent for Extractive Desulfurization of Fuel", *Fuel*, 87, 79-84, 2008.
- [13] A. Luisa, Alberto A., Maria F., Ana S., "Thiophene Separation from Aliphatic Hydrocarbon Using the 1-ethyl-3-methylimidazolium ethylsulfate Ionic Liquid", *Fluid Phase Equilibria*, in press.
- [14] A. P. Abbott, G. Capper, D.L. Davies, R.K. Rasheed, V. Tambyrajah, "Novel solvent properties of choline chloride/urea mixtures", *Chemical Communications*, 70-71, 2003.
- [15] A.P. Abbott, D. Boothby, G. Capper, D.L. Davies, R.K. Rasheed, "Deep Eutectic Solvents Formed between Choline Chloride and Carboxylic Acids: Versatile Alternatives to Ionic Liquids", *Journal of the American Chemical Society*, 126 , 9142-9147, 2004.
- [16] K. Shahbaz, S. M. Farouq, M. A. Hashim and M. A. Inas. "Using Deep Eutectic Solvents for the Removal of Glycerol from Palm Oil-Based Biodiesel." *Journal of Applied Sciences* 10(24): 3349-3354, 2010.
- [17] D. Lindberga, M.F. Revengab and M. Widersten. "Deep eutectic solvents (DESs) are viable co solvents for enzyme-catalyzed epoxide hydrolysis." *Journal of Biotechnology* 147: 169–171, 2010 .
- [18] H.R. Jhong, D. S.-H. Wong, C.-C.Wan, Y.-Y.Wang and T.-C.Wei. "A novel deep eutecticsolvent-based ionic liquid used as electrolyte for dye-sensitized solar cells." *ElectrochemistryCommunications* 11(1): 209-211, 2009.
- [19] M.A. Kareem, F. S. Mjalli, M. A. Hashim and I. M. AlNashef "Phosphonium-Based Ionic Liquids Analogues and Their Physical Properties." *Journal of Chemical & Engineering Data* 55(11):4632-4637, 2010.
- [20] M.A. Kareem, F. S. Mjalli, M. A. Hashim and I. M. AlNashef "Liquid–liquid equilibria for the ternary system (phosphonium based deep eutectic solvent–benzene–hexane) at differenttemperatures: A new solvent introduced." *Fluid Phase Equilibria* 314(0): 52-59, 2012a.
- [21] M.A. Kareem, F. S. Mjalli, M. A. Hashim, M. K. O. Hadj-Kali, F. S. G. Bagh and I. M. Alnashef "Phase equilibria of toluene/heptane with tetrabutylphosphonium bromide based deep eutecticsolvents for the potential use in the separation of aromatics from naphtha." *Fluid Phase Equilibria* 333(0): 47-54, 2012b.
- [22] I. Changping , Dan L., Shuanshuang Z., Zhuo L., Jingmei Y., Ailing W., Yingna C., Zhilong Y., Qi Z., "Extraction Desulfurization of Fuels With Ammonium-based Deep Eutectic Solvents", *Green Chemistry*, 15, 2793-2799, 2013.

Chemical Composition and Antibacterial Activity of *Ceratonia siliqua* L. Growing in Boumerdes (Algeria)

N. Meziou-Chebouti, A. Merabet, N. Behidj, M. Kirouani and S. Aliouat

Abstract-This work is a contribution to the knowledge of physicochemical characteristics of mature carob followed by evaluation of the activity, antimicrobial phenolics leaves and green pods of *Ceratonia siliqua* L. physicochemical study shows that mature carob it has a considerable content of sugar (50.90%), but poor in proteins (7%), fat (8%) and also has a high mineral content. The results obtained from phenolic extracts of leaves and green pods of *Ceratonia siliqua* L. show a wealth leaf phenolic extract especially flavonoids (0,545mg EqQ / g) relative to the extract of green pods (0,226mgEqQ / g). Polyphenols leaves have a slightly inhibitory effect on the growth of strains: *Staphylococcus aureus*, *Escherichia coli*, *Klebsiella pneumoniae*, *Streptococcus sp* and *Sanmonella enteritidis*, a strong inhibitory effect on the growth of *Pseudomonas strain aerogenosa*. Moreover, polyphenols pod have a slightly inhibitory effect on the growth of *Streptococcus sp* strains, *Pseudomonas* and *aerogenosa Sanmonella enteritidis*, a slightly inhibitory effect on the growth of *Klebsiella pneumoniae* strains, *E. coli* and *Staphylococcus aureus*.

Keywords-Antimicrobial activity, bacteria, clove, *Ceratonia siliqua* and polyphenols.

I. INTRODUCTION

The carob tree (*Ceratonia siliqua* L. 1753, Fabaceae Cesalpinoïdae) whose origin appears to be the eastern Mediterranean. It agro-forestry-pastoral species with enormous socio-economic and ecological interests. The carob tree is of interest increasingly growing not only because of its hardiness, its indifference vis-à-vis the nature of the soil, the wood quality, its ornamental and landscape value, but mainly for its seeds which are the subject of commercial transactions whose value far exceeds that of timber production. Thus, whole cloves, pulp, seeds and gum are subject to significant trade towards Europe and are widely used in the food industry [1].

Carob is currently much interest in Algeria, or industrial dispute the international market, for export in the form of flour derived from the pulp and seeds for their farming culture. Furthermore, this tree is of considerable economic importance; pods, rich in sugar cane and sugar beet are used in food industry and pharmacology, particularly as antidiarrheal, their fiber confers cholesterol-lowering and glucose-lowering properties; phenolic compounds they contain are responsible for their antioxidant property [2]. The carob tree (*Ceratonia siliqua*) is an agro-forestry-pastoral species with enormous socio-economic and ecological interests. With its aptitude to develop the different strategies to adapt to water stress, the tree moved favorably in arid and semi-arid areas.

University of Boumerdes, Algeria department of Biology,
Affiliation : Laboratory soft technology physicochemical recovery and biodiversity
E.mail : chNADJIBA@yahoo.fr
E.mail : meramelk@yahoo.fr
E.mail : behidj_nassima@yahoo.fr

Mediterranean ecosystems are characterized by low and erratic precipitation and long dry summer periods. These climatic constraints combined with human pressure, generally lead to degradation of plant cover and rapid soil erosion. To counteract this problem, save soil fertility and improve the living standards of the rural population, the use of multiple-use pioneer tree species such as carob, adapted

to climatic and can settle on marginal lands in reforestation programs and restoration of degraded soils remains a good strategy [3].

II. MATERIALS AND METHODS**Biological Material**

The biological material used in this study consists of the pods and leaves of the carob tree *Ceratonia siliqua* and certain human pathogenic microbial strain.

Plant Material

Mature pods of the carob tree *Ceratonia siliqua* were collected in the region of Lakhdaria (Bouira) in August 2012, in order to achieve a physicochemical study.

In order to study the antimicrobial activity, extraction of polyphenols is made on immature pods and leaves of carob harvested in April 2013, in the forest of Sidi Douad (Boumerdes).

Botanical classification of *Ceratonia siliqua* is as follows:

Kingdom: Plantae

Phylum: spermaphytes

Sub-Phylum: Angiosperms

Class : Equisetopsida

Order : Fabales

Family : Fabaceae

Genus: *Ceratonia*

Species: *Ceratonia siliqua* L. [4]

Carob is an ecologically important tree, industrial and ornamental indiscutable. En terms of products, the tree and all its components are useful, especially the fruit. It is used for afforestation and reforestation of areas affected by erosion and desertification, also used as an ornamental plant on roadsides and gardens (Fig.1) [4].

Currently, he is considered one of the most successful fruit and forest trees, since all its parts (leaves, flowers, fruits, wood, bark and roots) are useful and have values in several fields (Fig.2 , Fig.3) [5].

The fruit of the carob or carob pulp consists of a wrapping regular seeds. Indeed the sweet pulp of the carob has long been used as cattle feed side other foods such as barley flour [6].



Fig.1. The carob tree



Fig. 2. Leaves of the carob tree Fig. 3. The fruit of the carob tree

Carob is frequently grown in the Saharan Atlas and it is common in the tell [7] It is found naturally in association with *Prunus dulcis*, *Olea Europea* and *Pistacia Atlantica* in hot semiarid floors, sub-humid and humid, with an altitude ranging from 100m to 1300m in the cool valleys that protect

it from frost, with a temperature of 5 ° C to 20 ° C and rainfall of 80mm to 600mm / year[8].

Microbial Tested Strains

To evaluate the antimicrobial activity of the polyphenol extract of the pod and leaf carob, eight microbial strains were evaluated six bacteria *Staphylococcus aureus*, *Streptococcus* sp, *Klebsiella pneumoniae*, *Pseudomonas aeruginosa*, *Escherichia coli*, *Salmonella enterica*, and *Aspergillus Niger* and yeast *Candida albicans*.

The microbial strains are stored on nutrient agar for bacteria and the mushroom to Sabouroud and yeast.

Physico-Chemical Study

The assay is performed according carbohydrates method [3]. [9] The protein characterization is performed quantitatively. The determination of lipids was performed with a Soxhlet appliance.

Determination of Ash Content (Mineral Matter)

The principle consists of a biological material incineration in a muffle furnace, in a porcelain crucible at a temperature of 900° C.

III. RESULTS AND DISCUSSION

Determination of Dry Matter

The rate of the pulp in the dry matter of the carob *Lakhdaria* The area was estimated to 88.5%. The result of this study is almost identical to those found by [10]. who found value of 88.68% for pulp Blida, but slightly less than that of the pulp and pulp of Tlemcen, Jijel which are respectively 89.40% and 90.40% that indicated by its but in this case the difference is not significant, and against it is less than that given by [11], [12]. Which were respectively 90%. 95.4%. The water content is 11.5% of the study is a dry variety variety because it has a lower water content to 26% as shown. This low water content fruit protects against the growth of microorganisms which promotes its long shelf life.

TABLE I

Physicochemical Characteristics Of The Carob Pulp.

Settings	Values
Water content	11.5%
The dry matter content	88.5%
Total sugar content	50.9%
Protein content	7%
Lipid content	8.8%
titratable acidity	2.1%
Rate ashes	3.64%
Soluble solid residues	14.4%
pH	5.52

The rate of total sugar 50.9% MF, also this value is lower than that specified by [1], 75% and it is higher than that carried out by [13]. which is 40% value protein of carob pulp is 7% of the MF, (Tab.I) the value is equal to that carried out by [13]. that it is close to the pulp, [14]. which is 7.1%. But it is higher than that found in [15]. which has a reported value of 1% to 2% MF.

The fat content of the carob pulp is 8.8%, this value is greater than that found in [16]. , which is 4.80%. While the result is much higher than those of [11], which is (0.74%), to Jordan, those is (0.6%) for Italy [17].

The fat of the carob pulp was 8.8%. This value of the joining [17]. which is 6.6% for the most part represented by oleic acid (34.4%) and linoleic acid (44.5%), whereas palmitic acid (16.2%) and stearic acid (3.4%) were the major saturated fatty acids. Which gives the carob the property of reducing the risk of cardiovascular disease.

The rate of ash is the total amount of minerals present in a sample, the value of the carob pulp is in the order of 3.64%, it exceeds the range of 2% to 3% [18], against our value is less than 8.83% [19]. This can be explained by the geographical origin of the samples, including climate conditions and soil characteristics of the soil [20].

Element Analysis of Minerals

TABLE II

Mineral Composition Element of The Pulp of The Carob Tree

Mineral Element	Na	Zn	Cu	Mg	Ca	K
Quantity in mg/100g Of The Carob Pulp	14.86	0.66	0.46	39.77	206.90	1132.96

The result of this study is close to those reported by [21] is the following value (1486.25mg/100g). The magnesium content of the carob pulp is 39.77mg/100g MF (Tab. II) It is below the values 66,89mg/100g, 60 mg /100g indicated by [22] and [23].

Yield Phenolic Compounds

The yield of the phenolic compound or methanoic extracting polyphenols obtained from the crushed leaves and green pods are respectively 20%, 10% of the fresh material. The yield of the phenolic compound of the sheets is greater than 2 times per input to yield phenolic compound green pods. This result confirms the work [24] and [25] have shown that the leaf and bark are rich in phenolic compounds over other parts of the tree.

TABLE III

Content Of Phenolic Compounds Extracted From The Leaves And Green Pods.

Concentration Of Active Principle	Concentration Of Total Polyphenols (EAG mg/gMF)	Flavonoid Concentration (mg EqQ/g MF)
The leaf	1.55	0.545
The pod	1.57	0.226

Total Polyphenol Content

The extract of green pods is a major source of total polyphenols comparable to the extract of the leaves. Green carob pods contain 4.52 mg/g of total polyphenols that are greater than this study [26].

Antimicrobial Activity

Diffusion Test on Agar Medium

TABLE IV

Diameter Of Inhibition Zone Of The Polyphenolic Extract Of Pods

Diameters Of Inhibition Zones (mm)	1st test	2nd test	3rd test	Mean Diameter
<i>Staphylococcus aureus</i>	4	15	10	9.66±5.50
<i>Streptococcus sp</i>	14	20	25	19.67±5.50
<i>Escherichia coli</i>	11	5	15	10.33±5.05
<i>Klebsiella pneumoniae</i>	11	14	13	12.66±1.52
<i>Pseudomonas aerogenosa</i>	18	16	15	16.33±1.52
<i>Sanmonella enteritidis</i>	18	17	16	17±1
<i>Candida albicans</i>	/	/	/	/
<i>Aspergillus niger</i>	/	/	/	/

TABLE V

Diameter Of Inhibition Zones Leaves Extract

Diameters Of Inhibition Zones (mm)	1st test	2nd test	3rd test	Mean Diameter
<i>Staphylococcus aureus</i>	15	14	17	15.33±1
<i>Streptococcus sp</i>	25	23	27	25±2
<i>Escherichia coli</i>	20	19	22	20.33±1.52
<i>Klebsiella pneumoniae</i>	21	19	22	20.66±1.52
<i>Pseudomonas aerogenosa</i>	24	25	27	25.33±1.52
<i>Sanmonella enteritidis</i>	20	22	19	20.33±1.52
<i>Candida albicans</i>	/	/	/	/
<i>Aspergillus niger</i>	/	/	/	/

The polyphenol extract *Cumoinum cyminum* L. has no effect on the growth of strains, *Serratia sp*, and *Bacillus subtilis*, it is only on the growth of *Staphylococcus aureus* [27] and confirms hypersensitivity latter strain our phenolic extract of the leaves. This hypersensitivity of the *Staphylococcus aureus* strain may be explained by the capacity of the bactericidal carob pulp with respect of *Staphylococcus aureus*. Also carob adsorb enterotoxins produced by certain strains of *Escherichia coli* and *Staphylococcus*, as well as the cholera vibrio, this adsorption mechanism could be explained by the presence of tannins and insoluble in the active part of the locust bean [28].

The antimicrobial activity of the extract of the leaves is greater phenolic especially intestinal strain relative to the phenolic extract pod. These results are demonstrated by experimental studies in Turkey, carob leaves used in medicine 'traditional' to treat diarrhea and dietary food [29]. These leaf extracts have also been identified as carriers of cytotoxic and antimicrobial activities [30] antifungal. Activité practice is zero for both phenol extract (leaf, clove immature) by cons according to [31] carob also has antimicrobial and antifungal activity which is due to its content of phenolic compounds.

IV. CONCLUSION

A comparative study between the statements of the pod and leaf of the plant is desirable. It is very interesting to complement and enhance this study by:

A detailed HPLC polyphenolic profile separation of various polyphenolic fractions and evaluation of antimicrobial and antioxidant activities for each fraction separately. And to think about the contribution to the study of other biological activities.

REFERENCES

- [1] B. Biner, H. Gubbuk, M. Karhan Aksu and M. Pekmezci, - Sugar profiles of the pods of cultivated and wild types of carob bean (*Ceratonia siliqua* L.) in Turkey," *Food Chemistry*, (100), 2007, pp. 1453–1455.
- [2] A. Hariri, N. Ouis, F. Sahnouni et D. Bouhadi, "Mise en oeuvre de la fermentation de certains ferments lactiques dans

- des milieux a base des extraits de caroube," *Rev. microbiol. ind. san et environn.* (18), 2009, pp. 37–55.
- [3] M. N. Rejeb, "Le caroubier en Tunisie: Situations et perspectives d'amélioration. Dans: Quel avenir pour l'amélioration des plantes. " Ed. aupelf-uref. John Libbey Eurotext, Paris, 1995, 417P.
- [4] I. Batlle et J. Tous, " Lineas de investigación sobre el algarrobo (*Ceratonia siliqua* L.). " Ed. IRTA, Cataluña, Spain, 1988, 234P.
- [5] A. Aafi, "Note technique sur le caroubier (*Ceratonia siliqua* L.)" Cent Nat de la Rech Forestière, Rabat, 1996, 100P.
- [6] M. Ait Chitt, M. Belmir. et A. Lazrak, "Production des plantes sélectionnées et greffées du caroubier" Transfert de technologie en Agriculture, N°153, IAV Rabat, 2007, 5: 1-4.
- [7] P. Quezel et S. Santa, "Nouvelle flore de l'Algérie et des régions désertiques méditerranéennes", Ed. CNRS. Paris, 1962, 356P.
- [8] H. Rebou, "fruits Méditerranéens" Ed. la maison rustique, Paris, 1968, 330P.
- [9] G. H. Duchateau and M. Florkin, "Arch. Insect. Physiol," *Biochem.* 67, 1959, p. 306
- [10] N. Gaouar, "Etude de la valeur nutritive de la caroube de différentes variétés Algériennes," Thèse d'ing. agro, Fac. Sci, Tlemcen, 2010, 95 p.
- [11] A. K. Yousif and H. M. Alghzawi, "Processing and Characterization of Carob Powder," *Food Chemistry*, 69 (3): 2000, pp. 283–287.
- [12] L. Rosil, C. Jaume, M. Francisco, T. David and B. Joaquim, "L'utilisation de la farine de caroube dans les aliments de sevrage et son influence sur les performances et la santé des porcelets," *Jour. Rech. Porcine*, (34), 2002, pp. 97–101
- [13] J. C. Frentz, and P. Zert, "Territoires et alimentation. L'encyclopédie de la charcuterie," Ed. Soussana, 1990, p. 845
- [14] S. L. Naghmouchi, M. Khouja, A. Khaldi, M. N. S. Rejeb Zgoulli, P. Thonart et M. Boussaid, "Biochemical Diversity of Wild Carob Tree Populations and Its Economic Value," *Topics in Conservation Biology*, (25), 2012, pp. 953–978.
- [15] H. Sbay et M. Abourouh, "Apport des espèces à usages multiples pour le développement durable : Cas du pin pignon et du caroubier," Centre de Recherche Forestière. Haut Commissariat aux Eaux et Forêts et à la Lutte Contre la Désertification. Rabat, (10), 2006, pp. 1–9.
- [16] R. Owen, R. Haubner, W. Hull, G. Erben, B. Spiegelhalder and H. Bartscha, "The phenolic compounds of *Ceratonia siliqua* pulps and seeds," *Food Chem. Toxicol.*, (41), 2003, pp. 1727–1738.
- [17] R. Avallone, M. Plessi, M. Baraldi and A. Monzani, "The phenolic compounds of *Ceratonia siliqua* pulps and seeds. *Jour. food compos. analys.*, (10), 1997, pp. 166–172.
- [18] P. A. Dakia, B. Wathelet and M. Paquot, "Isolation and chemical evaluation of carob (*Ceratonia siliqua* L.). *Seed germ Food Chemistry*, (6), 2007, pp. 1368–1374.
- [19] Z. Puhan and M. W. Wielinga, "Products derived from carob pods with particular emphasis on carob bean gum (CBG). Report Technical Committee of INEC (unpublished), (12), 1996, pp. 123–127.
- [20] B. M. Abd- El-Lateef, et E. M. Salem, "The Effect of Nutritional Carob Pods Flour Components on Sensory and Biological Evaluations of Rolled Biscuits," *J. Agric. Sic.* Mansoura Univ, 21(4), 1996, pp. 1355–1372.
- [21] A. Bezzala, 2005 "Essai d'introduction de l'arganier dans la zone de M'doukel et évaluation de quelques paramètres de résistance à la sécheresse," Magister en Sciences Agronomiques, Université El Hadj Lakhdar, Batna, p. 152
- [22] M. Eman, D. Salem and A. Awlya Ohaad Fahad, "Substituting of Cacao by Carob Pod Powder in Milk

Chocolate Manufacturing. *Australian Journal of Basic and Applied Sciences*, (3), 2012, pp. 572–578.

[23] M. Petit and J. Pinilla, "Production and purification of a syrup from carob pods," *Lebensm-Wissu-Technol*, (28): 1995, pp 145-152.

[24] M.M. Ozcan, D. Arslan, and H. Gökçalik, "Some compositional properties and mineral contents of carob (*Ceratonia siliqua*) fruit, flour and syrup," *Nt. J. Food Sci Nutr.*, (8), 2007, pp. 652–660.

[25] L.O. Whiteley and D.M., Klurfeld, "Nutrition and Cancer. *Trends Food Sci. Tech.*, (36): 2000, pp. 131-149.

[26] A. Tahiri, F.S. Fadel Tahrouch, S. El Madidi et A. Hatimi, "Symposium sur les composés phénoliques. Ed. Amyris. Agadir, Maroc, 2009, p. 145

[27] R. Abi Azar, "Complexation des protéines laitières par les extraits de gousses vertes de caroubier Propriétés technologiques des coagulum obtenus," *Mém. Agence Universitaire de la Francophonie*, 2007, p. 196

[22] S. Athamena, I. Chalhém, A. Kassah-Laouar, S. Laroui et S. Khebri, "Activité anti-oxidante et antimicrobienne d'extraits de *cuminum cyminum* L." *Lebanese science journal*, (116), 2010, pp. 9–81.

[28] P. Tolentino, "Mécanismes et limites de l'action thérapeutique de la farine de caroube dans les diarrhées infantiles: étude clinique et expérimentale," *Journal. Paed.*, (20), 1950, pp. 200–222.

[29] T. Baytop, "Therapy with medicinal plant in Turkey (Past and Present)," Publication of the Istanbul University. *Food Control*, (15): 1984, pp. 169–172.

[30] B. Kivçak and T. Mert, "Antimicrobial and cytotoxic activities of *Ceratonia siliqua* L. extracts," *Turk. Journal Biol.*, (4), 2002, pp. 197–200.

[31] A. Ben Hsouna, M. Trigui et S. Jaoua, "Evaluation of antimicrobial and antioxidant activities of the ethyl acetate extract of endemic *Ceratonia siliqua* L," *Journal of agricultural and food chemistry*, (4), 1986, pp. 827–829.

A Novel Automatic Thresholding Method Based on Shape of Histogram for Microscopic Blood Cell Images

Engin AVCI¹, Turker TUNCER², Resul ÇÖTELİ³, Esin DOĞANTEKİN⁴

¹Firat University, Technology Faculty, Department of Software Engineering, 23119, Elazig, TURKEY

²Firat University, Technology Faculty, Department of Digital Forensic Engineering, 23119, Elazig, TURKEY

³Firat University, Technology Faculty, Department of Energy Systems Engineering, 23119, Elazig, TURKEY

⁴Zirve University, Emine-Bahaeddin Nakiboglu Medicine Faculty, Gaziantep, TURKEY

Abstract—Image thresholding is the most powerful method used for segmentation processing. So far, there have been many methods in image thresholding but these methods may not give satisfactory results for every image types. The Otsu thresholding method is the most commonly used and best-known in these methods. The thresholding is performed in both single and multiple. In this study, a novel threshold algorithm based on histogram's shape (TAHS) can be used for determining the multiple thresholding. This novel TAHS threshold algorithm works based on histogram. Implementation of the proposed algorithm is simple and quick. The main purpose of this algorithm is to determine the valley point in histogram and to mark them as threshold. The effective of proposed thresholding method were evaluated by using microscopic blood cell images.

Keywords— Automatic thresholding method; Microscopic blood cell images; multiple thresholding method; histogram shape.

I. INTRODUCTION

Image thresholding is very important for computer vision and image processing. The main problem of image processing is to find the right automatically thresholding. Threshold must be correctly and automatically chosen for to be

strong of the image segmentation.

Nowadays, Sezgin and Sankur [1] divided in to 5 groups the image thresholding. These groups are based on histogram's shape, entropy, cluster, object property, and spatial correlation. The simplest way for image thresholding is to convert to gray level and take a threshold point.

The mathematical equation for such image thresholding method can be given as follows.

$$\text{If } f(x, y) > T \text{ then } f(x, y) = 0 \text{ else } f(x, y) = 1 \quad (1)$$

In Eq (1), $f(x,y)$'s mean is gray level of image, and T is threshold point. According to Eq.1, bigger values than values of T are assigned to zero whereas values of T are equal to 1 for other status.

This method is the most primitive. To apply this method, It is needed that it must be choosen a different T point for each image. This process prevents automatic working of systems. Using of automatic threshold is a must due to the all these reasons. The peak and valley points are determined in automatic thresholding method based on the histogram.

Thresholding process is fulfilled by being chosen the most appropriated thresholds. In selecting of these thresholds, high and low points are used. In some automatic thresholding studies, entropy is used. These entropy kinds are Shannon, Cross and Renyi entropies. The best kind of entropy is Renyi entropy for automatic image threshold.

In nowadays, the image processing algorithms have been commonly used because of many advantages such as better detection of adherent or overlap blood cells. In this study, a novel threshold algorithm based on histogram's shape (TAHS) can be used. In here, the main reasons of this algorithm are counting and recognition of the blood cells. Thus the blood

This work is supported by Scientific and Technological Research Council of Turkey (TUBITAK) with project numbered 113E155.

Engin Avci, Firat University, Technology Faculty, Department of Software Engineering, 23119, Elazig, TURKEY phone: 424-237-0000; e-mail: enginavci@firat.edu.tr).

Turker Tuncer, Firat University, Technology Faculty, Department of Digital Forensics Engineering, 23119, Elazig, TURKEY phone: 424-237-0000; e-mail: turkertuncer@firat.edu.tr).

Resul Cotelı, Firat University, Technology Faculty, Department of Energy Systems Engineering, 23119, Elazig, TURKEY phone: 424-237-0000; e-mail: rcoteli@firat.edu.tr).

Esin Dogantekin, Zirve University, Emine-Bahaeddin Nakiboglu Medicine Faculty, Gaziantep, TURKEY phone: 424-237-0000; e-mail: enginavci23@gmail.com).

cells can be better detected from microscopic blood cell images.

II. PREVIOUS THRESHOLDING METHODS

The automatic image thresholding methods in literature are divided into six main groups. These automatic image thresholding methods can be given as below:

A. The Automatic Image Thresholding Methods based on Histogram-Entropy

In this method, the thresholding points of image are automatically calculated by using histogram – entropy features of image. The points having the largest entropy value is taken as the threshold reference points. In this method, mostly Shanon and Reny entropy types are used.

B. The Automatic Image Thresholding Methods based on Shape of Histogram

The main aim of this automatic image thresholding method is find the lowest points namely valley points in histogram.

C. The Automatic Image Thresholding Methods based on Clustering in Measure Space

This automatic image thresholding method is divided into two groups. The first group aims for image thresholding by making several statistical analyzes. At other group, main aim is separate object from background.

D. The Automatic Image Thresholding Methods based on Spatial Properties

In this automatic thresholding method, the discrete wavelet transform features, the discrete cosine transform features, etc. are used for automatic detection of thresholding points. These features can be optimized by using optimization methods such as genetic algorithm, particle swarm optimization, etc.

E. The Automatic Image Thresholding Methods based on Spatial Properties

In this automatic thresholding method, local adaptation is calculated for different threshold value of each pixel as depending on local properties. This method is depending on regional location. In this method, a few parameters must be used to adjust the threshold value as local.

III. THE PERFORMANCE CRITERIA FOR AUTOMATIC THRESHOLDING METHODS

The performance criteria for automatic thresholding methods can be given as below:

A. The Automatic Image Thresholding Methods based on Spatial Properties

This method is statistical and is presented by Levine. The irregularity of grayscale equation can be given in Eq.(2).

$$GTDS = \frac{P_{nesne} \sigma_{nesne}^2}{\sigma_{max}^2} \quad (2)$$

Here, σ is variance of all histogram. σ_{nesne} is variance in the cluster of jth class, P_{nesne} is total probability in jth cluster.

B. Wrong Classification Error

This operator calculates the probability of wrong classification error for each of pixels images.

$$YSH = \frac{|E_0 \cap E_T| + |F_0 \cap F_T|}{|E_0| + |E_T|} \quad (3)$$

IV. APPLYING OF THE NOVEL THRESHOLD ALGORITHM BASED ON HISTOGRAM'S SHAPE

The main aim of this novel threshold algorithm based on Histogram's Shape (TAHS) is to automatically find the valley points in histogram. Thus, automatic thresholding process is realized by using these valley points. TAHS is based on statistical. The TAHS algorithm divides the histogram of image to equal parts according to precision of image. TAHS algorithm is applied on 8-bit image. TAHS algorithm can be explained with following steps.

Step 1: The histogram of image is obtained.

Step 2: Histogram is divided into parts of n. In practices, Histogram is divided into 8 parts.

Step 3: Standard deviation of every parts of histogram is calculated.

Step 4: The maximum difference between the elements which are calculated for each of the eight parts.

Step 5: If the any calculated maximum difference is bigger than the standard deviation of related part, minimum point in this difference is determined as the valley point.

Step 6: The thresholding values are calculated by shifting the valley points until a selected constant value.

The mathematical expression of the TAHS algorithm can be given as below:

$$\max fark = \sum_{i=1}^{256/n} \sum_{j=i+1}^{256/n} \max(|x_i - x_j|) \quad (4)$$

$$x' = \frac{1}{N} \sum_{i=1}^N x_i \quad (5)$$

$$\sigma = \sqrt{\frac{1}{N} \sum_{i=1}^N (x_i - x')^2} \quad (6)$$

$$\max fark > \sigma \} threshold_s = j + k \quad (7)$$

H_n is the part of histogram, x_i is the pixel values in histogram, x' is the arithmetic mean of the histogram values, σ is the standard deviation of the related histogram and k is

calculated as the thresholding parameter respectively. Value of k parameter in related algorithm is taken as 16.

The formula of the standard deviation is shown in Eq(6). At step 6, the sum process is carried out by shifting process. An image is 8-bit. The pixel values of the images are 256 pixels values between 0 and 255. Value of the square root of 256 is 16. Therefore, 16 is added to valley value. The following 3 gray-level images of blood cells were used to test the thresholding performance of TAHS algorithm.

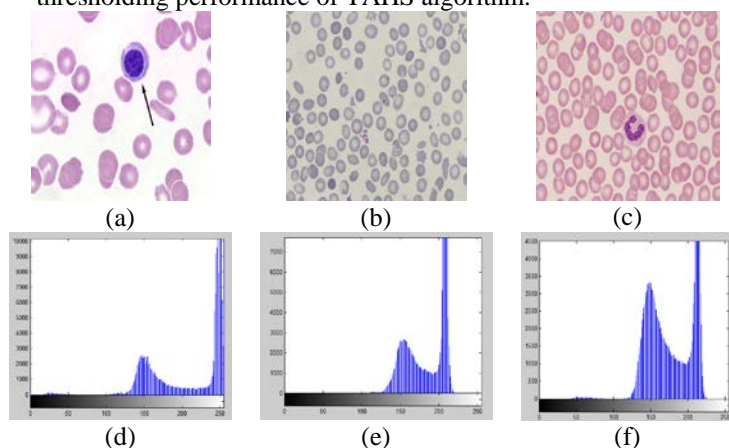


Fig 1. (a) k1.jpg, (b) k2.png, (c) k3.tif, (d) The histogram of k1 image, (e) The histogram of k2 image, (f) The histogram of k3 image.

The following 3 gray-level images of blood cells were used to test the thresholding performance of TAHS algorithm. The found thresholding values for these images by using TAHS algorithm can be given at Table 1.

Table 1. The found thresholding values for these images by using TAHS algorithm

Image	Thres.-1	Thres.-2	Thres.-3	Thres.-4	Thres.-5	Thres.-6
k1.jpg	18	53	83	125	155	183
k2.png	54	111	130	159	184	222
k3.tif	61	89	141	151	182	227

Different thresholding points were found for each of these images as depending on their histogram shapes. For example, TAHS automatic thresholding algorithm has applied the Kids.tif image and 2 thresholding points were calculated. These thresholding points are 18 and 50.

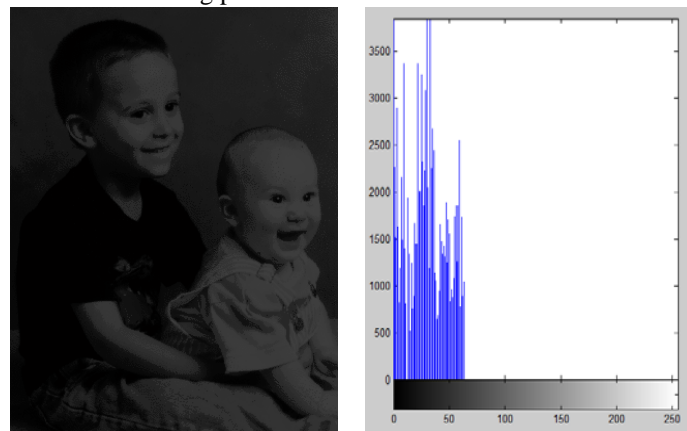


Figure 2. (a) Kids.tif (b) Histogram of Kids.tif

If a more sensitive thresholding is wanted, histogram should be divided into more parts from 8. A threshold image was observed for each of obtained thresholding points. This state can be explained at Eq.(8).

$$S = n + \frac{n(n-1)}{2} \quad (8)$$

Here, S is the number of the thresholding images and n is the number of the thresholding points. Since there are total of n thresholding points, total of n images are obtained by using the thresholding with single point. However, $\frac{n(n-1)}{2}$ expresses the thresholding images with multiple points. The best automatic thresholding result can be obtained by optimizing total of S thresholding images. The thresholding images of k1.jpg, k2.png, and k3.tif by using TAHS algorithm can be given in Fig.3:

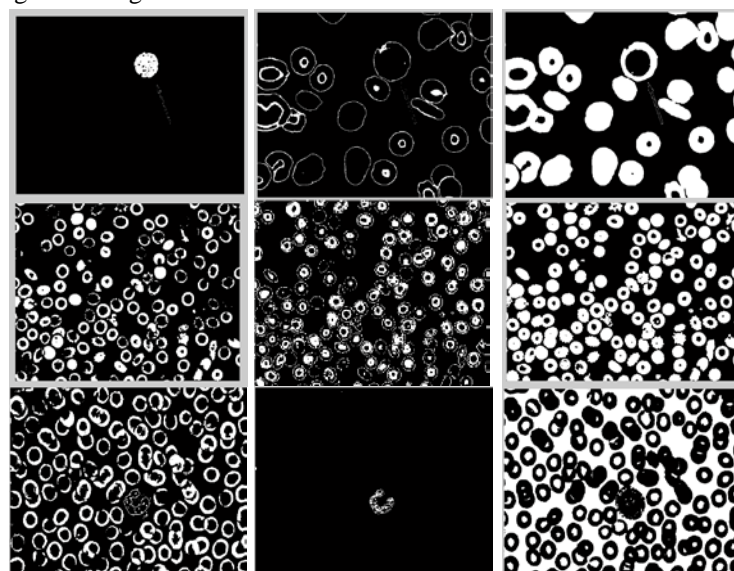


Fig.3. The thresholding images of k1.jpg, k2.png, and k3.tif by using TAHS algorithm

V. CONCLUSION

In this study, a novel threshold algorithm based on histogram's shape (TAHS) can be used for determining the multiple thresholding. This novel TAHS threshold algorithm works based on histogram. Implementation of the proposed algorithm is simple and quick. The main purpose of this algorithm is to determine the valley point in histogram and to mark them as threshold. The effective of proposed thresholding method were evaluated by using microscopic blood cell images in Table 1.

ACKNOWLEDGMENT

Microbiology in 2010. She works as Assistance Professor at Zirve University, Emine-Bahaeddin Nakiboglu Medicine Faculty.

This work is supported by Scientific and Technological Research Council of Turkey (TUBITAK) with project numbered 113E155.

REFERENCES

- [1] Sezgin M, Sankur B. Survey over image thresholding techniques and quantitative performance evaluation. J Electron Image 2004;13:146-65
- [2] Wong B. S., Tui C. G., Bai W., P. H. Tan, B. S. Low, K. S. Tan, Thermographic evaluation of defect composite materials, Insight vol: 41, no.8, August 1999.
- [3] Moysan J., Corneloup G., Sollier T., Adapting an ultrasonic image threshold to eddy current images and defining validation domain of thresholding method, NDT&E International, 32, 1999, 79-84
- [4] Kraus H.J., Hohman R., Grünklee M., M. Maus, Aircraft wheel and fuselage with eddy current and SQUID, Insight, vol:42, no:3, March 2000.
- [5] Kundu T., Ehsani M., Maslov K.I., Guo D., C-scan and L-scan generated image of the concrete /GFPR composite interface, NDT&E International, 32, 1999, 61-69.
- [6] Sezgin M., Bircik S., Visual Inspection of Reflective Materials, International Conference on Quality Controls by Artificial Vision, 28-30 May 1997, France.
- [7] Sezgin M., Sankur B., Evaluation of categories of Thresholding algorithms, submitted to Machine Vision and Application.
- [8] Zhang Y. J., A survey on evaluation methods for image segmentation, Pattern Recognition, vol:29, no.8, s:1335, 1346, 1996.

Engin Avci in Elazig, Turkey, in 1978. He received the B.S. degree from the Firat University, Technical Education Faculty, Department of Electronics and Computer Education in 2000, M.Sc. degree from the Firat University, Technical Education Faculty, Department of Electronics and Computer Education in 2002, and Ph.D. degree from Firat University, Engineering Faculty, Department of Electrical and Electronics Engineering in 2005. He works as Associate Professor at Firat University, Technology Faculty, Department of Software Engineering. He received the B.S. degree from the Firat University, Technical Education Faculty, Department of Electronics and Computer Education in 2000, M.Sc. degree from the Firat University, Technical Education Faculty, Department of Electronics and Computer Education in 2002, and Ph.D. degree from Firat University, Engineering Faculty, Department of Electrical and Electronics Engineering in 2005. He works as Associate Professor at Firat University, Technology Faculty, Department of Software Engineering. His research interests concern pattern recognition techniques, communication, signal processing, radar target recognition, and intelligent systems, data hiding, information security.

Turker Tuncer was born in Tunceli, Turkey, in 1986. He received the B.S. degree from the Firat University, Technical Education Faculty, Department of Electronics and Computer Education in 2009 and M.S. degree in telecommunication science from the Firat University in 2011. He is PHD student department of software engineering at Firat University. He works as research assistant Digital Forensic Engineering, Firat University. His research interests include data hiding, image hiding, cryptography, image processing.

Resul Cotel was born in Elazig, Turkey, in 1978. He received the B.S. degree from the Firat University, Technical Education Faculty, Department of Electric Education in 2000, M.Sc. degree from the Firat University, Technical Education Faculty, Department of Electric Education, and Ph.D. degree from Firat University, Engineering Faculty, Department of Electrical and Electronics Engineering. He works as Associate Professor at Firat University, Technology Faculty, Department of Energy Systems Engineering.

Esin Dogantekin was born in Elazig, Turkey, in 1981. She received the B.S. degree from the Firat University, Medicine Faculty in 2005. Ph.D. degree from Firat University, Medicine Faculty Department of Medicine and Clinic

The Mechanism of PMF Nanoparticles in Invading A549 cells, A New Selective Drug Delivery for Cancer Therapy

Gehan A-R. Ahmed^{1,2,3*}, Faten A. Khorshid^{4,5}, Alaa Khedr⁶, Salem M. El-Hamidy⁴, Numan A. Salah⁵

¹Biochemistry Department, Science College, King Abdulaziz University(KAU), Jeddah –KSA

²Medical Biophysics Research Lab. -King Fahd Medical Research Centre, KAU, Jeddah –KSA

³Spectroscopy Department, Physics Division, National Research Centre- Cairo, Egypt

⁴Tissue Culture Research Unit, King Fahd Medical Research Centre, KAU, Jeddah –KSA

⁵Biology Department, Science College, KAU, Jeddah –KSA

⁶Faculty of Pharmacy KAU- Pharm. Dep Assut University-Egypt

⁷Center of Nanotechnology, King Abdulaziz University, Jeddah-KSA

., +966-6952000 ex lab 25240; fax: +966-02-6952076; e-mail: jahmed@kau.edu.sa or gehan_raouf@hotmail.com

Abstract—Nanomedicine and nanotechnology are new fields of research for cancer therapy that are enlarged steadily. Although most trends are directed for manufacturing nanoparticles, PMF is fraction extracted from camel urine (PM701) that proved to be selective anticancer agent for many types of cancer cells. PMF were studied by scanning electron microscope (SEM), Transmission electron microscope (TEM), energy dispersive X-ray (EDX) and the vibrational spectroscopy. Lung cancer cells A549 were treated with PMF for different time intervals ranging from 2 seconds up to 1 minute. The treated cells were examined with (TEM). The results revealed that PMF contains different types of macro and nanoshells with different types of metals that attack first, the A549 cell membrane and influenced the membrane polarity, packing and the hydrocarbon chain length of the phospholipids. These changes were indicated by the changes in the asymmetric stretching CH_2/CH_3 , symmetric stretching of membrane CH_2/CH_3 , symmetric stretching $\text{CH}_2/\text{total lipids}$ ratios respectively. Second, these Nanoparticles directed after endocytosis to the nucleus and other cell organelles. Some of these metals are responsible for the selectivity of PMF fraction to cancer cells only. This new smart drug based on the most new frontiers in nanotechnology which include nanoshells as drug carrier.

Keywords—A549 Lung cancer cells, Nanomedicine, PMF, Vibrational Spectroscopy, Membrane lipids, Electron Microscope, LCMS /GCMS, LC-MSMS – IonTrap, Cancer treatment.

I. INTRODUCTION

The most common use of nanotechnology on medicine has been in areas of developing novel therapeutic and imaging modalities¹. Intelligent drugs are the new agents that could potentially allow increased cancer selectivity, changes in pharmacokinetics, amplification of cytotoxic effects.^{2,3} The drug used in chemotherapy has a narrow therapeutic index. In contrast, targeted therapy that directed specifically against cancer cells and signaling pathways proved to limit nonspecific and toxicities. Thus, targeted therapies represent a

new and promising approach to cancer therapy, one that is already leading to beneficial clinical effects.⁴

As the physical scale of nanomaterial is of the same order as viruses one might expect they will have highly variable interactions with cells and tissues dependent on their size, shape, surface patterning, and charge.⁵ An important goal in nanomedicine is to combine several of the special features of materials to improve the selectivity and the agent's therapeutic index. The simplest way to achieve this is by combining the functions of targeting and killing with cytotoxic missile.⁶ Camel urine is rich in many organic and inorganic compounds. PMF is a fraction extracted from PM701 camel urine that proved to be highly selective agent for many types of cancer in tissue culture levels and in the animal model as well.⁷⁻⁹ It have been tested on healthy volunteers and passed the clinical trial phase I successfully.¹⁰

In this study we tried to explore various PMF Nanoparticles structure and their mechanism of action on A549 cells when treated with PMF at different time intervals ranging from 2sec up to 1 min by using SEM, TEM, Raman microscopy, FTIR, SEM-EDX, LCMS /GCMS and LC-MSMS – IonTrap

II. MATERIALS AND METHODS

The experimental work of the present study was conducted at the Medical Biophysics Laboratory at King Fahd Medical Research Center, King Abdulaziz University, Jeddah, Kingdom of Saudi Arabia.

A. Scanning Electron Microscopy (SEM)

For SEM studies the PMF was suspended in distilled water, then treated in an ultrasonic bath (BRANSON, 1510) about 20 min. A small drop of this suspension placed on the double side carbon tape on Al- Stub and dried in air. The specimens were analyzed - without gold coating- by using energy dispersive analyzer unit (EX-23000BU) which attached to the scanning electron microscope (JSM-6360LA, JEOL, Tokyo, Japan). The microscope was operated at an accelerating voltage of 20 kV. Quantitative method ZAF, and characterization method as pure.

B. LCMS/GCMS, LC-MSMS – IonTrap

High-performance liquid chromatography-with Ion Trap 6320 MSMS (LC-MS) from Agilent (HPLC-1200 series quaternary pum, solvent selector, degasser, autosampler, column compartment, Ion Trap 6320 Agilent technologies, USA), the system and data integration were handled with Chemstation for LC-MS.

HPLC column was Agilent Zorbax Extend C18, 150 mm (length) x 4.6 mm (internal diameter), 5 μ m (particle size), 80Å (porosity). Pre-column used was, Agilent Zorbax Eclipsed XDB C18, 4.6 mm x 12.5 mm, 80 Å, 5 μ m (Agilent Technologies, Palo Alto, CA, USA). The column oven adjusted at 35 °C.

The ion-Trap was set as follow: The MS-Ion trap system was calibrated from 15 to 2200 using Agilent tuning mix applying, in sequence, scan calibration, fragmentation calibration, and isolation calibration and defining positive ion-masses; 118.09, 322.05, 622.05, 922.01, 1521.97, 2121.93.

A gas chromatograph (GC)–mass spectrometer (MS), Clarus 500 GC/MS (PerkinElmer, Shelton, CT) was used. The software controller/integrator was TurboMass, version 4.5.0.007 (PerkinElmer). An Elite-5MS GC capillary column (30 x 0.25-mm x 0.5 μ m, PerkinElmer) was used. Calibrant used was heptacos (15–650 m/z).

Screw capped autosampler vials (V-shaped 300- μ L and 1.8 mL) were from Alltech (Alltech, GmbH, Unterhaching, Germany). Heating oven (Heraeus, Kendro, Hanau, Germany) was adjusted at 60 °C. Calibrated digital micro-transfer pipettes 5–250 μ L, Brand, Wertheim, Germany, were used. Labufuge 200 Centrifuge 5300 rpm (Heraeus Kindro, Germany).

Chromatographic conditions**[A] A gas chromatograph (GC)–mass spectrometer (MS):**

The carrier gas was helium (purity 99.9999%) at a flow rate of 1.0 mL/min (32 p.s.i., flow initial 45.0 cm/s, split; 1:50). Temperature conditions were: inlet line temperature, 180°C; source temperature, 170°C; trap emission, 100°C; and electron energy, 70 eV. The column temperature program was: 50°C for 2 min, increased to 280°C (rate, 20°C/min), and held for 5 min. The injector temperature was 260°C, MS scan was performed from 50 to 400 m/z. The NIST Mass Spectral Program for the NIST/EPA/NIH Mass Spectral Library, version 2.0f, build Oct 8, 2008 USA was used for confirmation and identification of peaks. Matching probability of >50% were considered.

[B] LC-MS; For LCMSMS-Autoscan-TIC with Autofragmentation and smart fragmentation:

Mobile system-I (for separation and identification of major compounds):

ammonium acetate, 0.05M (A), acetonitrile (B); pumped at flow rate of 0.2 mL/min as follow

	Time, min	%A	%B
1	0 - 5	100	0
2	5- 60	0	100
3	61	100	0

Mobile system-II (for separation and identification of Estrogens):

Prepared by mixing 900 mL methanol, 99.5 mL water, and 0.5 mL formic acid, filtered through 0.45 μ Nylon membrane, degassed and pumped at a flow rate of 0.2 mL/min. Injection volume is 20 μ L

[C] Ion-trap mass conditions for LC-MSMS-MRM;

The MS parameters were defined as follow; peak width 2.0, isolation = on, fragmentation = off, Nebulizer 25 psi, Dry gas 11 L/min, Temperature 350 °C, m/z range and target mass was selected based on the MSMS operation, max accumulation time 200 MS ramp range 4500 – 1500 v. The MS Chromatogram was then retrieved and integrated using AUTO- MS mode for Total-Ion Chromatogram of the selected m/z (All-TIC-MS-n). Peaks were verified by m/z and retention time. Major ion MS peaks were selected as candidate for direct MSMS and fragmentation at different voltages. The MSMS data of each single ion was then matched with NIST2008. The Identified peaks were then analyzed by LC-MS applying MRM mode (Mixture Reaction Monitoring).

For direct MSMS the Ion-Trap conditions adjusted to; Nebulizer 15, Dry Gas 7, Temp 325 °C, fragmentation voltage 0.2 – 8.0 V (default 1.0V).

Procedure:

[A] About 50 mg of PMF was dissolved in 2 mL water.

[A-1] This sample was checked for the major constituent without any modification. Part of this sample (1 mL) was transferred to syringe-pump for direct MSMS. Direct MSMS analysis was performed to estimate the major ions that NOT observed in blank injection (water). A list of major ions was written and checked by MSMS-Single ion monitoring with fragmentation / isolation applying variable voltages (0.1 to 8V). Each single trapped ion was left 5 minutes to run for fragmentation with a flow rate of 5 μ L/hour. The saved files were downloaded and the Σ MS(n) was retrieved and investigated for similarity and matching with NIS-MSMS-Ion-Trap library (applying the same fragmentation voltage as per the library).

[A-2] A gradient LC elution program was applied with Auto-MSMS mode for the detected peaks over the threshold of average noise level of TIC-Baseline. By this procedure we could also confirm the major constituents with characteristic MSMS, which is then checked for similarity with the NIST-MSMS-Ion Trap data. Elution was programmed to deliver 100% 0.05M ammonium acetate pH 6.5 for 5 min, then to 100% acetonitrile within 55 min, at a flow rate of 0.2 mL/min.

[B] Enzymatic hydrolysis, sample preparation and analysis:

This procedure was applied to investigate the conjugated compounds. This enzyme is used to hydrolyze any glucuronides or sulphate conjugated compounds.

In a glass test tube (15-mL with screw cap) A weight of 500 mg of PMF was dissolved in 1 mL water and 2 mL 0.1M sodium acetate (pH 5.5), and mixed with 100 μ L β -glucuronidase arylsulphatase. The reaction mixture was left for 24 hours at 42 °C in water bath thermostatically controlled.

The mixture was cooled and extracted with 10 mL dichloromethane. The organic layer was separated and evaporated by bubbling nitrogen gas over a water bath at 50 °C. The dried extract was reconstituted in 400 µL dichloromethane, and divided to two portions. One microliter from the first portion was injected for GC-MS analysis and then the remaining amount was derivatized with MSTFA and analyzed by GC-MS. The second portion was dried again under N₂ gas and reconstituted with 200 µL acetonitrile. This solution was subjected to direct LC-MSMS analysis (Auto MSMS/Scan/Fragmentation), LC-MSMS-Autofragmentation (for identification, using mobile system-I), and analysed for searching estrogens (dansylation procedure, using mobile-II). The confirmed compounds were then analyzed by LC-MSMS using MRM mode, maximum 10 ions, to confirm the chromatographic profile of each compound, with a maximum of 3 overlapped peaks. MRM was applied for the analysis of different PMF batches to identify the average/ limit and the incidence of impurities.

B. Tissue culture

[A]. Media

The following commercially available media were prepared according to published literature, these include: Ordinary media, Minimal essential medium (MEM) (10%FCS): MEM is a rich, multipurpose medium that was used for cultivation of human lung cancer cells (A549). Phosphate Buffer Saline (PBS) is a Phosphate-Buffered physiological Saline solution. Calcium and Magnesium free Solution Trypsin.¹¹ Examined media: PMF (extracted from PM 701) is a natural product, easily available, cheap, sterile, and non-toxic according to our chemical and microbiological testing. PMF added to the ordinary media with ratio 2.5 µg : 1 ml media

[B]. Human Lung Cancer Cells line:

Human Lung Cancer Cells, non- small cell carcinoma (A549) was obtained from cell strain from (ATCC) American Type Cultural Collection, available in the cell bank of Tissue Culture Unit, King Fahd Medical Research Center (KAU, Jeddah).

In vitro proliferation of cells

1. Human Lung Cancer Cells (A549) were suspended in culture medium MEM.
2. The cells were dispensed in 3X (6wells plate), 1x10⁵/ml in each well.
3. Each group of cells was incubated 24 hrs in suitable media and apoptosis was induced by incubating cells in PMF at different time points [2, 5, 10, 20seconds and 1 minute].

D. Transmission Electron Microscope

Fixation of A549 cells

1-Fix in Trump's fixative for ½ to 1 hr which is prepared as follows:

40 ml of the 50% glutaraldehyde, 800 cc of 0.2 M Sodium cacodylate buffer, 30 ml of 37% Formaldehyde Mix well and adjust the pH to 7.2 then add buffer to make a final volume of 1000 cc. Aliquot 10 cc into red top tubes, label as Trump's Fixative/ poison and store the tubes in rack in refrigerator.

2-Rinse cells twice in distilled water for 15 min

3-The Agar- Enrobement procedure as described elsewhere¹² and summarized as follows: Lightly we centrifuge the culture/fixative mix at room temperature to generate a very loose pellet after Trump's fixation. We removed carefully the supernatant and gently flow several milliliters of buffered glutaraldehyde /formaldehyde fixative, at room temperature onto the loose pellet of cells. After 15 min, lightly we centrifuge the cells to form a loose pellet and remove the fixative using a pipe with taking care not to aspirate the cells. Using a warmed plastic pipet, quickly transfer approx 50 µL of warm agar onto the loose cells and gently stir the cells with the tip of the plastic pipet to suspend the cells in the warm agar. The tubes containing the suspended cells were placed in refrigerator until the agar solidifies. We put several milliliters of buffer into the tubes and used a spatula to dislodge the agar plug containing the cells. The agar pieces containing the enrobed cells were transferred into Petri dish containing buffer and trim the agar into 1 to 2 mm cubes.

4-Cells were post-fixed in Osmium tetroxide for ½ to 1hr. Rinse cells twice in distilled water 15 min each. Uranyl acetate for 20 min.

5-Dehydration: the cells were dehydrated through graded ethanol series (70%, 95% for 15 min, three times with 100% ethanol for 10 min and two changes of Propylene oxide for 8 min each.

6-Propylene oxide: resin (equal volumes 1:1) 30-45 min. Resin infiltration pure 30-45 min.

7-Embedded in pure resin into blocks at 60C overnight

E. Infrared spectroscopy

At various time points, the cells treated with PMF were harvested and washed twice (by centrifugation for 3 min at 300 g). The cell pellet was kept at -80 C and lyophilized prior to IR measurements. The lyophilized samples – from three different separated experiments - were dispersed in potassium bromide (KBr) discs by mixing them gently in an agate mortar and with pestle to obtain homogenous mixture as described earlier.^{13,14} The mixture then pressed in a die at 5 metric tons force for 10 s, creating a 1.1 cm diameter transparent disc with imbedded sample. The FTIR spectra were recorded in absorbance form using Shimadzu FTIR-8400s spectrophotometer with continuous nitrogen purge. The spectra were obtained in the wavenumber range of 4000-400 cm⁻¹ with an average of 20 scans to increase the signal to noise ratio and at spectral resolution of 4 cm⁻¹. All the samples were baseline corrected and normalized to amide I band by using IR Solution software. Infrared spectrum of PMF sample was also obtained in potassium bromide (KBr) discs.

F. Raman Microscopy

Raman spectrum was measured using a DXR Raman Microscope, Thermo Scientific, using a 532 nm laser as the excitation source at 600 mW power. The PMF sample was dissolved in distilled water. The spectrum was accumulated over 5 min with 300 scans.

G. Chemicals

PMF fraction was prepared by from Camel's urine as dried brownish past. Dansyl chloride (Dns-Cl, $\geq 99.0\%$ HPLC for fluorescence BioChemika) was purchased from Sigma-Aldrich, (Sigma-Aldrich, St. Louis, MO, USA). β -glucuronidase/arylsulfatase (Helix pomatia, Type HP-2 ≥ 500 Sigma units β -glucuronidase and ≤ 37.5 units sulfatase activity) was obtained from Sigma Chemical Co. (St. Louis, MO) All solvents used were of HPLC grade. Sodium acetate trihydrate and formic acid were of Analytical grade. N-Trimethylsilyl-N-methyl trifluoroacetamide, MSTFA, $>98.5\%$ GC, was purchased from Sigma-Aldrich, Germany. Reference standard of Estrogens and 5 potential metabolites were purchased from STERALOIDS; Estrone (E1), Estradiol (E2), and Estriol (E3), 2-MeOE1 (E4), 4-OHE1 (E5), 4-MeOE2 (E6), 16 α -OHE1 (E7) and 4-OHE2 (E8).

All other chemicals and solvents were of HPLC grade (BDH, London, England).

III. RESULTS AND DISCUSSION

PMF Surface Morphology

To examine the surface morphology of PMF we used the Scanning Electron Microscope (SEM). PMF images (Fig. 1) demonstrated different nanoparticles, crystals, and nano-rods with varying shapes and sizes which mainly indicates the presence of Calcium oxalate, Cystine, Tyrosine, Uric acid crystals in addition to Ammonium urate and Calcium Phosphate. El-Shahawy¹⁵ detected earlier the presence of Glycine, Alanine, Arginine in PMF.

Receptor tyrosine-specific protein kinases are a subclass of cell-surface growth-factor receptors with an intrinsic, ligand-controlled tyrosine-kinase activity. They regulate varied functions in normal cells and have a vital role in oncogenesis.¹⁶ Tyrosine kinases are an especially important target because they play an important role in the modulation of growth factor signaling.⁴ Glycine and cystine are amino acids that enter to glutathione structure. Glutathione is the famous antioxidant in the body, depletion of this small tripeptide molecule will lead to the accumulation and increased reactive oxygen species and consequently affect the immune system.¹³ Thus, presence of tyrosine enhance the targeting and selectivity of PMF to cancer cells and the presence of Glycine and Cystine are amino acids improve the immune system to kill cancer cells. In addition, PMF has many cluster of rods attached in such strange pattern (Fig. 1H) may be due to a magnetic effect.

PMF major constituents

The PMF major constituents confirmed by LCMS /GCMS, LC-MSMS – IonTrap were given in (Table 1-3). In addition to the previously mentioned amino acids arginine was detected and hippuric and benzoic acids as well. The role of the L-arginine/nitric oxide (NO) pathway in tumor therapy has been well-studied. Members of this pathway have been reported to be promising and targeting therapeutic molecules in tumor therapy.¹⁸ Furthermore, arginine has several immunomodulatory effects such as stimulating T- and natural killer cell activity and influencing pro-inflammatory cytokine levels. This may be through activation of interleukin -12 (IL-12).¹⁹ Moreover, it has been reported that induction of IL-23 leads to the production of interferons (IFNs) and other tumor-suppressive factors. These molecules are activated as part of the antitumor immunity response and promote apoptosis to tumor cells.²⁰

The International Immunology Foundation (IIF) is dedicated to the study of the relationships between the immune system of the patient and his or her cancer. Their goal is to enhance and unblock immune function so as to help this elegant system to successfully deal with cancer. The immune suppression that is generated by the cancer cell to protect itself from the patient's immune system can be removed. When the patient's immune system is unblocked it can identify and destroy cancer cells. A mature technology that removes immune suppression in cancer patients is Immuneapheresis and it is important than stimulating the immune system (IIF). Three decades ago M. Rigdon Lentz, MD and others established this technique. They showed that cancer cells produce soluble inhibitors that block the tumor cytotoxicity of tumor necrosis factor (TNF). These inhibitors can be removed from the blood safely and efficiently; and that once removed, the unblocked immune system can rapidly kill cancer cells. In clinical experience to date this immune unblocking has yielding significant clinical responses, including complete tumor remissions (IIF).

Tamás²¹ studied the effect of mixtures of amino acids and other small molecules in cancer patients. They found that administration of the product to cancer patients significantly improved their quality of life but they did not investigate the anticancer activity of these products. By contrast, Gyula²² detected inhibition ranging between 40% to 69% in mice tumor when treated with active mixture of amino acids that possesses a selective toxic effect on tumor cells in vitro and in vivo. Gyula²³ tested the potentiating effect of D(+)-mannose, orotic, and hippuric acid sodium salt on selective toxicity of circulatory system in culture for various tumor cell lines and found these compounds have play part of the defense system. Lei²⁴ proved the effect of cinnamic acid as a natural product that has anti-tumor activity. They revealed this activity in part to the inhibition of protein isoprenylation known to block mitogenic signal transduction.

PMF major elements

To identify the possible elements that could be present in PMF we tested it with Energy Dispersive X-ray (EDX) (data not shown) and with Inductively Coupled Plasma/Mass Spectra

(ICP/MS) (Table 4). We identified several ions that present in PMF in a relatively high concentration such as K, Ca, Cd, Y, Eu, Th and zinc, zinc is present in form of ZnO and Ca, Cd & Y are in form of sulfates as confirmed by the oxide and sulfate bands in the FTIR spectrum of PMF (Fig. not shown). The FTIR spectrum of PMF in the range of $4000\text{--}400\text{cm}^{-1}$ which showed the characteristic bands of glycine indicated by the amide absorbance doublet bands in the range $1450\text{--}1500\text{cm}^{-1}$. Zinc is present in the form of ZnO indicated by the IR absorbance band around 567cm^{-1} . Sulfate ions are observed at $1074, 1137\text{cm}^{-1}$ while carbonate ions around 1030 and 830cm^{-1} .

We thought that PMF selectivity may be due to many factors such as the presence of ZnO nanoparticles, and/or Cs and Rb at alkali pH.⁹ The novel findings of cell selective toxicity towards potential disease causing cells indicate a potential utility of ZnO nanoparticles in treatment of cancer and/or autoimmunity.²⁵ Cd and Y may be the core of nanoshell Y has a high magnetic properties.

Table 1: Compounds in PMF confirmed by LC-MSMS – IonTrap

tR [min]	Compound Name	Area	Max. m/z(MH ⁺)	Height	Area %
13.99		2144039		52552	
9	HIPPURic acid	484	179.92	031	45.5
		1311173		41727	
15.12	PhenacetURic acid	081	193.92	416	27.8
		1101779		23867	
5.082	CREATINine	506	114.05	673	23.4
		6465934		31684	
3.449	Phenyl-3-propyl	1	136.85	30	1.4
26.88		4372653		33322	
1	Alpha-biSABolol	0	222.89	37	58.2
		2981110		92249	
7.732	Benzeneacetic acid	0	136.94	1	0.6
20.65		2804461		33761	
7	PROSTAGLANDIN E2	7	353.16	73	37.3
18.39		2616037		53173	
9	CRYSol	2	109.10	7	0.6
18.37		1810993		67407	
7	BenZoic acid	0	123.06	9	0.4
36.64					
1	Cis-5,8,11-Eicosatrienoic acid	3416775	306.98	23019	4.5

Table 2: PMF major constituents. Compounds confirmed by GC-MS (not TMS-derivatives), enzymatically hydrolyzed sample

tR, min	GC-MS Confirmed compound	M+
8.97	Phenol, 2-(ethylamino)-4-methyl-	151
7.8	Phenol, 2-pentyl	164
7.49	Benzoic acid, 2-amino-, methyl ester	151
6.93	Phenol, 3-propyl-	136
6.45	1,2-Benzenediol	110
6.24	Phenol, 3-ethyl-	122
4.6	Phenol	94
5.5	o-Cresol	108

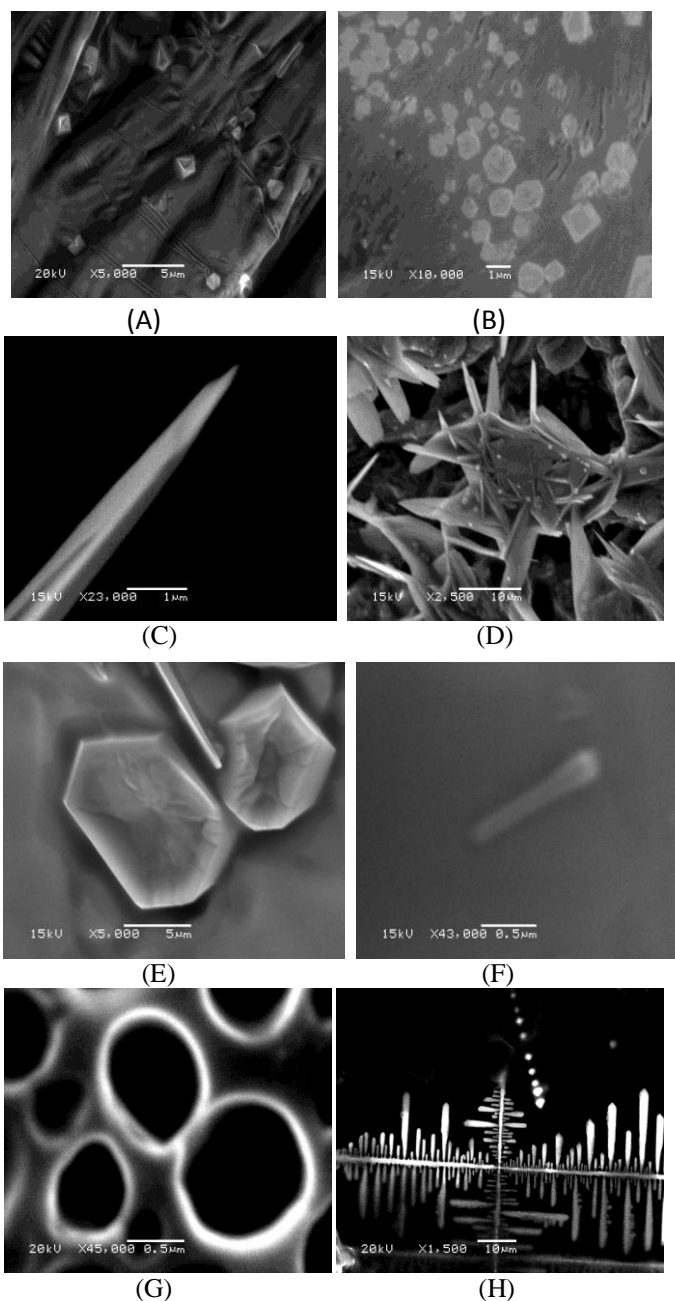


Fig.1. SEM images of PMF showed the presence of A) calcium oxalate crystals, B) Cystine crystals, C) Tyrosine, D) Uric acid crystals, E) Ammonium urate, F) Calcium Phosphate, PMF nanoshells with different diameters (G) and clusters of nano-rods connected and arranged in tremendous pattern due to magnetic effect (H).

PMF internal morphology

In an attempt to explore the internal morphology of PMF we used Transmission Electron Microscope (TEM) (Fig. 2). Interestingly, we found several spherical nanoparticles in form of nanoshells with diameter range between 26 up to 57nm. Nanoshells and dendrimers nanodelivery systems are synthesized to allow more specific targeting of the drug in treating cancer to minimize its side effects.²⁶

Table 3: PMF major constituents. Compounds confirmed by GC-MS as TMS derivative, enzymatically hydrolyzed sample

Glycine, N-(trimethylsilyl)-, trimethylsilyl ester	219	
Benzenepropanoic acid, trimethylsilyl ester	222	8.06
Benzenecetic acid, trimethylsilyl ester	208	7.24
dl-3-Aminoisobutyric acid, trimethylsilyl ester	175	7.17
Benzoic acid trimethylsilyl ester	194	6.9
3-Ethylphenol, trimethylsilyl ether	194	6.87
Silane, trimethyl(3-methylphenoxy)-	180	6.17
Silane, trimethylphenoxy-	166	5.4

Polyamindoamine (PAMAM) dendrimers contain tertiary amines and amide linkages which allow for binding of numerous targeting and guest molecules.²⁷

Examining of PMF in liquid form with Raman microscope (Fig. 3) revealed that PMF consists of different microshells with multilayers and different cores.

The Raman spectra obtained from different shells and the light core revealed that the outer and inner shells have the same spectrum. Moreover, almost the shell and the light core have the same structure (Fig. 4). The light core has little differences in the band intensity around 1030, 567 cm^{-1} indicating an increase in carbonate and ZnO concentrations in the light core compared to the shell. The Raman spectrum of the dense core gives information about the constituent of this core which indicates the presence of magnetic core of Ytterbium (III) sulfate.

V. The mechanism of PMF nanoparticles insertion into A549 cells

In order to evaluate the high efficiency, target specificity and to find out the mechanism of PMF in inducing apoptosis to A549 cells we took the FTIR spectra (Fig. 5) and TEM imaging (Fig. 6) to these cells after 2, 5, 10, 20 sec, and 1min of PMF treatment. We calculated and then plotted the intensity ratios $I(2921\text{cm}^{-1})/I(2871\text{cm}^{-1})$, $I(2852\text{cm}^{-1})/I(2871\text{cm}^{-1})$, and $I(2925\text{cm}^{-1})/\text{total lipid}$ from the FTIR spectra of the treated cells with the positive control A547 cells (Table 5) in order to investigate the membrane polarity, packing and the hydrocarbon chain length of A549 cells respectively prolong the treating time. The membrane polarity and packing decreased significantly in all treated cells for different times; the minimum values were detected for cells treated for 1min while cells treated for 5 sec showed a relatively higher values in these ratios compared to the other treated cells although they still have lower values compared to the control A547 cells. This increase in the membrane fluidity may be due to the presence of, K^+ , Ca^{2+} , Eu^{3+} ions. Same results was obtained by Fan²⁸ when detected a decrease in the rigidity of acyl chains of phosphatidylcholine (PC) and bovine serum albumin (BSA) complex when used these ions as a membrane model to study the interaction of metal ions with membrane lipid.

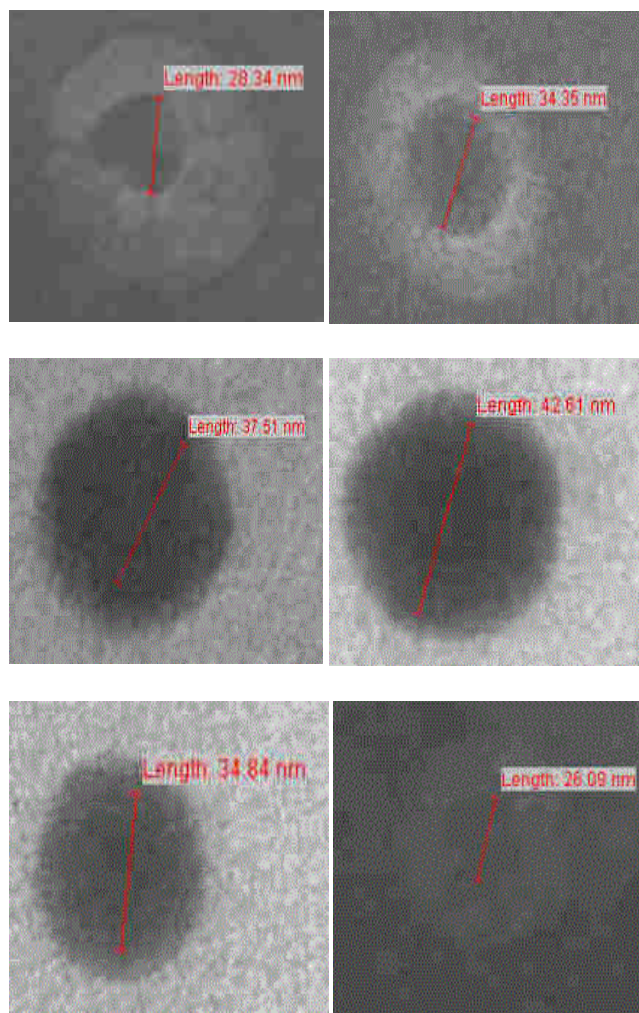


Fig. 2. TEM images demonstrate the internal structure of PMF nanoparticles. Spherical nanoshells with different diameters and different cores; light and dense cores.

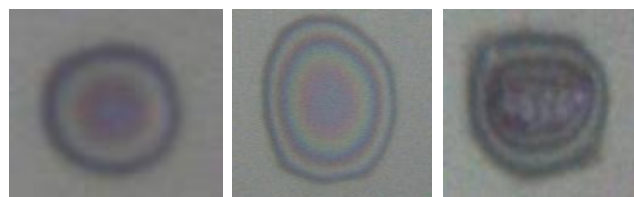


Fig. 3. FT-Raman microscope image of PMF fraction. The images show different microshells with multilayers and also light and dense cores.

Accompanied the increase in membrane fluidity we also detected an increase in the length of hydrocarbon chain as indicated by the increase in the $I(2925\text{cm}^{-1})/\text{total lipid}$ ratio.

We next tried to determine whether the detected nanoparticles can invade and induce apoptosis to A 547 cells. Particle shape significantly impacts the cellular and tissue interactions of nanomaterials. Endocytosis of shapes that are non-spherical are highly dependent on the local shape at the

Table 4. Part of the major PMF elements detected by ICP/MS.

Element	Mass	Concentration	SQ Unit	CPS
K	39	very high		over response
Na	23	7172.82	mg/l	28217881180
Mg	24	1137.07	mg/l	2154712288
Fe	56	4.95	mg/l	86920298.7
Sr	88	4.42	mg/l	53345799.21
Rb	85	1.77	mg/l	15917799.76
Zn	66	121.08	ug/l	460777.57
Mn	55	6.61	ug/l	78250.7
Pb	208	1.61	ug/l	96212.96
Co	59	1.09	ug/l	38824.97
Sb	121	687.29	ng/l	4320.78
Pd	105	600.20	ng/l	9232.95
Y	89	178.31	ng/l	4561.17
Hg	202	172.07	ng/l	1870.21
Cd	111	71.40	ng/l	390.03
Cs	133	48.78	ng/l	1200.1
Ag	107	38.07	ng/l	1720.17
Th	232	1.43	ng/l	90.01

interface of the cell with the nanomaterial or the tangential angle that nanomaterial shape makes with the cell.²⁹⁻³¹ PMF possesses, in addition to spherical nano particles, rods and spike like structures. Actually, the shape of the nanoparticles and the degrees of membrane fluidity during PMF treatment facilitate and play a great role in the nanoparticles endocytosis by the cancer cells.

The hypothesis that the army of PMF nanoparticles attacks A549 cells in successive stages or steps was made. First the cell membrane as early as 2sec post PMF treatment starts to be less packing with increasing the hydrocarbon chain length of its fatty acids and logically decreased the membrane polarity which in turn weekend the Wan der wall forces between the polar head groups and hence increases the membrane fluidity.

These findings have been proved by FTIR calculated intensity ratios and morphologically by TEM images (Fig. 6). These enable the larger nanoparticles which possessed a relatively high content of negatively charged amino acids [aspartic & glutamic acids] to escape immediately inside the of the membrane of these observed nanocarrier. After the initial burst, a very fast nanoshells with different diameters release was observed together with different separate cell. or spikes (Fig. 6A). After 5sec the membrane restored part of its

rigidity and polarity. Cancer cells are addicted to glycine; The cells engulfed specifically these nanoparticles and/or rods there are only a few clinically approved nanocarriers that incorporate molecules to selectively bind and target cancer cells³²; most probably glycine inter in the formation nanoshells that attack the nuclear membrane and the other cell organelles. Glycine is abundant in PMF as detected by GC/MS.

Thus nanoshells invade the cytoplasmic and nuclear membrane start to create transit pores after 5 sec of PMF treatment²⁹ (Fig. 6B). These temporary pores may allow the heavy nanocarrier particles and/or the carrier vehicle to escape easily through the cellular membrane and the nuclear envelope and hence drain its load inside the cells after 5, 10, and 20 sec (Fig. 6C). After 1 min all types of PMF forms was seen inside the cancer cells crystals, needles and nanoparticles (Fig. 6D). The nanoshells are completely paralyzing the cancer cells. Swollen and rupture or degenerated mitochondria are sign of apoptosis were seen in the figure.

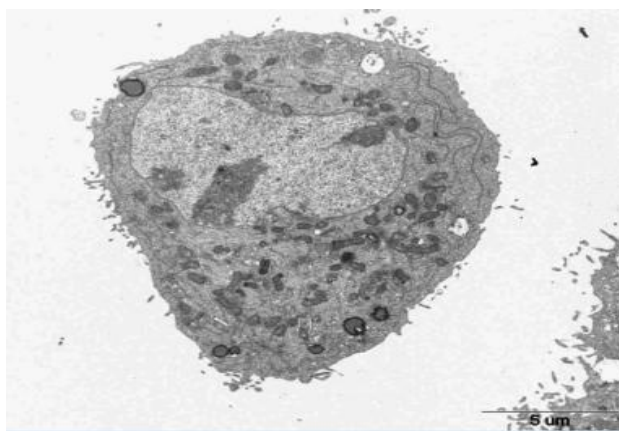
We put another hypothesis that Y acquires its magnetic property when the negative ions and negatively charged amino acids traveling inside the cell between the negatively charged inner membrane and the positively charged outer nuclear membrane. By using Fleming's left hand rule thus, at any angle of insertion the Y based nanoparticle directed forward to

Table 5: The calculated intensity ratios obtained from FTIR spectra of the tested groups to indicate the membrane lipid polarity, packing and the hydrocarbon chain length.

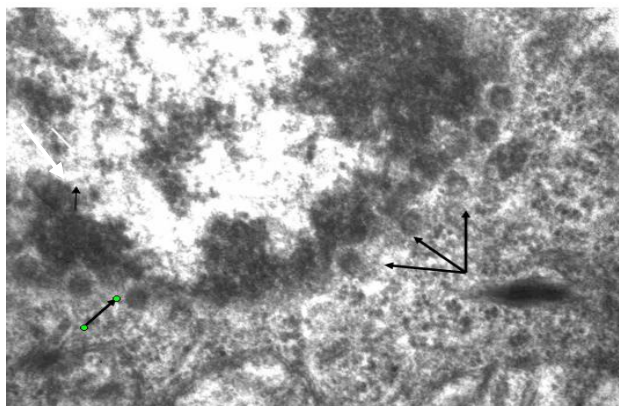
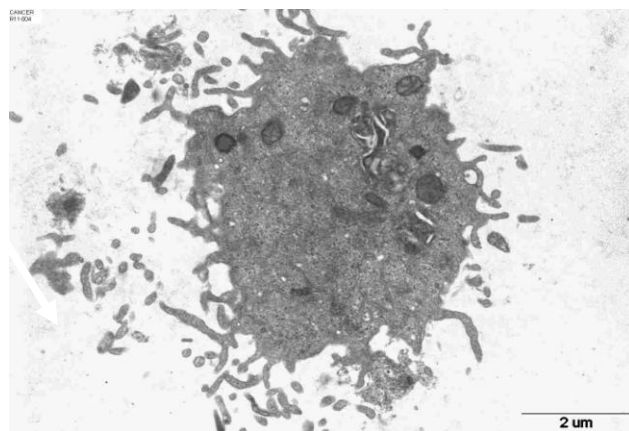
Intensity ratio/ Tested time	cont	2sec	5sec	20sec	1min
as CH₂ /sCH₃, I (2925cm ⁻¹)/I (2871cm ⁻¹) [lipid polarity]	1.787	1.676	1.753	1.690	1.676
s CH₂/sCH₃, I (2852cm ⁻¹)/ I(2871cm ⁻¹) Membrane packing	1.148	1.073	1.089	1.078	1.059
asCH₂ /total lipids I(2925cm ⁻¹)/ total lipid The hydrocarbon chain length	0.609	0.610	0.617	0.611	0.613

The intensity values were taken from the average of three different measured IR spectra of each sample for each tested time.

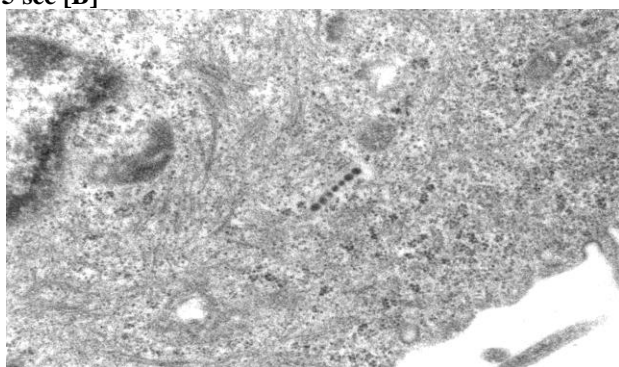
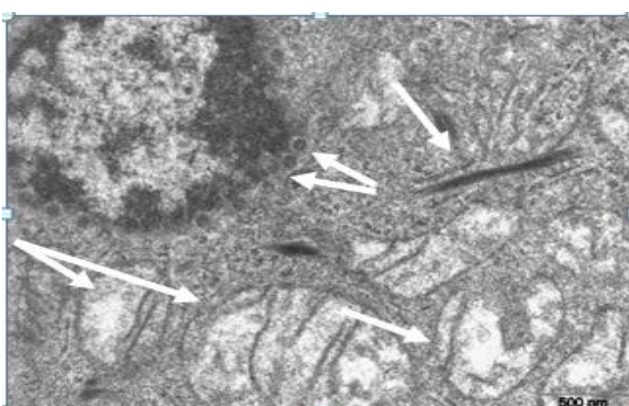
the inside the cell i.e. undeviating to the nucleus. This explains the appearance of a cluster of these magnetic nanoparticles first, after 5 sec, the nuclear envelop was surrounded by huge



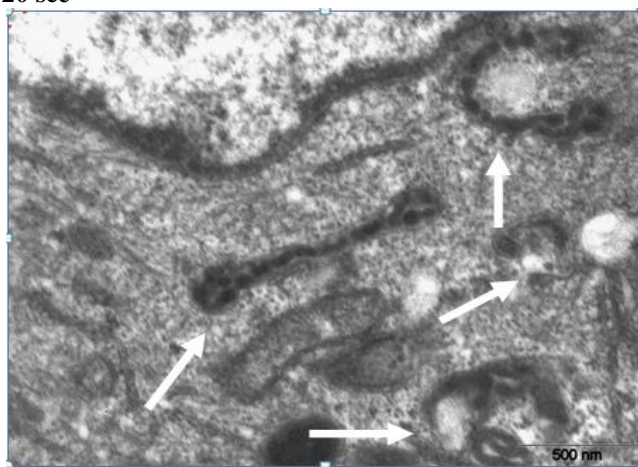
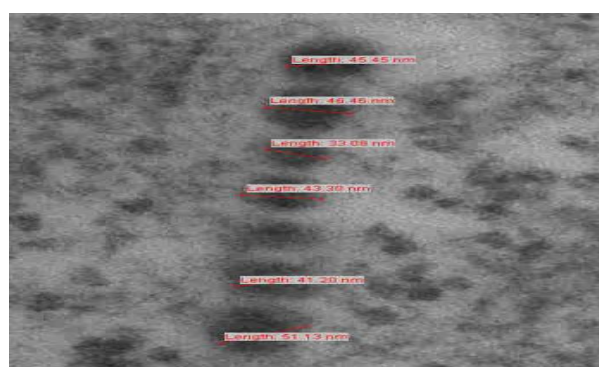
2 sec [A]



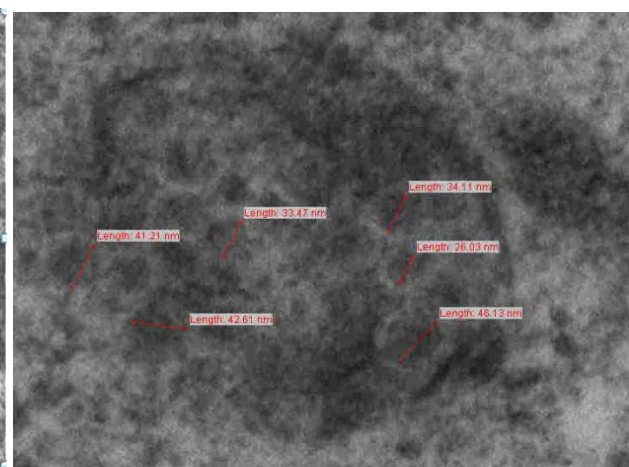
5 sec [B]

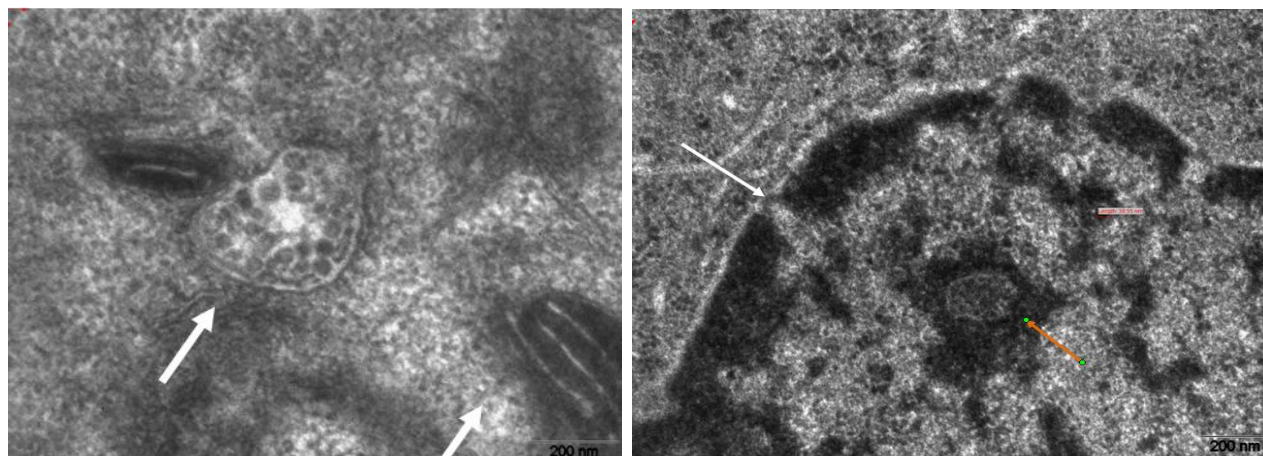


20 sec



20sec





1 min [D]

Fig. 6. A549 lung cancer cells after PMF treatment A) after 2 sec; spherical nanoparticles engulfed by the cells B) after 5 sec of treatment; Swollen and ruptured/degenerated mitochondria (sign of apoptosis), a spherical nanoparticles reach and invade the nuclear envelop and a nano rods was seen inside the cells. C) after 20 sec; larger nanocarrier and cluster of magnetic particles connected together inside the cells (left) and group of nanoparticles invade the lysosome of A549 cell or a cluster of nanoparticle inside a vesicle (right). D) after 1 min; (left) Nucleus completely occupied by nano particles, other cell organelles lose its features and structures, eg smooth endoplasmic reticulum (SER) have a diluted cisternae. Right) the nano particles of PMF surrounded the lysosomes, invaded the endoplasmic reticulum (ER) ER and damaged the Golgi apparatus (GA) and mitochondria. The figure also showed the presence of nanocarrier vessel loaded with nanoparticles inside the cancer cell after 20 sec and 1min of PMF treatment (yellow arrow).

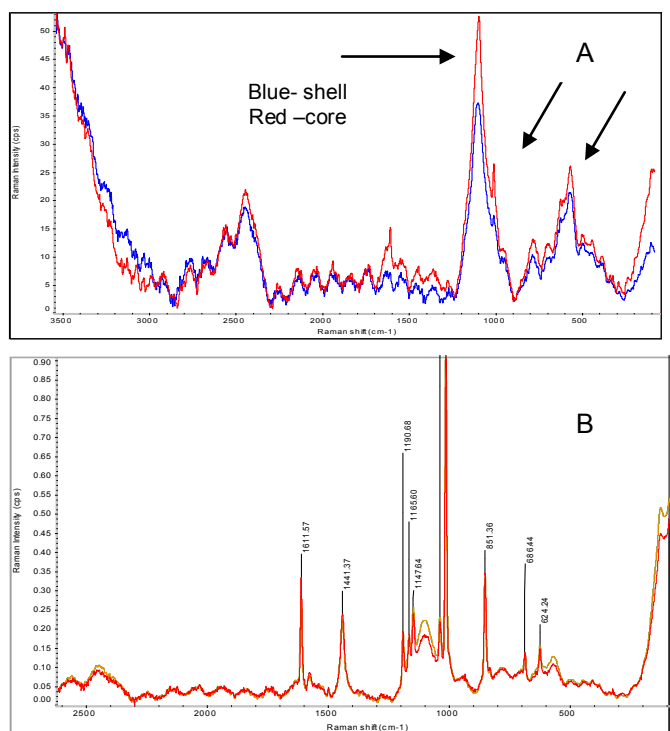


Fig 4. (A) The Raman spectra obtained from different shells and the light cores: The outer and inner shells have the same spectrum (left) while the shell and the light core have the structure but the core has a slight change in the band intensities of carbonat and ZnO bands (arrows-right). (B) FT-Raman spectra of different dense cores: The characteristic bands of CdSO₄ around 686,569 cm⁻¹, CaCO₃ Calcium carbonate around 1441, 850 cm⁻¹, thiocyanate bands at 2456, 2557 cm⁻¹, SiO₂ indicated by the presence of bands around 1100, 1147 cm⁻¹ and ZnO nanoparticle 567 cm⁻¹ were also detected in Raman spectrum of the dense core.

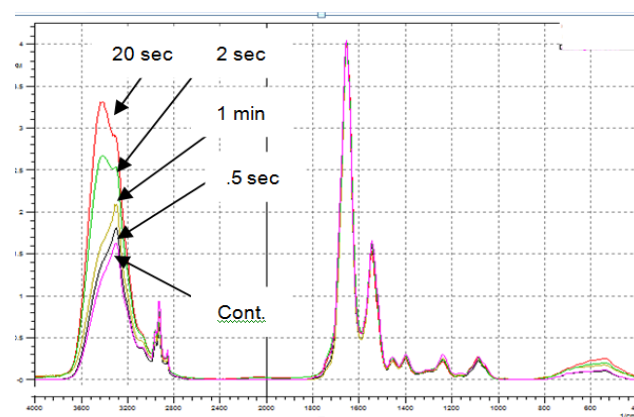


Fig. 5. The FTIR Spectra, in Kubelka Munk algorithm for clarity, of A549 cells at different time intervals of PMF treatment.

number of nanoparticles and hence the process of pore formation starts.^{9, 33} Second, after 20 sec of PMF treatment, 7 connected aggregates appeared inside the cancer cells (Fig. 6 C) which were observed earlier in (Fig. 1H).

With regards to cancer treatment, most current anticancer regimes do not effectively differentiate between cancerous and normal cells.²⁵ This indiscriminate action frequently leads to systemic toxicity and debilitating adverse effects in normal body tissues including bone marrow suppression, neurotoxicity, and cardiomyopathy.^{34, 35} QDs consists of a typical core/shell structure composed of heavy metals³⁶⁻³⁸ include a cadmium selenide or cadmium sulfide core coated with zinc sulfide shell. NPs applied as drug delivery systems are submicron-sized particles (3-200 nm), and are devices or

systems that can be made using a variety of materials including polymers (polymeric NPs) micelles, or dendrimers), lipids (liposomes), viruses (viral NPs), carbon based nanostructures (nanotubes) and even inorganic/organic core/shell hybrid NPs.³⁹ Various types of organic particles like liposomes and dendrimers should be mentioned, as these are already being used in cancer therapy and clinical treatment.⁴⁰ These synthetic nanoparticles matches in their properties and action the PMF detected nanoparticles

IV. CONCLUSION

PMF nanoparticles usually form a core of nanomaterial. They have surfaces for molecular assembly, that composed of inorganic materials revealed by the EDX, FTIR and FT-Raman spectra mainly Zn, Ag, Y, Cs, Rb. They are also in the form of nano-vesicle surrounded by a membrane layer or layers. The shape is often spherical with different sizes. The size and size distribution play an important role in certain situations. PMF possesses a variety of amino acids that makes with the above mentioned elements its unique selectivity to cancer cells. Thus, natural occurring nanoparticles obtained from PMF that have been passed phase I clinical trial, combines pH-triggered, drug-release and many of modes of selectivity offer a more targeted approach and promises significant improvements in the treatment of cancer. These nanoparticles proved to induce apoptosis in A549 lung cancer cells.

Acknowledgments

The authors thank Nourah Alotaibi M.Sc. student, Tahani Dakhakhni (M. Sc.) in KFMRC – KAU for assistance with Raman and FTIR measurements; Hanady kashkary (M.Sc.) tissue culture unit- KFMRC – KAU for assistance with tissue culture. The authors thank also Mr. Helmy A. Shahab senior technician (research assistant) Electron microscope unit – KFMRC for assistance with TEM imaging. This work was funded by ALZAMEL Scientific Chair for Cancer Researches no "429/3/KBM.

References:

- Frank, A., June-Wha, R., Jerome, P., Aleksandar, F., Radovic, M., Robert, L., Omid, C. New frontiers in nanotechnology for cancer treatment Urologic Oncology. *Seminars and Original Investigations*. **26**, 74-85 (2008).
- Haberzettl, C. A. Nanomedicine: destination or journey? *Nanotechnology*. **13**, R9 (2002).
- Whitesides, G.M. The once and future nanomachine. *Sci. Am*. **285**, 78-83 (2001).
- Amit, A., and Eric. M. Scholar, Role of Tyrosine Kinase Inhibitors in Cancer Therapy. *J. Pharma. Experm. Therap*. **315**(3), 971-979 (2005).
- Whitesides, G. M. The 'right' size in nanobiotechnology. *Nat. Biotechnol*. 2003; **21**:1161-1165.
- David, A. S., Carlos, H. V., Freddy, E. E., and Michael R. McD. Conscripits of the infinite armada: systemic cancer therapy using nanomaterials. *Nature Reviews Clinical Oncology* . **7**, 266-276 (2010).
- Khorshid, F.A.** Preclinical evaluation of PM 701 in Experimental animals. *Int. J. Pharma*. **4**(6), 443-451(2008).
- Khorshid, F.A.** Potential Anticancer Natural Product against Human Lung Cancer Cells. *Trends in Medical Research* . **4** (1): 9-15 (2009).
- Faten, A. K., Gehan, A. R., Salem, M. El., Gehan, S. Al., Nourah A. Al., Taha A. K. PMF, Cesium & Rubidium Nanoparticles Induce Apoptosis in A549 Cells. *Life Sci. J*. **8**(3):534-542 (2011).
- Khorshid, F.A.**, Shazly, H., Al-Jefery A., and Osman, A.A. Dose Escalation Phase I Study in Healthy Volunteers to Evaluate the Safety of a natural product PM 701. *Int. J. of pharma. toxic*. **5**(3): 91-9 (2010).
- Giaever, I., Keese, C.R., IEEE Transactions on Biomedical Engineering BME-33 (2), pp. 242-247, 1986.
- Methods in Molecular Biology-Electron Microscopy – Methods and Protocols, 2nd Edition John Kuo, Humana Press-Totowa, New Jersey
- Paul, G. L., Robert, D. S., Cancer grading by Fourier transform infrared spectroscopy. **4**, 37-46 (1998).
- Raouf, G. A., Khorshid, F.A., Kumosani, T., FT-IR Spectroscopy as a Tool for Identification of Apoptosis-Induced Structural Changes in A549 Cells Dry Samples Treated with PM 701. *Int.J. Nano and Biomaterials*. **2**(1/2/3/4/5), 396-408 (2009).
- El-Shahawy, A., El-Sawi, N., Backer, W.S., **Khorshid, F.A.**, and Geweely, N.S. Spectral Analysis, Molecular Orbital Calculations And Antimicrobial Activity Of PMF-G Fraction Extracted From PM-701. *Int. J. of Pharma and Bioscience*. **1**(2):1-19 (2010).
- Andreas, G., Oliver, M. F., & Axel, U. The discovery of receptor tyrosine kinases: targets for cancer therapy *Nature Reviews Cancer*. **4**:361-370 (2004).
- Gustavo, B. Whey protein concentrate (WPC) and glutathione modulation in cancer treatment. *Anticancer Research* **20**, 4785-4792 (2000).
- [Ma, Q.](#), [Wang, Z.](#), [Zhang, M.](#), [Hu, H.](#), [Li, J.](#), [Zhang, D.](#), [Guo, K.](#), [Sha, H.](#) Targeting the L-arginine-nitric oxide pathway for cancer treatment. *Curr. Pharm. Des*. **16**(4):392-410 (2010).
- Lin, W.W., Karin, M., A cytokine-mediated link between innate immunity, inflammation, and cancer. *J. Clin. Investig*. **117**(5):1175-1183 (2007).
- [Maria, M.](#), [Leslee, S.](#), [Harika, N.](#), [Michelle, P.](#), and [Fabian B.](#) Toll-Like Receptors as Novel Therapeutic Targets for Ovarian Cancer. *ISRN Oncology*. 2012 ID 642141, 8 pages(2012).
- Tamás, C., Zoltán, L., Mária, B., Csilla, Z., Mária, G., Gyula K., Safety, Tolerability, and Effect on Quality of Life of a Mixture of Amino Acids and Other Small Molecules in Cancer Patients. *Cancer Biotherapy & Radiopharmaceuticals*. **29**(3): 124-134 (2014).
- Gyula, K., Dezső, G., Péter, I. K., Ákos, S., Tamás, C., A mixture of amino acids and other small molecules present in the serum suppresses the growth of murine and human tumors *in vivo*. *International Journal of Cancer*. **132**(5): 1213-1221 (Mar 2013).
- Gyula, K., PhD, Synergistic Potentiating Effect of D(+)-Mannose, Orotic, and Hippuric Acid Sodium Salt on Selective Toxicity of a Mixture of 13 Substances of the Circulatory System in Culture for Various Tumor Cell Lines. *Cancer Detectoin and Prevention*. **24**(5), 485495 (2000).
- Lei, L., Robert, W. H., Sonsoles, S., Mu, Q. Y., and Dvorit, S., Cinnamic acid: A natural product with potential use in cancer intervention. *International Journal of Cancer* **62**(3), 345-350 (1995).

- 25- Cory, H., Janet, L., Alex, P., Reddy, K.M., et al., Preferential killing of cancer cells and activated human T cells using ZnO nanoparticles. *Nanotech.* **19**(29), 295103 (2008).
- 26- Dhruva, J. B., Marianne, K. [...], and Shaker, A. M. Nanoparticles and cancer therapy: A concise review with emphasis on dendrimers *Int. J. Nanomedicine.* **4**, 1-7 (2009).
- 27- Tomalia, D. A., Reyna, L. A. and Svenson, S. Dendrimers as multi-purpose nanodevices for oncology drug delivery and diagnostic imaging. *Biochemical Society*. 61-67(2007).
- 28- Fan, W., Zhanlan, Y., Yong, Z., Shifu, W., Li, Z., Jinguang, Wu. Influence of metal ions on phosphatidyl choline-bovine serum albumin model membrane, an FTIR study. *J. Molec. Str.* **794**, 1-11 (2006).
- 29- Chithrani, B.D., Ghazani, A.A & Chan, W. C. Determining the size and shape dependence of gold nanoparticle uptake into mammalian cells. *Nano. Lett.* **6**, 662-668 (2006).
- 30- Champion, J. & Mitragotri, S. Role of target geometry in phagocytosis. *Proc. Natl. Acad. Sci. USA* **103**, 4930-4934 (2006).
- 31- Zhang, K., Fang, H., Chen, Z., Taylor, J., Wooly, K. Shape effects of nanoparticles conjugated with cell-penetrating peptides (HIV Tat PTD) on CHO cell uptake. *Bioconjug. Chem.* 2008;19:1880-1887.
- 32- Dan, P., Jeffrey, M. K., Seungpyo, H., Omid, C. F., Rimona, M., & Robert, L. Nanocarriers as an emerging platform for cancer therapy *Nature Nanotechnology* **2**, 751 – 760 (2007).
- 33- Raouf, G.A., Khorshid, F.A., Kumosani, T.A. FT-IR Spectroscopy as a Tool for Identification of Apoptosis-Induced Structural Changes in A549 Cells Treated with PM 701. *Int. J. Nano and Biomaterials.* **2**(1/2/3/4/5) , 396-408 (2009).
- 34- Nie, S., Xing, Y., Kim, G., Simons, J. Nanotechnology applications in cancer. *Annu. Rev. Biomed. Eng.* **9**, 257-88 (2007).
- 35- Bosanquet, A., Bell, P. Ex vivo therapeutic index by drug sensitivity assay using fresh human normal and tumor cells. *J. Exp. Ther. Oncol.* **4**, 145-54 (2004).
- 36- Michalet, X., Pinaud, F.F., Bentolila, L.A., Tsay, J.M., Doose, S., Li, J.J., et al. Quantum dots for live cells, in vivo imaging and diagnostic. *Science*. **307**, 538-44(2005).
- 37- Smith, A.M., Duan, H., Mohs, A.M., Nie, S. Bioconjugated quantum dots for in Vivo molecular and cellular imaging. *Adv Drug Del Rev.* **60**, 1226-40 (2008)
- 38- Rhyner, M.N., Smith, A.M., Gao, X., Mao, H., Yang, L., Nile, S. Quantum dots and multifunctional nanoparticles: new contrast agents for tumor imaging. *Nanomedicine.* **1**, 209-17 (2006)
- 39- Cho, K., Wang, X., Nie, S., Chen, Z., Shin, D., Therapeutic nanoparticles for drug delivery in cancer. *Clin. Cancer Res.* **14**, 1310-6 (2008).
- 40- Miriam, C., Fabio, C., Diego, F. HER2 targeting as a two-sided strategy for breast cancer diagnosis and treatment: Outlook and recent implications in nanomedical approaches. *Pharmacological Res.* **62**(2), 150-165 (2010).

Planckian distributions in molecular machines, living cells, and brains: *The wave-particle duality in biomedical sciences*

Sungchul Ji

Abstract --- A new mathematical formula referred to as the *Planckian distribution equation* (PDE) has been found to fit long-tailed histograms generated in various fields, including protein folding, single-molecule enzymology, whole-cell transcriptomics, T-cell receptor variable region diversity, brain sciences, and econometrics. PDE can be derived from the Gaussian distribution law by applying the simple rule of transforming the random variable, x , non-linearly, while keeping the Gaussian y coordinate constant. There appears to be a common mechanism underlying all Planckian processes (defined as those physicochemical processes generating numerical data that obey PDE), which has been suggested to be the SID-TEM-TOF mechanism, the acronym for Signal-Induced Deactivation of Thermally Excited Metastable state leading TO Functions. The universal applicability of PDE to many long-tailed histograms is attributed to (i) its role in generating functions and organizations through goal-directed selection of subsets of Gaussian processes, and (ii) the wave-particle duality operating in living systems.

Keywords --- blackbody radiation, fMRI, Planckian distribution equation, single-molecule enzymology, wave-particle duality, whole-cell metabolism, decision-making process

S. Ji is with the Department of Pharmacology and Toxicology, Ernest Mario School of Pharmacy, Rutgers University, Piscataway, N.J. (609-240-4833; sji.conformon@gmail.edu).

I. INTRODUCTION

Blackbody radiation refers to the emission of photons by material objects that completely absorb photons impinging on them (hence appearing black). An example of blackbody radiation is given in **Figure 1 a)** which shows the emission of different wavelength light as a function of temperature. When the light intensity of a blackbody is measured at fixed temperatures, the so-called “blackbody radiation spectra” are obtained as shown in **Figure 1 b).**

M. Planck (1858-1947) succeeded in deriving the mathematical equation given in Equation (1) that quantitatively accounted for the blackbody radiation spectra. The key to his successful derivation of the so-called *Planck radiation equation* was his assumption that light is emitted or absorbed by matter in discrete quantities called “quanta of action,” which led to the birth of *quantum mechanics* revolutionizing physics in the early 20th century [1].

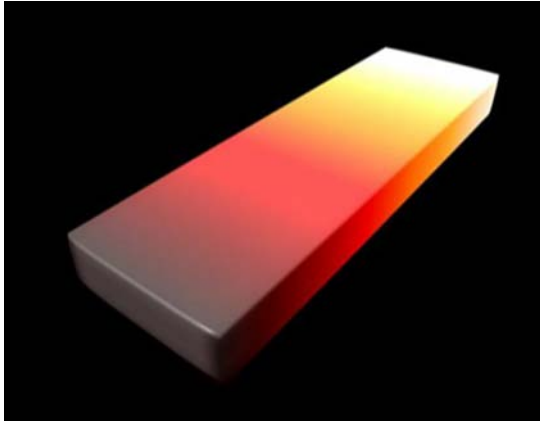
In 2008 [2, Chapter 11], the author noticed that the single-molecule enzyme-turnover-time histogram (see the bar graph in **Figure 3 a)** published by Lu et al. [3] resembled the blackbody radiation spectrum at 4000 °K (**Figures 1 b) and 2 b)**). This observation led me to generalize the Planck radiation equation, Eq. (1), by replacing its universal constants and temperature by free parameters as shown in Equations (2) and (3), the former having 4 parameters, a , b , A and B , and the latter 3 parameters, A , B and C . Depending on the data set to be analyzed, either the 4- or 3-parameter equation can be employed. The

“generalized equation” was originally referred to as the “blackbody radiation-like equation” (BRE) [4], but as the equation was found to apply to more and more data sets, it was thought appropriate to refer to it as either the “generalized Planck equation” (GPE), or more simply as the “Planckian distribution equation” (PDE), in analogy to the Gaussian distribution equation (GDE). The 4-parameter equation can be transformed to the 3-parameter equation utilizing the transforming Equations (4), (5)

and (6).

The main objective of this paper is (i) to demonstrate the ability of PDE to fit long-tailed histograms reported in many fields, ranging from atomic physics (see Fig. 2) to econophysics (see Figs. 7g and 7h), and (ii) to discuss possible mechanisms underlying individual data sets fitting PDE as well as the common mechanisms underlying the universality of PDE.

a)



b)

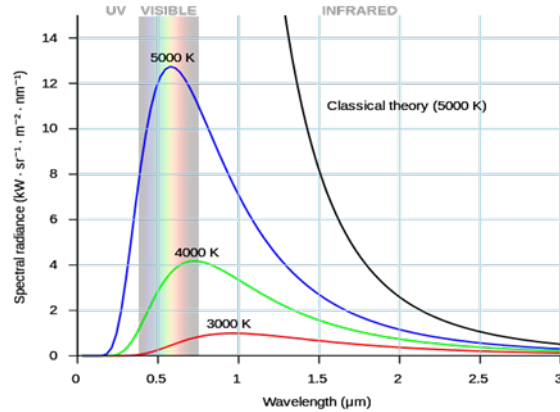


Figure 1. a) Blackbody radiation. Reproduced from <http://www.creativecrash.com/maya/downloads/shaders/c/black-body-radiation>
b) The blackbody radiation spectra. Reproduced from http://en.wikipedia.org/wiki/Black-body_radiation.

$$E(\lambda, T) = \frac{2\pi hc^2}{\lambda^5 (e^{\frac{hc}{\lambda T}} - 1)} \quad (1)$$

where

- E = Energy
- λ = Wavelength
- c = Speed of light
- k = Boltzmann constant
- h = Planck's constant
- e = 2.71828182

$$\begin{aligned}
[T] &= \text{Kelvin (temperature)} \\
[\lambda] &= \text{Meters} \\
h &= 6.626.1034 \text{ J.s} \\
c &= 2.998.108 \text{ m/s} \\
k &= 1.381.10^{-23} \text{ J/K.}
\end{aligned}$$

Number of standing waves per unit frequency per unit volume

Average energy per standing wave

$$y = \frac{a}{(Ax + B)^5} \cdot \frac{1}{e^{b/(Ax + B)} - 1} \quad (2)$$

$$y = \frac{A}{(x + B)^5} \cdot \frac{1}{e^{C/(x + B)} - 1} \quad (3)$$

$$A = a/A^5 \quad (4)$$

$$B = B/A \quad (5)$$

$$C = b/A \quad (6)$$

II. METHODS

A. Digitization of long-tailed histograms

Due to the difficulties encountered in obtaining the original numerical data of most of the published histograms analyzed in this paper, it was necessary to digitize the graphs of interest in order to test whether they fit the Planckian distribution equation (PDE). Our digitization involved two steps: (i) using either the original graph or after amplifying it by 2-3 fold by xeroxing at an expanded scale, and (ii) digitizing a given histogram either by “hand” using a ruler or by using the digitization program *Paint*.

To test the accuracy of our “hand-digitization” technique, we compared the hand-digitized data set of a published

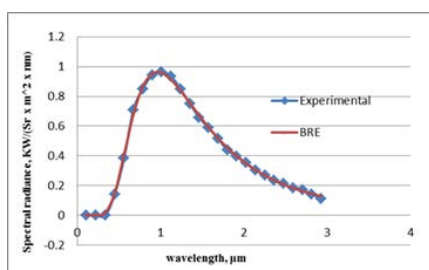
histogram (Figure 2 in [5]) and the original data set of the graph kindly provided by Dr. K. Dill, one of the authors of [5]. When the former was plotted against the latter, a linear correlation was obtained with the equation, $y = 1.0059x - 0.245$, with the R^2 value of 0.9999, indicating that our hand-digitization technique is reliable. Further evidence for this conclusion is provided by **Figures 2 a), b) and c)**, in which PDE reproduced the blackbody radiation spectra at three different temperatures almost exactly. The numerical values of the parameters of PDE fitting the hand-digitized curves are given in **Table I**. The root means square deviations (RMSD) calculated by the *Solver program* in Excel and the visual inspection of **Figures 2 a), b) and c)** indicate that the agreement between PDE-predicted and the actual blackbody

radiation spectral data hand-digitized by us is excellent.

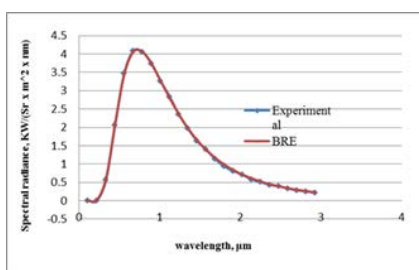
Table I. Simulating the blackbody radiation spectral data hand-digitized by the author and inputted into the Planckian distribution equation (PDE), Eq. (2). The b/A ratio is proportional to the width (or spread) of the Planckian distribution.

Temperature (°K)	a	b	A	B	RMSD	b/A
3000	1.53×10^5	20.208	4.215	0	0.0121	4.79
4000	1.34×10^5	14.705	4.061	0	0.0237	3.62
5000	4.40×10^8	34.952	12.020	0	71.35	2.91

a)



b)



c)

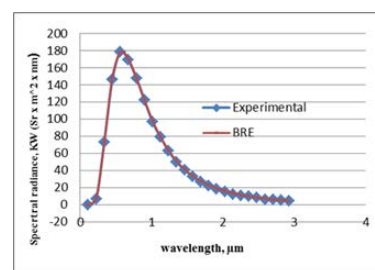


Figure 2. The hand-digitized data from the blackbody radiation spectra at a) 3000 °K, b) 4000°K, and c) 5000 °K shown in **Figure 1 b)** were reproduced almost exactly by the Planckian distribution equation, Eq. (2).

B. The invariance of the parameter ratios of the Planckian distribution equation (PDE)

More than one sets of the numerical values of PDE parameters were found to fit a given set of data with comparable accuracies as measured with the root mean square deviation (RMSD) values. For example, when the mRNA level data from human breast cancer tissues [6] that are associated with CGI (kinase binding protein), MAPK (mitogen-activated protein kinase), and ZFP (zinc finger protein) were

fit into PDE (see **Figure 7 c)**), at least four sets of the numerical values each could fit the data more or less equally well (e.g., see **Table II**). What is interesting is that, although the numerical values of the parameters, a, b, A and B, vary widely, the ratios, b/A, B/b and B/A remain relatively constant. Because the size of the b/A ratio is 10^2 - 10^3 fold larger than the other two ratios, this ratio was chosen as a representative of a given data set.

Table II. The invariance of the parameter ratios of the Planckian distribution function.

	a	b	A	B	b/A	B/b	B/A
CGI	7.579×10^6	17.695	4.99	-0.492	3.546	-0.0278	-0.0986
	7.398×10^8	44.233	12.495	-1.230	3.540	-0.0278	-0.0984
	8.000×10^8	45.072	12.732	-1.253	3.540	-0.0278	-0.0984
	8.090×10^8	45.031	12.732	-1.249	3.536	-0.0277	-0.0981
MAPK	5.755×10^6	19.519	7.261	-2.363	2.688	-0.121	-0.325
	7.396×10^8	51.589	19.048	-6.106	2.708	-0.118	-0.321
	8.000×10^8	52.519	19.391	-6.216	2.708	-0.118	-0.321
	7.970×10^8	52.603	19.101	-6.004	2.754	-0.114	-0.314
ZFP	2.219×10^7	24.175	7.387	-1.098	3.273	-0.045	-0.149
	7.383×10^8	48.731	14.891	-2.214	3.273	-0.045	-0.149
	8.000×10^8	49.644	15.170	-2.255	3.273	-0.045	-0.149
	8.080×10^8	49.610	15.163	-2.250	3.272	-0.045	-0.148

B. Gibbs free energy of protein folding

III. COMPUTATIONAL RESULTS AND DISCUSSIONS

A. Simulation of the blackbody radiation spectra with PDE

Figure 2 and Table I demonstrate that PDE (Planckian distribution equation), Eq. (2), can simulate the blackbody radiation spectra at 3000, 4000 and 5000 °K almost perfectly. Comparing Eqs. (1) and (3) and taking into account the fact that $B = 0$, it follows that parameters A and C of the Planck distribution are related to hc^2 and hc/k , respectively, the significance of which remaining to be investigated.

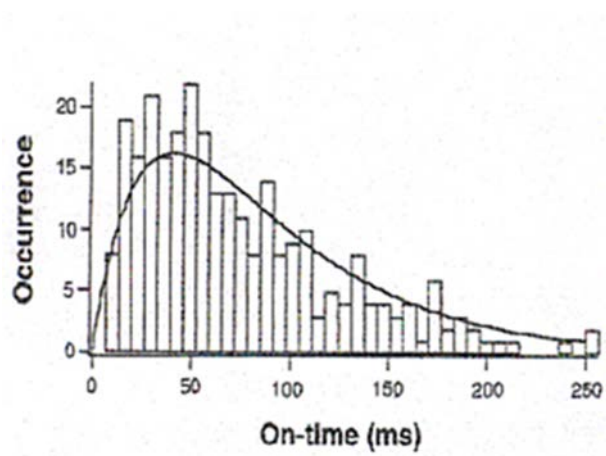
Under normal biological conditions of constant temperature (T) and pressure (P), all spontaneous changes, including protein folding from unfolded to folded states, are driven by a decrease in Gibbs free energy [7, 8], i.e., by a negative Gibbs free energy change, $\Delta G < 0$. Conversely, when a protein unfolds, the accompanying free energy change is positive, i.e., $\Delta G = G_{\text{unfolded}} - G_{\text{folded}} > 0$, which is referred to as the *free energy of protein folding* or *protein stability* [5]. Gibbs free energy G is defined as $G = H + PV - TS$, where H is enthalpy or heat content, V is the volume of the thermodynamic system under consideration, and S is the entropy of the system. Under the conditions of constant T and P , this equation leads to $\Delta G = \Delta H + P\Delta V - T\Delta S$ [8]. Based on experimentally determined enthalpy,

entropy, heat capacity, and the length distributions of 4, 3000 proteins from *E. coli*, Dill and his coworkers derived a theoretical equation for protein stability which generated the experimental curve shown in **Figure 7 a)** [5]. As evident in the figure, this theoretical curve can be simulated by the Planckian distribution equation, Eq. (3), with a great precision.

C.1. Single-molecule enzyme catalysis

The technique of measuring the single-molecule enzyme kinetics is outlined in [3]. The enzyme turnover-time histogram shown

a)



b)

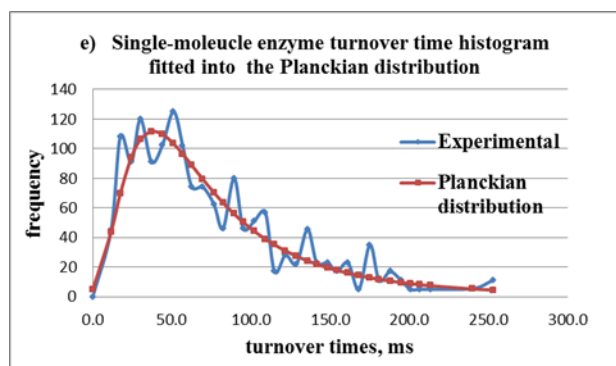


Figure 3. a) Single molecules of cholesterol oxidase isolated and embedded in gel can be observed to undergo “blinking” of fluorescent light due to its coenzyme FAD which fluoresces when in its oxidized state and is non-fluorescent when it is reduced by its substrate, cholesterol. One cycle of blinking of the coenzyme constitutes one turnover time of the enzyme. The turnover times of the enzyme were not constant but varied widely, generating a histogram as shown here. Lu et al. [3] fitted the histogram with a double exponential function (see the curve). **b)** The same data as in **a)** were simulated using the Planckian distribution equation, Eq. (3).

C.2. Quantization of energy levels in enzymes

Just as the fitting of the blackbody

radiation spectra to Planck's radiation equation, Eq. (1), is synonymous with the *quantization of the energy levels* of electrons in an atom, so it is postulated here that the fitting of the single-molecule enzyme-turnover times of Lu et al. [3] to the Planckian distribution equation, Eq. (2) or (3), as demonstrated in **Figure 3 b)**, implies that the conformational states (and hence conformational energy) of an enzyme molecule are quantized. This postulate is consistent with the concept of "conformational substates" of Frauenfelder

et al. [9] and the quantization of the Gibbs free energy levels of an enzyme [2, Section 12.14]. Gibbs free energy, G , rather than energy, E , must be considered here because, under the conditions of constant temperature and pressure, it is G , not E , that drives all spontaneous processes in living systems [7, 8]. The quantization of *Gibbs free energy* (hereafter called *energy* for brevity) in enzymes is schematically represented in **Figure 4 b)** in analogy to the energy quantization in atoms shown in **Figure 4 a)**.

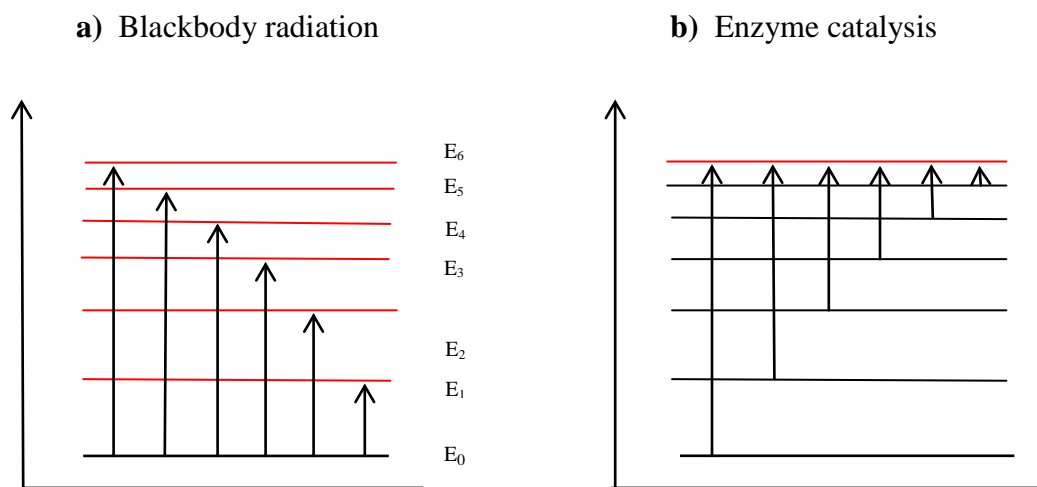


Figure 4. The postulated isomorphism between *energy quantization* in atoms and the discretization/quantization of the conformational states (and hence of Gibbs free energy levels) in enzymes. **(a)** The quantization of the energy levels of electrons in an atom suggested by the fitting of the blackbody radiation spectra with the Planck radiation equation discovered in 1900 [1]. **(b)** In analogy to the quantization of the energy levels of electron in an atom entailed by the Planck's radiation law, i.e., Equations (1), it is postulated that the fitting of the single-molecule turnover time histogram of cholesterol oxidase by the Planckian distribution law, Eq. (2) or (3), implied a similar quantization of energy levels of enzymes, most likely due to the existence of discrete conformational states of enzymes, denoted as C_i , where the index i running from 1 to n , the number of conformational states of an enzymes [9]. Reproduced from [2, Section 11.3.3.].

Blackbody radiation involves promoting the energy levels (vibrational, electronic, or vibronic) of oscillators from their ground

state E_0 to higher energy levels, E_1 through E_6 . The wavelength of the radiation (or quantum of action) absorbed or emitted is

given by $\Delta E = E_i - E_0 = h\nu$, where E_i is the i^{th} excited-state energy level, h is the Planck constant, ν is the frequency, and ΔE is the energy absorbed when an oscillator is excited from its ground state to the i^{th} energy level. Blackbody radiation results when electrons transition from a given energy level to a lower energy level within matter, e.g., from E_1 to E_0 , or from E_2 to E_0 , etc. [2, Section 11.3.3].

A single molecule of cholesterol oxidase is postulated to exist in n different conformational states (i.e., conformational substates of Frauenfelder et al. [9]). Each conformational state (also called a conformer, or conformational isomer) is thought to exist in a unique Gibbs free energy level and carries a set of sequence-

specific conformational strains (called conformons) [2, Chapters 8 and 11] and can be excited to a common transition state (denoted as C^\ddagger) by thermal fluctuations (or Brownian motions), leading to catalysis [2, Section 11.3.3].

C.3. The Energy Quantization as a Prelude to Organization

A possible meaning of the energy quantization invoked in **Figure 5 b**) to account for the fitting of the single-molecule enzyme kinetic data into the Planckian distribution function, Eq. (2), was proposed in the following quote reproduced from [2, p. 111]:

“Quantization (or discretization) may be essential for any organization, since organization entails selection and selection in turn requires the existence of discrete entities to choose from. In Sections 11.3.3 and 12.12, experimental evidence is presented that indicates that biological processes such as single-molecule enzymic activities . . . , whole-cell RNA metabolism . . . and protein folding . . . are quantized because they all obey mathematical equations similar in form to the blackbody radiation equation . . . that was discovered by M. Planck in physics in 1900 which led to the emergence of quantum mechanics two and a half decades later. . . .

To make the blackbody radiation data fit a mathematical equation, Planck had to assume that the product of energy and time called “action” is quantized in the unit later called the Planck constant, h , which has the numerical value of 6.625×10^{-27} erg·sec. This quantity seems too small to have any measurable effects on biological processes which occur in the background of thermal fluctuations involving energies in the order of kT , where k is the Boltzmann constant, 1.381×10^{-16} erg/degree and T is the absolute temperature. The numerical value of kT is 4.127×10^{-14} ergs at room temperature, $T = 298$ °K, which is thirteen orders of ten greater than h . Thus it appears reasonable to assume that biological processes are quantized in the unit of k rather than in the unit of h as in physics, which leads me to suggest that

*“The Boltzmann constant k is to biology
what the Planck constant h is to physics.”* (4-36)

Thus by combining the evidence for the quantization of biological processes provided by Table 4-6 and Statement (4-36), it appears logical to conclude that

*“Biological processes at the molecular and cellular levels
are quantized in the unit of the Boltzmann constant k .”* (4-37)

Elsewhere in [2, p. 110], I also suggested that both information and energy are essential for organization:

“For the purpose of discussing living processes, it appears sufficient to define ‘organization’ as the nonrandom arrangement of material objects in space and time. I have long felt that both energy and information are required for any organization, from the Belousov-Zhabotinsky reaction-diffusion system . . . to the living cell . . . and higher structures. This vague feeling may now be given a more concrete expression by asserting that ‘organization’ is the complementary union of information and energy or that information and energy are the complementary aspects of organization In other words, the information-energy complementarity may well turn out to be the elusive physical principle underlying all organizations not only in living systems but also nonliving systems including the Universe Itself”

If these conjectures turn out to be true in the future, the fitting of experimental data into the Planckian distribution equation displayed in **Figure 7** may provide the empirical basis for integrating *energy quantization*, *organization*, and the *information-energy complementarity* into a coherent theoretical framework previously referred to as “gnergetics”, defined as the integrated science (-etics) of *information* (gn-) and *energy* (-erg) [2, pp. 15-18].

C.4. ‘Raser’ Model of Enzyme Catalysis and the SID-TEM-TOF Mechanism

It seems possible that, just as the blackbody radiation equation of Planck was found to apply to the single-molecule enzyme turnover times of cholesterol oxidase as shown in **Figure 3 b)** and [2, Chapter 11], so the subatomic mechanisms underlying the phenomenon of laser may apply (analogically) to the molecular mechanism of enzyme action, as indicated in **Figure 5 b)**:

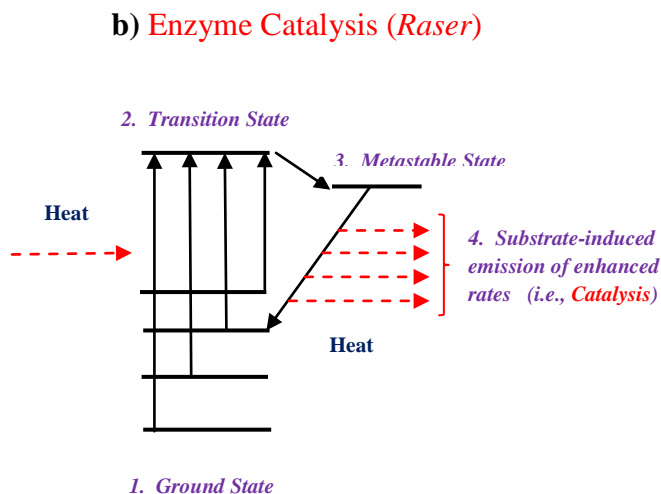
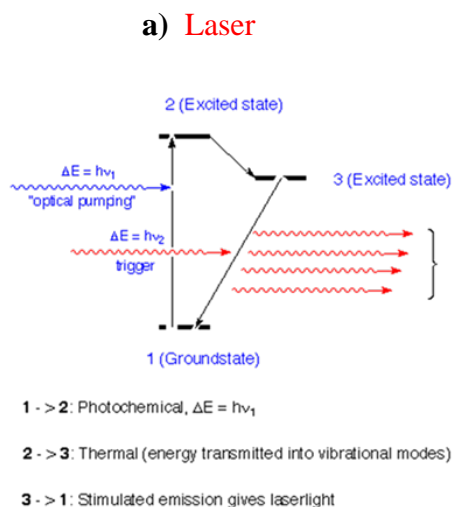


Figure 5. a) Mechanism underlying **Laser** (Light Amplification based on the Stimulated Emission of Radiation). **b) Raser** (Rate Amplification based on the Substrate-Enhanced reaction Rates) model of enzyme catalysis, also called the SID-TEM-TOF mechanisms (**S**timulus-**I**nduced **D**eactivation of **T**hermally **E**xcited **M**etastable state leading **TO** **F**unction).

In the mechanism of laser, the input of “pumping” photons, $h\nu_1$, causes the electrons of the atoms constituting the laser medium (e.g., ruby crystal) to undergo a transition from the ground-state energy level to the excited-state energy level (see the 1 to 2 arrow in **Fig. 5 a)**). The excited state is short-lived, lasting for only about 10^{-12} seconds, and lose some of its energy as heat and undergo a transition to a lower energy level called “metastable” state (see the 2 to 3 arrow, **Figure 5 a)**). State 3 is more stable than State 2 but still much more unstable than the ground state (see 1). When there are enough number of electrons in the metastable/excited state (thereby creating the so-called “population inversion”), the arrival of triggering photons, $h\nu_2$, induces the de-excitation of electrons from the metastable excited state back to the ground state (see the 3 to 1 arrow), accompanied by the emission of photons identical to the triggering photons, $h\nu_2$, but larger in number than the original triggering photons, leading to amplification. The emitted photons are “coherent” in that they are identical with respect to (i) amplitude, (ii) frequency, and (ii) phase.

Unlike electrons in atoms that are all in the lowest-energy ground state before absorbing photons, enzymes appear to exist in different ground states to begin with, before thermal excitation (i.e., before absorbing thermal energy), as indicated by the four solid bars in Figure 5 b), which is enabled by the quantization of the Gibbs free energy.

It is possible that, when an enzyme molecule absorbs enough thermal energies through Brownian motions, it is excited to the transition state lasting only for a short

period of time, probably for 10^{-14} to 10^{-12} seconds, the periods of chemical bond vibrations. The thermally excited enzyme is thought to undergo a transition to a more stable state called the “metastable” or “activated” state lasting probably up to 10^{-9} seconds. It appears that the metastable/activated state can be deactivated in two ways – (i) spontaneously (as in “spontaneous emission” in laser), and (ii) induced by substrate binding (as in “induced emission”). During spontaneous deactivation of the active/metastable state of an enzyme, the excess energy may be released as uncoordinated random infrared photons, whereas, during the substrate-induced deactivation, the excess energy of the enzyme-substrate complex may be released in a coordinated manner, resulting in catalysis, just as the triggering photon-induced de-activation of population-inverted electrons in atoms results in the amplification of emitted photons in laser.

The enzyme catalytic mechanism depicted in **Figure 5 b)** may be referred to as the SID-TEM-TOF mechanism because it embodies the following three key processes:

- (i) **S**ubstrate- or **S**timuli-**I**nduced **D**eactivation in Step 4,
- (ii) **T**hermally **E**xcited **M**etastable state in the 1 to 2 and 2 to 3 steps
- (iii) leading **TO** **F**unction i.e., catalysis, in the 3 to 1 Step.

It is here postulated that the SID-TEM-TOF mechanism underlies many processes (and/or their records/results) that obey the Planckian distribution, Eqs. (2) or (3).

D. RNA levels in budding yeast

When glucose is switched to galactose within a few minutes, budding yeast cells undergo massive changes in the copy numbers (from 0 to several hundreds) of its mRNA molecules encoded by 6,300 genes over the observational period of hours [10,11]. Garcia-Martinez et al. [10] measured the levels of over 5,000 mRNA molecules at 6 time points (0, 5, 120, 360, 450, and 85 minutes) after glucose-galactose shift using microarrays, generating over 30,000 mRNA level data points. Of these data, 2159 mRNA levels were chosen arbitrarily and grouped into 250 bins to generate a histogram shown in **Figure 7 b)** (see Experimental). As can be seen in this figure, the histogram fits the Planckian distribution almost exactly, with RMSD value of 10.64. The numerical values of the Planckian distribution parameters are given in **Table IV**, Row b).

E. RNA levels in human breast tissues

Perou et al. [6] measured the mRNA levels of 8,102 genes in the normal cells, the breast cancer tissues before and after treating with the anticancer drug, doxorubicin, in 20 breast cancer patients using microarrays. Of 8,102 genes, we analyzed 4,740 genes and their transcripts from 20 patients. A total of $4,740 \times 20 = 94,800$ mRNA levels were divided into 60 bins to generate a histogram shown in **Figure 7 c)** (see Experimental). Again the experimental curve fitted the Planckian distribution equation with great fidelity, the RMSD value being 368.8. (It should be pointed out that the magnitude of the RMSD values depend on the total number of the points in the data set; the greater the number of data points, the greater is the RMSD even if the fit between the experimental and

theoretical curves are comparable by visual inspection.)

F. Human T-cell receptor variable region gene sequence diversity

The T-cell receptor consists of two chains, α and β , and each chain in turn consists of the transmembrane, constant and variable regions. The variable regions of T-cell receptors, called CDR3 (Complement Determining Region 3), recognize pathogens and initiate an immune response. The CDR3 length between conserved residues ranges from 20 to 80 nucleotides. Murugan et al. [12] analyzed the nucleotide sequence data of T-cell beta chain CDR3 regions obtained from nine human subjects, each subject generating on average 232,000 unique CDR3 sequences. The germline DNA encoding the beta chain of human T-cell receptors has 48 V-genes, 2 D-genes and 13 J-genes. These gene segments are recombined via a series of stochastic recombination mechanisms catalyzed by appropriate enzymes to generate a large repertoire of CDR3 sequences. Each CDR3 sequence can be viewed as the result of a generative event describable by several random variables, including V-, D- and J-gene choices.

From the set of observed CDR3 sequences, Murugan et al. [12] was able to construct a mathematical equation called the *generative probability function* that predicts the probability of generating CDR3 sequence σ , $P_{\text{gen}}(\sigma)$. $P_{\text{gen}}(\sigma)$ is the sum of the probabilities of all recombination events involved in producing CDR3 sequence σ . A typical example of the CDR3 sequence histogram predicted by $P_{\text{gen}}(\sigma)$ for one subject is given in **Figure 7 d)** (see Experimental). This histogram was obtained by transforming the original left long-tailed histogram to the right long-tailed histogram by replacing $-\log P_{\text{gen}}(\sigma)$ with $(30 -$

$|P_{\text{gen}}(\sigma)|$), where $|P_{\text{gen}}(\sigma)|$ is the absolute value of $P_{\text{gen}}(\sigma)$. (It was subsequently found that the original left long-tailed histogram could be fitted into PDE just as well, without any transformation.) As evident in **Figure 7 d**), the agreement between the $P_{\text{gen}}(\sigma)$ distribution and the Planckian distribution is excellent.

G. Decision-time histogram

The drift-diffusion model (DDM) of decision-making is a widely employed theoretical model in behavioral neurobiology [13, 14, 16, 17, 18]. DDM accurately reproduces the decision-time histograms (see Experimental in **Figure 7 e**), reflecting the well-known phenomena [13] that it takes the brain longer to process more difficult tasks than easier ones. **Figure 6 a**) depicts the two essential features of DDM, i.e., (i) the Gaussian-distributed drift rates (i.e., the rates of evidence accumulation in the brain), which can be represented as $\tan \alpha$, where α is the arctangent of the drift rate, D/t , with D as the decision threshold (i.e., the level at which, when reached by accumulating evidence, a decision is made) and t is the time when a decision is made, and (ii) the non-linear relation between the independent variable of the Gaussian distribution function and the decision times.

Because of these two features, the Gaussian-distributed drift rates can produce a right-long-tailed decision-time histogram as shown in **Figure 6 b**), where the right-long tailed distribution was derived from the Gaussian distribution based on two operations: (i) transform the x coordinates of the Gaussian distribution (obtained by hand-digitizing the Gaussian curve found at http://en.wikipedia.org/wiki/Normal_distribution) to $D/\tan \alpha$, and (ii) retain the y coordinates of the Gaussian distribution unchanged. As **Figure 6 b**) demonstrates,

the Gaussian distribution transformed according to Operations (i) and (ii) above coincides with the Planckian distribution based on x , demonstrating that the Planckian distribution can, in principle, be derived from the Gaussian distribution based on DDM; i.e., DDM can act as the bridge between the Gaussian and Planckian distributions.

As shown in **Figure 7 e**), the experimentally observed decision-time histogram was almost exactly simulated by the Planckian distribution equation. Just as random mechanisms can be claimed to underlie the Gaussian distribution, so it is here claimed that the SID-TEM-TOF (Signal-Induced Deactivation of Thermally Excited Metastable state leading TO Function) mechanism underlies the Planckian distributions. The SID-TEM-TOF mechanisms, in turn, can be viewed as the generalized Raser model of enzyme catalysis (**Figure 5 b**)).

It would be convenient to define as the “Planckian processes” all those processes in nature that obey the Planckian distribution equation or law, just as the Gaussian processes can be defined as those processes that obey the Gaussian distribution law. Since random processes are implicated in all Gaussian processes, so it would be reasonable to assume that, underlying all Planckian processes, there exists one or more non-random mechanisms common to many, if not all, Planckian processes. One of such common mechanisms is suggested to be the SID-TEM-TOF mechanism, i.e., **Figure 5 b**), or its equivalent.

The mathematical relation between the Gaussian and Planckian distributions can be established based on the drift-diffusion model (DDM) of decision making [18]. It should be noted that t and x are synonymous (**Figure 6 a**)). The Planckian distribution can be derived from the Gaussian distribution based on the simple algorithm

consisting of two steps – (i) change x to $D/\tan \alpha$, where α is the arctan of D/x , where

D is the decision threshold, and (ii) keep the y coordinates unchanged.

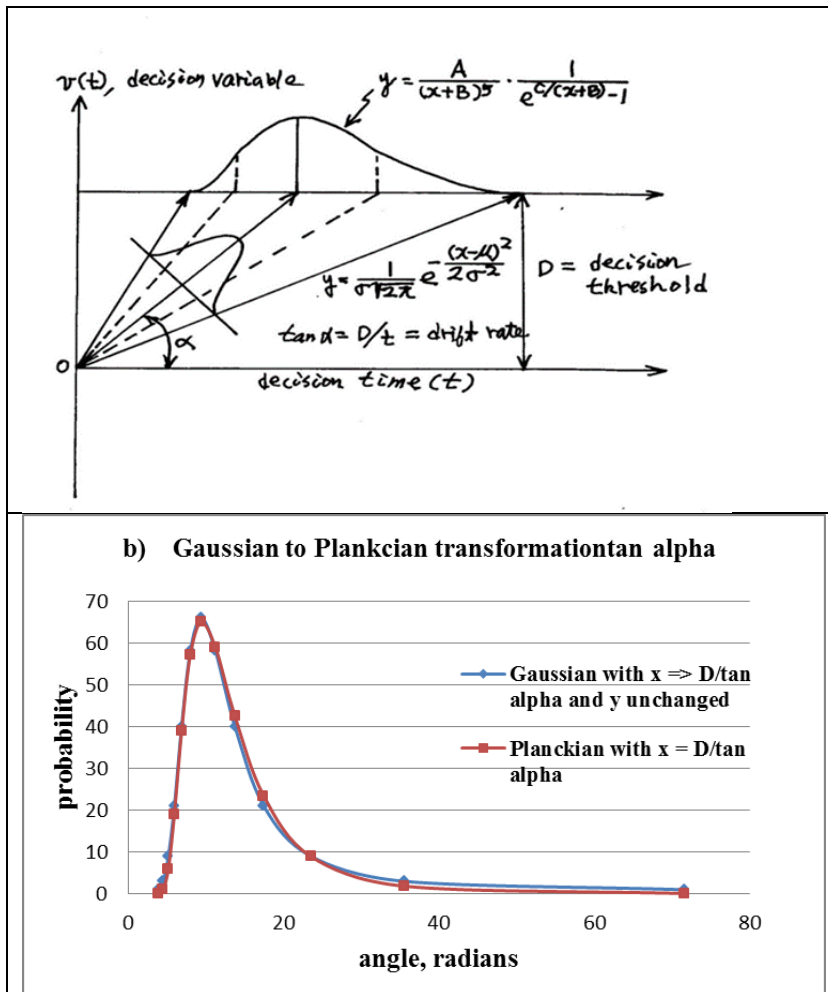


Figure 6. a) A schematic representation of the drift-diffusion model (DDM) of decision making adopted from [18]. **b)** The derivation of the Plankian distribution from the Gaussian distribution based on the DDM of decision making.

H. fMRI signals from the human brain before and after psilocybin

The functional magnetic resonance imaging (fMRI) technique, when applied to the human brain, allows neuroscientists to monitor neuronal firing activities in different regions of the brain noninvasively within seconds of infusing a psychedelic drug such as psilocybin. Carhart-Harris et al. [15] measured the fMRI signals from the brains of 15 healthy volunteers before and after the intravenous infusion of psilocybin lasting for 60 seconds. The subject's consciousness, cerebral blood flow (CBF), and fMRI signals responded within seconds. CBF values decreased in all regions of the brain and the subject reported that their "thoughts wandered freely". Out of the 9 brains regions examined (2° visual, 1° visual, motor, DAN, auditory, DMN, R-FP, L-FP, salience), four regions exhibited significant changes in their fMRI signals characterized by increases in the deviations of the local signals from their mean, i.e., an increase in variance. By "local" is meant to indicate brain tissue volume elements (voxels) measuring a few mm in linear dimensions. When the distances of the signals from individual voxels from the group-mean fMRI signal are calculated and grouped into bins and their frequencies are counted, histograms are obtained such as shown in **Figures 7 f)**, which could be fitted reasonably well to the Planckian distribution equation (see Planckian). The numerical values of the Planckian distribution equation fitting these two histograms differed, especially the b/A ratios which increased from 0.93 to 1.62 by the psilocybin infusion (see Row f in **Table IV**).

I. The ultraviolet catastrophe in econophysics

The Rayleigh-Jeans law [19] predicts that the power of radiation emitted by a heated

body increases with the frequency raised to a fourth power. This exponential law works fine at long wavelengths but fails dramatically at short wavelengths, leading to the so-called the "ultraviolet catastrophe" [20].

Some physicists [21] have suggested that the distribution of incomes in a society can be modeled using the Boltzmann-Gibbs equation, a power law, making the analogy that money can be treated as energy (see **Table III**). Again this statistical mechanical approach works fine for high income levels but fails badly at low income levels (see **Figures 7 g)** and **h)**). However, the Planckian distribution law, Eq. (2), fits the 1996 and 2013 US annual income distributions almost exactly.

If we assume that the exponential distributions shown in **Figures 7 g)** and **h)** are analogous to the Rayleigh-Jeans law and the Planckian distributions to the Planck radiation law, Equation (1), we can reasonably conclude that the deviation of the exponential distributions from the observed income distributions are analogous to the 'ultraviolet catastrophe' in the physics of over one hundred years ago.

The resolution of the ultraviolet catastrophe in physics in the early decades of the 20th century with the discovery of Planck's radiation law introduced a new concept into physics, i.e., *quantum of action*, as the unit of organizing matter and energy in abiotic systems. Similarly, the resolution of the "econophysics" version of the ultraviolet catastrophe with the Planckian distribution equation demonstrated in **Figures 7 g)** and **h)** may introduce another novel concept into natural and human sciences – the **quantization of organization** in terms of the *Planckian information*, I_P , defined as follows:

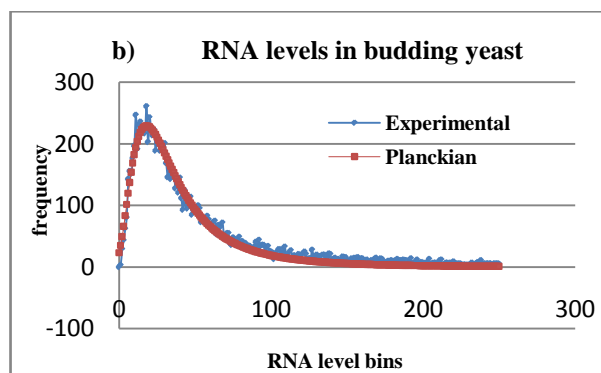
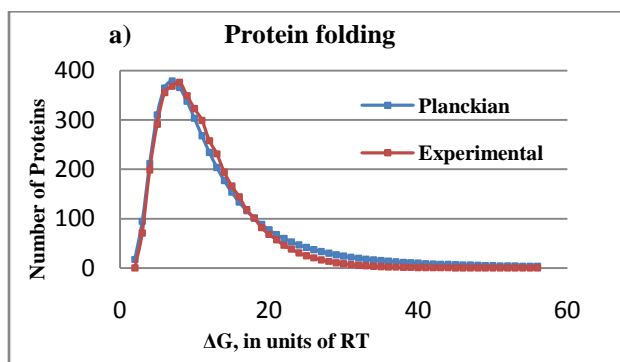
$$I_P = \log_2 [\text{AUC(P)}/\text{AUC(G)}] \text{ bits} \quad (8)$$

where AUC(P) stands for the area under the curve of the Planckian distribution and AUC(G) the area under the curve of the Gaussian distribution whose rising phase coincides with the rising phase of the

Planckian distribution [22]. These and related ideas are collected in **Table III**.

Table III. A comparison between the ‘ultraviolet catastrophes’ in quantum physics and econophysics.

	Ultraviolet Catastrophe in	
	Quantum Physics	Econophysics
1	energy	money
2	frequency	annual income
3	blackbody radiation spectra	annual income distribution
4	laws of thermodynamics (energy, entropy, work)	laws of organization & selection (energy, entropy, information; i.e., gnergy [2])
5	Boltzmann-Gibbs law	Planckian distribution law
6	$y = ae^{-bx}$	$y = a/(Ax + B)^5 / (e^{b/(Ax + B)} - 1)$
7	organization of energy in atoms	organization of income in society (?)



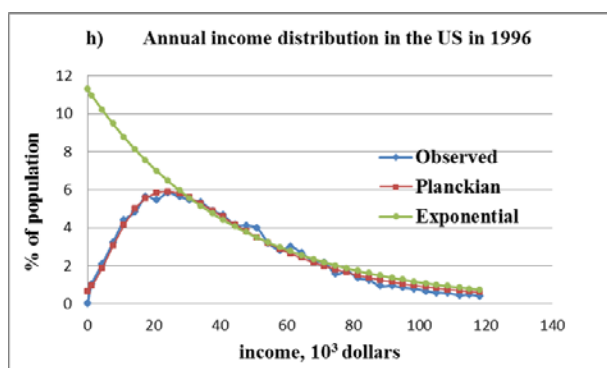
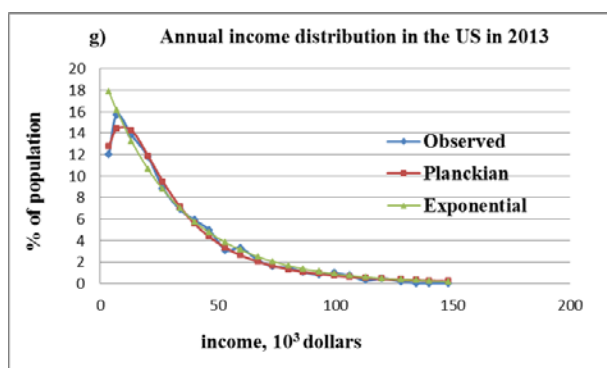
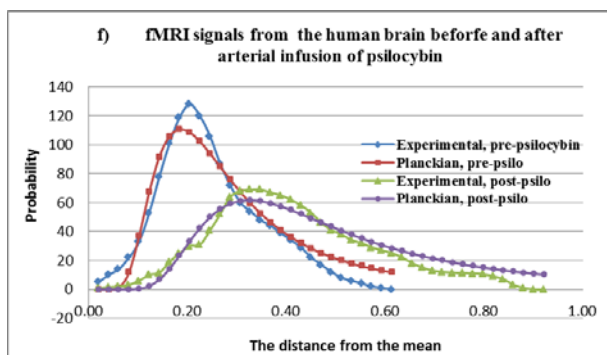
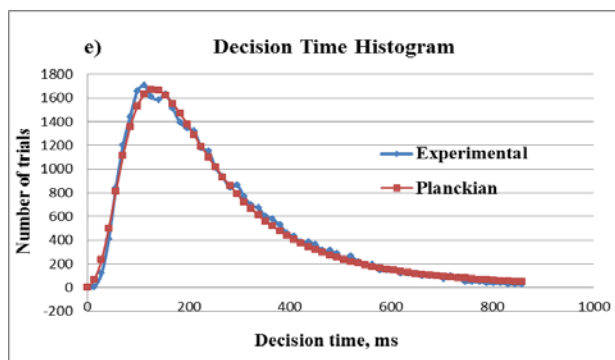
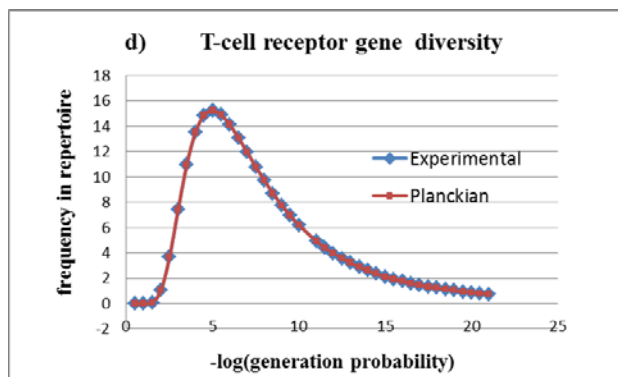
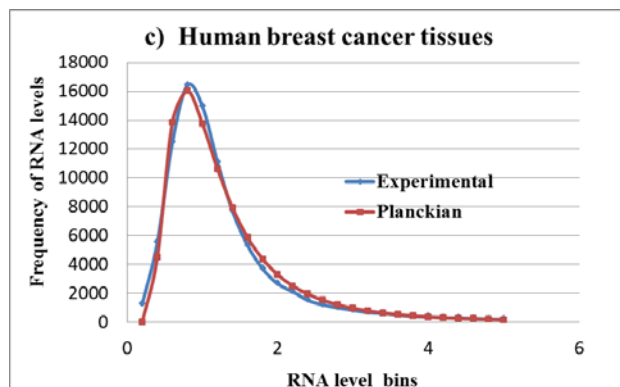


Figure 7. The universality of the Planckian distribution. **a)** protein folding [5]; **b)** RNA metabolism in unicellular organism [2, Chapter 12]; **c)** RNA metabolism in human breast tissues [6]; **d)** human T-cell variable region gene diversity [12]; **e)** the decision-time histogram of the human brain [13, 16, 17, 18]; **f)** fMRI (functional magnetic resonance imaging) data from human brains before and after the arterial infusion of psilocybin [15]; **g)** the annual income distribution in the US in 2013 [21]; and **h)** the annual income distribution in the US in 1996 [21].

The numerical values of the parameters of the Planckian distribution equation fitting

the diverse sets of data shown in Figure 8 are summarized in Table 3.

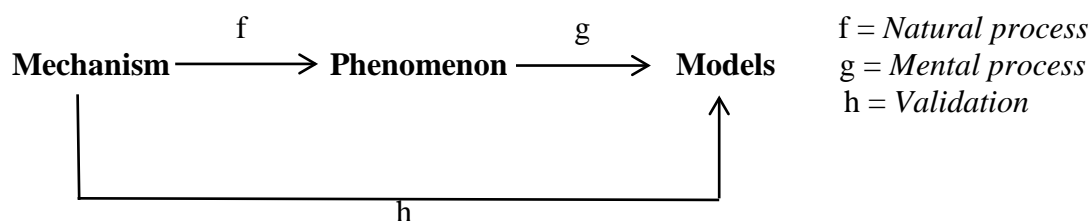
Table IV. The numerical values of the parameters of the Planckian distribution, Equations (2) or (3), that fits the histograms shown in **Figure 8**. The italicized lower values in the last row are the post-psilocybin values.

Histogram	a	b	A	B	C	b/A
a) Protein folding	1.24×10^{14}	368.3	9.45	6.82	-	38.97
b) RNA levels (yeast)	-	-	1.11×10^{12}	13.962	159.30	
c) RNA levels (breast tissues)	8×10^{10}	40	8	1.7	-	5.00
d) DNA sequence	-	-	7.019×10^6	0.063	25.00	
e) Decision times	8.5×10^{11}	101.49	0.1077	6.345	-	942.34
f) fMRI signals	7.6×10^{10}	107.67	115.9	0	-	0.928
	4.4×10^{10}	43.17	26.7	0	-	1.617
g) US income 2013	1.10×10^{12}	275.4	1.93	36.87	-	142.60
h) US income 1996	1.60×10^{12}	247.6	1.71	17.33	-	144.91

J. The MPM category: Mechanism, Phenomenon, and Model

The concept of a mathematical category is universal in that it can be applied to all fields of human intellectual activities from physics, to chemistry, to biology, to

mathematics, and to philosophy [23]. One example of a category that has a universal applicability consists of the triad of *mechanism*, *phenomenon*, and *model* as diagrammed in **Table V**. This so-called *MPM category* can be viewed as a type which has many tokens, including semiotics, the study of signs [25, 26] (see Row 6 in **Table V**).

Table V. The MPM category. For a definition of a category, see [24].

Discipline	Phenomenon (P)	Models (M)	Mechanisms (M)
1. Physics	Blackbody radiation (Fig. 1)	Planck radiation equation (Eq. 1)	Transitions between atomic orbitals (Fig. 5 a)
2. Chemistry	Chemical reactions	Kinetic equations or laws (zero th , first, second order, etc.)	Molecular mechanisms (e.g., electrophilic or nucleophilic attacks)
3. Biology	Enzyme catalysis	Planckian distribution law (Fig. 3 b)	SID-TEM-TOF mechanisms (Fig. 5 b)
	Cell biology	Planckian distribution law (Fig. 7 b), the Bhopalator model [28])	Conformon-driven IDS underlying all cell functions [2, Section 12.15]
	Evolution	Zeldovich-Shakhnovich model [29]	Protein stability- and comparative genomic data-based mechanisms [29]
4. Neuroscience	Decision-making [14,16,17,18]	Ex-Gaussian distribution [13]	Diffusion-drift mechanism [13]
		Planckian distribution (Fig. 7 e)	SID-TEM-TOF mechanisms (Fig. 5 b)
	fMRI signals [15]	Planckian distribution (Figs. 7 f)	SID-TEM-TOF mechanisms (Fig. 5 b)

5. Mathematics	“Names” of Burgen’s fundamental triad [23, Fig. 1]	“Naming relations” [23, Fig. 1]	“Support” [23, Fig. 1]
6. Peircean Semiotics [25, 26]	Sign	Interpretant	Object

K. The Universality of the Planckian distribution

As evident above, the Planckian distribution equation, Eqs. (2) or (3), has been found to fit the experimental data measured from a surprisingly wide range of disciplines, from atomic physics (i.e., blackbody radiation) to enzymology, to cell biology, and to brain neurophysiology (**Figure 7**). These unexpected findings may indicate that, underlying all the varied phenomena obeying the Planckian distribution equation, there exists a common mechanism, just as all the phenomena obeying the Gaussian distribution law implicate a common mechanism, namely,

random processes. The connection between the Gaussian and the Planckian distributions may not be as haphazard as it may appear from this casual statement but much more substantial.

Another possible common mechanism underlying the universal applicability of the Planckian distribution equation may be sought in the postulated universality of the wave-particle duality in all organized material systems, from atoms to cells to brains to the Universe itself, and this possibility is partially supported by the fact that the first term of the Planck radiation equation, Eq. (2), is related to the number of standing waves in a physical system. This idea is depicted in **Figure 8**.

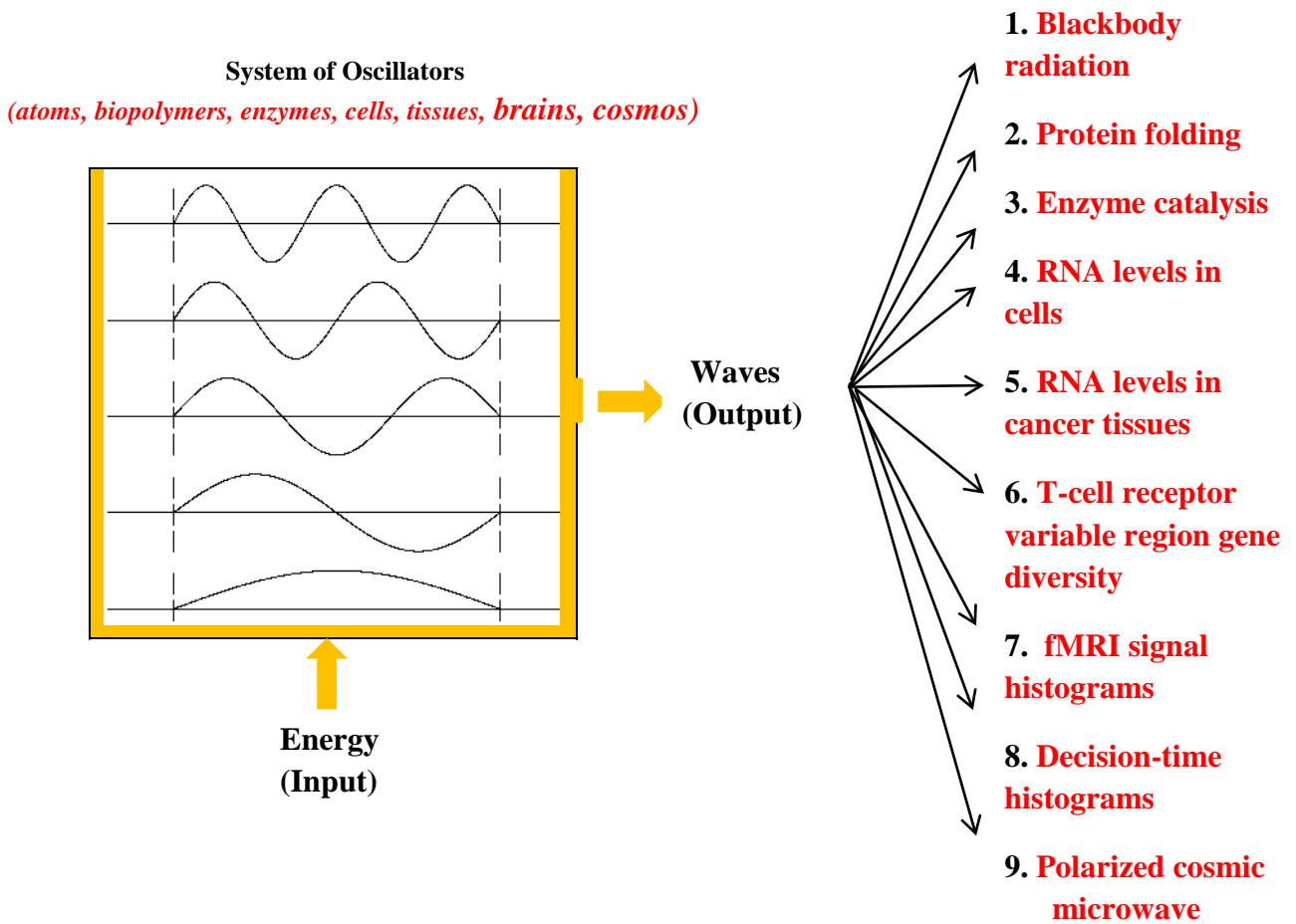


Figure 8. One possibility to account for the universality of the Planckian distribution equation in nature is the postulate that the wave-particle duality, first discovered in atomic physics, may operate at all scales of material systems, from atoms to the cell to the brain and to the Universe [22].

IV. CONCLUSIONS

A. *The universality of the Planckian distribution.* We have demonstrated that the Planckian distribution, Eqs. (2) or (3), is a new distribution law, comparable to the Gaussian distribution, that applies to a wide range of experimental data measured from atoms, biopolymers, living cells, and brains (**Figure 7**). One plausible explanation for

these unexpected findings is that, underlying all Planckian processes, there are common physical processes mediated by ‘standing waves’ (electromagnetic, gravitational, mechanical, and concentration) as represented by the first term in the Planckian distribution law, Eq. (2). The number of standing waves present within a system is determined by the volume and topology of the system being heated, as schematically represented in **Figure 8**.

B. *Planckian processes as selected Gaussian processes.* Many, if not all, Planckian processes may derive from the

subset of Gaussian (or random/chaotic) processes that have been selected because of their functional roles in physical systems under given environmental conditions. The mechanisms enabling such a function-realizing selection processes may be identified with the SID-TEM-TOF mechanism which is in turn dependent on the Raser model of enzyme catalysis (**Figure 5 b**)).

C. The wave-particle duality in biomedical sciences. Since (i) the Planckian distribution, Eqs. (2) or (3), consists of two components – one related to the number of standing waves per volume and the other to the average energy of such oscillatory modes, (ii) the wave aspect of the Planck radiation equation is fundamental in accounting for not only blackbody radiation spectra but also subatomic organization of atoms in terms of atomic orbitals, and (iii) the Planck distribution applies to both atoms (**Figure 2 a**), **b**) and **c**)) and living systems (**Figures 7 a**), **b**), **c**), **d**), **e**), **f**), **g**) and **h**)), it appears logical to infer that the wave aspect of the wave-particle duality plays a fundamental role in the behavior of living structures and processes in biology and medicine. In other words, it may be impossible for biomedical scientists to completely account for living processes, both normal and diseased, without taking into account their wave aspect along with their particle aspect.

D. Science as an irreducible triad of data, mathematical models, and mechanisms. The concept of an irreducible triad is basic to the triadic philosophy of C. S. Peirce [25, pp. 1-16]. Applying this concept to the definition of science leads to the conclusion that science cannot be defined in terms of two or less of the triad, i.e., data (also known as measurement), mathematical models, and physical mechanisms. We may refer to this

philosophical position as the $M \times M \times M$ or M^3 *doctrine of science*, where the first M stands for *measurement*, the second for *mathematical models*, and the third for *physical mechanisms*, all of which are simultaneously required to define science. The M^3 doctrine of science described here may be viewed as a token or example of the MPM category defined in **Table V**.

ACKNOWLEDGEMENT

I thank my students for their invaluable help in computing in the Theoretical and Computational Cell Biology Lab at Rutgers. My special thanks go to Kenneth So for introducing the parameters, A and B, in the Planckian distribution equation, Eq. (2).

REFERENCES

- [1] See Planck's Law at http://en.wikipedia.org/wiki/Planck's_law.
- [2] S. Ji, *Molecular Theory of the Living Cell: Concepts, Molecular Mechanisms, and Biomedical Applications*, New York: Springer, 2012.
- [3] H. P. Lu, L. Xun, and X. S. Xie, "Single-Molecule Enzymatic Dynamics," *Science*, vol. 282, pp. 1877-1882, 1998.
- [4] S. Ji, "Experimental and Theoretical Evidence for the Energy Quantization in Molecular Machines and Living Cells, and the Generalized Planck Equation (GPE)," a poster presentation at the *EMBO/EMBL Symposium on Molecular Machines: Lessons from Integrating Structures, Biophysics and Chemistry*, Heidelberg, May 18-21, 2014.
- [5] K. A. Dill, K. Ghosh, and J. D. Schmit, "Physical limits of cells and proteomes," *Proc. Nat. Acad. Sci. USA*, vol. 108, no. 44, pp. 17876-17582, 2011.
- [6] C. M. Perou, T. Sorlie, M. B., et al.,

- “Molecular portraits of human breast tumors,” *Nature*, vol. 406, no. 6797, pp. 747-52, 2000.
- [7] M. A. Lauffer, “The Significance of Entropy-Driven Processes in Biological Systems,” *Comments Mol. Cell. Biophys.*, vol. 2, no. 2, pp. 99-109, 1983.
- [8] H. B. Callen, *Thermodynamics: An introduction to the physical theories of equilibrium thermostatics and irreversible thermodynamics*, New York: John Wiley & Son, Inc., 1985, pp. 90-101.
- [9] H. Frauenfelder, B. H. McMahon, R. H. Austin, K. Chu, and J. T. Groves, “The role of structure, energy landscape, dynamics, and allostery in the enzymatic function of myoglobin,” *Proc. Nat. Acad. Sci. (U.S.)*, vol. 98, no. 5, pp. 2370-74, 2001.
- [10] J. Garcia-Martinez, A. Aranda, and J. E. Perez-Ortin, “Genomic Run-On Evaluates Transcription Rates for all Yeast Genes and Identifies Gene Regulatory Mechanisms,” *Mol Cell*, vol. 15, pp. 303-313, 2004.
- [11] S. Ji, A. Chaovalitwongse, N. Fefferman, W. Yoo, and J. E. Perez-Ortin, “Mechanism-based Clustering of Genome-wide mRNA Levels: Roles of Transcription and Transcript-Degradation Rates,” in *Clustering Challenges in Biological Networks* (S. Butenko, A. Chaovalitwongse, and P. Pardalos, eds.), Singapore: World Scientific Publishing Co., 2009, pp. 237-255.
- [12] A. Murugan, T. Mora, A. M. Walczak, C. G. Callan Jr, “Statistical inference of the generation probability of T-cell receptors from sequence repertoires,” *arXiv:1208.3925v1 [q-bio.QM]*, 20 Aug 2012.
- [13] R. D. Luce, *Response Times: Their Role in Inferring Elementary Mental Organization*. New York: Oxford University Press, 1986, Figure 11.4.
- [14] G. Deco, E. T. Rolls, L. Albantakis, R. Romo, “Brain mechanisms for perceptual and reward-related decision-making,” *Progr. Neurobiol.*, vol. 103, pp. 194-213, 2013.
- [15] R. L. Carhart-Harris, R. Leech, P. J. Hellyer PJ, et al., “The entropic brain: a theory of consciousness informed by neuroimaging research with psychedelic drugs,” *Front Human Neurosci*, vol. 8, pp. 1-22, 2014.
- [16] A. Roxin, A. Lederberg, “Neurobiological Models of Two-choice Decision Making Can Be Reduced to a One-Dimensional Nonlinear Diffusion Equation,” *PLoS Computational Biology*, vol. 4, no. 3, pp. 1-13, 2008.
- [17] J. Vandekerckhove, F. Tuerlinckx, “Fitting the Ratcliff diffusion model to experimental data,” *Psychonomic Bulletin & Review*, vol. 14, no. 6, pp. 1011-1026, 2007.
- [18] R. Ratcliff, G. McKoon, “The Diffusion Decision Model,” <http://digitalunion.osu.edu/r2/summer06/web/index.html>, 2006.
- [19] http://en.wikipedia.org/wiki/Rayleigh%E2%80%9393Jeans_law
- [20] http://en.wikipedia.org/wiki/Ultraviolet_catastrophe
- [21] Yakovenko, V. M. (2008). *Econophysics, Statistical Mechanics Approach to*. arXiv:0709.3662v4 [g-fin.ST] 3 Aug2008.
- [22] S. Ji, “The wave-particle duality in molecular machines, living cells, and human brains,” a poster presented at the 59th Annual Meeting of the Biophysical Society, February 7-11, 2015, Baltimore, Maryland.
- [23] M. Burgin, “Unified Foundations for Mathematics,” arXiv:math/0403186[math.LO], 2004..
- [24] Arbitrariness of signs. See, for example, [http://en.wikipedia.org/wiki/Sign_\(linguistics\)](http://en.wikipedia.org/wiki/Sign_(linguistics)).
- [25] R. Marty, “76 Definitions of The Sign by C. S. Peirce,” 2014,

<http://www.cspeirce.com/rsources/76defs/76defs.htm>

[26] C.S. Peirce at http://en.wikipedia.org/wiki/Charles_Sanders_Peirce.

[27] Category Theory at http://en.wikipedia.org/wiki/Category_theory

[28] S. Ji, “The Bhopalator – A Molecular Model of the Living Cell Based on the Concepts of Conformons and dissipative Structures,” *J. theoret. Biol.*, vol. 116, pp. 399-426, 1985.

[29] S. Ji S, “The Zeldovich-Shkhnovich and the MTLC Models of Evolution,” in *Molecular Theory of the Living Cell: Concepts, Molecular Mechanisms, and Biomedical Applications*, New York: Springer, pp. 509-519, 2012.

Authors Index

Ahmed, G. A.-R.	104	Li, Z.	83
Al Tawil, E.	18	Mansurov, Z. A.	74
Ali, E.	91	Merabet, A.	96
Aliouat, S.	96	Meziou-Chebouti, N.	96
Anarghya, A.	11	Mohamad-Saleh, J.	60
Atman, A.	42	Monnier, A.	18
Atupelage, C.	27	Mulyono, S.	91
Avci, D.	23, 38	Nagahashi, H.	27
Avci, E.	100	Nguyen, Q. T.	18
Behidj, N.	96	Onami, S.	27
Coteli, R.	100	Park, M.-H.	33
Deschrevel, B.	18	Ranjith B. S.	11
Dogantekin, E.	100	Rao, N.	11
El-Hamidy, S. M.	104	Rosdi, B. A.	60
Gobouri, A. A.	53	Salah, N. A.	104
Gurumurthy, B. M.	11	Semenchenko, A.	42
Hadj-Kali, M.	91	Sun, Y.-A.	83
Ji, S.	115	Tuncer, T.	100
Ke, W.	83	Wang, G.	83
Khalifa, M. E.	53	Wang, J.	68
Khedr, A.	104	Wang, K.	83
Khorshid, F. A.	104	Yakno, M.	60
Kim, D.-W.	33	Yatthesha, R. B.	11
Kirouani, M.	96	Zhang, Q.	83
Kyoda, K.	27	Zhao, B.	68
Li, H.	68		